CO_2 mass transfer and interfacial studies for application of carbonated water injection

Axisymmetric pendant drop analysis for simultaneous calculation of CO_2 diffusion coefficient and interfacial tension

by

Nikhil Bagalkot

Thesis submitted in fulfilment of
the requirements for the degree of
PHILOSOPHIAE DOCTOR
(PhD)

Faculty of Science and Technology
Department of Energy and Petroleum Engineering
2019

University of Stavanger
NO-4036 Stavanger
NORWAY
www.uis.no

ISBN: 978-82-7644-823-8
ISSN: 1890-1387
PhD: Thesis UiS No. 439

Abstract

Worldwide, enhanced oil recovery (EOR) projects have been on a gradual rise since early 2000, especially EOR by CO_2 injection. Globally, at present, EOR by CO_2 injection contributes approximately 67.5% of projects (83 of 123) among carbonate reservoirs, and approximately 23.5% of projects (50 of 213) among sandstone reservoirs and is expected to rise by 0.1 % per year. Additionally, the application of CO_2-EOR is expected to increase, due to its contribution to mitigating anthropogenic CO_2 (geological CO_2 sequestration). However, problems associated with CO_2-EOR, such as poor sweep efficiency, early breakthrough, high transportation cost, and trouble of CO_2 availability, have reduced its value. Additionally, CO_2-EOR may not be a safe option for geological storage of CO_2, due to the upward movement of injected CO_2. These problems have lead to the search for alternative injection strategies, which can increase EOR efficiency and, at the same time, promote increased CO_2 geological storage capacity.

In recent years, carbonated water injection (CWI) has shown to be a promising enhanced oil recovery (EOR) method and a suitable alternative to CO_2-EOR. Laboratory and field studies have demonstrated that the injection of CO_2 saturated water (carbonated water, CW) is a practical option for both EOR and CO_2 sequestration. From an EOR point of view, carbonated water injection (CWI) enhances the sweep efficiency and mobility by reducing the gravity segregation that is frequently encountered by CO_2-EOR, hence increasing the residual oil recovery. In addition to the EOR method, the CWI also promotes safe, increased, and long-term geological storage of CO_2, as the carbonated water has a higher density, compared to native brine (formation water).

At the pore scale CO_2 mass transfer, fluid-fluid interfacial phenomena, mass transfer kinetics, and property alteration of hydrocarbon are critical in understanding and optimising CWI. CO_2 mass transfer into the oil,

coupled with CW-oil interfacial tension (IFT) alterations, is one of the first and primary processes which affect critical parameters like viscosity and density alterations, swelling and hence mobilisation of hydrocarbon. However, there is a lack of understanding of CO_2 mass transfer and interfacial phenomena, and the factors influencing them for both CO_2-EOR and CWI. Further, unlike other recovery methods, such as waterflooding and CO_2-EOR, for CWI the effect of additives like salts and nanoparticles has not been fully understood.

This thesis aims to address five main aspects that have been overlooked and are critical in understanding the mechanisms that form the principal part of oil recovery by CWI. The first is the estimation of CW-hydrocarbon IFT and the development of a method to estimate the dynamic IFT. The second is to develop a mathematical and numerical model, which validates with experimental results, for calculating the effective CO_2 diffusion coefficient. The model should be versatile so that it may be applied for both CO_2-hydrocarbon and CW-hydrocarbon systems. The third is to analyse the interdependency of critical parameters such as diffusion coefficient, IFT, density, viscosity, mass/mole fraction, Gibbs free energy, temperature, pressure, and concentration gradient. The fourth aspect is to investigate the influence of combining additives such as nanoparticles/nanofluid and salts with CW on CO_2 mass transfer and interfacial properties. Finally, the influence of three phases of CO_2 (gas, liquid, and supercritical) on the IFT, CO_2 mass transfer, and fluid properties of liquids in which CO_2 is dissolved must be studied.

The present thesis combines experimental, theoretical, and numerical approach to address the above five challenges. In the experimental section, an Axisymmetric Drop Shape Analysis (ADSA) pendant drop method has been used for a large pressure range (up to 160 bar) at temperatures of 25^{o}C, 35^{o}C, and 45^{o}C. The experimental setup was modified to address the effect of nanofluid on CO_2 solubility in water.

IFT and dynamic volume increments of the pendant drop are obtained from the experiments.

In the mathematical approach, a compositional model was developed that combines the existing analytical equations and experimental volume with obtained mass/mole fractions, density, and viscosity of the hydrocarbon pendant drop as a function of time. The compositional model is combined with the experimental section to obtain the dynamic IFT. Further, in the theoretical part, a Gibbs free energy model (Eyring's absolute rate theory approach), based on the viscosity of the hydrocarbon pendant drop was used. The Gibbs energy model was presented to help better understand the behaviour of IFT with temperature, especially near the critical temperature of CO_2.

In the numerical approach, a new model, based on finite difference method, was developed to estimate the CO_2 diffusion coefficient in the hydrocarbon. The model couples with the experimental results to estimate the CO_2 diffusion coefficient, and can be used for a wide range of pressures and temperatures. Further, a relatively new approach was used in the numerical model that is capable of adapting the CW-hydrocarbon interface, due to swelling, as observed in real-time experiments. The approach eliminates error of about 36% arising from the assumption made by the conventional methods of a static boundary/volume.

The results indicated that IFT between CW and hydrocarbon is a function of the CO_2 phase and solubility. At pressures where CO_2 is in the gaseous phase, the IFT is directly proportional to the pressure, however, when CO_2 is supercritical or liquid phases, IFT is inversely proportional to the pressure. Further, the maximum IFT, the maximum density reduction, and the minimum diffusion coefficient occurred for pressure close to and lower than the phase change pressure of CO_2 (64 bar at 25ºC, and 74 bar at 35ºC and 45ºC). The dependency of the IFT on the density difference between CW and the hydrocarbon was found to be a main reason for this

behaviour of IFT with pressure. IFT reduced with increase in temperature for both CO_2-hydrocarbon and CW-hydrocarbon. However, IFT at 35ºC did not show a similar trend to that at 25ºC and 45ºC.

CO_2 diffusion coefficient in hydrocarbon was found to be influenced by IFT and CO_2 solubility. The IFT was observed to be the major contributor to the observed decrease in diffusion coefficient of CO_2 with the increase in pressure (up to phase-change pressure of CO_2), followed by a gradual increase in the diffusion coefficient with increase in pressure (above phase-change pressure).

For the combination of CW+nanoflids, it was observed that the dispersed nanofluid in CW enhanced the CO_2 mass transfer into the hydrocarbon (2% at 10 bar to 45% at 60 bar) and reduced the hydrocarbon viscosity (40% and 29%) and density. The silica nanofluid in CW led to a significant increase in the swelling of the hydrocarbon (3% at 10 bar to 48% at 60 bar). The nanofluid in CW increased the CO_2 solubility in water (17%). The Brownian motion was suggested as the main reason for the enhanced CO_2 solubility (CO_2 mass transfer). The nanofluid was also successful in reducing the CW-hydrocarbon IFT.

When salts were combined with CW, it was found that CW+$MgCl_2$ reduced both the CW-n-decane IFT (36.5%) and CO_2 mass transfer, while CW+Na_2SO_4 increased both the IFT and CO_2 mass transfer (57%). It is suggested that a reduction in IFT for CW+$MgCl_2$ combination is mainly due to the higher hydration energy of Mg^{2+}, whereas, for CW+Na_2SO_4, an increase or no alteration in the IFT was seen.

Acknowledgments

Swami Vivekananda once said, "*The secret of life is not enjoyment but education through experience*". I am grateful that I had an opportunity to learn through experience during my PhD research at the University of Stavanger. Carrying out my research at UiS has had a significant impact on me. I want to reflect on the people who have supported and helped me throughout this period.

Firstly, I would like to express my sincere gratitude to my advisor, Professor Aly A Hamouda for his continuous support, for his patience, motivation, constructive criticism, and immense knowledge. His guidance helped me in all the time of research and writing of this thesis. I could not have imagined having a better advisor and mentor for my PhD study. Further, I would like to thank all the engineers and technicians for their guidance on the construction of the experimental setup. I would also like to express thanks to current and previous leaders of PhD and Postdoc committee and my fellow PhD scholars for creating a great social environment.

Finally, I want to thank my wife and daughter for understanding (mostly ignoring) my absence from their lives during my PhD. I am grateful for their tolerance to my long hours away from home, and still stood like a pillar of support.

Nikhil Bagalkot

List of Papers

Paper-I — **Bagalkot, Nikhil**, and Aly A. Hamouda. "Experimental and numerical method for estimating diffusion coefficient of the carbon dioxide into light components." *Industrial & Engineering Chemistry Research* 56, no. 9 (2017): 2359-2374.

Paper-II — **Bagalkot, Nikhil,** and Aly A. Hamouda. "Diffusion coefficient of CO_2 into light hydrocarbons and interfacial tension of carbonated water–hydrocarbon system." *Journal of Geophysics and Engineering* 15.6 (2018): 2516-2529.

Paper-III — **Bagalkot, Nikhil,** and Aly A. Hamouda, and Ole Morten Isdahl. "Dynamic interfacial tension measurement method using axisymmetric drop shape analysis." *MethodsX* 5 (2018): 676-683.

Paper-IV — Aly A. Hamouda, and **Bagalkot, Nikhil**. "Experimental investigation of the influence of temperature on the interfacial tension and its relationship with alterations in hydrocarbon properties in the carbonated water-hydrocarbon system." *International Journal of Chemical Engineering and Applications, 9(2): 58-63.*

Paper-V — **Bagalkot, Nikhil**, and Aly A. Hamouda. "Interfacial tension and CO_2 diffusion coefficients for a CO_2+ water and n-decane system at pressures of 10 to 160 bar." *RSC Advances* 8.67 (2018): 38351-38362.

Paper-VI — **Bagalkot, Nikhil**, Aly A. Hamouda and Isdhal, M. "Influence of Silica Nanofluid on CO_2 Mass Transfer and Hydrocarbon Properties Alteration in a Carbonated Water-Hydrocarbon System." *Defect and Diffusion Forum* ***(accepted, in press).***

Paper-VII — Aly A. Hamouda, and **Bagalkot, Nikhil**. "Effect of slats on the interfacial tension and CO_2 mass transfer in carbonated water injection process." ***(under review).***

Table of Contents

List of Figures and Illustrations

List of Tables

List of Symbols, Abbreviations, and Nomenclature

Abbreviations

EOR - Enhanced oil recovery

CWI - Carbonated water injection

CW - Carbonated water

IFT - Interfacial tension

ADSA - Axisymmetric pendant drop analysis

CCS - Carbon dioxide capture and sequestration

GI - Gas injection

1D - One dimensional

2D - Two dimensional

3D - Three dimensional

DGT - Density gradient theory

EOS - Equation of state

CB - Carbonated brine

DIW - De-ionised water

SSW - Synthetic sea water

C_{SSW} - Carbonated synthetic sea water

$C_{SSW\text{-}MgCl2}$ - Carbonated synthetic sea water without $MgCl_2$

$C_{SSW\text{-}Na2SO4}$ - Carbonated synthetic sea water without Na_2SO_4

CW_{+MgCl2} - Carbonated water with $MgCl_2$

$CW_{+\ Na2SO4}$ - Carbonated water with Na_2SO_4

CNF - Carbonated nanofluid

DSA - Drop shape analyser

CHHC - CO_2-H_2O-Hydrocarbon

CWHC - CW-Hydrocarbon

CT - Computerized tomography

PDE - Partial differential equation

FEM - Finite element method

FDM - Finite difference method

FVM - Finite volume method

Symbols in Figures

VC - Pressure/PVT-Cell

HP - Hand driven pump

PI - Pressure indicators

TI - temperature indicators

PG - pressure generators

CC - CO_2 piston cylinder

WS - Water side

GS - Gas side

Symbols in equations

J - Molar flux

C - Concentration

x - Axis/direction

D - Diffusion coefficient

t - Time

D_{CO2} - Diffusion coefficient of CO_2

μ - Viscosity

M - Molecular weight

V - Molar volume

T - Temperature

P - Pressure

P_C - Critical pressure

T_C - Critical temperature

T_r - Reduced temperature

P_i - Parachor value

α_c - Ridel factor

Γ_m - Monolayer surface excess concentration

K_s - Adsorption constant

x_s	-	Mole fraction of solvent
R_1	-	Radii of curvature in the *z-x* plane
R_2	-	Radii of curvature in the *x-Θ* plane
R_o	-	Radius of curvature at the apex of the drop
ΔP	-	Laplace pressure
ρ	-	Density
$\Delta\rho$	-	Density difference
g	-	Acceleration due to gravity
B	-	Bond number/Shape factor
S	-	Arc length
A	-	Surface area
V_{PD}	-	Volume of hydrocarbon in drop phase
V_{CO2}	-	Volume of the diffused CO_2 in drop phase
V_{HC}	-	Volume of the drop phase
G	-	Gibbs free energy
h	-	Planck's constant
G_m	-	Molar Gibbs free energy
N	-	Avogadro's number
n_t	-	Total moles of CO_2 present in the test cylinder
n_{free}	-	Moles present in free space above the water

n_{water} - Mole present in water

K - Compressibility factor of CO_2

R_D - Radius of the spherical drop

C_{avg} - Volumetric average of the CO_2 concentration in the pendant drop

C_o - Initial concentration of CO_2

V_{exp} - Experimentally obtained volume of drop phase

V_o - Initial volume

SF - Swelling factor

F - Optimisation/objective function

1 Introduction and Objectives

1.1 Introduction

1.1.1 Background

Since its discovery, oil has emerged as a primary source of energy, and since then the demand for oil has increased continuously. However, the discovery of new reservoirs has declined over the years and the existing reservoirs are being depleted. Therefore, one of the options of keeping up with the demand is to recovery more oil from the existing reservoirs. As the primary energy of the reservoir tends to deplete, it necessary to maintain the pressure inside the reservoir to achieve optimum production and maximise ultimate recovery. Waterflooding is the most widely used method to increase the reservoir pressure. The success of waterflooding in lengthening the oil-production period by years made it the typical option, after primary production, to recover additional oil. However, most of the existing oilfields are approaching their tail end of production [1]. Further, the efficiency of waterflooding is lower, due to the early breakthrough of water caused by preferential flow through large pores, leading to a significant amount of oil being left behind [2]. Therefore, there is a need for enhanced oil recovery (EOR) methods that can improve the recovery of oil from the reservoirs.

Gas injection (GI) is a common EOR method, in which gases, such as propane, butane, and CO_2, are injected into the reservoir. CO_2 is more popular option for EOR by GI. Globally, at present, EOR by CO_2 injection contributes approximately 67.5% of projects (83 of 123) among carbonate reservoirs, and approximately 23.5% of projects (50 of 213) among sandstone reservoirs and is expected to rise by 0.1 % per year [3]. The main advantage of CO_2 injection is that, at most reservoir conditions,

it is a supercritical in phase, which is likely to develop miscibility with the oil. In reservoirs where miscibility cannot be achieved, CO_2 injection can lead to additional recovery by mixing with the oil and modifying the oil properties. CO_2 has the property of mixing with the oil to swell it, reduce viscosity, and possibly alter the wettability, causing the oil to flow more freely within the reservoir, so that it can be "swept up" in the flow from injector to producer well [4, 5]. Higher solubility of CO_2 in water, compared to other hydrocarbon components, causes more oil swelling, thus reducing the negative impact of water blocking upon the diffusion process between oil and CO_2, for those oil ganglia that have not been directly accessed by CO_2 [4, 6].

Along with its advantages and capabilities the CO_2-EOR has its fair share of limitations. Although CO_2 injection generally has excellent microscopic displacement efficiency, it often results in poor sweep efficiency, due to the higher mobility of CO_2 than the oil. CO_2 injection also has a problem of early breakthrough due to fingering; this will cause a shorter contact time with the crude oil reservoirs. Further, in direct CO_2 injection, due to low sweep efficiency and gravity segregation, there can be a time scale of several years for CO_2 diffusion in oil [7, 8]. Another reality is that, in majority of the cases, CO_2 is not readily available, or the sources are far away from the reservoir. In most cases, the source is anthropogenic CO_2 from coal-fired plants (industrial source). If CO_2 is captured from industry, the actual cost incurred of capture, compression, and transport to the reservoir is high.

An alternative to CO_2-EOR and a more attractive approach could be carbonated water injection (CWI). In CWI, CO_2 is first dissolved in water forming carbonated water (CW) before being injected into the reservoir. The pore level recovery mechanism for CWI is similar to that occurs in CO_2-EOR. When CW contacts the residual oil, the CO_2 from CW diffuses into oil, causing swelling and reduction in oil viscosity and density. The swollen oil globules subsequently coalesce and are produced by the injected CW [6, 8]. However, the major difference

between CO_2-EOR and CWI is that instead of CO_2 as a free phase in CO_2-EOR, the CO_2 is dissolved in water for CWI, this has major implications. The carbonated water has higher density than both water and CO_2, this significantly reduces the gravity segregation experienced during CO_2 injection, thereby improving the sweep efficiency and, hence, mobility [9, 10]. Figure 1.1 (inspired from [10]) shows the pictographic representation of the comparison between CO_2-EOR and CWI with respect to sweep efficiency and sweep profile. It may be seen from Figure 1.1 that, for CO_2-EOR, the injected CO_2 is more susceptible to uneven distribution, the effect which is termed as "fingering", and is more prominent in low permeable porous media [11]. In contrast the carbonated water mobility is more favourable than CO_2 in the gas-oil system, as it forms a single phase. For CWI, CO_2 is evenly distributed in the reservoir, as CW mixes with the in situ water, further this would also retard the CO_2 breakthrough, thus improving sweep efficiency. Compared to CO_2-EOR, CWI uses a smaller amount of CO_2 (available from nearby oil and gas fields) and yet can lead to a greater increase in oil recovery [12]. CWI has recorded a higher increment in residual oil recovery, compared to waterflooding, due to the mass transfer of CO_2 from CW to the oil phase, causing the oil phase to become more mobilised [13]. At reservoir conditions, the CO_2 solubility in water is higher than that of other hydrocarbon gases, making water a good fluid to transport CO_2 in the reservoir for enhanced oil recovery. Recent laboratory study [6] has shown that CWI may be successfully used as both secondary and tertiary recovery methods. Therefore, CWI may prove to be a good advancement to CO_2-EOR, while, at same time, having the capability to act as a CO_2 sequestration method.

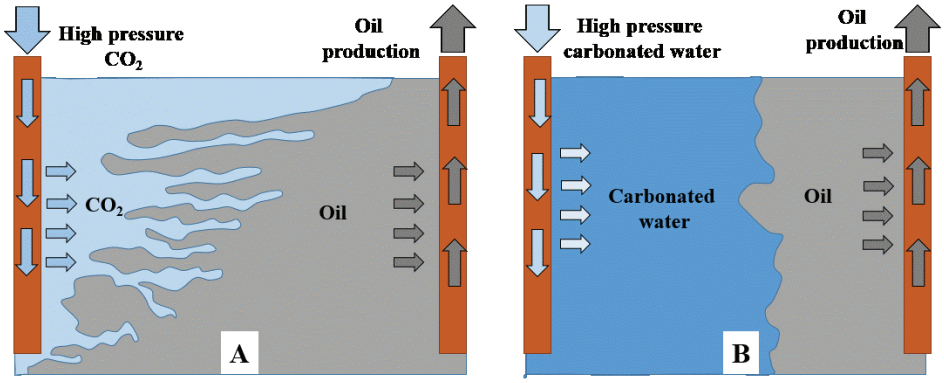

Figure 1.1: Graphical comparison of sweep front for the case of (A) CO_2 flooding and (B) carbonated water injection.

Due to escalations in the emission of anthropogenic CO_2 and its impact on the environment, there is a need to reduce the amount of CO_2 in the atmosphere. One way is by the injection of CO_2 into geological reservoirs. CO_2-EOR is being considered as option for coupled CO_2 sequestration and oil recovery option. However, there are a few problems associated with the coupled CO_2-EOR and sequestration process. First, as CO_2 is lighter than the oil or brine, there is a risk of CO_2 leakage to the surface, due to the upward movement of injected CO_2, which would make CO_2-EOR an unsafe method of CO_2 storage. Further, in terms of CO_2 storage potential, the poor sweep efficiency associated in case of CO_2-EOR also implies lower storage capacity [9]. In terms of CO_2 sequestration, CWI provides one of the safest method. In CWI, since the injected CO_2 is in solution form (CW), which has higher density than brine and, hence, sinks to the bottom of the reservoir, as opposed to the case of bulk CO_2 injection, where CO_2 floats under the cap rock, representing significant leakage risks [6, 12]. Therefore, CWI may be both a better option regarding hydrocarbon recovery and, simultaneously, a safer option for CO_2 sequestration.

1.1.2 Recovery mechanism of CWI

Majority of studies [1, 6, 9, 12-21] on CWI provide proof of greater recovery by CWI. These studies focus mainly on the recovery aspect of CWI, using core flooding studies and neglect the physics responsible for the observed enhanced recovery by CWI. The literature on CWI has overlooked the underlying mechanisms such as CO_2 mass transfer, fluid-fluid interfacial phenomena, mass transfer kinetics and property alteration of hydrocarbon, which are critical for understanding and optimising CWI. Few studies have looked into the aspect of wettability and IFT alteration [22-24]. However, there is lack of understanding of CO_2 mass transfer and the factors influencing CO_2 mass transfer. Figure 1.2 illustrates the pore level recovery mechanism in a CWI. Consider a pore space with isolated small oil ganglia left at the end of waterflooding as shown in Figured 1.2A. Now if CWI is followed by waterflooding (Figure 1.2B), the injected CW contacts with isolated oil ganglia. Due to higher solubility of CO_2 in hydrocarbon than in water the CO_2 from CW diffuses into the oil ganglia through the CW-oil interface, resulting in swelling of the isolated oil ganglia as depicted in Figure 1.2C. The swelling may lead to coalesces of oil ganglia, the coalesces together with reduction in viscosity of oil may lead to mobilization of oil out of pore spaces as depicted in the Figure 1.2D. Therefore, the whole process of swelling, coalesces, and mobilisation of oil was initiated by the mass transfer of CO_2 from the CW into the residual oil through the CW/oil interface (Figure 1.2E). Indicating, that the CO_2 mass transfer and CW/oil interfacial phenomena may be fundamental parameters for recovery mechanism by CWI. Therefore, the knowledge obtained by such a study would help in understanding the fundamental aspect of recovery by CWI.

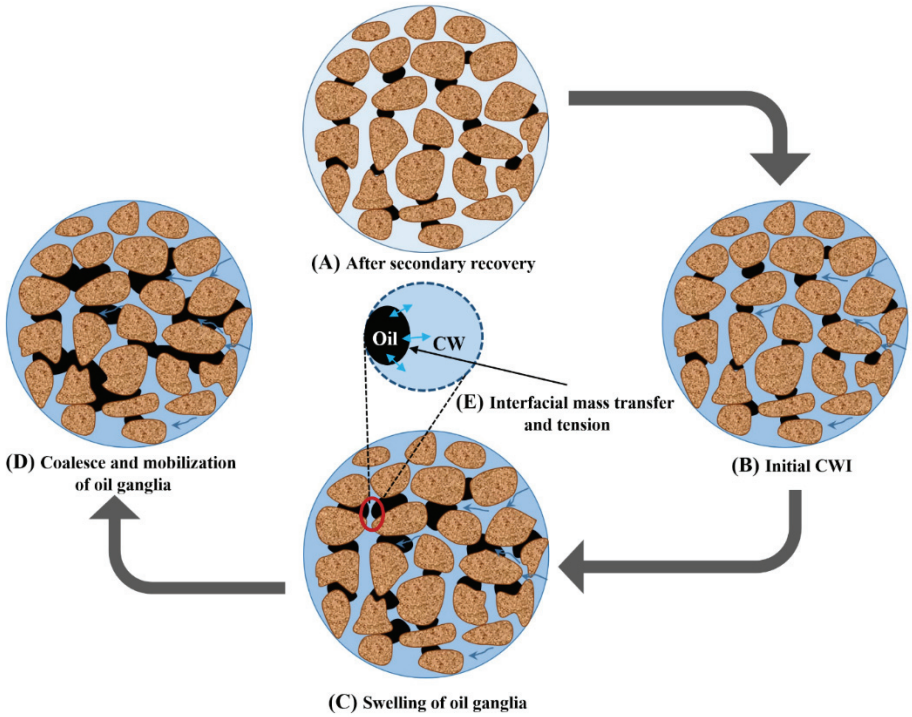

Figure 1.2: Graphical representation of pore level recovery mechanism by CW during CWI.

1.1.3 Applications of CO_2 mass transfer and fluid-fluid interfacial tension

The present study of CO_2 mass transfer and resulting fluid-fluid interfacial alteration may be applied to all the CO_2 based systems and gas-liquid systems. Instances where CO_2 mass transfer and IFT is relevant include, but are not limited to:

i. The mass transfer of CO_2 and the resulting mechanisms, such as swelling and IFT alteration, dictate the degree of oil recovery in CO_2 based EOR methods such as CO_2-EOR, CWI, and chemical EOR [6, 25]. The diffusion coefficient which represents the mass

transfer rate is critical for the feasibility evaluation of the solvent assisted recovery method [26].

ii. The molecular diffusion and, hence, the diffusion coefficient give information about the mixing of a solvent like CO_2 into oil, on which the numerical simulations are based [27].

iii. The rate of CO_2 mass transfer (diffusion coefficient) is critical for assessment of sequestration of CO_2 in saline aquifers and depleted hydrocarbon reservoirs. The CO_2 diffusion determines the potential of the aquifer for the application of CO_2 storage. Estimating the diffusion coefficient is critical for predicting the cumulative amount and duration for trapping CO_2 gas and time [28].

iv. The interfacial tension is of primary importance in the context of multiphase flow in reservoirs, and it is pivotal in the control of miscibility behaviour [29].

v. Further, from the perspective of CO_2 storage, the interfacial tension-dependent CO_2 distribution in a liquid-liquid system plays an important role [30].

vi. If the parameters controlling CO_2 mass transfer and IFT are identified, then available tools like nanotechnology and salts may be combined with CWI to enhance the efficiency of CWI as a method of both oil recovery and CO_2 sequestration.

1.1.4 CW/hydrocarbon IFT

Although the knowledge of CO_2 mass transfer for CO_2-hydrocarbon system may be extended with modifications to the CW-hydrocarbon system. However, this may not be true in case of IFT.The knowledge from neither water-hydrocarbon nor CO_2-hydrocarbon can be extended to understand the interfacial behaviour of CW-hydrocarbon systems. For CW-hydrocarbon system, pH, dissolution of CO_2 in water, phase of CO_2 and density alteration, are some of the additional parameters that may have an effect on determining the IFT. Moreover, for CW-hydrocarbon

systems, there is a limited number of studies available [24, 31]. However, this knowledge is not sufficient to fully understand the interfacial phenomena of CW-hydrocarbon systems. Apart from the calculation of IFT, it is critical to identify the parameters that influence and are influenced by the IFT. Further, studies have rarely investigated the collective influence of different phases of CO_2 (gas, liquid, and supercritical) on the IFT of CO_2-hydrocarbon or CO_2-water-hydrocarbon or CW-hydrocarbon systems.

1.2 Motivation

Based on the background, below is the summary of research issue relating to CWI that have been overlooked:

i. Few studies have investigated the influence of CO_2 mass transfer on the performance of CWI. Most the studies carried out rely on either an experimental approach or simulation. Neither of these approaches carried out separately will be beneficial for studying the CO_2 diffusion process and estimating the diffusion coefficient. Hence, there is a need to develop a numerical model that couples with experimental results to estimate the diffusion coefficient of CO_2 from CW into hydrocarbon.
ii. The previous literature has neglected the IFT of CW-hydrocarbon and its complex relationship with temperature. There is also a need to collectively study the influence of different phases of CO_2 (gas, liquid, and supercritical) on the IFT. Further, previous studies lack a dynamic analysis of IFT, which provides understanding of the progress of IFT with time and its relation to CO_2 mass transfer into hydrocarbon.
iii. The interdependency of major physics, such as CO_2 mass transfer, interfacial phenomena, and fluid kinetics, is missing in the previous works on CWI and need to be addressed.

iv. There is a lack of studies that investigate the influence of additives such as nanoparticles and salts on the physics dominating the recovery process by CWI.

1.3 Objectives

I. Interfacial tension studies

Address the inconsistencies in results reported in the literature on the relationship between temperature and IFT.

Develop a method to calculate the dynamic and equilibrium IFT for CO_2/pure hydrocarbon and CW/pure hydrocarbon systems.

Design experimental setup for wide rage or pressure and temperature so that the influence of different CO_2 phase (gas, liquid, and supercritical) and CO_2 saturation on IFT of CW/hydrocarbon system may be studied.

II. CO_2 mass transfer studies

Develop a numerical model that validates with experimental results to estimate the CO_2 diffusion coefficient and composition of the hydrocarbon for both gas-liquid (CO_2/hydrocarbon) and liquid-liquid (CW/hydrocarbon) systems.

III. Additives

The study also aims to understand the role additives such as silica nanoparticles, and various salts especially Na_2SO_4 and $MgCl_2$ on the CO_2 mass transfer and interfacial properties.

1.4 Organisation of thesis

The work is presented in six chapters. Chapter 2 combines a literature review and the fundamentals of the related phenomena, and the chapter has been divided into two sections. The first section (Section 2.1)

discusses fundamentals of CO_2 mass transfer, determination of CO_2 diffusion coefficient, influence of various parameters like pressure, temperature, CO_2 phase, and additives to enhance mass transfer. The second section (Section 2.2) discusses the fundamentals of the interfacial tension, various methods used to estimate IFT, the effect of pressure and temperature of IFT, the effect of CO_2 phase and CO_2 saturation on IFT and the influence of salt and nanofluid on CW/pure hydrocarbon IFT.

Chapter 3 starts with a brief discussion on various experimental methods used to estimate IFT, and how the current method is suitable. Further Chapter 3 discusses in detail the experimental method, materials, equipment, experimental procedure for estimating IFT, the preparation of samples, and the procedure for estimating the density, volume, and viscosity of the CO_2+hydrocarbon mixtures. Chapter 3 also examines the importance of dynamic IFT and proposes a novel method for its estimation.

Chapter 4 starts with earlier developed methods to estimate the diffusion coefficient of gases in liquids and compares them with the proposed method. Chapter 4 further discusses the model developed to estimate the diffusion coefficient of CO_2 in hydrocarbons. Chapter 4 also provides a brief history of previous methods used and their drawbacks and, in doing so, details how the proposed model is advanced. Further, the novel dynamic interface method is described.

Chapter 5 presents the major findings of the present study and a detailed discussion on the findings.

Chapter 6 is the concluding section, which summarises the findings of the present study.

The thesis ends with collection of six scientific articles published in various journals and one article under review as a result of present work. The information about these article can be found in “List of papers” section.

2 Literature Review and Fundamentals

2.1 Fundamentals of CO_2 mass transfer

The mass transfer phenomenon between gas-liquid and liquid-liquid impacts various enhanced recovery methods, such as solvent-based EOR, low salinity flooding, nanoparticle-based EOR, and also on CO_2 sequestration. Several physical situations occur in nature where there exist two phases separated by an interface. The two phases may be gas-liquid like CO_2-oil or maybe liquid-liquid like water-oil, brine-oil and carbonated water-oil. Similar to the single-phase transport, the concentration gradient of the transporting species in all the phases determines the overall rate of mass transport. The direction of the mass transfer acts in a way as to move the system towards equilibrium, and the concentration-driven mass transfer stops when equilibrium is achieved.

Diffusion is generally used to represent the mass transfer of a component (gas or liquid) from a region of higher concentration to a region of lower concentration. Diffusion is defined as a process by which molecules, ions or particles move from regions of relatively high concentration into regions of lower concentration. The phenomenon of diffusion may be analysed in two ways. First, by studying the mass transfer coefficient. Second, by describing the mass transfer with Fick's law and the diffusion coefficient. It is the second method that has been emphasised in the present thesis.

2.1.1 Fick's law of diffusion

Through his experimental studies involving binary mixtures, Fick (1855) came up with laws describing the diffusion of one component into another. Adolf Fick's work led to the proposal of two laws: Fick's first law (steady state) and Fick's second law (transient) [32]. In the simplest

terms, Fick's first law at a steady state condition may be described as the diffusive flux proportional to the concentration gradient between the regions of different concentration. Therefore, according to Fick's first law, diffusion occurs due to a concentration gradient, represented as the change in concentration as a result of a change in position ($\partial C/\partial x$), as shown in Equation (2.1).

$$J_i \propto \frac{\partial C_i}{\partial x} \tag{2.1}$$

which may be rewritten as Equation (2.2).

$$J_i = D_{ij} \frac{\partial C_i}{\partial x}, \tag{2.2}$$

where J_i is the molar flux of component i in the x direction; C_i is the concentration of component i in j; and the proportionality constant, D_{ij}, is the diffusion coefficient of the molecule i in j.

Fick's second law deals with transient diffusive flux movement. If the change of concentration of component i in a binary mixture occurs over a period, then, according to Fick's second law, the rate of change of concentration at a point in space is proportional to the second derivative of concentration with space (Equation (2.3)).

$$\frac{\partial C_i}{\partial t} = D_{ij} \frac{\partial^2 C_i}{\partial x^2} \tag{2.3}$$

In this work, a 3D (three-dimensional) form of Equation (2.3) is used to analyse the mass transfer of CO_2 in hydrocarbon for different fluid-fluid systems. A detailed mathematical model is discussed in Chapter 4.

2.1.2 Determination of diffusion coefficient

The diffusion coefficient of gas in liquids through a gas-liquid or liquid-liquid interface is of importance in numerous fields of science and

engineering. The molecular diffusion and, hence, the diffusion coefficient give information about the mixing of a solvent like CO_2 into oil, on which the numerical simulations are based [27]. The focus in this work will be on the determination of the diffusion coefficient of CO_2 in pure hydrocarbons for gas-liquid (CO_2–alkane) and liquid-liquid systems (CW-alkane).

Several studies have come up with the empirical correlation of CO_2 diffusion coefficients in liquids. For the CO_2-oil system, Davies, et al. [33] developed an equation relating the diffusion coefficient of CO_2 with the viscosity of the oil (Equation (2.4)).

$$D_{CO2,oil} = a\mu^{b}, \tag{2.4}$$

where $D_{CO2,oil}$ is the diffusion coefficient of CO_2 in oil (m^2/s) and μ is the viscosity of the oil (Pa.s); a and b are the dimensionless constants and, using fitting, it was found that $a = 1.41*10^{-7}$ and $b = -0.47$.

A more complex correlation, which involved additional parameters like pressure (P), temperature (T), molar volume of CO_2 (V_{CO2}), viscosity of oil (μ_o) and molecular weight of CO_2 (M_{CO2}), was given by Renner [27] (Equation (2.5)).

$$D_{CO2,oil} = 10^{-9} \cdot \mu_O^{-0.4562} \cdot V_{CO2}^{-1.706} \cdot P^{-1.831} \cdot T^{4.524} \cdot M_{CO2}^{-0.6896}, \tag{2.5}$$

Similarly, Unver and Himmelblau [34] have reported the diffusion coefficient of CO_2 in water as given by Equation (2.6).

$$D_{CO2,water} = 5.72 \times 10^{-12} \frac{T}{\mu_w}, \tag{2.6}$$

where T is temperature (K) and μ_w is the viscosity of the water (Pa.s). Recently, new and improved experimental methods, like compositional analysis [35-37], or a combination of experimental and numerical analysis, like the pressure decay method [38-40] and Axisymmetric Drop

Shape Analysis (ADSA) [41], have been used to estimate the CO_2 diffusion coefficient. These methods are more reliable and may be carried out at elevated pressures and temperature for a large range of fluid-fluid systems. The present thesis employs the modified and advanced ADSA method, the details of which will be provided in Chapter 4.

2.1.3 Effect of pressure and temperature on CO_2 mass transfer

Numerous studies have been carried out to estimate the diffusion coefficient of CO_2 in liquid for the CO_2-liquid system. Table 2.1 reports the diffusion coefficient data from the literature. It may be noted from Table 2.1 that, at the isothermal condition, the measured CO_2 diffusion coefficient increases as the pressure increases. This may be attributed to an increase in the solubility of CO_2 in liquids as pressure increases. Figure 2.1 shows the data for solubility of CO_2 in water for pressures 0-90 bar and at 25^{o}C, 35^{o}C and 45^{o}C. The solubility data has been obtained from the model given by Chang, et al. [42]. It may observed that, at isothermal conditions, the solubility of CO_2 in water increases as pressure increases; the same is also true with pure hydrocarbons [43]. The increase in diffusion coefficient with the increase in pressure may be credited to mainly two parameters: the viscosity alterations of liquid [41] and the solubility of CO_2 in the liquid. At isothermal conditions, as the pressure increases, the viscosity of the CO_2 saturated liquid decreases, causing an increase in the CO_2 diffusivity [41]. Further, an increase in CO_2 solubility with pressure would mean an increased affinity of CO_2 towards the hydrocarbon, leading to a rapid rate of mass transfer.

Table 2.1: CO_2 diffusion coefficient (m^2/s) in liquids from the literature.

System	Pressure (bar)	Temperature (^oC)	Diffusion coefficient (10^{-9} m^2/s)
CO_2-brine [44]	18.8 – 47	27^{o}C	0.45 – 1.0
CO_2-decane [45]	30 – 50	25^{o}C	1.175 – 1.75
CO_2-crude oil [46]	3.2– 43.9	27^{o}C	0.47 – 2.49
CO_2-decane [47]	10 – 60	29^{o}C	0.38 – 2.29
CO_2-decane [48]	13 – 50	25^{o}C	3.21 – 5.71

The temperature has a complex effect on CO_2 mass transfer. The major impact of an increase in temperature would be a decrease in CO_2 solubility in liquids [42, 49-51] (Figure 2.1). A decrease in CO_2 solubility would reduce the CO_2 concentration gradient, which would reduce the mass transfer of CO_2 into hydrocarbon. Studies [45, 51-53] have observed that the total mass transfer of CO_2 into hydrocarbon reduces with an increase in temperature. However, a different story unfolds when it comes to the rate of CO_2 mass transfer. The diffusion coefficient (rate of mass transfer) for the CO_2-hydrocarbon system increases as the temperature is raised [45, 54]. The increase in diffusion coefficient, despite a reduction mass transfer driving force, may be explained by two phenomena. First, the viscosity of the hydrocarbon decreases with the increase in temperature; this favours a greater mass transfer of the CO_2 into the n-decane drop phase [45, 49]. Second, for a fluid system, an increase in temperature would increase the entropy (motion of the molecules); this in turn would increase the kinetic energy, leading to a faster rate of mass transfer [45, 49, 51].

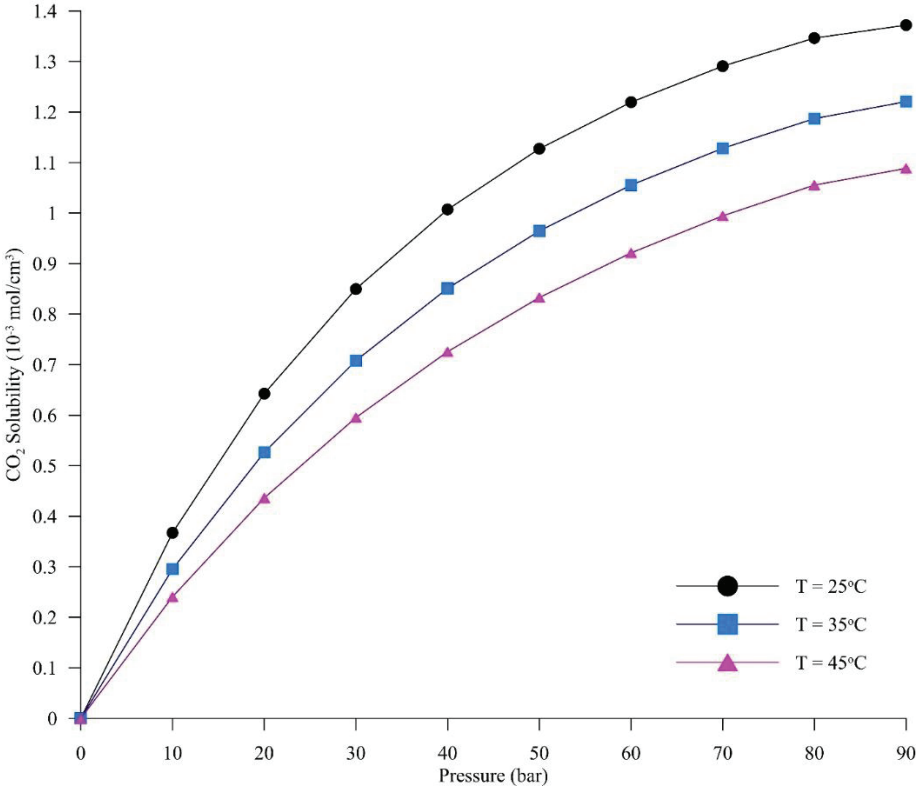

Figure 2.1: Solubility of CO_2 data in water for pressures 0-90 bar and at 25°C, 35°C, and 45°C.

The studies including in that shown in Table 2.1 on the CO_2 diffusion coefficient have conducted experiments at pressure and temperature range in which the phase of CO_2 is gaseous. However, in most of the real-time applications, like CO_2-EOR and CCS, CO_2 is used at a higher-pressure range, where it may be supercritical or liquid in state. Depending on the temperature, after certain critical pressure (>64 bar at 25°C, and >73 bar 35°C and 45°C), the CO_2 may be liquid (≤25°C) or supercritical (≥25°C). The density of CO_2 changes significantly as the phase of the CO_2 changes from gas to liquid or gas to supercritical. For example, at 25°C, the CO_2 density increases by approximately 290% (0.191g/ml to 0.743g/ml), as the CO_2 phase changes from gas (63 bar) to

liquid (70 bar); this alters the composition and intermolecular interaction between the molecules present in the binary mixture (CO_2+liquid). Despite its importance and physical significance, there is lack of data in literature on CO_2 mass transfer with a special focus on supercritical CO_2 (CO_2). For CO_2-brine and CO_2-oil systems, Mosavat, et al. [53] showed that the swelling of the hydrocarbon increased with the pressure up to the phase change pressure of CO_2 (74 bar at 45^{o}C) and then decreased as the pressure increased above 74 bar. In other words, the swelling has a peak value near the phase change pressure of CO_2. The reduction in swelling was attributed to the fact that more hydrocarbon components were extracted at higher pressures (above phase change pressure). Bagalkot and Hamouda [51] observed a similar trend of swelling vs pressure to that in Mosavat, et al. [53]. Bagalkot and Hamouda [51] credited the increase in density of CO_2 as phase changes to the observed reduction in the swelling of the hydrocarbon above the phase change pressure of CO_2.

2.1.4 Influence of salts on CO_2 mass transfer

To date, the majority of studies have concentrated on examining the influence of salts on wettability and the IFT alteration aspects of CO_2-oil, CW-oil, water-oil, and carbonated brine-oil systems. Only few studies, associated with synthesis gas (syngas) fermentation, have shown that the salts dissolved in water can enhance the mass transfer of gas in water [55]. Zhu, et al. [55] showed that anions are more influential in enhancing the CO mass transfer into water. Further, Zhu, et al. [55] observed that, among sulphate, nitrate, and chloride salts, the sulphate showed maximum CO mass transfer into water, and concluded that the sulphate ions stopped the coalescence of CO bubbles there, by increasing the effective surface area between CO and water. Biswal and Singh [56] observed that, in a system consisting of surfactant + nanoparticle + water/oil, the adsorption of nanoparticles on the water/oil interface blocked the mass transfer of surfactant from bulk fluid to the interface. Collins [57] showed that, in a solution containing salts, the larger size

(radius) ions (similar to SO_4^{2-}) have higher entropy and the mobility of the water molecules around them would increase. The increase in entropy and mobility would lead to a convective movement in bulk liquid, which might increase the momentum transfer and possibly enhance the mass transfer. So, other than wettability and IFT alterations, the salts may have the potential to improve CO_2 mass transfer.

2.1.5 Influence of nanoparticles

CO_2 mass transfer into the hydrocarbon is essential parameter in CO_2 based EOR methods. Therefore, enhancing the mass transfer would possibly increase the oil recovery. The utilisation of nanoparticles/nanofluid would be a way to improve the CO_2 mass transfer into residual oil. The application of nanoparticles for EOR has gained interest during the last decade. Numerous studies have focused on utilising nanoparticles for rock wettability alteration [58-64]. Recent studies have shown that, in addition to altering the rock wettability, the nanoparticles have demonstrated a capacity to enhance the mass transfer of gases into liquids [65, 66].

Several studies have been carried out to estimate the alteration in the solubility (mass transfer) of gases in liquids due to nanoparticles. Lee and Kang [66] found that the solubility of CO_2 in NaCl increased by 7 to 11%, depending on the temperature, when Al_2O_3 nanoparticles were suspended in NaCl. Kim, et al. [65] showed that silica nanoparticles lead to a 24% increment in mass transfer of CO_2 into water containing SiO_2 nanoparticles, relative to pure water. Haghtalab, et al. [67] studied the effect of zinc oxide (ZnO) and silica (SiO_2) nanoparticles on the solubility of CO_2 in water. Enhancements in CO_2 mass transfer in water, due to the addition of silica nanoparticles in water, were shown by Zhu, et al. [68], who observed that at atmospheric pressure approximately 1.9 times increase in CO_2 mass transfer, compared to that without nanoparticles. Hence, there is considerable evidence to demonstrate that

nanoparticles suspended in liquid would enhance the mass transfer of gases in liquids.

The mechanism(s) responsible for the augmentation in mass transfer due to nanofluids are still a part of the ongoing discussion. However, in the literature, three mechanisms have been suggested for the increase in mass transfer: Brownian motion, leading to micro-convection [69], CO_2 adsorption [68, 70] and the breaking of CO_2 bubbles into a smaller size, thus increasing the surface area [20]. Therefore, merging nanotechnology and CW for EOR would be beneficial, as nanofluid enhance the CO_2 mass transfer into the residual oil.

2.1.6 Liquid-liquid systems

Like those presented in Table 1, most studies carried out on mass transfer focus on gas-liquid systems, especially the CO_2-liquid system, due to its relevance to CO_2-EOR. For liquid-liquid systems present in petroleum reservoir, such as water-oil, and brine-oil, there is hardly any mass transfer across the interface, hence, it may not be necessary to carry out mass transfer studies. For liquid-liquid systems, the focus is mainly on interfacial tension and adsorption at the interface. For CWI, as explained in Figure 1.2, when the injected CW contacts the oil, there will be CO_2 mass transfer from CW into the oil, and this mass transfer is substantial [6, 71].

Another problem would be that the knowledge and theory learnt from studying CO_2 mass transfer for CO_2-liquid systems cannot be completely extended to CW systems, due to the presence of dissolved CO_2 in water, rather than pure CO_2. Therefore, there is a need to carry out mass transfer studies for CW-hydrocarbon systems, to build the knowledge base that may be used to interpret further studies. Few studies [71] have analysed the mass transfer studies for CW-hydrocarbon systems. Riazi, et al. [71] carried out a 1D simulation using COMSOL to demonstrate the changes at interface for the CW-hydrocarbon system. Their focus was mainly on

the swelling of hydrocarbon and the resulting interfacial movement. A model relying on empirical correlation was used to estimate the diffusion coefficient, which was further used it to simulate the changes in volume and interface. Further, the model was 1D, which is difficult to apply to real-life situations. However, there is a lack of understanding of CO_2 mass transfer and the factors influencing CO_2 mass transfer especially for CW/hydrocarbon systems. This presents an opportunity and scope for substantial work. An interesting question, compared to the CO_2 - hydrocarbon system, how would the CO_2 mass transfer be in the CW-hydrocarbon system? Would it be less or more?

2.2 Fundamentals of interfacial tension

The interfacial tension between two immiscible fluids (phases) has been defined in several ways, a few of which are given below:

The interfacial tension is described as the work which must be spent to increase the size of the interface between two immiscible phases (liquid-liquid or gas-liquid).

The interfacial tension between two immiscible phases is the amount of work that should be provided to bring the molecules from the bulk phases to the contact boundary to create a new interface of unit area.

Interfacial tension is the balance of the cohesive or excess energy present at an interface arising from the imbalance of forces between molecules of two immiscible phases.

The interfacial tension plays a significant role in numerous applications like emulsion stability [72], contamination transport [73], oil recovery [22, 24, 74, 75], pharmaceuticals [76] and, more recently, CO_2 sequestration [77, 78]. The petroleum reservoir often encounters multiphase flows, where the capillary pressure between different phases

impacts the mobility of oil in the reservoir. The capillary pressure and the IFT are related. IFT becomes ever more vital for the cases of salinity flooding [74, 79, 80] and nanoparticle-assisted flooding [81, 82], where the focus is on IFT alteration by the ions and nanoparticles.

2.2.1 Measurement of IFT

Numerous methods have been proposed in the past few decades for estimating the gas-liquid or liquid-liquid interface. These methods may be broadly classified as traditional [83, 84] and experimental [29, 31] IFT prediction models.

The theoretical models have widely been used to estimate the IFT of multiphase systems. The majority of the models used to calculate IFT are based upon the parachor method [83, 85], corresponding states principle [84, 86] and thermodynamics [87]. The most widely applied parachor method is the one presented by Weinaug and Katz [88], originally given by Sugden [89]. For gas-liquid (methane-propane), Weinaug and Katz [88] came up with Equation (2.7) to estimate the IFT. Empirical density correlations are applied in the parachor model to estimate the IFT. Equation (2.7) may also be applied to other fluid-fluid systems.

$$\gamma^{\frac{1}{4}} = \sum_{i=1}^{N} P_i \left(\frac{\rho}{M_l} x_i - \frac{\rho_g}{M_g} y_i \right), \tag{2.7}$$

In Equation (2.7), M and ρ are the molecular weight and density, respectively; subscripts g and l represent gas and liquid, respectively, and P_i is the parachor value. x_i and y_i are the mole fractions of liquid and gas phase, respectively. The parachor can be visualised as a comparative volume between two liquids and is independent of temperature. The parachor values and method to calculate them may be obtained from numerous studies [85, 90, 91]. A typical parachor value of CO_2 would be 79.2 [83]. The parachor model performs excellently for simple systems like CO_2-n-decane; however, it shows poor performance for complex

systems (multicomponent) like crude oil-CO_2 [86]. Further, the parachor model may be applied only to gas-liquid systems.

The "corresponding states principle" correlates IFT to critical properties, instead of densities are in the parachor method [92]. There are various relations of IFT based on corresponding states principle; the earlier version is given in Equation (2.8) [92].

$$\frac{\gamma}{P_C^{\frac{2}{3}} T_C^{\frac{1}{3}}} = \left(0.132 \cdot \alpha_c - 0.279\right)(1 - T_r)^{\frac{11}{9}} \tag{2.8}$$

In Equation (2.8), P_C and T_C are critical pressure and temperature, respectively; T_r is reduced temperature (T/T_C), and α_c is the Ridel factor. The corresponding states principle cannot be extended to multicomponent mixtures [86].

In recent years, few empirical relations have been provided specifically for the application of petroleum. For CO_2-brine systems, Bachu and Bennion [93] gave a generic empirical correlation for IFT as a function of temperature and pressure.

$$\gamma = A(T,S)P^{-B(T,S)} \tag{2.9}$$

In Equation (2.9), A and B are variables, as a function of temperature and salinity, and P is the pressure.

Yarranton, et al. [94] related the IFT to the concentration of the surface-active components, as shown in Equation (2.10).

$$\gamma = \gamma o - RT \cdot \Gamma_m \ln(1 + K_s \cdot x_s) \tag{2.10}$$

In Equation (2.10), γ_o is the IFT between pure solvent and water, Γ_m, K_s, and x_s are the monolayer surface excess concentration, adsorption

constant and mole fraction in the organic phase, respectively; R is the universal gas constant, and T is the temperature.

Bennion and Bachu [95] gave an empirical equation to generically predict the IFT of CO_2-brine systems, based on CO_2 solubility over the range of salinity, temperature and pressure (Equation (2.11)).

$$\gamma = -0.0004(x_{CO2})^4 + 0.0241(x_{CO2})^3 - 0.3836(x_{CO2})^2 - 0.7305(x_{CO2}) + 73.264 \quad (2.11)$$

In Equation (2.11), x_{CO2} is the solubility of CO_2 at standard conditions. The theoretical models and the empirical relations presented above require molecular parameters of the two phases. The density gradient theory (DGT) is another well-known theoretical model to estimate IFT, which relates the equation of state (EOS) to surface properties of homogeneous and non-homogeneous systems. DGT uses statistical techniques and the Helmholtz free energy model to estimate the IFT [96]. Some models require molecular energy, chemical potential and density at equilibrium of the coexisting phases [96]. Most of the models have limitations on the type of system they can be applied to, and some of the models give an approximate estimate of IFT [96]. Models also demand values of advance parameters, such as parachor values, the solubility of gases in liquids, mole fractions, and adsorption data, to name a few. Further, additional experiments or models must be designed to obtain these parameters. Therefore, the theoretical models or the empirical equations may not be a suitable option for estimating the IFT or either gas-liquid and liquid-liquid systems. Over the years, numerous reliable experimental methods have been developed to estimate the IFT of multiphase systems like the ring method, plate method, drop volume method, spinning drop, bubble pressure method, and pendant drop method. A simple schematics of various experimental methods used to determine IFT has been shown in the Figure 2.2.

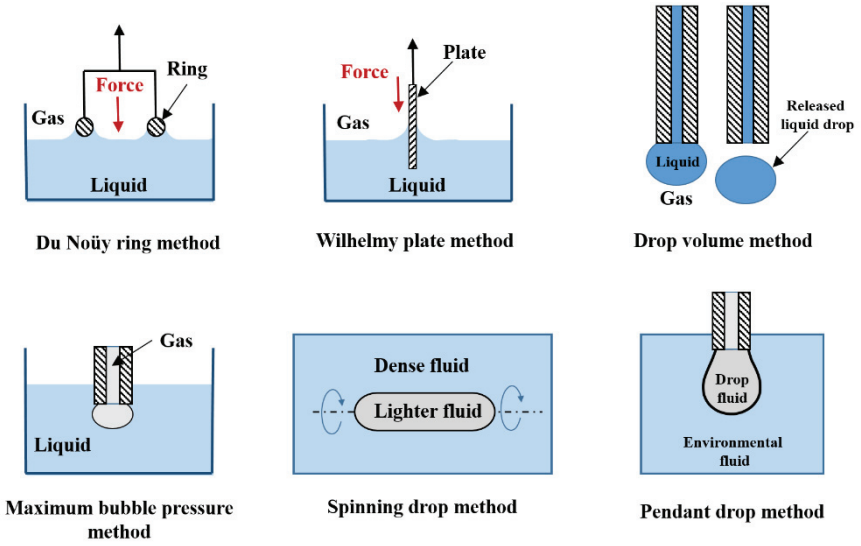

Figure 2.2: Simple schematics of various experimental methods for IFT estimation.

A Table 2.2 describes a brief working principle of widely used experimental methods. Each of the experimental methods has a different principle for calculating IFT; hence, each of them has a specific set of advantages and limitations. For example, the Du Noüy ring and Wilhelmy plate method are comparatively easy to implement with good precision [97] for gas-liquid systems. However, both the ring and plate methods require calibration before any measurement can be taken, making it a complicated setup. The Du Noüy ring additionally requires a correction factor for the calculation of interfacial tension. Further, Du Noüy ring and Wilhelmy plate methods cannot be applied to dynamic systems, liquid-liquid systems, and when the IFT is below 5 m N/m [98]. The spinning drop method is one of the most widely used methods and, unlike the ring or plate methods, it can measure low IFT (below 0.1 m N/m) [97]. However, it is not useful for measuring IFTs that are above 1-5 m N/m [98], and the phases should have a significant density difference [97], making it infeasible for liquid-liquid systems. Another problem with the spinning drop method is the need to manually deposit

small oil drops, using a syringe, which makes the method not applicable to high viscous fluids [97]. The drop volume method requires manual intervention, which is time-consuming and may lead to errors. The most important limitation of methods such as the ring, plate, spinning drop, drop volume, and maximum bubble pressure is their inability to calculate IFT in the presence of impurities/additives such as salts, nanoparticles or polymers to name few which are critical to oil and gas applications. Further, only a few methods can analyse both liquid-liquid and gas-liquid systems, and most of the methods in Table 2.2 cannot estimate the dynamic IFT changes. The pendant drop method may be applied to both gas-liquid and liquid-liquid systems and also with fluids consisting of any form of impurities (salt, nanoparticles, etc.). Further, the pendant drop method can carry out both dynamics and equilibrium IFT measurement and for a wide range of IFT values. However, the pendant drop method would be expensive, due to the involvement of advanced optics and computational schemes.

Table 2.2: Different methods for calculating IFT, with their working principle.

Method	Working Principle
Du Noüy ring	In this method, a ring mostly made of platinum is gradually raised from the surface of the liquid. The force needed to lift the ring from the liquid surface is measured and correlated to liquid surface tension [99].
Wilhelmy plate	In this method, a thin plate is aligned, perpendicular to the liquid interface. Then, a tensiometer is used to measure the force on the plate due to wetting of the liquid; this force is then used to estimate the surface tension [99].

Drop volume	In this method, drops of a liquid are created in a vertical capillary surrounded by a second liquid. The drops are made to detach, and the volume at which they disconnect is calculated. The drop at the tip of the capillary will disconnect when its weight (volume) reaches the magnitude balancing the surface tension of the liquid [100].
Maximum bubble pressure	In this method, air or gas is passed through a capillary submerged in another liquid. The gas comes out of the capillary as a bubble, and the maximum pressure in the bubble at the tip of the capillary is measured. As the gas bubble comes out of the capillary tip, its radius of curvature first decreases to a hemisphere, before increasing again. The surface tension is calculated by relating the capillary radius and the radius of curvature. [100, 101].
Spinning drop	In this method, the gas bubble or less dense drop is made to rotate horizontally (horizontal tube) in a denser liquid. The rotation of the horizontal tube creates a centrifugal force towards the tube walls, which deforms the bubble/drop and elongates in shape. The elongation of the drop stops when the interfacial tension and centrifugal forces are in equilibrium. The surface or interfacial tension between the two liquids can then be determined from the shape of the drop at this equilibrium point [100, 102].
Pendant drop	In this method, the liquid drop is suspended from the capillary tube surrounded by another fluid (liquid/gas). The shape of the pendant drop, which is balanced by interfacial tension and gravity forces, is analysed. The surface tension or interfacial tension is calculated from

	the shadow image of a pendant drop, using drop shape analysis [103].

2.2.2 Influence of pressure and temperature on IFT

The influence of pressure on CO_2-hydrocarbon IFT is studied thoroughly in the literature [29, 44, 45, 104, 105]. The typical trend was a decrease in IFT with an increase in pressure. Yang, et al. [105] attributed the decrease in IFT with pressure to an increase in the CO_2 solubility in hydrocarbons. The behaviour changes quite a bit for liquid-liquid systems. For water-decane systems, the IFT increases linearly and marginally with increase in pressure up to 3000 bar at various temperatures [106, 107]. A similar observation is also made for brine-live reservoir oil by Firoozabadi and Ramey Jr [108], brine-crude oil by Wang and Gupta [109], and CW-decane by [51]. Unlike pressure, only a few studies have analysed the influence of temperature on CO_2-hydrocarbon IFT or water/CW/brine-hydrocarbon systems; this is due to their unpredictable relationship with temperature [45]. For example, Bagalkot and Hamouda [45] showed that IFT of CO_2-decane decreases with increase in temperature, while Yang, et al. [105] and Yang and Gu [41] showed that the IFT increases with increase in temperature. For a CO_2-hydrocarbon/brine IFT, Yang and Gu [41] and Yang, et al. [105] credited the increase in IFT to decreasing the solubility of CO_2 in hydrocarbon with an increase in temperature. While, Bagalkot and Hamouda [45] and Honarvar, et al. [22] argued that CO_2 solubility is not the only controlling factor and IFT may also be influenced by kinetic energy, especially when temperature is increased. The kinetic energy and the entropy of the CO_2+n-C_{10} increase with temperature, hence, increasing the total energy. The increment in the total energy would reduce the free energy, resulting in the reduction of the IFT. Further, according to studies [45, 79, 110-112], for systems consisting of CO_2, the increase or decrease of IFT with temperature comes with a condition:

at low pressure, the IFT increases with increase in temperature, while, at high pressure, the IFT decreases with increase in temperature. The point of transition is generally near the critical pressure of CO_2 (31.5 bar).

2.2.3 Influence of pH on IFT

The pH of brine (aqueous solutions) in contact with the oil phase influences the IFT. The oil in contact with the brine provides an electrical negative charge at the brine–oil interface, due to the adsorption of hydroxyl ions (OH^-) at the interface from the brine, leading to a reduction in the IFT [113]. Wangersky [114] showed that increasing the pressure (decreasing the pH when CO_2 is present) would lead to an increase in ion paring, due to which the number of free ions would be low and, hence, fewer surface-active ions would be available, therefore resulting in an increase in IFT with an increase in pressure (up to 70 bar). Ferdous, et al. [113] observed that, for brine-hexane systems, the IFT was lower when the fluid was more basic (pH = 8-12); however, they did not observe a noticeable difference in IFT for acidic (pH < 7) and neutral brine, which remained constant. A similar observation was also made by Buckley [115] for oil-carboxylic acid IFT. Poteau, et al. [116] found that, for oil-water systems, the IFT was lower for both acidic and basic fluids and maximum at neutral pH. They explained that, at low or high pH, the asphaltenes in the oil are changed, thereby enhancing the surface activity and reducing the IFT. For CW-crude oil systems, Manshad, et al. [24] showed that, with the decrease in pH, the reduction in IFT was enhanced. From the perspective of pH and IFT, the decrease in pH of the carbonated brine (CB) would mean that the concentration of H+ ions is high; this acts in such a way as to oppose the adsorption of ions on the interface and reduce the concentration of surface-active ions [117], which would lead to an increase in the CB/n-decane IFT with a decrease in pH.

2.2.4 Influence of salts on IFT

Salts, when dissolved in water, generally dissociate into positive and negative particles (molecules/ions). The particles may either migrate towards or be repelled away from the interface; this movement of particles describes the phenomenon of adsorption. If the bulk consists of charged particles like ions, then the adsorption of ions on the interface would alter the IFT. Salt in the form of low-salinity water flooding or brine flooding has been part of studies related to oil recovery for a considerably long time. However, the data presented by previous studies show contrasting trends. Kumar [117] has summarised the literature studies on the effects of salts in the water on the IFT of brine/hydrocarbon and carbonated brine/hydrocarbon systems. From their study it may be said that for similar systems, there are wide-ranging results on the influence of salts on IFT. For example, Gomari and Hamouda [118] (brine-decane) and Serrano-Saldaña, et al. [119] (brine-dodecane) showed that salts like $MgCl_2$, Na_2SO_4, and NaCl reduced the IFT, whereas Ikeda, et al. [120] (brine-hexane) and Cai, et al. [121] (brine-alkanes) observed that salts like NaCl, $MgCl_2$, and $CaCl_2$ increased the IFT. Further, Aveyard and Saleem [122], Manshad, et al. [24] and Lashkarbolooki, et al. [74] showed that the increase or decrease in the IFT of brine-hydrocarbon systems is a function of the type of salt present in the brine. Lashkarbolooki, et al. [74] observed that, for crude oil-brine systems, $MgCl_2$ reduced IFT, while NaCl and KCl increased the IFT, whereas Cai, et al. [121] and Badakshan and Bakes [123] argued that the IFTs of brine-hydrocarbon systems are weakly dependent on salt type in brine. Not only the type of salt but also the concentration of the salt plays a critical role in determining the alteration of IFT. Serrano-Saldaña, et al. [119] and Hosseini, et al. [80] have observed that IFT is inversely proportional to the concentration of salts, while Manshad, et al. [24] observed an opposite trend. Additionally, studies like those of Gomari and Hamouda [118], Hosseini, et al. [80], and Lashkarbolooki, et al. [74] have proved that there are special ions like Mg^{2+}, which show

a larger reduction in IFT, compared to other ions. Lashkarbolooki and Ayatollahi [124] and Moeini, et al. [75] have claimed that, apart from the composition of brine, the composition of the oil also plays an important part. The majority of studies on IFT and salts have dealt mainly with brine-hydrocarbon systems, although limited studies are available for CW-hydrocarbon systems [23, 31]. However, this knowledge is not sufficient to understand one of the fundamental physics of fluid-fluid interaction connected to CWI. In CW-hydrocarbon systems, the presence of both CO_2 and salt in the water would change the physics compared to only salt in the water. Recently Nowrouzi, et al. [31] and Manshad, et al. [24] have studied the influence of salt in CW on crude oil/CW IFT, and both have observed a reduction in IFT. Further, Manshad, et al. [24] showed that the presence of CO_2, along with salt and water, enhanced the reduction in IFT. The uncertainty and lack of studies on the influence of salt on CW-hydrocarbon IFT, together with its importance to oil recovery, shows the vast scope of salt in CWI.

2.2.5 Effect of nanoparticles on IFT

Similar to salts (ions) the nanoparticles are charged and may be surface active; therefore, if dispersed in liquid-liquid systems, they may alter the IFT. Numerous studies have been carried out in recent years that prove that nanoparticles have the ability to alter the IFT [64, 125-127]. Metin, et al. [64] showed that polyethylene glycol coated (PEG) silica nanoparticles can greatly reduce the IFT of decane-water systems. Suleimanov, et al. [127] combined anionic surface-active agents with light non-ferrous metal nanoparticles and observed an approximately 70–90% reduction in surface tension on an oil boundary, when compared to surface-active agent aqueous solution. Hendraningrat, et al. [128] showed that, for brine-oil systems, the nanoparticles in brine decrease the IFT; further, they also showed that IFT reduction is a direct function of nanoparticle concentration. However, Metin, et al. [64] observed that uncoated silica nanoparticles did not significantly alter the decane-water

IFT. A similar observation was also made by Isdahl [129] for CW-decane systems.

3 Experimental Methodology

In the present work, the axisymmetric pendant drop analysis (ADSA) method is used to obtain two major parameters: the volume of the pendant drop and the interfacial tension.

3.1 Principle of pendant drop method

A detailed history of the pendant drop and its working principle may be obtained from works like those of Del Rıo, et al. [130], Berry, et al. [131] and Song, et al. [132]. Therefore, in the following discussion, only a brief outline of the working principle is presented.

Figure 3.1 (inspired from [133]) shows the three-dimensional schematic of a typical pendant drop hanging from a capillary surrounded by a second fluid. In Figure 3.1, the pendant drop is symmetric about the vertical axis (*z*-axis), hence the name axisymmetric pendant drop. The drop phase is the fluid present in the pendant drop, while the environmental phase is the fluid surrounding the drop phase. The shape of the pendant drop (drop phase) is the most critical parameter for the calculations by pendant drop method. The balance between the interfacial and gravity forces defines the shape of the pendant drop [117, 132]. The gravity acts in such a way as to elongate the drop, while the interfacial tension acts similarly to hoop stress, seeking to minimise the interfacial area, and tends to give a spherical shape to the drop. The magnitude of these forces depends on the density difference between the drop and environmental phases [117].

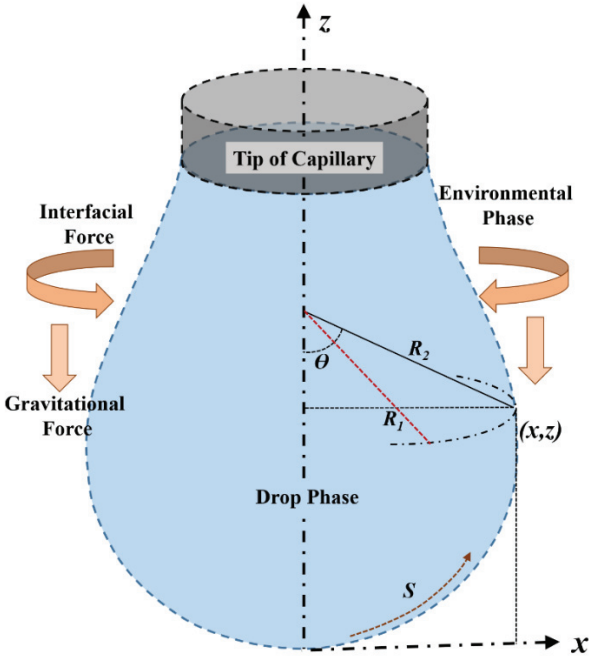

Figure 3.1: A three-dimensional schematic of the pendant drop under the capillary.

3.1.1 Evaluation of surface or interfacial tension

In the ADSA method, the IFT of the fluid-fluid system is calculated from the analysis of the shadow of the digital image captured by the camera using the drop shape analysis (DSA) software. The drop shape analysis relies on the Young-Laplace equation (Equation (3.1)), which correlates the Laplace pressure across the interface, the curvature of the interface, and the interfacial tension [134-136].

$$\Delta P = \gamma \bullet \left(\frac{1}{R_1} + \frac{1}{R_2} \right) \tag{3.1}$$

In Equation (3.1), R_1 and R_2 are the radii of curvature in the z-x and x-Θ planes, respectively. ΔP is the Laplace pressure, which is the pressure change across the interface, and γ is the interfacial/surface tension. The Laplace pressure may further be represented as a difference between the reference pressure and the hydrostatic pressure, as in Equation (3.2) [131].

$$\Delta P = \Delta P_o - \Delta \rho g z \tag{3.2}$$

Substituting Equation (3.2) in Equation (3.1) to obtain Equation (3.3).

$$\Delta P_o - \Delta \rho g z = \gamma \bullet \left(\frac{1}{R_1} + \frac{1}{R_2} \right) \tag{3.3}$$

In Equation (3.2) and (3.3), $\Delta\rho$ is the density difference between the drop phase and the environmental phase, and ΔP_o is the reference pressure at $z = 0$. It may be observed from Figure 3.1, that, due to the shape of the pendant drop near the collar (top), the two radii of curvature (R_1 and R_2) will have opposite signs, whereas, at the base (bottom), they will have the same sign, which would give a higher mean curvature. Therefore, the above Equation (3.3) can be solved analytically only if the droplet profile is spherical, and the solution would be inconsistent for the pendant drop profile [131]. Hence, to solve Equation (3.3) for the pendant drop profile, a non-dimensional factor/parameter was necessary. Merrington and Richardson [137] introduced a non-dimensional term called the "Bond number" or the "shape factor" (B), which describes the shape of the pendant drop as given by Equation (3.4).

$$B = \frac{\Delta \rho . g . R_o^{\,2}}{\gamma} \tag{3.4}$$

In Equation (3.4), R_o is the radius of curvature at the apex of the drop or maximum horizontal diameter of the unmagnified pendant drop. Mathematically, the non-dimensional Bond number (B) is the single

parameter that determines the shape of the pendant drop. Therefore, from Equation (3.4), if the B and R_o are estimated, then it would be easy to obtain the IFT. Analytical determination of B is a complicated and challenging task. Thanks to the advancement of computing and image analysis technology, the calculation of B and R_o is now carried out efficiently by drop shape analysis software. In brief, the digital images of the pendant drop are acquired, then the actual dimensions of the pendant drop are measured from the digital image; thus, R_o is obtained. The shape of the pendant drop is determined from the obtained dimension of the drop. The bond number (B) is then adjusted in a numerical method until the calculated drop shape resembles the actual shape. Once the B and R_o are obtained, the IFT is calculated from Equation (3.4).

3.1.2 Evaluation of volume and surface area of the pendant drop

The volume of the pendant drop and the surface area of the pendant drop may also be extracted by solving the above Young-Laplace equation. For an axisymmetric pendant drop, both volume (V) and surface area (A) may be represented in the form of ordinary differential equations [130], as shown below.

$$\frac{dV}{dS} = \pi x^2 \sin\theta \tag{3.5}$$

$$\frac{dA}{dS} = 2\pi x \tag{3.6}$$

In Equations (3.5) and (3.6), S is the arc length, as shown in Figure 3.1. Applying boundary conditions, the above equations may be transformed into a simple integral form [131]:

$$V = \pi \int (r^2 \sin\theta) ds \tag{3.7}$$

$$A = 2\pi \int (r)ds \tag{3.8}$$

Similar to IFT, both the volume and the surface area of the pendant drop are obtained from the drop analysis software. There are two types of the arrangement of the drop phase concerning the capillary. Either the drop is hanging from the capillary (when the drop is of higher density than the environmental fluid), or it may be resting on the capillary (the drop is of lower density than the environmental fluid). Both these arrangements are used in this work.

3.1.3 Advantages of ADSA

i. The ADSA method is considered the most robust and accurate method for IFT determination. Further, due to the usage of image analysis and high-level computation carried out by software, the method has become more straightforward to use and eliminates any human interference.
ii. The method can be used to estimate the interfacial/surface tension of those gas/liquid, liquid-liquid, liquid/solid (contact angle) systems, which cannot be estimated by other methods.
iii. Apart from calculating the IFT for homogenous and pure substances, the method can also estimate the IFT, even if the fluids contain contaminants/additives such as salts, microbes, nanoparticles, polymers, or colloids.
iv. Depending on the material of the equipment, the method can estimate the IFT for fluids for a wide range of pH (acidic, base, and alkaline). Therefore, experiments involving supercritical and liquid CO_2 may be carried out without the fear of contamination due to corrosion by low pH, which is usually associated with CW (pH between 2-3).
v. Depending on the design of the experimental setup, the calculations may be carried out over a broad range of pressures and temperatures. For the current setup, the maximum pressure

limit is 63MPa, and the maximum temperature is 180°C. Therefore, the experimental setup may be used to study at conditions which may be found in most of the practical applications associated with petroleum reservoirs.

vi. The ADSA method has an accuracy of ±0.05 mN/m when estimating the IFT [29, 105].

vii. Apart from calculating the IFT, pendant drop analysis can simultaneously provide the data volume, surface area, and contact angle (depending on the system). Therefore, IFT, wettability, and mass transfer studies may be carried out by performing just one experiment, thus avoiding separate experiments for each analysis.

3.1.4 Limitations of ADSA

i. The pendant drop equipment is not ideal for the measurement of fast dynamic IFT processes (i.e. time-steps of less than 1 second).

ii. The performance of the ADSA method relies mainly on the ease with which the software can recognise the difference between the drop and the surrounding environment. Therefore, if there is not enough contrast between the drop and the surrounding environmental phase, which may happen for low-density difference phases, then there may be no result, or error may be high.

iii. The system relies mainly on the value of the Bond number, which may be a restriction, depending on the value of the Bond number [97].

iv. Another concern with the current design is the inability to perform analysis for dynamic systems (flowing fluids), meaning neither of the phases, gas-liquid or liquid-liquid, is in motion, the analysis being carried out in a static environment. The absence of advection may be a drawback, depending on the requirement of the analysis.

3.2 Materials

3.2.1 Gases

In the present study, CO_2 was the only gas used. CO_2 is mainly used to produce CW and to carry out studies for CO_2-hydrocarbon systems. The CO_2 gas provided by PRAXAIR has a purity greater than 99.9%.

3.2.2 Liquids

Both saturated CW and unsaturated CW have been used in the present study. The dissolution of CO_2 into water would give the CW. The procedure for obtaining the CW in the present study is described in detail in section 3.6.3.

Five types of brines of different composition have been used in the present study. NaCl, $MgCl_2$, Na_2SO_4, $CaCl_2$, KCl, and $NaHCO_3$ salts were dissolved in deionised water (DIW) to prepare different brines, as shown in Table 3.1. The composition of each of these salts in the brine was maintained according to synthetic sea water (SSW), as given by Hamouda and Maevskiy [138].

The brines (Table 3.1) were saturated with CO_2 to obtain carbonated brines (CB). From this point on in this study, the combination of CO_2+SSW will be termed C_{SSW}, which means carbonated synthetic sea water. Similar terms will be used for the following combinations: $C_{SSW\text{-}MgCl2}$ (CO_2+SSW-$MgCl_2$), $C_{SSW\text{-}Na2SO4}$ (CO_2+SSW-Na_2SO_4), CW_{+MgCl2} (CO_2+DIW+$MgCl_2$), and $CW_{+\ Na2SO4}$ (CO_2+DIW+Na_2SO_4).

In the present study, three pure hydrocarbons, n-decane, n-heptane, and n-hexane, have been used; these form the drop phase. All hydrocarbons used were manufactured by Merck KGaA with 99% purity.

Table 3.1: Composition and purpose of different brines used in the present study.

Brine name	Composition (g/l)						Effect of salts
	NaCl	$MgCl_2*6H_2O$	Na_2SO_4	$CaCl_2*2H_2O$	KCl	$NaHCO_3$	
SSW	23.38	9.05	3.41	1.91	0.75	0.17	On CO_2 mass transfer and IFT
SSW-$MgCl_2$	23.38	0	3.41	1.91	0.75	0.17	In absence of Magnesium on IFT and CO_2 mass transfer
SSW-Na_2SO_4	23.38	9.05	0	1.91	0.75	0.17	In the absence of Sulphate on IFT and CO_2 mass transfer
DIW+ $MgCl_2$	0	9.05	0	0	0	0	Single salts (Magnesium) effect on CO_2 mass transfer and IFT

DIW+$NaSO_4$	0	0	3.41	0	0	0	Single salts (Sulphate) effect on CO_2 mass transfer and IFT

Numerous researches have shown that the type of salt has a significant effect on the IFT of brine/hydrocarbon [24, 139]. Few studies have observed that for brine/hydrocarbon system that $MgCl_2$ specifically Mg^{+2} ions leads to lower IFT compared to other salts or ions present in their study [74, 80, 118]. Additionally, Nowrouzi, et al. [31] observed that for carbonated smart water injection the combination of $MgCl_2$ + K_2SO_4 leads to a higher reduction in IFT compared to other salts.

In the literature, there is little evidence of slats in enhancing the mass transfer of gases in liquids. Zhu, et al. [55] has shown that for CO/water system the sulphate salts showed maximum enhancement in the volumetric mass transfer. Therefore, these studies motivated us to use $MgCl_2$ and Na_2SO_4 slats to determine the effect of salts on IFT reduction and mass transfer enhancements in a CB/pure hydrocarbon system. The results from these salts would help us to investigate further on the mechanism and possibility of other salts and effect of varying the concentration.

3.2.3 Additives

The present study has used silica nanofluid. The nanofluid (DP9711) was supplied by Nyacol® Nano Technologies, Inc and is a colloidal silica surface modified fluid. The nanofluid is 30wt%, with a nominal particle size of 20 nm, viscosity of 5 cP at 25°C, specific gravity of 1.2, and a pH of 3 at 25°C. According to the manufacturers, the nanofluid is stable over a wide range of pH, time, and temperature. The nanofluid is dispersed in

water and then saturated with CO_2 to obtain carbonated nanofluid (CNF). CNF of different concentrations was prepared.

3.3 Experimental setup

3.3.1 Equipment and components

Figure 3.2 shows the high-pressure and high-temperature pendant drop equipment (PD-E1700 LL-H), along with the major components manufactured by KRUSS and EUROTECHNICA. The high-pressure pendant drop apparatus is a universal applicable tool for the determination of physical properties like interfacial tension, contact angle and also heat and mass transfer phenomena at elevated pressure and temperature.

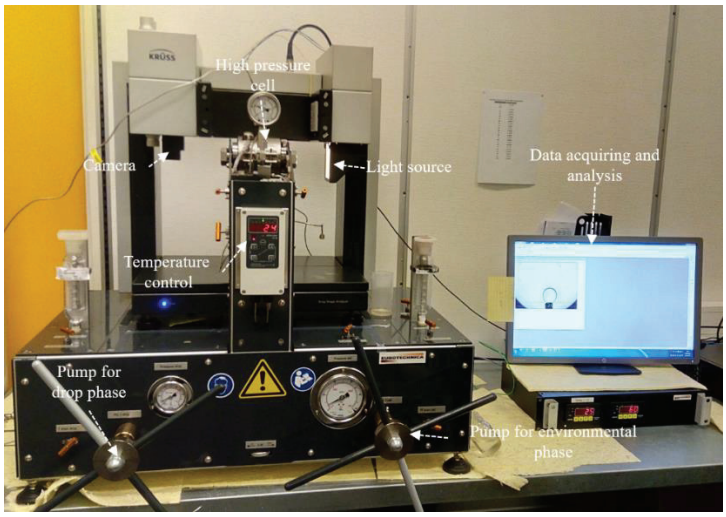

Figure 3.2: Pendant drop equipment with data acquiring system used for the interfacial and mass transfer analysis.

Figure 3.3 shows the schematic of the pendant drop equipment shown in Figure 3.2. As shown in Figure 3.3, the components of the equipment may be divided into four sections: 1) drop phase section (black hashed

region); 2) environmental phase section (blue hashed region); 3) measurement section (red hashed region); and 4) analysis section (not shown in Figure 3.2. The drop phase section consists of components like the hand driven pump (HP1), comprising drop liquid and a series of valves (A, DD, B, and C) that help to create a pendant drop in the view/pressure cell (VC). The environmental phase section also consists of a hand driven pump (HP2), comprising environmental fluid surrounding the drop phase (pendant drop) and valves (H, F, and E) that help in filling and removing environmental fluid in the VC. The measurement section consists of the VC and other associated components like camera, light source, controllers, and sensors that carry out various measurements (IFT, contact angle, heat, and volume changes). The final section takes care of the gathering and analysis of the data and mainly comprises a computer with drop shape analyser (DSA) software installed (seen in Figure 3.2). Below are the details of the major components, with their functionality:

i. View/pressure cell (VC): Is a corrosion resistant, Teflon-coated cylindrical chamber with see-through lids. The VC is 18 mm in diameter and has a capacity of 25 ml. The VC is temperature controlled and can withstand maximum temperature of 180ºC and pressure of 68.9 MPa.
ii. Temperature controller: The temperature of the VC is controlled by PT 100, which jackets the VC.
iii. Sensors (PI and TI): PI is the pressure indicator and consists of a pressure transducer (WIKA, Germany) which has an accuracy of ±0.1 MPa. TI is the temperature indicator (TP20 temperature sensor). TP20 is capable of highly accurate measurement of temperatures. It has a large measuring range (-50 to 400ºC) with a precision of ±0.1°C at 0°C to ±0.8°C at 400°C. Measurement is carried out immediately at the sensor tip, thus reproducing the actual conditions.

iv. Pressure generators (PG1 and PG2): Two pressure generators, one for the drop phase (PG1) and the other for the environmental phase (PG2), are part of the setup. The pressure generators are also corrosion-resistant and can withstand pressure up to 68.9 MPa. The PGs are hand-driven piston cylinders; this gives greater control and accuracy in forming the pendant drop.

v. Camera: The camera (CF03) captures and facilitates high-resolution images (1200 × 800 pixels) to be transmitted at high speed to the desktop via a USB 3.0 port. The rate of transmission ranges from 200 fps to 2000 fps; this enables the measurement of IFT/contact angles with precision, even for rapidly evaporating liquids.

vi. Connecting lines: The capillary tube and line connecting the VC from PG1 and PG2 have an outer diameter of 1.59 mm and an inner diameter of 0.8 mm.

In the present study, both gas-liquid (CO_2-hydrocarbon) and liquid-liquid (CW-hydrocarbon) systems have been studied; therefore, there are two different experimental setups, as discussed in the following section. Further, the experimental setup described in Figure 3.2 and 3.3 has been modified to suit the needs of different systems.

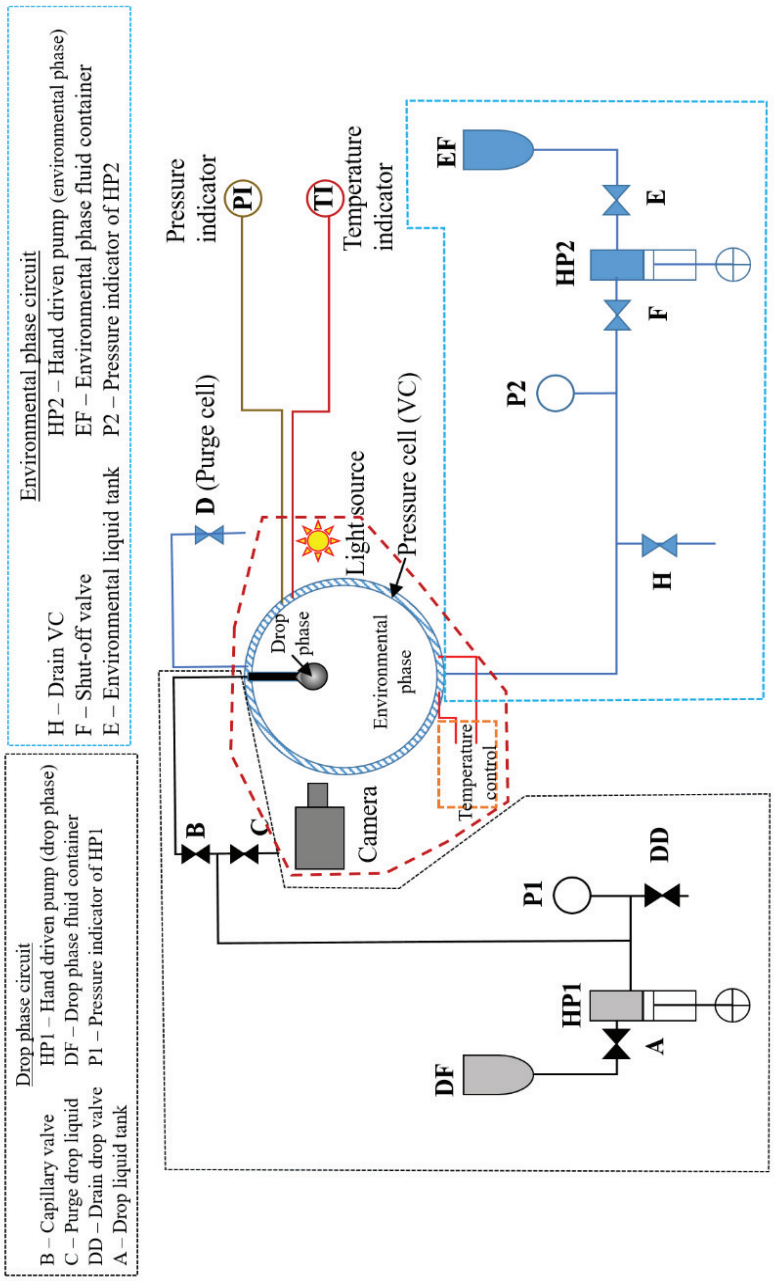

Figure 3.3: Schematic of the high-pressure pendant drop equipment, with different sections.

3.3.2 Experimental setup for CO_2-hydrocarbon system (gas-liquid)

In this work, CO_2-n-decane, CO_2-n-hexane, and CO_2-n-heptane constitutes the gas-liquid system. A detailed schematic of the experimental setup to capture and evaluate dynamic drop volume, drop surface area and interfacial tension for the CO_2-hydrocarbon system is shown in Figure 3.4. For the CO_2-hydrocarbon system, the hydrocarbon (n-decane, n-hexane, and n-heptane) forms the drop phase, while CO_2 is the environmental phase. Compared to the original setup (Figure 3.3), few modifications have been made to correspond to the CO_2-hyhdrocarbon system. The modifications were mainly made in the environmental phase section (blue hashed region). It may be observed that, in the environmental phase section, the HP2 is now replaced by a quick response electronic pump (GILSON, 30MPa), consisting of an electronic pump with a wide range of flow rates. Another modification is the inclusion of a CO_2 cylinder (CC). These modifications were made as the quick response pump would be more effective in carrying out isobaric experiments than a hand-driven HP2, especially for systems involving gas. Figure 3.5 shows the orientation of the hydrocarbon drop and surrounding CO_2 inside the VC and as seen by the camera.

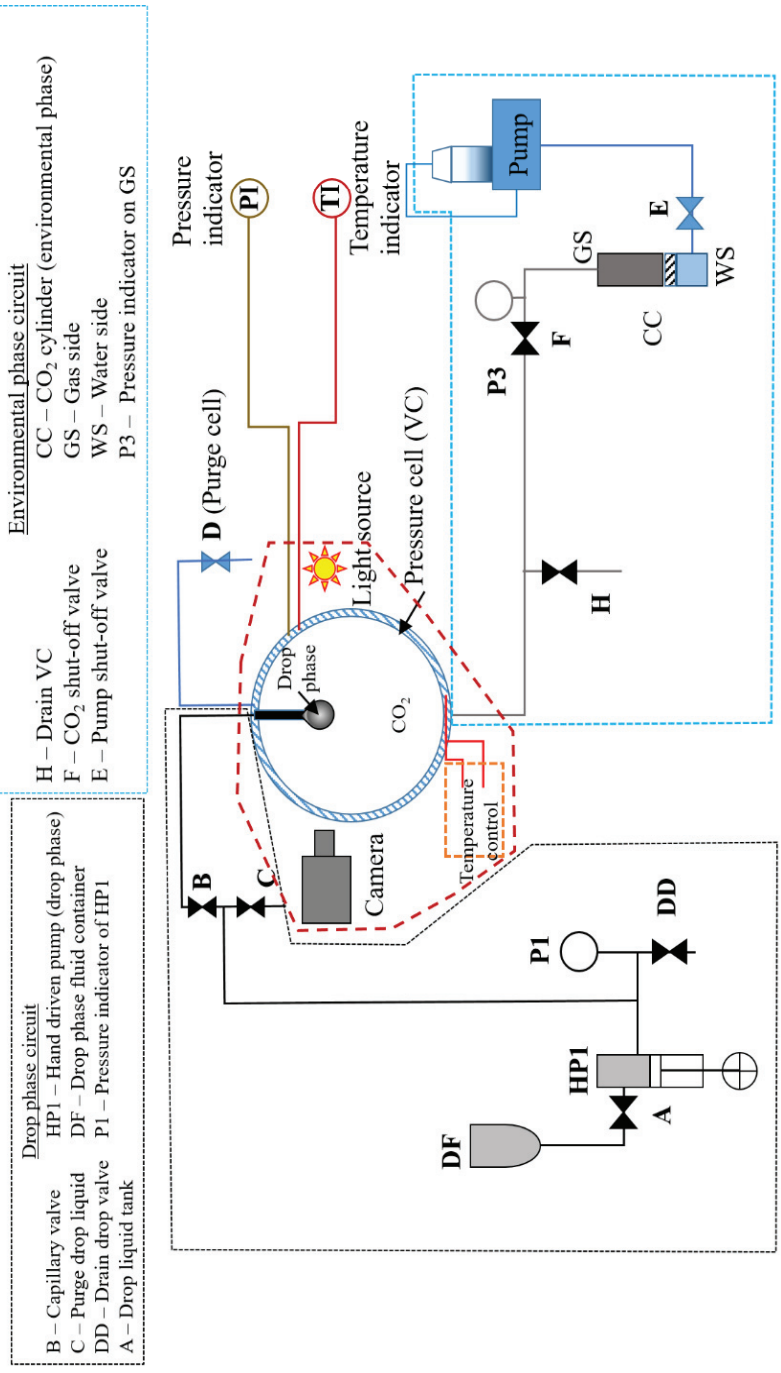

Figure 3.4: Schematic of the experimental setup for the CO_2-hydrocarbon system.

3.3.3 Experimental procedure for CO_2-hydrocarbon system

The following were the steps carried out during the process of the experiment:

i. Before the start of the experiment, the entire setup was examined for any leaks at high pressures.
ii. The pressure cell (VC) and the fluid lines connecting the VC was cleaned with acetone and then deionised water. Finally, dry air was blown into the lines and VC to remove any residual moisture.
iii. The DF was filled with the hydrocarbon (n-decane, n-hexane, and n-heptane), which forms the drop phase and, from the DF through valve A, the hydrocarbon was transferred to PG1, driving the piston out. This process was continued until PG1 is filled with hydrocarbon. To make sure that no air is present in PG1, valve DD was opened, and a few drops of the hydrocarbon are let out from PG1, by driving the piston inside.
iv. On the environmental phase circuit/section, the piston cylinder (CC) was filled with the CO_2 (environmental fluid). The cylinder has two openings one for CO_2 (gas side, GS) and the other is for water (water side, WS). The water side of the CC is connected to the pump through valve E, while the GS is connected to the VC through valve F.
v. The temperature control unit was used to set the required temperature inside the VC.
vi. Once the required temperature was obtained, the pump is set to the experimental pressure and started. Keeping valves F and H closed, valve E was opened; this positioning of valves was maintained until the pressure indicator P3 reads the required experimental pressure (set in the pump). The pump was kept running at all times, until the experiment is terminated.
vii. Next, opening valve F and closing all the other valves, the CO_2 was slowly pumped through the CC into the VC; the pumping of

CO_2 automatically stops once the pre-set experimental pressure was reached. The continuously operating pump always maintains the pressure in the VC. The VC was kept in this state for some time to allow uniform distribution of temperature.

viii. The pressure of the hydrocarbon in the HP1 is slowly brought to pressure just above that in the VC (by 1 bar); during this process, all the valves in the drop phase circuit were closed. Once the pressure in HP1 was obtained, valve B was slowly and steadily opened and, simultaneously, then HP1 was driven slowly until a pendant drop was formed inside the VC. Once the drop was formed, valve B was closed.

ix. As soon as the pendant drop was formed, the camera, along with the DSA 100 software, was started to capture the high-resolution digital images of drop for further analysis.

x. Further, the quick response pump makes sure that pressure loss due to CO_2 mass transfer was compensated for immediately.

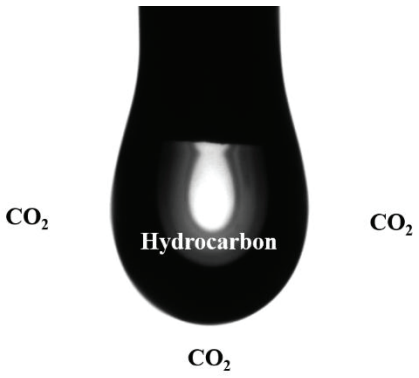

Figure 3.5: Orientation of hydrocarbon pendant drop in a CO_2-hydrocarbon system inside the VC.

3.3.4 Experimental setup for CW/liquid-hydrocarbon system (liquid-liquid)

In the present thesis, for the liquid-liquid system, the drop phase consisted of n-decane or n-hexane, while the environmental phase was water, brine, carbonated brine, nanofluid, carbonated nanofluid or CW. Figure 3.6 shows the schematic of the experimental setup used in the liquid-liquid analysis. Major modifications had to be made to the setup shown in Figure 3.3 to correspond to the current liquid-liquid system. It may be observed from Figure 3.6 that modifications have been made to the drop phase section (black hashed region), measurement section (red hashed region) and environmental phase section (blue hashed region). The environmental fluid section is similar to that of the original setup shown in Figure 3.3. However, for the CW-hydrocarbon experiments (Figure 3.6) a CO_2 supply cylinder is added to the environmental fluid section to obtain CO_2 saturated water (carbonated water) in the VC. For the CW-hydrocarbon system, the environmental phase (CW) is denser than the drop phase (hydrocarbon). Therefore, as shown in the Figure 3.7, in the VC, the capillary to which pendant drop is attached is now from the bottom, and, not from the top as for the gas-liquid system. The drop phase section is similar to that of the original setup (Figure 3.3), except that the fluid line from valve B is now connected to the VC from the bottom rather than from the top. Finally, inside the VC, the fluid system consists of three phases: the hydrocarbon drop phase, the surrounding CW and the volume of CO_2 about CW, which acts as the CO_2 source for water and keeps the water saturated with CO_2 at all times. Figure 3.7 shows the orientation of the hydrocarbon pendant drop surrounded by the CW, as seen by the camera.

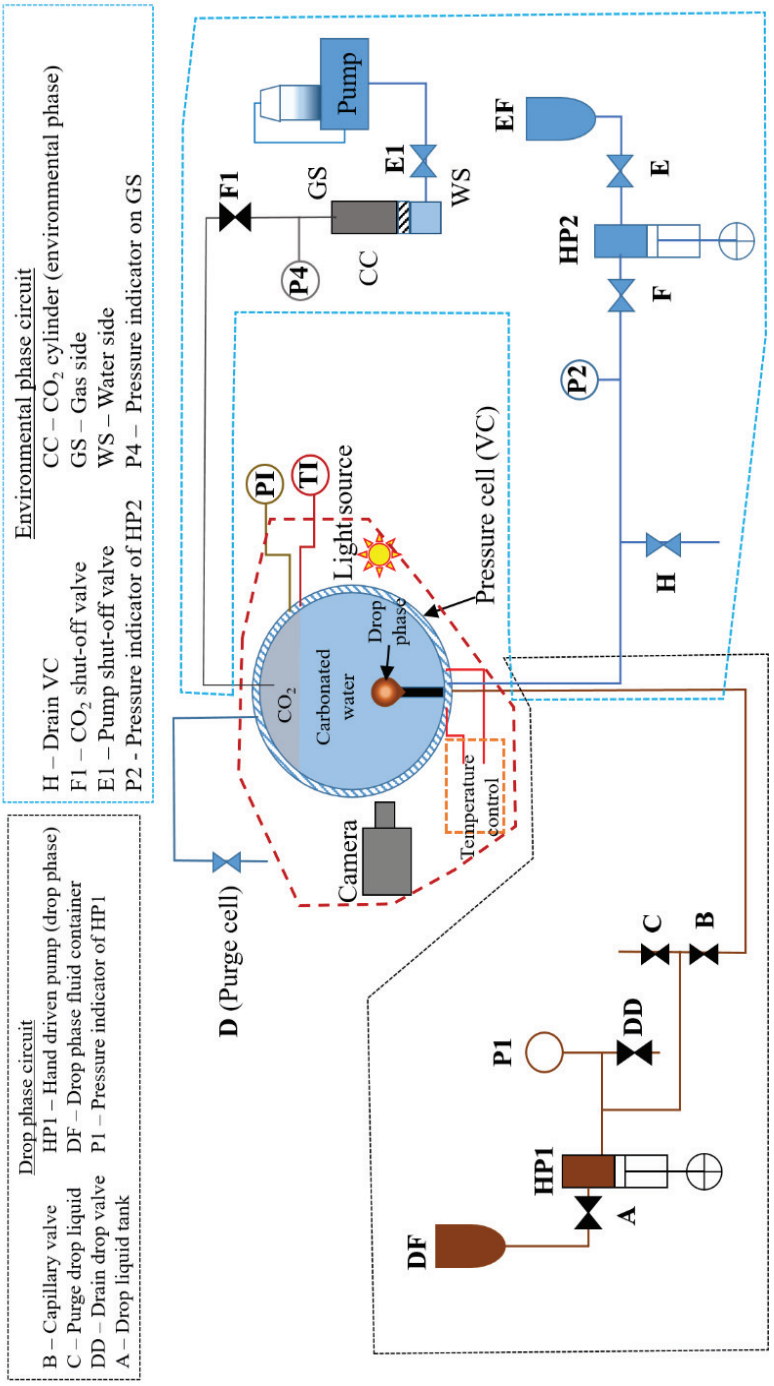

Figure 3.6: Schematic of the experimental setup for the liquid-liquid (CW-hydrocarbon) system.

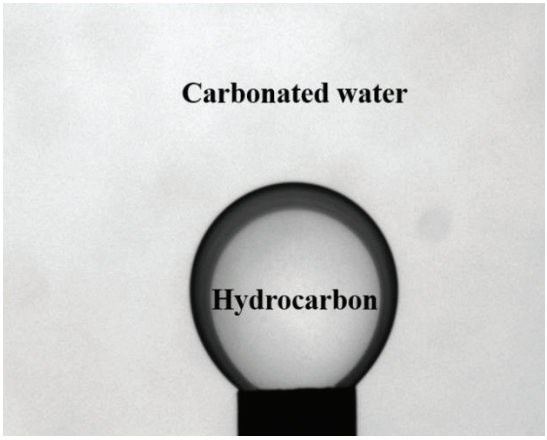

Figure 3.7: Orientation of the pendant drop and the surrounding CW for CW-hydrocarbon system.

3.3.5 Experimental procedure for CW/liquid-hydrocarbon system

The following were the steps carried out during the process of the experiment:

i. Before the start of the experiment, the entire system was tested for any leakage at high pressures.
ii. The pressure cell (VC) and the line connecting the VC were cleaned with acetone and then deionised water. Then, dry air was blown to remove any residual moisture.
iii. A hand driven piston (HP1) was filled with the hydrocarbon forming the drop phase (n-decane and n-hexane) from the DF through the valve A. HP1 is linked to the VC drop capillary through valve B.
iv. Similarly, hand driven piston pump (HP2) was filled with deionised water (environmental phase) from tank EF through valve E. HP2 was connected to the VC through valve F.

v. The required temperature inside the VC was set by the temperature control unit, and temperature of VC was indicated on TI.

vi. After the required temperature was obtained, the VC was filled with water from the HP2. During this process, except for valves F and D, the rest of the valves were closed. As water enters the VC, the air from the VC was driven out through open valve D. The VC was filled with 20 ml of water, keeping a small volume (5 ml) above the water for CO_2 to occupy.

vii. The pump was set at required experimental pressure and started. Keeping valve F1 closed, valve E1 was opened; this positioning of valves was maintained until the pressure indicator P4 read the required experimental pressure. The pump was kept running at all times, until the experiment was terminated.

viii. When the P4 showed the required experimental pressure, valves F1 was opened, and the CO_2 was slowly pumped through the CC into the VC. In the VC, the volume above the water was filled by CO_2, as shown in Figure 3.6. The volume of the CO_2 above the water acts as a source of CO_2 for CW.

ix. The pumping of CO_2 automatically stops once the pre-set experimental pressure is reached. The continuously operating pump always maintains the pressure in the VC. The VC is kept in this state for some time, to allow uniform distribution of temperature.

x. The pump continuously injects CO_2 into the VC, until the water reached saturation (at the predetermined pressures and temperatures) and can accept no more of the gas. Experiments using a gas flow meter were carried out at various pressures at 25^{o}C to estimate the saturation level of CO_2 in the water surrounding the HD. A detailed process of saturation of water with CO_2 is discussed in section 3.6.3.

xi. Once the water in the VC was saturated with CO_2, the pendant drop was created by simultaneously opening valve B and driving

the HP1 at the end of the capillary. Care was taken to make sure that the capillary line, through which the hydrocarbon pendant drop was introduced, was at the same pressure (not more than 0.5 bar greater) as that of the VC when the drop is being launched in the VC. This would eliminate any error occurring due to a significant difference between the drop and the surrounding water phase.

xii. As soon as the pendant drop was formed, the camera and the DSA 100 software start to capture the high-resolution digital images of the pendant drop for the analysis.

3.3.6 Experimental pressure and temperature

One of the objectives of the present thesis was to investigate the impact of the gaseous, liquid, and supercritical phases of the CO_2 on the IFT and CO_2 mass transfer. The pendant drop experiments were carried out for pressures 10 to 160 bar at three temperatures 25ºC, 35ºC, and 45ºC. For the selected experimental conditions, CO_2 is in a gaseous phase for $P<64$ bar at 25ºC and $P<73$ bar at 35ºC and 45ºC. For $P>64$ bar at 25ºC, CO_2 is in a liquid phase and $P>73$ bar at 35ºC and 45ºC, CO_2 is supercritical. Therefore, the selected experimental pressure and temperature include the entire spectrum of the CO_2 phase diagram, which will be beneficial in accessing the influence of CO_2 phase on CW-hydrocarbon IFT and CO_2 mass transfer. Figure 3.8 shows the density behaviour of CO_2 with pressure at 25ºC, 35ºC, and 45ºC [140]. As it may be observed, the changes in density as it changes to liquid is large compared to change into the supercritical region. This effect is part of the reason it is important to cover gaseous, liquid, and supercritical phases of CO_2.

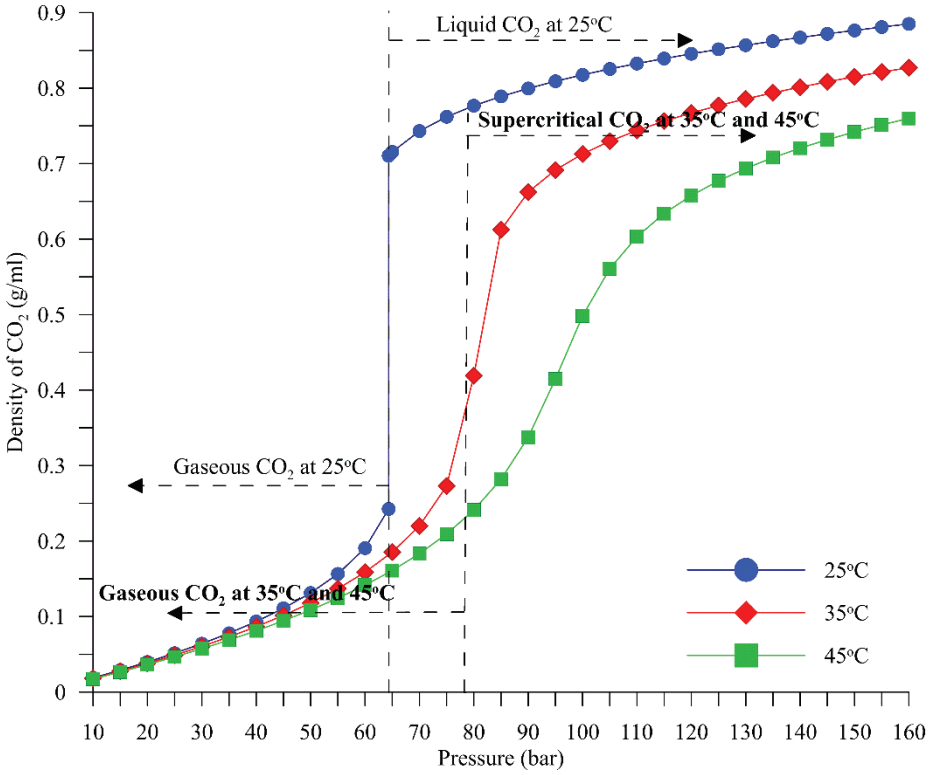

Figure 3.8: Density of CO_2 at different temperature for pressures 10-160 bar.

3.4 Calculation of density and viscosity

The IFT measurement by pendant drop and Young-Laplace equation depends on the density of the two phases (Equation (3.4)). In systems like CO_2-hydrocarbon, CO_2-water/brine and CW-hydrocarbon, as CO_2 interacts with the hydrocarbon/water, it diffuses and dissolves into the liquids, forming a multicomponent mixture. The diffusion of CO_2 into hydrocarbon would change the composition of the hydrocarbon, which in turn would alter the fluid properties like the density and viscosity of the hydrocarbon and CO_2 mixture. A relatively simple compositional mode that utilises the mass of CO_2 transferred into hydrocarbon, estimated from the dynamic experimental HD volume, has been developed to calculate the density and viscosity of the CO_2+hydrocarbon

mixture as a function of time. A detailed description of the method to obtain the density and viscosity of CO_2+hydrocarbon may be seen in Bagalkot and Hamouda [141] and Bagalkot, et al. [136]. The model may be applied to both gas-liquid and liquid-liquid systems. The model is based on the following assumptions:

i. The mixture of CO_2+hydrocarbon is an ideal mixture, so that the total volume of the pendant drop is the summation of the volume of the hydrocarbon and the volume of diffused CO_2 [15, 71].
ii. Due to the significantly lower solubility of water in hydrocarbon than CO_2, the mass transfer of water into hydrocarbon is neglected [141].

From the start of the experiment, when the CO_2 in the environmental phase contacts the hydrocarbon drop phase, the volume of the pendant drop is the summation of the volume of hydrocarbon (V_{PD}) and the volume of the diffused CO_2 into hydrocarbon (V_{CO2}). The time-dependent volume of the pendant drop (PD) is obtained from experiments. At the start of the experiment (time $t=0$), the PD consists of only hydrocarbon; therefore, the volume of PD at the start of the experiment is the volume of hydrocarbon (V_{HC}).

$$V_{HD}(t) = V_{CO2}(t) + V_{HC} \tag{3.9}$$

Equation (3.9) may be rearranged to obtain the volume of CO_2 (V_{CO2}) as a function of time:

$$V_{CO2}(t) = V_{PD}(t) - V_{HC} \tag{3.10}$$

The volume or the volume fractions of CO_2 and hydrocarbon may be used to obtain the mass/mole fraction of CO_2 and hydrocarbon in the drop phase, as a function of time. Further, the data of mass and mole fractions may be used to estimate the density and viscosity of the mixture of CO_2+hydrocarbon constituting the drop phase. Equation (3.11), given by Herning and Zipperer [142] for binary mixtures, may be used to

obtain the viscosity of CO_2+pure hydrocarbon mixture. According to Herning and Zipperer [142], for hydrocarbon mixtures, the data obtained from Equation (3.11) has an accuracy of 1.5% average deviation and 5% maximum deviation.

$$\mu_{drop} = \left(\frac{(\mu_{co_2} \cdot x_{co_2} \cdot \sqrt{M_{co_2}}) + (\mu_{HC} \cdot x_{HC} \cdot \sqrt{M_{HC}})}{(x_{co_2} \cdot \sqrt{M_{co_2}}) + (x_{HC} \cdot \sqrt{M_{HC}})} \right)_{P,T} \tag{3.11}$$

In Equation (3.11), x_{CO2} and x_{HC} are mole fraction of CO_2, and the hydrocarbon, respectively; M_{CO2} and M_{HC} are molecular weight of CO_2 and the hydrocarbon, respectively, and μ_{CO2} and μ_{HC} (cP) are the viscosity of CO_2 and the hydrocarbon, respectively. Similar to viscosity (Equation (3.11)), the density of the drop phase may also be found out by analytical relation. Equation (3.12) [143-145] may be used to estimate the density of the drop phase constituted by CO_2 and hydrocarbon.

$$\rho_{drop} = \left((x_{CO_2} \cdot \rho_{CO_2}) + (x_{HC} \cdot \rho_{HC}) \right)_{P,T}, \tag{3.12}$$

where ρ_{CO2} and ρ_{HC} are the individual densities of CO_2 and hydrocarbon in the drop, respectively.

3.5 Dynamic and equilibrium IFT measurement

A screenshot of the IFT analysis by DSA software is shown in Figure 3.9; it may be observed that the software requires the input of density, viscosity and expansion coefficients. As noted from Equation (3.4), at isothermal conditions, only the value of density would be required to calculate the IFT. From Equation (3.4), it may be noted that, besides density difference ($\Delta\rho$), the rest of the parameters are obtained by the DSA software. The user must only provide the density of the phases. Therefore, even if the software is computationally advanced with high accuracy, an inaccurate phase density input would result in an incorrect IFT estimation. Therefore, as described in Section 3.4, it is critical to

calculate and use a reliable density of the phases while estimating the IFT.

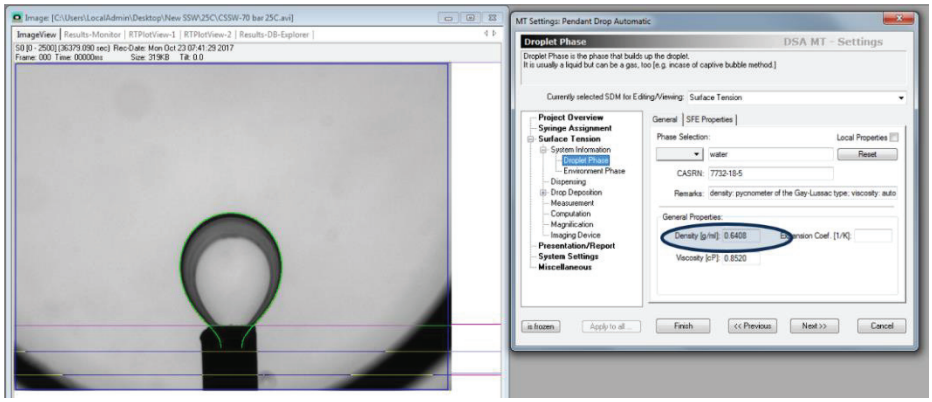

Figure 3.9: Screenshot of the IFT measurement by DSA software with data input panel.

Apart from the IFT at equilibrium, the dynamic IFT plays a vital role, especially in systems like CO_2-water and CW-oil, which normally take a long time to reach equilibrium (depending on temperature, and pressure). The change of the IFT with time would give an insight into the process. A major issue while estimating the dynamic IFT is obtaining the density of dynamic complex mixtures like CO_2+water and CO_2+oil, especially at elevated temperatures and pressures and, most importantly, as a function of time. The majority of studies [44, 104] have ignored the density changes due to the solubility effects of dissolved gases (CO_2) in bulk liquids (hydrocarbon) and have opted to use the density of pure fluids or at equilibrium to estimate the dynamic IFT. The present thesis developed a simple and effective method to measure the dynamic and equilibrium IFT of the fluid-fluid system. The developed method avoids a complicated EOS model or expensive additional instrumentation. The importance of using the correct density for the IFT calculation, as well as the consequence of not doing so, has been well described by Bagalkot, et al. [136]; therefore, a brief discussion on this is provided below.

Consider three different situations/cases of density inputs: case-1 (density of the pure phases is used), case-2 (equilibrium density of the phases is used), and case-3 (time dependent density of the phases is used, as calculated from Equation (3.12)). Among cases 1-3, only case-3 (the present method) takes into the account the time variation of the density of the phases. Figure 3.10 shows the dynamic IFT obtained for case-1, case-2, and case-3 for the reference system of CO_2-n-decane (50 bar and 25^oC). Interestingly, for none of cases 1-3 is the IFT vs time variation similar, emphasising the dependency of the IFT measurement on the phase density. Since both case-1 and case-3 do not consider the dynamic change in the density of the pendant drop, due to the solubility of a gas in a liquid, the dynamic IFTs measured by these methods are different from those where the solubility effect is considered (case-3). As for case-1 and case-2, where the dynamic change in the density of pendant drop due to the solubility of a gas in a liquid is neglected, the dynamic IFT measured by these methods would be different from that of case-3, where the solubility effect is taken into account. The deviation in the estimation of IFT among different methods varies from a maximum of 13.4% to a minimum of 0.2% for case-1, and 14.7% to 0.2% for case-2, when compared to case-3. If the particular study requires only data at equilibrium, then the scenario described by case-2 may be applied. However, if the dynamic changes in the IFT, as well as the equilibrium IFT, are to be analysed, then case-3 would be the best option (developed in the present study), as the densities of the phases are calculated at different time intervals until equilibrium is reached. Obtaining IFT using the case-1 approach would lead to misinterpretation, as the density represents only the initial state of the system, not the equilibrium or the dynamic.

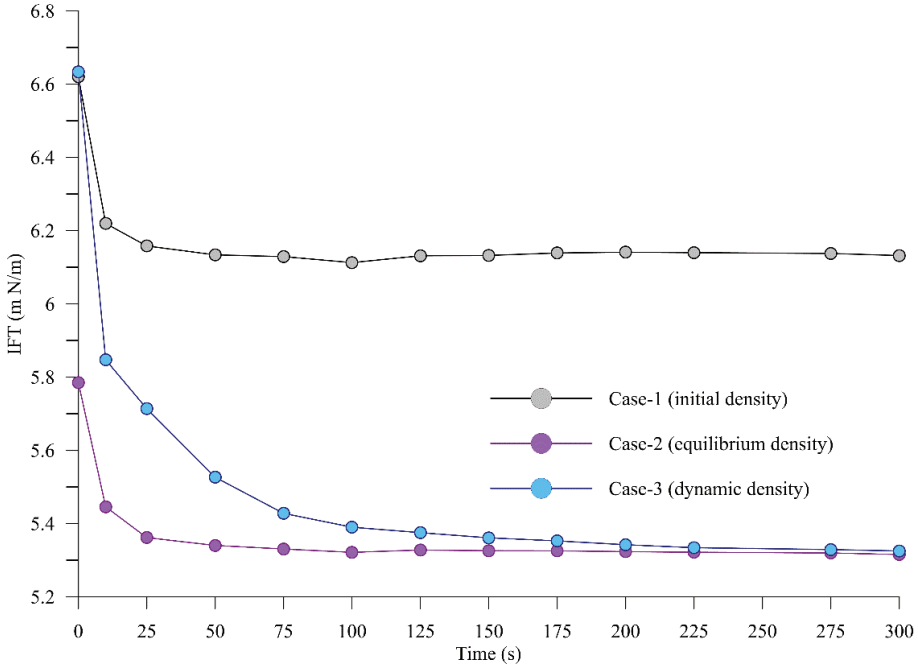

Figure 3.10: Dynamic IFT CO_2-decane system for case-1, case-2 and case-3 at 50 bar and 25°C [137].

Figure 3.11 gives a flow chart of a systematic representation of the procedure involved in obtaining the dynamic and equilibrium IFTs. A detailed procedure for obtaining dynamic/equilibrium IFT by the present developed method may be seen in Bagalkot, et al. [136].

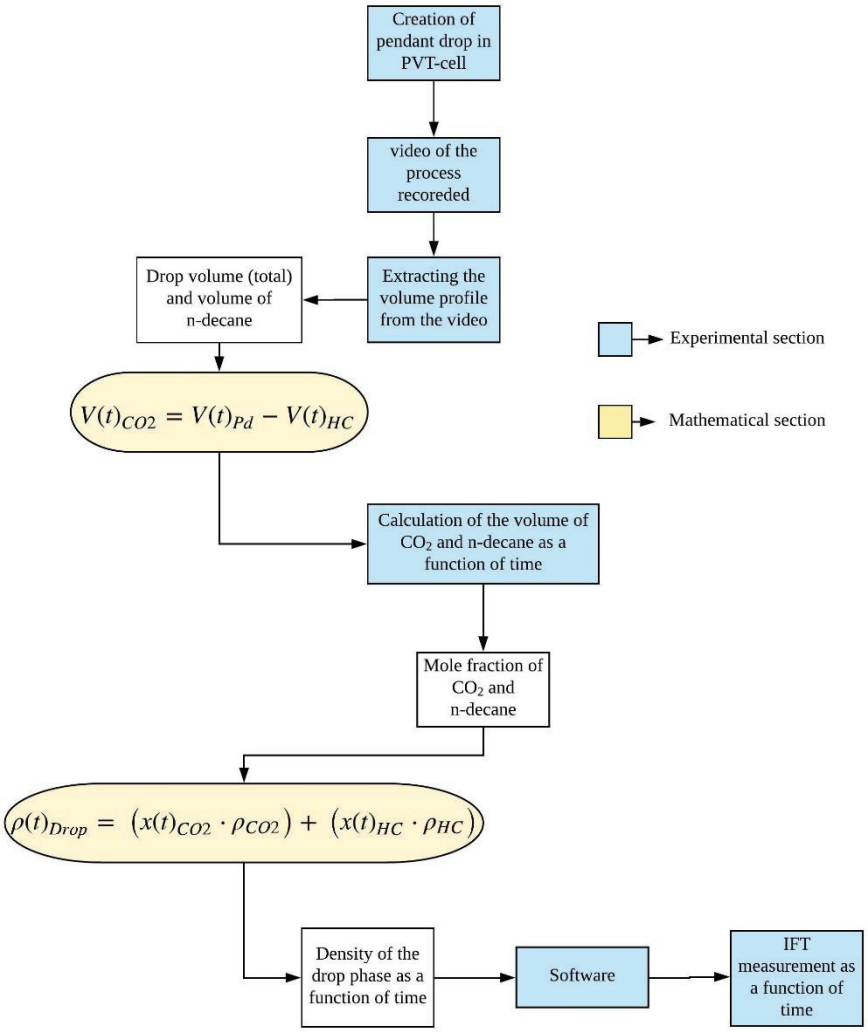

Figure 3.11: Systematic representation of the process involved in the measurement of IFT [136].

3.6 Calculation of Gibbs free energy

The Gibbs classical model was employed to explain the behaviour of CW-hydrocarbon IFT with temperature and pressure. The interfacial

energy is a direct function of Gibbs free energy (ΔG), therefore, estimating the change in free energy of the system would assist in explaining the experimental observations on IFT. The absolute rate theory approach proposed by Eyring related the viscosity of liquid mixtures to the change in Gibbs free energy (Equation 3.13) [146].

$$\mu = \frac{hN}{V_m} \exp\left[\frac{\Delta G_m}{RT}\right], \tag{3.13}$$

where μ is the dynamic viscosity of the mixture (*Kg/m.s*), h is Planck's constant ($Kg.m^2/s$), N is Avogadro's number (mol^{-1}), V_m is the molar volume of the mixture (m^3/mol), ΔG_m is the molar Gibbs free energy of activation for the flow process (*J/mol*), and T is the absolute temperature (*K*). In the present thesis, the viscosity of both the surrounding environmental phase (CW) and drop phase (n-decane+CO_2) is estimated as described in the section 3.4. The viscosities are then used to determine the change in Gibbs free energy (ΔG) as shown in Equation (3.14).

$$\Delta G_m = RT \ln\left[\frac{\mu V_m}{hN}\right] \tag{3.14}$$

Assuming the interface of CW-hydrocarbon to be thin the change in Gibbs free energy of the CW-hydrocarbon system may be represented as in Equation (3.15).

$$\Delta G_{System} = \Delta G_{Environment} + \Delta G_{Drop}, \tag{3.15}$$

where ΔG_{System} is the change in free energy (J) of the system; $\Delta G_{Environment}$ is the change in free energy (J) of the environmental phase; ΔG_{Drop} is the change in free energy (J) of the drop phase. $\Delta G_{Environment}$ and ΔG_{Drop} are obtained from Equation (3.14).

3.7 Experimental setup to study the influence of degree of carbonation

In the present thesis, the influence of the quantity of CO_2 in CW (degree of carbonation) on the IFT and associated properties has been studied by carrying out experiments in two different approaches. In the first approach the system consists of CO_2-water-decane, and in the second approach, the system consists of CO_2 saturated water (CW)-decane. The CO_2-water-decane will be abbreviated CHHC and CW-decane system as CWHC. The principal difference separating these two approaches is the level of carbonation of the environmental phase (water) enveloping the drop phase. For CHHC system the level of carbonation in water increases from zero at the start to max at equilibrium, indicating that a change in the carbonation as a function of time. Whereas for CWHC system the carbonation of water surrounding drop phase is constant (100% saturated with CO_2). Interestingly, these two approaches represent fluid-fluid interaction of two different practical scenarios CO_2 injection and CW injection. Figure 3.12 [141] shows the representative diagram for these two approaches, the dotted boundary may be represented as the wall of the PVT cell, while the oil may be considered as the pendant drop. Figure 3.12A represents the case of fluid-fluid interaction that may happen for the case of CO_2 flooding (CO_2-water-hydrocarbon, CHHC). In Figure 3.12A the oil drop symbolise the drop phase which is surrounded by the water, while the CO_2 above the water would represent the injected CO_2. Figure 3.12B represents the fluid-fluid interaction for the case of CWI (CW-hydrocarbon, CWHC), the pendant drop symbolise the oil, and the fluid surrounding the oil is the injecting CW. As indicated by the arrows (blue arrows), for CHHC system (Figure 3.12A) the CO_2 first diffuses/dissolves into the water and migrates towards the water-oil interface and then diffuses into the oil. Therefore for the CHHC system, the CO_2 in water increase from zero saturation to maximum, indicating the level of carbonation varies. However, for CWHC (Figure 3.12B) system the CO_2 directly diffuses from the CW into the oil, therefore, the

water is always saturated with CO_2 with maximum carbonation. Although EOR analysis is not carried out directly in the thesis, the main factors that affect these processes such as diffusion, viscosity, and interfacial tension (IFT) have been addressed. The experimental procedure for CWHC system is similar to that described in Section 3.3.5. The experimental procedure for CHHC is system is also similar to Section 3.3.5 except that there is not waiting period of 6 hours and pendant drop is created as soon that CO_2 is injected into the VC.

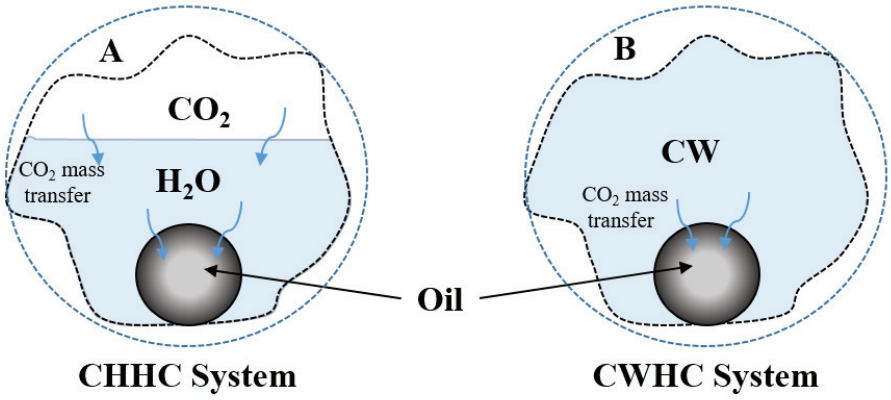

Figure 3.12: Representative diagram indicating the influence of level of carbonation [141].

3.8 Experimental setup to estimate the change in CO_2 solubility in water by nanofluid.

A pressure decay method was employed to measure the change in the CO_2 solubility in water containing silica nanofluid. The principle of pressure decay method is based on the estimation of the mass of molecules of gas dissolved in the bulk liquid in a chamber with a constant known volume. The diffusion of gas into the liquid would lead to a decay (loss) in the pressure of the system, the drop in pressure continues as long as diffusion continues. The mass flow of gas into the liquid is determined by monitoring of pressure decay in a chamber. The pendant drop

experimental setup shown in Figure 3.6 was modified as shown in Figure 3.13 to carry out the CO_2 solubility experiments. The drop phase circuit was disconnected by removing the capillary tube inside the pendant drop. Further, the camera and light source were disabled as there was no pendant drop. After modifications as shown in the Figure 3.13 the experimental setup consists of a gas phase circuit where the gas is the CO_2, and liquid phase circuit where the liquid is either water or water+nanolfluid.

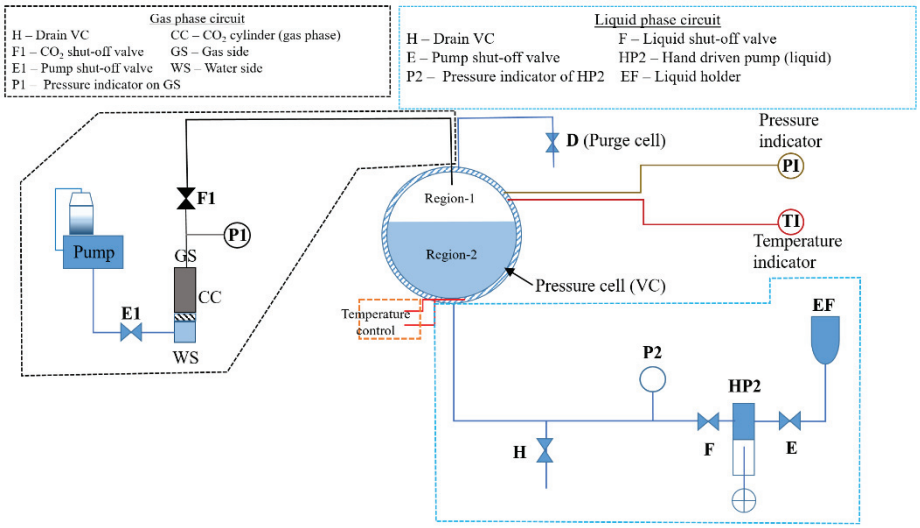

Figure 3.13: Schematics of the experimental setup to estimate the CO_2 solubility in water and water+nanofluids at elevated pressures and temperatures.

The following are the steps that were performed during the process of the CO_2 solubility experiment:

i. The pressure cell is partially filled with a known volume of liquid, using HP2 and opening valve F, so that it occupies Region-2.
ii. A know volume of CO_2 is pumped into the cell through CC and opening the valve F1, so that it occupies the Region-1.

iii. Once the required experimental pressure is obtained vales F1, D, H, and F are closed, this isolated the pressure cell.

iv. Monitor the decay in pressure due to diffusion of CO_2 from Region-1 into the liquid in Region-2.

v. Carry out the experiment until the pressure drop is stopped and equilibrium pressure is obtained.

vi. Calculate the number of mole of CO_2 present in Region-1 at the initial and equilibrium pressure using the Equation (3.16).

$$n_j = \frac{P_j V_j}{z_j RT}, \tag{3.16}$$

where n is the number of moles of gas; P, V, and T are pressure (Pa), volume (m^3), and temperature (K) respectively; z is compressibility factor of CO_2, and suffix j represents the initial and final.

vii. Find the difference in CO_2 moles in the Region-1, this difference would give the amount of CO_2 dissolved in the liquid present in Region-2.

viii. The CO_2 solubility in liquid was obtained by dividing the amount of dissolved CO_2 by the volume of the liquid in Region-2.

3.9 Uncertainties and error analysis

3.9.1 Uncertainties of the measurement given by the manufacturer

The manufacturer mentions that, in the case of the CO_2-hydrocarbon system, the IFT measurement uncertainty is ±0.3 mN/m. If water is present, uncertainties rise to ±0.5 mN/m. The uncertainty depends on the absolute value of the density difference and becomes greater as the density difference decreases [147, 148]. Further, both the pressure and

temperature sensors have been pre-calibrated by the manufacturer (Kruss and Eurotechnica).

3.9.2 Uncertainties in the calculation of IFT and density

The calculation of the IFT by the pendant drop method is predominantly a function of shape parameter/Bond number (B) and density difference ($\Delta\rho$) between the phases, as described in Equation (3.4) [103, 134]. The shape parameter is estimated by the image-processing software (DSA, Kruss), while the density of the phases is the input that the user must provide. Hence, uncertainty in IFT measurement lies in the density measurement of the phases. The densities of the drop phase (CO_2+hydrocarbon) are determined from the experimentally obtained volume profile of the drop phase. In the present thesis, multiple experiments were carried out at each experimental pressure and temperature to assess the repeatability and reliability of the experimental results. In Table 3.2, two such experiments, represented by D1 and D2, are reported. Part A and B in Table 3.2 show the density difference and IFT data at 30, 60, and 100 bar (25^{o}C) for D1 and D2 sets of repeat experiments for the CW-n-decane system. It may be observed from Part B that there is minimal difference in IFT values among different repeat experiments at a given pressure and temperature, indicating that the uncertainties in the calculation of IFT are low and repeatability is higher.

Table 3.2: Data about repeatability in density difference and IFT measurement.

Part-A			
Pressure (bar)	Density difference between CW and HD		Percentage difference in the density difference between D1 and D2
	D1	D2	
30	0.3882	0.3923	-1.05
60	0.5029	0.5123	1.83
100	0.0402	0.0405	-0.57
Part-B			
Pressure (bar)	IFT (m N/m)		Percentage difference in the IFT between D1 and D2
	D1	D2	
30	57.72	58.10	0.65
60	79.56	80.75	1.47
100	27.52	27.93	1.46

3.9.3 Uncertainties in preparing saturated CW

Below is a detailed description of the process of making carbonated water, the uncertainties associated with CO_2 solubility in water, and their effect on other measurement. Three steps have been carried out in the present experimental work to make sure that the water in the pressure cell (VC) is always enriched (saturated) with CO_2.

Step-1: As shown in Figure 3.5, the water in the VC was always in contact with CO_2 gas. With time, dissolution of CO_2 into water occurs and the pressure of the VC would drop. However, the VC was connected to the CO_2 cylinder via a pump, which compensates for the pressure drop by pumping CO_2 into the VC, making sure that the water will always have a CO_2 source at its disposal. The process of the pressure drop and the instantaneous pumping of CO_2 continues, until the water in the VC is saturated with CO_2.

Step-2: To allow enough time for the dissolution of CO_2 into the water, the CO_2 was exposed to water at experimental pressure and temperature for minimum of 6 hours before the hydrocarbon pendant drop was created in the VC. The residence time of 6 hours would be sufficient to enrich water with CO_2 (saturate).

Step-3: Auxiliary experiments were carried out to estimate the solubility of CO_2 in water in the VC (20 ml of water). The experiments were also used to test whether the residence time (6 hours) is enough. The experiments were carried out at two pressures, especially at lower pressures (20 bar and 50 bar), as the dissolution rate would be slow, and more residence time would be required. A sensitive gas flow meter (EL-FLOW Select F-120M, with accuracy of ±0.5% Rd plus ±0.1% FS) was connected between the CO_2 source and the VC. Figure 3.14 shows a simple schematic of the setup used to carry out a test for the saturation of CO_2 in water. The test cylinder is where the dissolution of CO_2 into water occurs and CO_2 saturation is measured. The test cylinder consists of the same volume of water (20 ml) as that in the PVT-cell (VC) of the original experiments. The CO_2 is supplied to the test cylinder from the CO_2 source cylinder, via a flow meter, by the pump set at the required pressure.

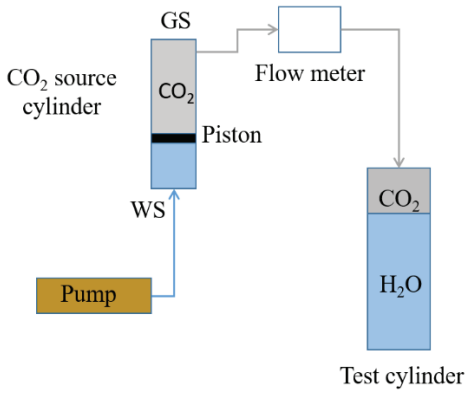

Figure 3.14: Schematic of the CO_2 saturation measurement experiment.

The procedure to estimate the saturation of CO_2 in water is as follows:

i. The test cylinder was filled with same volume of water (20 ml) and the volume of space above the water (5 ml) was maintained the same as that in PVT-cell (VC).
ii. Once the test cylinder was filled with water, the pump injects CO_2 into the test cylinder and the flow meter starts to register the mass of CO_2 passing into the test cylinder. The connection of the CO_2 source to the test cylinder will always be open and the pump keeps the CO_2 into the cylinder at the required pressure.
iii. The CO_2 above the water in the test cylinder dissolves into water, and the loss in mass of CO_2 was compensated for by the pump injecting more CO_2, so that the pressure is maintained at all times.
iv. The experiment was stopped after the reading in the flow meter showed no mass flow.
v. At the end of the experiment, the total mass of CO_2 given by the flow meter was subtracted from the mass of CO_2 present in the space above the water in the test cylinder, to obtain the mass of CO_2 present in the water (saturation of CO_2). The mass was calculated in terms of mole, using the real gas law, as show in Equation (3.16):

$$n_t = n_{free} + n_{water} \tag{3.16}$$

where n_t, n_{free}, and n_{water} are the total moles of CO_2 present in the test cylinder (as given by totalizer of the flow meter), moles present in free space above the water, and mole present in water, respectively. The moles of CO_2 present in the free space are calculated using the real gas laws, as given by Equation (3.17):

$$n_{free} = \frac{PV}{KRT}, \tag{3.17}$$

where P, V, and T are pressure (Pa), volume (m^3), and temperature (^oK), respectively; K is the pressure and temperature dependent compressibility factor of CO_2. Finally, the moles of CO_2 present in water are calculated from Equation (3.18):

$$n_{water} = n_t - \frac{PV}{KRT} \tag{3.18}$$

Table 3.3 shows the results of the experiments and their comparison with the results from the model given by Duan and Sun [149]. It may be observed that there is a minimal difference in the moles of CO_2 in water from the experiment and from that given by the model, indicating that the experimental process used in the present study ensures that the water is always enriched with CO_2 and hence, the CW surrounding the hydrocarbon drop is approximately 100% saturated. Therefore, from the point of uncertainties, this is minimal and would not influence the outcome of the results. A difference of 3-5% in the solubility of CO_2 in water would not make a considerable difference to the density of the CW and, hence, density difference across the interface would not affect the IFT values.

Table 3.3: Data from the CO_2 saturation in water experiment.

Pressure (bar)	Total moles of the CO_2 present in the test cylinder (n_t)	Moles of CO_2 present in free space above the water (n_{free})	Moles of the CO_2 present in water (n_{water})	Moles of CO_2 as given by Duan and Sun [149]	Percentage error
20	0.01567	0.00452	0.01115	0.01186	5%
50	0.03831	0.01499	0.02331	0.02403	3%

4 Numerical Methodology

4.1 Background and motivation

Numerous experimental and numerical methods have been presented previously to calculate the diffusion coefficient of gases in bulk liquids. Conventionally, compositional analysis [36, 37] and pressure decay [39, 150] are the most widely used. In compositional analysis, the diffusion coefficient is estimated by examining at various time steps the composition of the dissolved CO_2 in the bulk liquid that is extracted from the experimental setup. Gas chromatography is used to estimate the change in the mass of CO_2 with time and, hence, estimate the diffusion coefficient. The major problem with compositional analysis is the dependency of the results on correctly extracting the samples and carrying out chromatography. The whole process involves significant human interference and would lead to error in measuring the diffusion coefficient of the CO_2 in bulk liquids. The error may further escalate at high pressures and temperatures, as it would be significantly challenging to extract the sample at high pressures, while simultaneously carrying out chromatography at the same experimental conditions [41]. Further, due to the complicated process and involvement of multiple equipment, the compositional analysis method would turn out to be expensive [40]. The pressure decay method is a relatively simple approach and relies on observing pressure changes as a function of time, due to the diffusion of gas into bulk liquids [38-40, 150-152]. The pressure reduction data is then combined with a numerical model to estimate the diffusion coefficient. The pressure decay method eliminates the use of chromatography and extraction of the sample and thus overcomes the problems associated with the compositional analysis method. Although the pressure decay method is better than the compositional method, it has its limitations. First, the pressure decay methods require a long experimental time (20 hours to 100 hours or more) [40]. Second, and

most importantly, the estimated diffusion coefficient is for a range of pressure and not for a determined pressure [41, 45].

Experimental approaches are expensive and are associated with errors and complications; therefore, Zabala, et al. [153] utilised an entirely numerical approach. Zabala, et al. [153] used molecular simulations to obtain the diffusion coefficient of CO_2 in alkanes. However, the model demands the phase properties, such as the difference in chemical potential, and fugacity, which requires solving complex equation of state (EOS). In recent times, unconventional methods have been developed to calculate the diffusion coefficient of gases in bulk liquids. For example, Liu, et al. [47] used a microfocus X-ray CT scanning technique to compute the diffusion coefficient of CO_2 in n-decane and n-decane-saturated porous media. Zhang, et al. [154] relied on pH value to calculate the diffusion of CO_2 in saline water.

Table 4.1 [45] shows the data of the diffusion coefficient of CO_2 in hydrocarbons obtained by different studies along with the method and at similar experimental conditions. It may be observed from Table 4.1 Part A that there is an inconsistency in the measured CO_2 diffusion coefficient. The inconsistency is not limited to being across different methods, it is also seen among the same method. Another problem with most widely used methods is their incapability to carry out other analysis, apart from the mass transfer, especially the study of interfacial phenomena. The IFT and diffusion coefficient are dependent and should not be studied separately. This has provided the motivation for the present thesis: to search or develop a method that may be reliable and flexible enough to carry out multiple analyses (IFT, contact angel, mass transfer and others).

Table 4.1: Diffusion coefficient (m^2/s) obtained by different studies with CO_2 as environmental phase [45].

PART A (CO_2 – hydrocarbon)				
Analysis Method	**Gas Phase**	**Liquid Phase**	**Experimental Conditions**	**Diffusion Coefficient (10^{-9} m^2/s)**
Schmidt, et al. [35] (Compositional)	CO_2	Bitumen	50 bar, 20 - 200°C	0.28 – 1.75
Upreti and Mehrotra [38] (Pressure Decay)	CO_2	Hamaca Oil	35 bar, 21°C	4.8
Upreti and Mehrotra [150] (Pressure Decay)	CO_2	Athabasca Bitumen	40 – 80 bar, 25 – 90°C	0.17 – 1.08
Yang and Gu [41] Pendant Drop Analysis	CO_2	Heavy oil	20 – 60 bar, 23.9°C	0.199 – 0.551
Liu, et al. [47] (CT Scan)	CO_2	n-decane	10 – 60 bar, 29°C	0.38 – 2.29
Part B (CO_2 – n-decane)				
Grogan, et al. [48] (variable pressure)	CO_2	n-decane	13 – 50 bar, 25°C	3.21 – 5.71
Renner [27] (Pore scale, IFT measurement)	CO_2	n-decane	15 – 60 bar, 37°C	1.97 – 5.05
Liu, et al. [47] (Pore scale)	CO_2	n-decane	10 – 60 bar, 29°C	0.38 – 2.29
Zabala, et al. [153] (Numerical/Simulation)	CO_2	n-decane	0.2 – 0.8 CO_2 saturation	1.9 – 4.1

Of late, a new and unique method using Axisymmetric Drop Shape Analysis (ADSA) was developed by Yang and Gu [41] and Yang, et al. [44] to estimate the diffusion coefficient of gases in liquids. The method consists of three steps. First, the dynamic changes in the liquid pendant

drop surrounded by gases or another liquid are measured, using pendant drop equipment. Second, a computational scheme is employed to calculate the dynamic volume changes using the concentration distribution of the gas in the liquid. Finally, the diffusion coefficient of gas in the liquid is estimated by comparing the numerically calculated and the experimentally measured dynamic pendant drop volume; an objective function has been developed for this purpose. Estimation of the diffusion coefficient at elevated pressure and temperature may be carried out using the ADSA method (up to 60 MPa and 180ºC) [31]. Unlike the pressure decay method, diffusion coefficients may be obtained at isobaric conditions. As described in Chapter 3, the ADSA method is widely used for IFT analysis; therefore, without the need for an additional experimental setup, both interfacial and mass transfer phenomena may be studied simultaneously. The analysis by ADSA significantly minimises human interference, is more straightforward, takes less time and is flexible; this makes the ADSA method suitable for calculating the diffusion coefficient of gases into the bulk liquids. Further details of the ADSA method and novel modifications will be described in the following sections.

4.2 Estimation of effective CO_2 diffusion coefficient in hydrocarbon

4.2.1 Mathematical model

Diffusion is an important process in CO_2 associated EOR or CCS processes, and natural diffusion is a concentration-driven process. The present work studies the diffusion of CO_2 from the CW into the hydrocarbon drop. Hence, it is critical to determine the concentration of CO_2 in the hydrocarbon pendant drop, to understand the process of diffusion at different conditions and environment. In the present work, a series of mathematical equations has been adopted, which represents the mass transfer of CO_2 from CW into the hydrocarbon pendant drop. When

CW contacts the hydrocarbon drop, there is a diffusive mass transfer of CO_2 from CW into the drop, and the diffusion continues as long as there is a concentration gradient. Hence, the CO_2 spreads across the pendant drop, starting from the interface. A mathematical equation that can conveniently describe this process has to be applied to calculate the spreading of CO_2 in the pendant drop. Fick's second law of diffusion adequately describes the diffusive mass transfer process of CO_2 from the interface to the centre of the hydrocarbon drop. The mass transfer model presented in this work is adopted from [41, 155] (Equation (4.1)).

$$\frac{\partial C}{\partial t} = D(t)\left\{\frac{1}{r}\frac{\partial C}{\partial r} + \frac{\partial^2 C}{\partial r^2} + \frac{\partial^2 C}{\partial z^2}\right\}, \tag{4.1}$$

where C is the concentration of CO_2 in the hydrocarbon pendant drop phase (kg/m^3) and $D(t)$ is the diffusion coefficient (m^2/s). The pendant hydrocarbon drop and the surrounding CW phase form a symmetry about the vertical axis (z) passing through the centre of the pendant drop (Figure 3.1). Therefore, it would be better and justified to use a 2D axisymmetric rather than a complicated 3D Cartesian system. Hence, the diffusion of CO_2 from CW into the oil phase is an unsteady 2D axisymmetric system in the cylindrical coordinate system.

The diffusion of CO_2 from CW into the hydrocarbon is initiated after the drop is created in the CW. Therefore, at the onset of the experiment ($t = 0\ s$), the concentration of CO_2 in the pendant drop is zero at $t = 0$ (Equation (4.2)).

$$C(r, z, t = 0) = 0 \tag{4.2}$$

The interface is at thermodynamic equilibrium [156], indicating that the concentration of CO_2 at the interface remains constant, as long as the pressure and temperature of the system are held constant. On this basis, Equation (4.3) represents the boundary condition at the interface.

$$C(r = R_D, z = R_D, t > 0) = C_o, \tag{4.3}$$

where R_D is the radius of the drop, and C_o is the concentration of CO_2 at the interface. A zero (constant) flux boundary condition is employed to address the continuity at the centre of the drop ($r=0$) (Equation (4.4)).

$$\frac{\partial C(r = 0, z, t)}{\partial r} = 0 \tag{4.4}$$

Equation (4.1), along with its boundary and initial conditions (Equations (4.2) – (4.4)), is numerically solved, to obtain the time and space dependent CO_2 concentration in the pendant drop. A volumetric average of the CO_2 concentration in the pendant drop (C_{avg}) is computed at predefined time steps by using Equation (4.5). The C_{avg} (mm^3) gives the total volume of CO_2 diffused in the pendant drop for a given time, t.

$$C_{avg}(t) = \iint_{(r,z)\in P_d} \frac{C(r,z)}{C_o} r dr dz \tag{4.5}$$

The mass transfer of CO_2 into the pendant drop phase reduces the viscosity and leads to an increase in the volume of the drop (swelling). The amount of increase in volume is a function of the mass of CO_2 diffused into the pendant drop. Therefore, the parameter C_{avg}, which gives the volume of the CO_2 present in the drop may be used to calculate the swelling factor (SF). Swelling represents the ratio of the volume of the CO_2-saturated hydrocarbon (CO_2+hydrocarbon) to the initial volume of pure hydrocarbon. Equation (4.6) accounts for the swelling factor [155].

$$SF = 1 + \frac{\int_0^T \frac{\left[V_{\exp}(t) - V_o\right] C_{avg}(t) dt}{V_{\exp}(t)^2}}{\int_0^T \frac{\left[{C_{avg}}^2(t)\right] dt}{V_{\exp}(t)^2}}, \tag{4.6}$$

where $V_{exp(t)}$ is the experimentally obtained volume of hydrocarbon drop

at time *t,* and *T* is the total experimental or simulation time; V_o is the initial volume (*t=0)* of the hydrocarbon pendant drop, determined experimentally.

The volume of the pendant drop is the summation of the initial volume of drop (V_o) consisting of hydrocarbon and the increase in volume caused by the CO_2 diffused in the hydrocarbon (V_{CO2}). The increment in pendant drop volume is given as the product of C_{avg} and *SF-1* [41], as represented by Equation (4.7).

$$V(t) = V_o + (SF - 1) \cdot C_{avg}(t) \tag{4.7}$$

An optimisation/objective function (*F*) is developed (Equation (4.8)), which compares the experimental ($V_{exp}(t)$) and numerical volumes ($V(t)$) of the pendant drop as a function of time. The minimum of the optimisation function (F_{min}) is used to obtain the diffusion coefficient of CO_2 in the hydrocarbon pendant [41]. The lower the $F_{min,}$ the nearer the numerical result to the experimental result and the less will be the error.

$$F = \sqrt{\frac{1}{T}\int_0^T \frac{\left[V_{\exp}(t) - V(t)\right]^2 dt}{V_{\exp}(t)^2}} \bullet 100\% \tag{4.8}$$

The optimisation function is a function of numerical *V(t)* and experimental $V_{exp}(t)$ volumes. The experimental volume data at different time steps is experimentally obtained; therefore, the objective function depends entirely on *V(t)*. Further, the objective function through *V(t)* depends on the $C_{avg,}$ (Equation (4.7)) and the swelling factor (*SF*) (Equation (4.8)). C_{avg} is a function of the diffusion coefficient; therefore, *F = f (D, SF)*. Therefore, *D* and *SF* may be used as the adjustable parameter to minimise the objective function, *F*. Once the minimum objective function is found, the corresponding values of *D* and *SF* are the measured CO_2 diffusion coefficient and the swelling factor, respectively.

4.2.2 Assumptions and justifications

In developing the present mathematical model, the following assumptions were made.

i. The diffusion is the sole means of mass transport across the CO_2-hydrocarbon interface. This is achieved by eliminating density driven convection (small volume of pendant drop is used) and thermal convention (temperature is kept constant) [41]. The convection mass transfer inside the pendant drop is eliminated by using a vibration free table and setup [44]. The thermal induced natural convection in the fluid system is minimised by carrying out experiments at a constant temperature [44].
ii. No chemical reactions transpire during the experiment. Therefore, the mechanism transpiring is purely physical in nature.
iii. For the CW-hydrocarbon system, only CO_2 diffuses into hydrocarbon, and the diffusion of water into hydrocarbon and its influence on the swelling has been neglected. This assumption is justified as the solubility of water in hydrocarbon is significantly lower than CO_2; therefore, the mass transfer of water into hydrocarbon is negligible compared to CO_2.

4.2.3 Numerical scheme

The following modifications have been made in the present numerical model, compared to the original model [44], to make the simulation process easier and quicker.

i. An equivalent spherical bubble is considered in the numerical modelling, that is having the same volume and surface area as that of the drop phase that was formed originally in the VC.
ii. A simple finite difference method (FDM) is used to discretise the partial differential equations, instead of the finite element method (FEM) [41, 46].

iii. A novel adaptable interface (boundary) method has been developed, which is a major improvement compared to the previous assumption of no change in the shape and interface of the pendant drop [41, 44]. This part will be discussed in Section 4.2.4.

Figure 4.1A shows the pendant drop in the VC, along with the axis in consideration. Figure 4.1B shows the equivalent spherical drop phase, surrounded by the environmental phase used for the numerical analysis. A well-thought process is involved in modifying the experimental pendant drop to an equivalent spherical drop. First, from the DSA software, the initial volume and surface area of the pendant drop are obtained. From these data, the experimental radius is obtained. The experimental radius is then used to create the spherical drop for the numerical analysis. The surface area which governs the rate of mass transfer is used as the comparison parameter: experimental pendant drop and numerical spherical drop. The results of the comparison showed an error of 3 – 6% for the spherical drop, compared to the pendant drop, depending on the pressure. Therefore, it is justified to use a spherical drop for the numerical analysis, instead of the complex pendant shape. Spherical drop idealisation lessens the effort and complexity, while, at the same time minimising the error in the estimation of the diffusion coefficient.

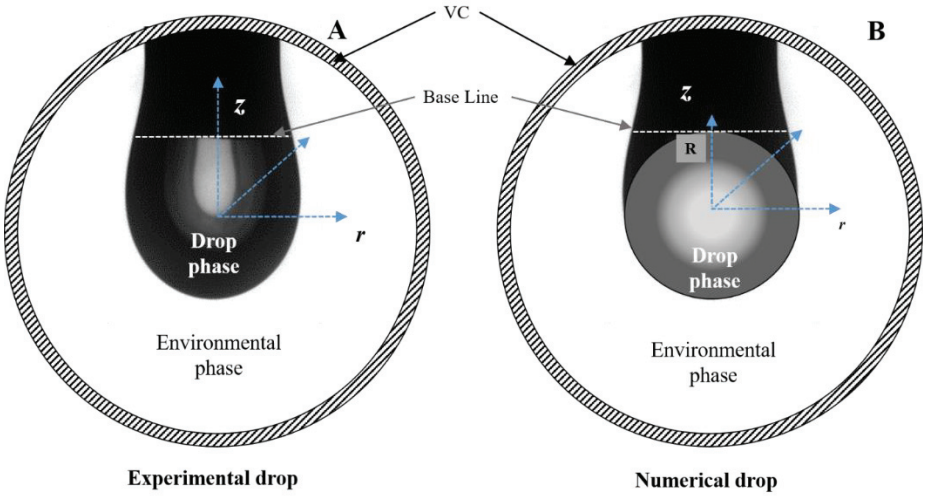

Figure 4.1: (A) Pendant drop phase surrounded by environmental fluid in the VC. (B) Equivalent spherical drop surrounded by environmental fluid for numerical analysis.

The partial differential equation (Equation (4.1)), along with boundary conditions presented in Section 4.2.1 (Mathematical model), cannot be solved straightaway, and must be transformed into a form that is suitable for numerical evaluation. Discretisation is the process which is carried out to transform the continuous equations into discrete counterparts. Discretisation is generally carried out as the first step in making partial differential equations (PDE) suitable for numerical solving. In general, finite difference (FDM), finite element (FEM) and finite volume (FVM) are the discretising methods that are used to transform the PDE. In the present thesis, the finite differnce method is preferred over the finite element method, which was used in the original model [41]. Compared to FVM, and FEM, the FDM is easy to implement, and it is perfectly suitable for systems which have no or minimal flow, as in the case of the present system. The governing Equation (4.1) is solved for the given set of initial and boundary conditions (Equations (4.2) – (4.4)) to investigate the diffusion of CO_2 in the hydrocarbon drop. A semi-implicit finite difference formulation is adopted to discretise the governing PDE. The

Crank-Nicolson discretisation scheme is used for the second-order terms representing diffusion in the drop phase (second and third terms on the right-hand side of Equation (4.1)). A two-point backward differencing is used to discretise the temporal term (first term on the left-hand side of Equation (4.1)). The semi-implicit and Crank Nicolson FDM schemes are unconditionally stable. Table 4.2 shows the comparisons of the diffusion coefficient obtained by the original model ([41]) and that obtained by the present thesis with the modifications, for the same experimental data (CO_2-water) given in Yang and Gu [41]. It may be observed that the diffusion coefficient obtained by the present simpler spherical drop model has a good match (6% error) with that estimated by Yang and Gu [41], therefore establishing the credibility of the present model.

Table 4.2: Verification of the present numerical model [45].

	Diffusion Coefficient (m^2/s), *D*	**Objective Function % *F***	**Swelling Factor *SF***
Yang et al. (2005)	$0.29 * 10^{-9}$	0.073	1.084
Present model	$0.275 * 10^{-9}$	0.066	1.093

4.2.4 Adaptable interface (boundary) model

The diffusion coefficient model proposed by Yang and Gu [41] and Yang, et al. [44] neglects the effects of CO_2 mass transfer on the pendant hydrocarbon drop shape and volume. The numerical model assumes that the pendant drop volume does not change with time or the diffusion of CO_2 [157]. This assumption of constant volume may turn out be a major drawback, as the experimental results indicate a significant increase in the volume of the hydrocarbon pendant drop, especially for CO_2-based systems. For example, Bagalkot and Hamouda [51] showed that, for a CW-decane system, there was a maximum of 100% increase in the

volume of the pendant drop, indicating that the position of the interface is not fixed, as assumed by the previous model.

Figure 4.2 shows the change in the position of the interface for initial (4.2A), intermediate (4.2B), and equilibrium time (4.2C) for a CW-decane system. At the start of the experiment ($t=0$), P_o is the position of the interface along the z-axis. As CO_2 diffuses into the hydrocarbon pendant drop, the volume of the pendant drop increases, and the position of the interface has now shifted to P_{it} from P_o (Figure 4.2B). At the equilibrium, when the hydrocarbon is saturated with CO_2, the position of the interface along the z-axis is now at P_{eq}. It may be clearly observed from Figure 4.2C that there is a significant shift in the position of the interface in both z and r axis (radius). However, the previous model on ADSA [41] [44] considers a static interface, meaning that, no matter the magnitude of volume increase, the model always considers P_o as the position of the interface and not P_{eq}. Further, from the mathematical point of view, from Equations (4.5), (4.6) and (4.7), the diffusion coefficient is a function of experimental value (V_{exp}) and numerical value (C_{avg}). From Equation (4.5), it may be said that C_{avg} is a function of the radius or the volume of the drop. If the interface of the drop (boundary) is considered static, as assumed by the conventional model [41], then the interface would not change its position (from P_o to P_{eq}). This could lead to a discrepancy between numerical and experimental input into the model, resulting in an error in the calculation of the diffusion coefficient.

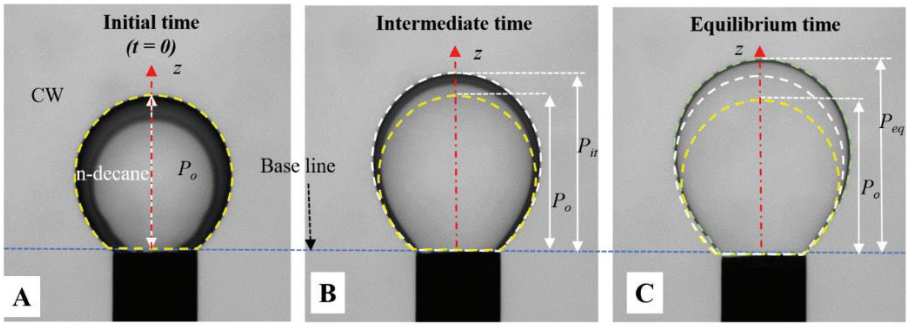

Figure 4.2: Movement of the interface at different time levels for CW-decane system.

In the present thesis, a simple method has been developed to incorporate the dynamic nature of the CW-hydrocarbon interface (boundary), and the following steps were undertaken to do so. Further details of the method may be found in Bagalkot and Hamouda [51].

i. At $t=0$, a fixed number of grids were assigned in the r- and z-directions, say N number of grids in the r and M grids in the z-direction.
ii. The volume of the drop at various time steps was determined from Equation (4.7).
iii. At every time step, the volume obtained at the present step was subtracted from that obtained from the previous time step ($V(t)$-$V(t-1)$).
iv. The $V(t)$- $V(t-1)$ was then transformed to $r(t)$-$r(t-1)$ (Δr); this, in turn, gave the radial shift by the interface.
v. The Δr was used to recalculate the number of grids in r (say n) and z (say m) directions. The additional grids in each direction were then added to the initial number of grids ($N+n$, $M+m$), to obtain the updated number of grids (N_{new}, M_{new})
vi. The updated grids (N_{new}, M_{new}) were used to solve the equations.
vii. This process was repeated for each time step (Δt) and each diffusion coefficient input.

For the same experimental data (25°C, CW-decane system), numerical calculations were made for the case when the interface was assumed static and the case when the interface was dynamic, as described above. The data of diffusion coefficient obtained for both the cases at various pressures are presented in Table 4.3 [51]. It may be noted that there is a distinct difference in the diffusion coefficient between the two cases, especially as the pressure is raised. Although the difference at low pressures (10 bar) is minimal (2%), it increases exponentially as the pressure increases (36% error at 60 bar). At 60 bar, the swelling of the n-decane is almost twice that of the initial volume. It is therefore clear that, even with moderate pressure (moderate swelling), the errors due to static boundary assumption are larger than 15%. Consequently, it is essential to include the effect of the dynamic interface when calculating the diffusion coefficient.

Table 4.3: Diffusion coefficient data for fixed and moving interface methods [51].

Pressure (bar)	Volume ratio ($V_{final}/V_{initial}$)	Diffusion coefficient (10^{-9} m^2/min)		% change in the D_{CO2} from static to dynamic interface
		Static interface method	Dynamic interface method	
10	1.031	5.3251	5.4234	2.015
30	1.155	2.2116	2.5392	14.812
60	2.134	0.5934	0.8073	36.045

4.3 Procedure for estimating the diffusion coefficient

After establishing the mathematical model and obtaining the experimental data, the following steps were carried out in the numerical

model to derive the diffusion coefficient. Detailed steps for the procedure may be obtained from Bagalkot and Hamouda [155].

i. The partial differential equation (Equation (4.1)), representing the spreading of CO_2 from the environmental phase into the drop phase, was discretised using the presented numerical method.
ii. The initial value ($t=0$) of the volume of the drop phase (V_o) and subsequent volumes at different time steps ($V_{exp}\ (t)$) were inputted to the numerical model.
iii. A predefined range of diffusion coefficients was set, $D_i\ (n > i > m)$. The predefined range was divided into equally spaced subintervals.
iv. For every value of D_i, the numerical model was solved, and $C_{avg}\ (t)$ was calculated from Equation (4.5). Further, the $C_{avg}\ (t)$ was used to estimate the swelling factor (SF) and numerical volume ($V(t)$), using Equations (4.6) and (4.7), respectively.
v. A best fit between the values of the numerically ($V(t)$) and experimentally ($V_{exp}\ (t)$) calculated volumes of the drop were compared, using Equation (4.8).
vi. Using the new value of the numerical volume ($V(t)$), the position of the boundary or the interface was updated using the procedure described in Section 4.1.4.
vii. For each input value of D_i, a corresponding value of F_i and SF_i was calculated. Then, F_i was plotted against D_i to obtain F_{min}. A typical F vs D curve is shown in Figure 4.3.
viii. The diffusion coefficient, for which F_{min} was obtained, is the optimum diffusion coefficient of the CO_2 in drop phase.
ix. The smaller the subintervals of D_i the higher will be the accuracy.

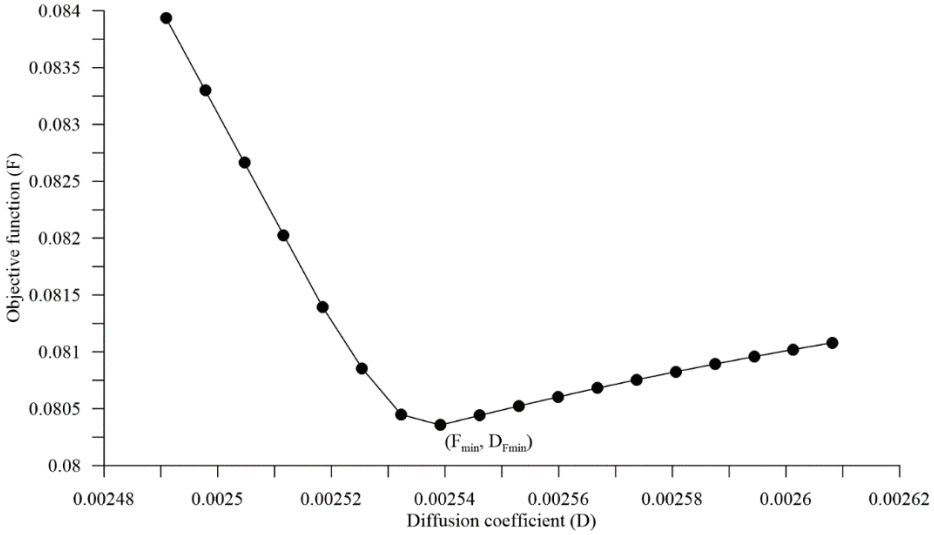

Figure 4.3: Typical F_i vs D_i curve with D at F_{min}.

4.4 Advantages and disadvantages of the model

Advantages:

i. The model can be used to estimate the effective diffusion coefficient of any gases in pure liquids.
ii. As the model works in conjunction with experimental data, the values obtained are more reliable.
iii. The model does not demand complicated and hard-to-estimate experimental values, such as fugacity and chemical potential, as in some EOS models.
iv. The model uses a spherical drop approach, which simplifies the model, at the same time maintaining the accuracy of the values.
v. The model has the ability to shift the interface (gas/liquid or liquid/liquid); hence, it is flexible enough to be applied in systems which experience higher changes in volume.

Disadvantages:

i. At present, the model can only be used to estimate the diffusion coefficient of gases in pure liquids and not complex multi-component liquids like crude oil.
ii. The model can only determine the diffusion coefficient due to concentration-driven mass transfer. It cannot be applied to mass transfer due to density-driven or thermal-driven processes.
iii. The model is not stand alone and may be used only if the volume vs time profile has been obtained; it is therefore limited to pendant drop or similar setups.

4.5 Uncertainty analysis

The estimation of the effective diffusion coefficient of CO_2 into the drop phase from the environmental phase depends on the volume profile of the drop phase, as described in Section 4.3. In the present thesis, multiple experiments were carried out at each experimental pressure and temperature to assess the repeatability and reliability of the experimental results. Figure 4.4 shows the relative volume as a function of time for three pressures (30, 60, and 100 bar) at 25ºC for two separate experiments (denoted by D1 and D2) at each condition. For each of the chosen pressures in Figure 4.4, 30 bar represents the behaviour in the region where CO_2 is in the gaseous phase, 60 bar represents a region near to the critical pressures of CO_2 (64 bar), and 100 bar represents the behaviour in the region where CO_2 is in the liquid phase. Therefore, it would be easy to assess the uncertainties in these regions. It may be observed from Figure 4.4 that, at 30 and 100 bar, there is a higher percentage of repeatability compared to that at 60 bar, which is near to critical pressure.

While reporting the diffusion coefficient, the average of the values obtained from different repeat experiments is taken. Table 4.4 shows the diffusion coefficient obtained for D1 and D2 at 30, 60, and 100 bar. It

may be observed from Table 4.4 that the error is not significant among different experiments, although there is a minimal error at 30 bar (1.65%) and 100 bar (-1.5%), while the error at 60 bar is comparatively more (8.7%). Therefore, it may be said that, for the estimation of the diffusion coefficient, the uncertainties are low; however, at pressures near to phase change pressure, there may be a higher uncertainty, compared to at other pressures (although low). This may be due to higher entropy at this pressure, owing to its closeness to phase-change pressure.

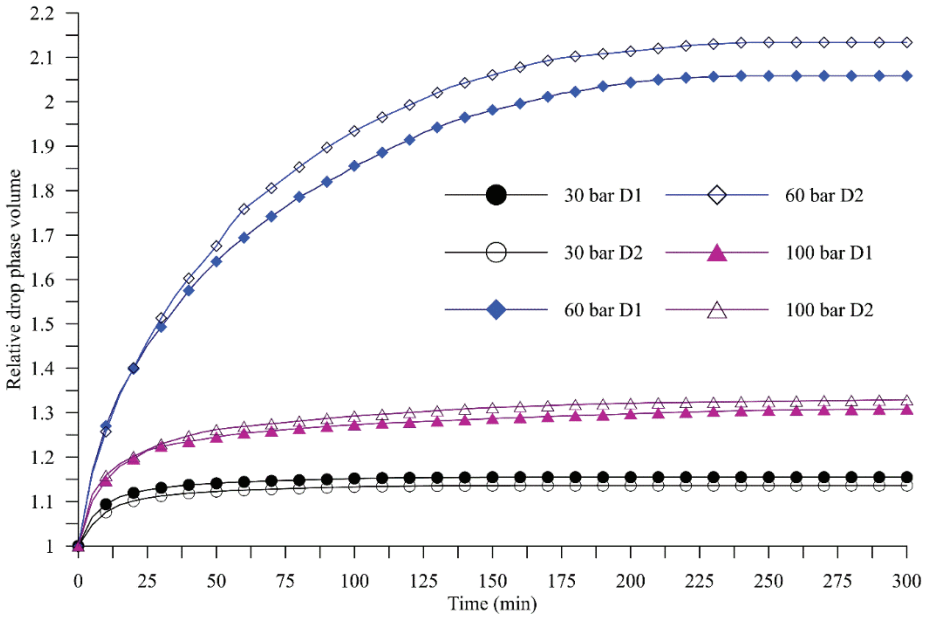

Figure 4.4: Dynamic relative volume of the n-decane drop phase at 30 bar, 60 bar, and 100 bar (25°C).

Table 4.4: Data depicting the validation of the current model for diffusion coefficient.

Pressure (bar)	**Diffusion coefficient (10^{-9} m^2/min)**		**Percentage error in diffusion coefficient between D1 and D2**	**Average diffusion coefficient (10^{-9} m^2/min)**
	D1	D2		
30	1.905	1.936	1.653	1.92
60	0.582	0.535	8.785	0.56
100	1.681	1.708	-1.582	1.69

5 Results and Discussions

This chapter includes the discussion of the main results obtained from various experimental and numerical analysis carried out in this work. The results are split into sections, based on the interfacial tension, diffusion coefficient, and drop phase property change for the following systems:

i. CO_2-hydrocarbon (n-decane, n-heptane and n-hexane)
ii. CW-hydrocarbon (n-decane and n-hexane)
iii. CO_2+water-hydrocarbon (n-decane)
iv. Nanofluid+CW-hydrocarbon (CNF-n-decane)
v. Salts+CW-hydrocarbon (CB-n-decane)

The majority of the results from the present work have been published, and the published articles are archived at the end of the thesis. Therefore, in this chapter, only the major results are discussed.

5.1 Interfacial tension

The interfacial tension was obtained by using the method described in Sections 3.4 and 3.5.

5.1.1 CO_2-hydrocarbon system

Figure 5.1 shows the CO_2-n-decane and CO_2-n-heptane IFT at 25^{o}C for a pressure range of 25-55 bar. It may be observed that for both fluid system the IFT decreases with the pressure, approximately 70% reduction in IFT is observed for CO_2-n-decane from 30-55 bar. The reduction in the IFT may be attributed to an increase in the CO_2 solubility in hydrocarbon with the pressure [46, 105]. Further the IFT is higher for CO_2-n-decane fluid system compared to the CO_2-n-hepatane system, indicating a greater resistance to the CO_2 mass transfer across the interface for n-decane compared to n-heptane. The molar mass of the

molecules of n-heptane are smaller compared to n-decane. Therefore, the intermolecular forces governed by London forces operating among n-heptane molecules will be lower, compared to those of n-decane, hence, a lower IFT.

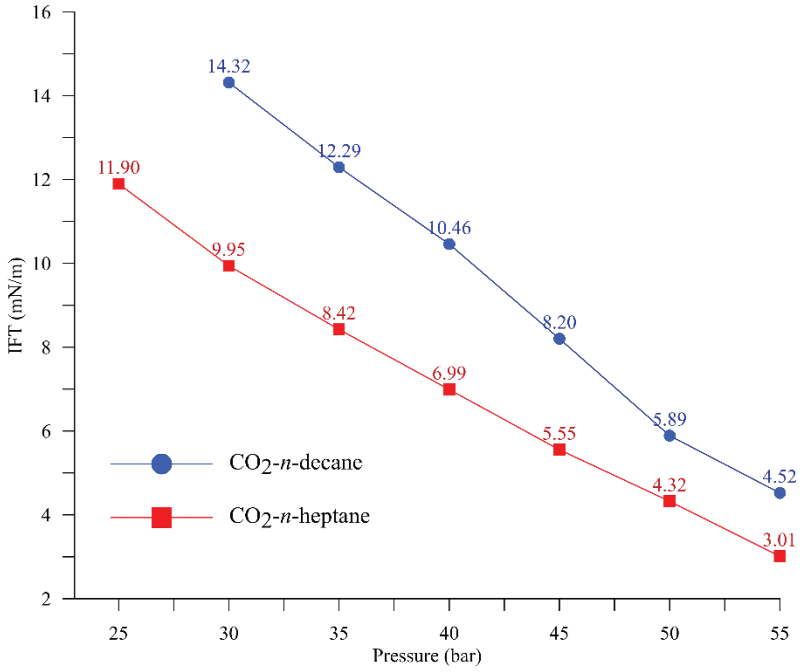

Figure 5.1: IFT of CO_2-n-decane and CO_2-n-heptane at 25°C for a pressure range of 25-55 bar.

Figure 5.2 shows the IFT of CO_2-n-decane at 25°C, 35°C, and 45°C for pressures 30-60 bar. It may be observed that at low pressures (below 35 bar) the IFT decreases as the temperature increases (IFT = f (1/T)). However, as the pressure is raised beyond 35 bar, the IFT increases with temperature (IFT = f (T)). Indicating a change from negative (reduction in IFT) to positive (increase in IFT) slope with temperature as the pressure increases from 30 bar to 60 bar. Similar observations have also been made by Zolghadr, et al. [158], and Yang and Gu [41]. They credited the reduction in the CO_2 solubility with increases in temperature for observations in Figure 5.2. However, in addition to CO_2 solubility the

density difference between the drop phase (hydrocarbon+CO_2) and environmental (CO_2) phase may also contribute observed (Figure 5.2) variation of IFT with temperature. Figure 5.3 shows the density difference between the drop and environmental phases at 25°C, 35°C, and 45°C for pressures 30 bar to 60 bar. It may be observed that that the density difference and temperature in Figure 5.3 follows a similar trend of IFT with temperature in Figure 5.2. Therefore, both CO_2 solubility and density difference contribute to the observed behaviour of IFT with temperature (Figure 5.2).

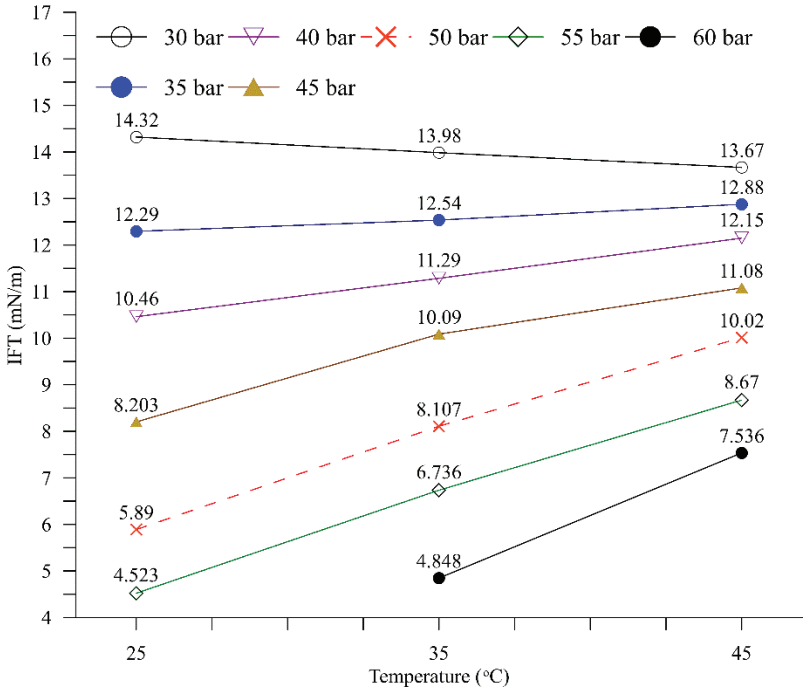

Figure 5.2: IFT of CO_2-n-decane at 25°C, 35°C, and 45°C for pressures 30-60 bar.

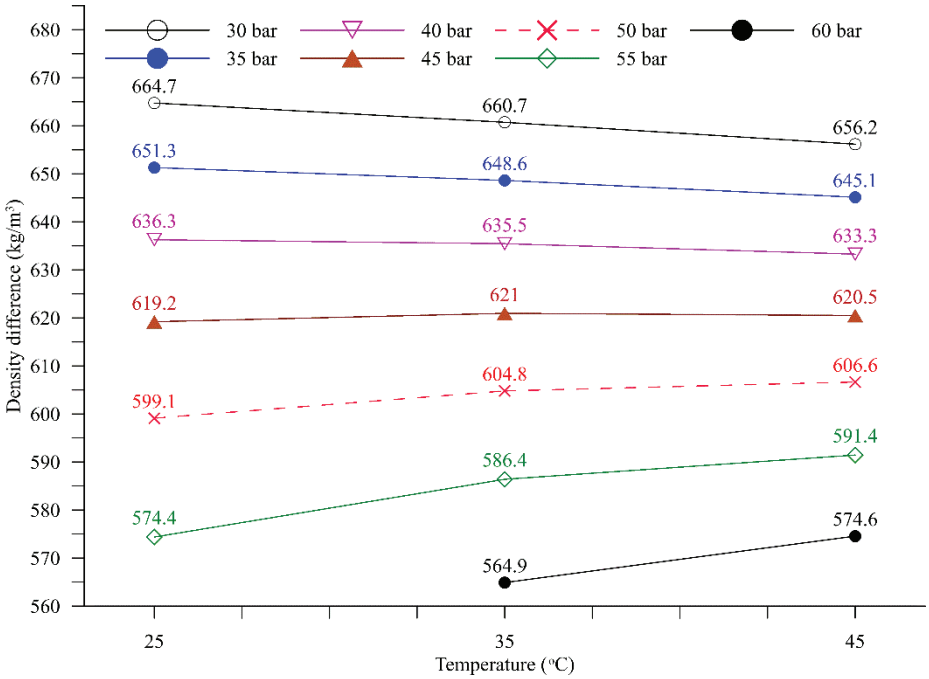

Figure 5.3: Density difference (kg/m^3) between the drop and environmental phases at 25°C, 35°C, and 45°C for pressures 30 bar to 60 bar.

Figure 5.4 shows the dynamic variation of IFT for CO_2-n-decane system for pressures 30-50 bar and at 25°C. It may be observed that for all the experimental pressures the IFT decreases as time progresses until it reaches a stable value (equilibrium IFT). The rate of reduction of IFT with time dependents on the pressure. At lower pressures (30 bar), the IFT reduces gradually and takes longer time to reach equilibrium IFT (50 sec) and curve is approximately linear. As pressure increases the time take to reach equilibrium gets shorter and IFT vs time profile changes from linear at 30 bar to elliptic at 50 bar. This observation may be again linked to increment in CO_2 solubility with pressure, indicating that at high pressure due to large CO_2 gradient there may be a greater CO_2 mass transfer into n-decane. Consequently, CO_2 saturates rapidly in the vicinity of the CO_2-n-decane interface at high pressures compared to low, leading to the observed dynamic IFT (Figure 5.4).

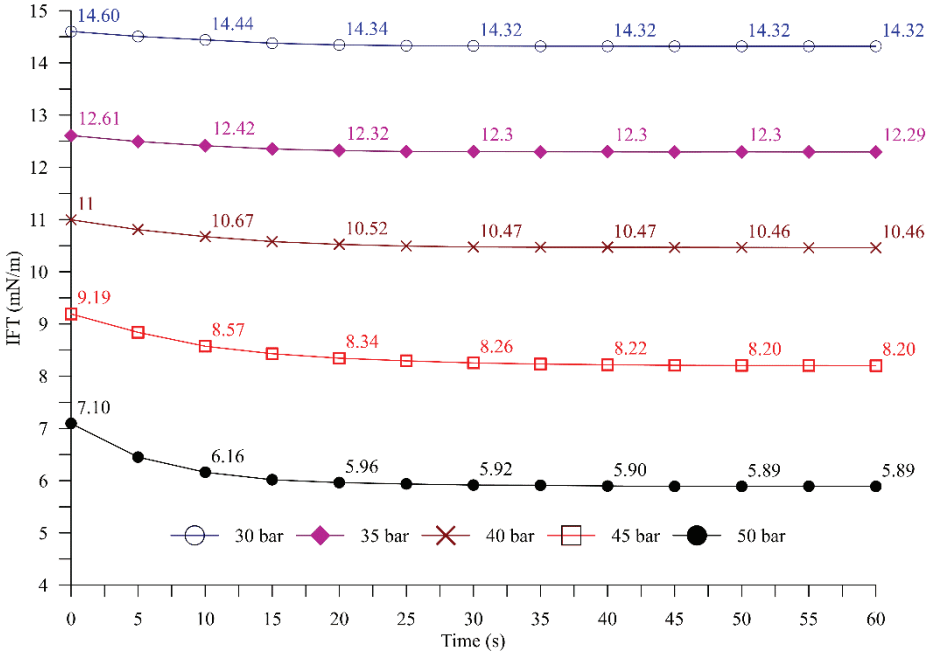

Figure 5.4: Dynamic variation of IFT for CO_2-n-decane system for pressures 30-50 bar at 25°C.

5.1.2 Carbonated water-hydrocarbon system

Figure 5.5 shows the IFT for CW-n-decane and CW-n-hexane system for pressures 10-100 bar at 25°C. Unlike CO_2-hydrocarbon system (Figure 5.1). IFT first increases almost exponentially up to the phase-change pressure of CO_2 (64 bar at 25°C, from gas to liquid). Above phase-change pressure, the IFT drops significantly (70 bar) and then continues to decrease gradually. The observations may be attributed to the density variations of both the environmental and the drop phases. Figure 5.5 shows that the IFT and density difference have a similar profile; up to 70 bar, the density difference increases and so does the IFT; above 70 bar, the density difference decreases with pressure and so does the IFT. The CO_2 solubility in both water and n-decane increases with the increase in pressure; therefore, there is a higher mass of CO_2 present in both water and n-decane.

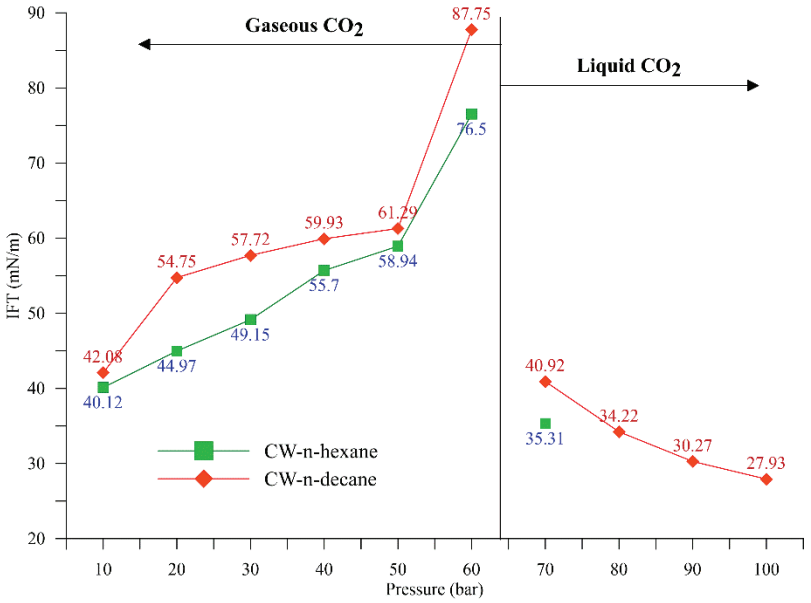

Figure 5.5: IFT for CW-n-decane and CW-n-hexane system for pressures 10-100 bar at 25°C.

The dissolution of CO_2 into water increases the density of water (CW) [159], whereas the dissolution of CO_2 in n-decane decreases the density. This would result in an increased density difference. Therefore, it may be observed from Figure 5.6 that the density difference increases with pressure, up to 70 bar. However, above 70 bar, there is a significant drop in the density difference, and continues to decrease with pressure. At 45°C above 64 bar, the CO_2 is supercritical in phase; it has a significantly higher density than that of gaseous CO_2, therefore, if a denser CO_2 mixes with n-decane, the resulting binary mixture will have a higher density than n-decane. Therefore, reducing the density difference, and hence, the IFT (Figure 5.5). A similar result for CW-crude oil was observed by Honarvar, et al. [22] for a pressure range of 70-100bar (supercritical CO_2).

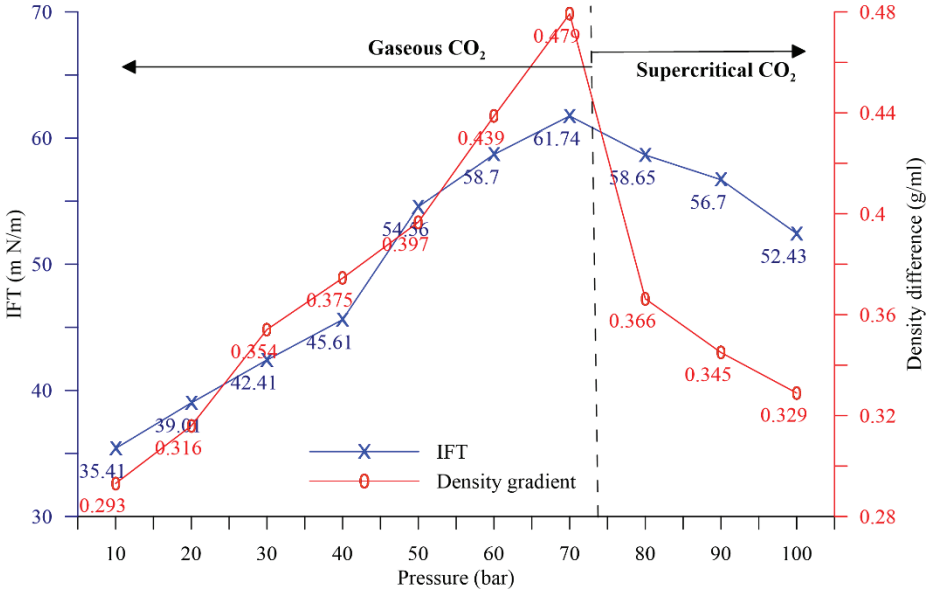

Figure 5.6: IFT and density difference between the drop and environmental phases at 45°C for pressures 10-100 bar.

Figure 5.7 shows the IFT of CW-n-decane at 25°C and 45°C for the pressure range of 10-100 bar. It is observed that the increase in temperature would bring about a reduction in the IFT. When the temperature of a fluid system is increased, the entropy and the kinetic energy of the molecules increase, thus increasing the total energy at the interface [22]. Higher entropy would reduce the Gibbs free energy of the system [22], leading to a reduction in IFT [22]. However, above the phase-change pressure (64 bar at 25°C and 74 bar at 45°C), it may be observed that the IFT at 45°C is greater than at 25°C, this reverse in IFT may be related to enthalpy energy and increase in the density of CO_2. The enthalpy energy for denser fluids is lower than that for the less dense fluids. Above phase-change pressure at 45°C, the CO_2 is supercritical, which is less dense than liquid CO_2 at 25°C; as a result, the energy for denser fluids is lower than that for the less dense fluids. Due to this the Gibbs free energy will be lower for the drop phase consisting of liquid CO_2+decane than for supercritical CO_2+decane. Hence, the IFT

associated with liquid CO_2 (25ºC) is lower than that associated with supercritical CO_2 (45ºC).

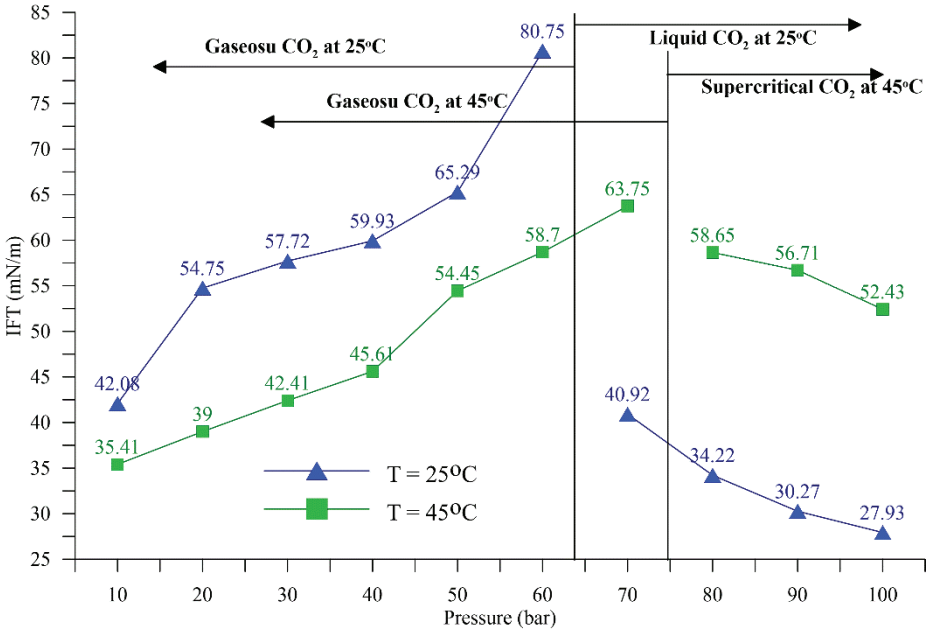

Figure 5.7: IFT of CW-n-decane at 25ºC and 45ºC for the pressure range of 10-100 bar.

Figure 5.8 shows the dynamic IFT (time function) for CW-n-decane system at 25ºC, for 10-100 bar. Unlike CO_2-hydrocarbon system (Figure 5.4), for CW-hydrocarbon the IFT increases with time for pressures 10-60 bar, reaching a value greater than the initial value. However, for a pressure range of 70-100bar, the IFT decreases with time. The observed dynamic IFT variations may again be connected to change in density difference between the drop and environmental phases. As discussed earlier (Figure 5.6) the density difference between the drop and environmental phases will be more when the CO_2 is in gaseous phase [160], leading to an increase in IFT. [13]. At 25ºC for pressure above 64 bar the CO_2 is in higher density (liquid phase), and the density difference between drop and environmental phase is smaller, leading to an increase

in IFT. Therefore, the IFT decrease with time for pressures above 64 bar at 25ºC for CW-hydrocarbon system, while it increase with time for pressures below 64 bar.

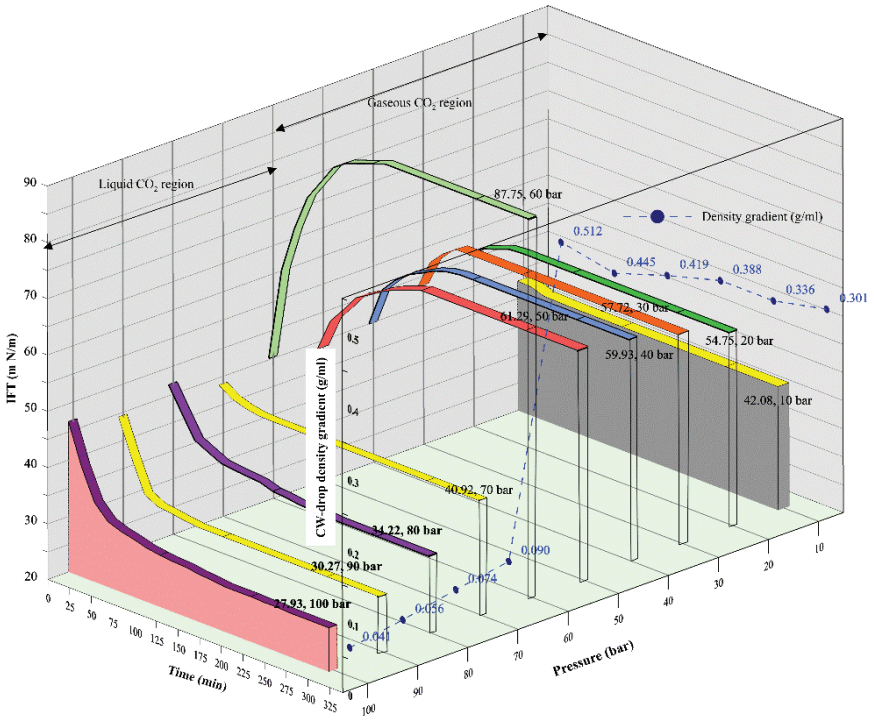

Figure 5.8: Dynamic IFT (time function) for CW-n-decane system at 25ºC, for 10-100 bar.

5.1.3 CO_2+water-hydrocarbon system

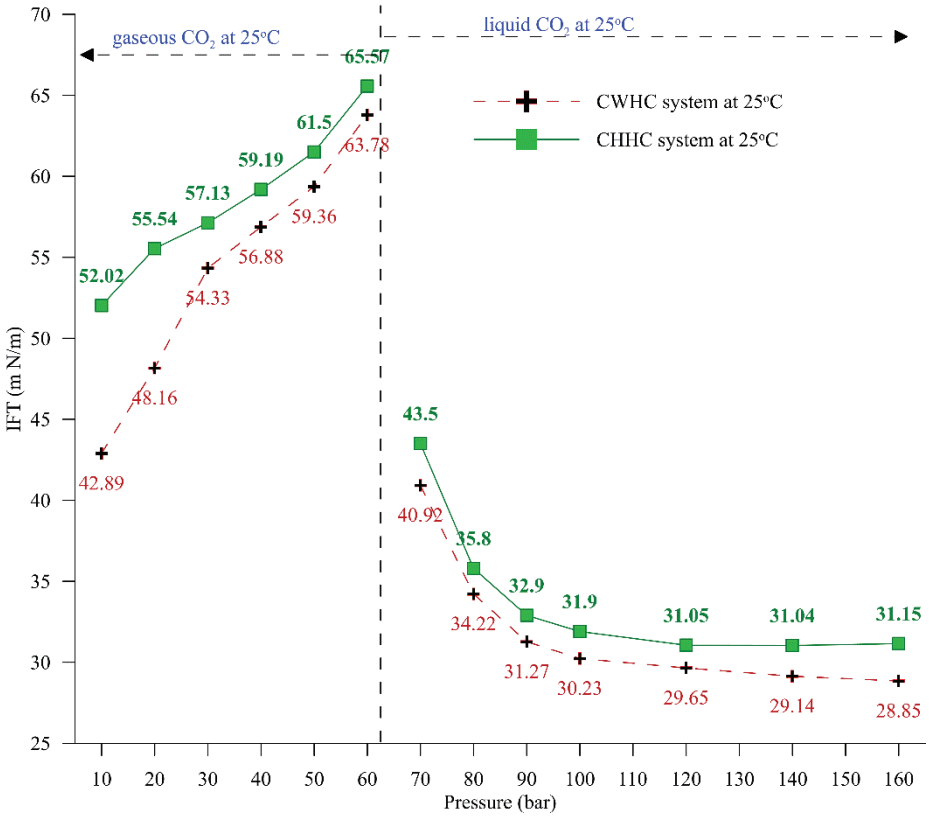

Figure 5.9: IFT values for CO_2+H_2O-n-decane (CHHC) and CW-n-decane (CWHC) at 25°C, for a pressure range of 10-160 bar.

The arrangement of CO_2+H_2O-n-decane system has been explained in Section 3.7. Figure 5.9 shows the IFT values for CO_2+H_2O-n-decane (CHHC) at 25ºC, for a pressure range of 10-160 bar. Figure 5.9 also include the IFT values of CW-hydrocarbon system (CWHC). It may be observed that the variation of IFT with pressure for both CO_2+H_2O-n-decane system is similar to that discussed for CW-hydrocarbon (Figure 5.5). For all the experimental pressures compared to CO_2+H_2O-n-decane system the IFT is marginally lower for the CW-hydrocarbon system. There is approximately 17% at 10 bar to 3% at 60 bar lower IFT for low

pressures (pressures at which CO_2 is in the gas phase), and average 6% reduction in IFT at high pressure (pressures where CO_2 is liquid) for CW-hydrocarbon system compared to CHHC system. The marginal decrease may be explained by studying the CO_2 concentration difference in Figure 5.10. It may be observed in Figure 5.10 that for CW-hydrocarbon the concentration difference of CO_2 reaches a constant value substantially earlier (between 120 - 250 min) than the CO_2+H_2O-n-decane system (above 300 min). Therefore, there may be a slower but a more substantial CO_2 mass transfer into drop phase for CO_2+H_2O-n-decane compared to CW-hydrocarbon system, increasing the density difference across of interface resulting in a marginally higher IFT for CO_2+H_2O-n-decane system.

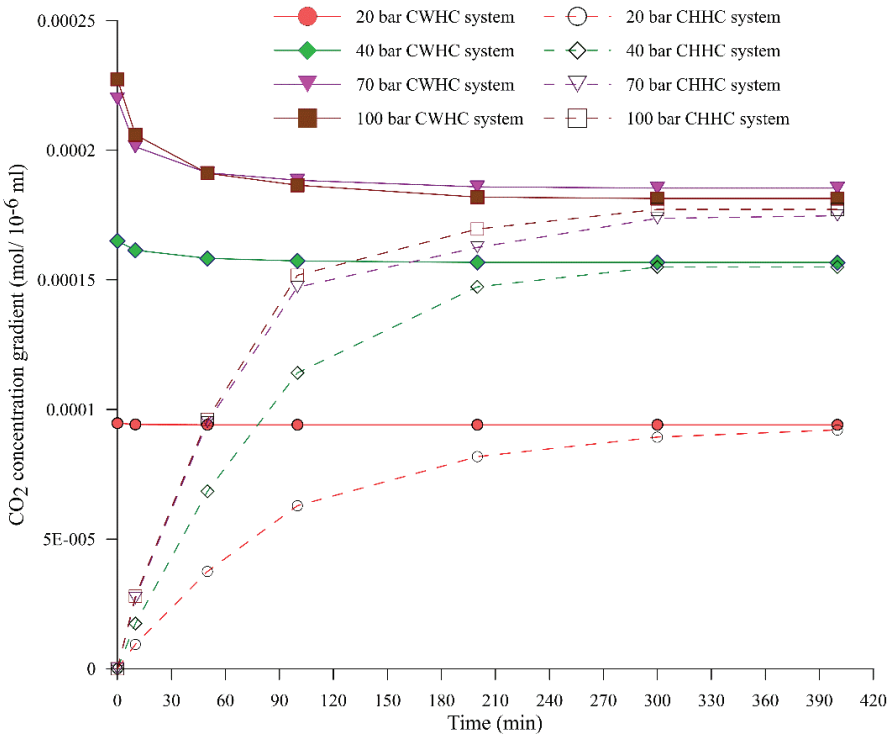

Figure 5.10: Concentration difference of CO_2 between the drop phase and the environmental phase for CW-n-decane and CO_2+H_2O-n-decane *system as a function of time at 25°C for 20-100 bar.*

The dynamic IFT for CO_2+H_2O-n-decane is similar to that of CW-hydrocarbon system, with difference only in the magnitude.

5.1.4 Salt+CW-hydrocarbon system

Figure 5.11 displays the CB-n-decane IFT at equilibrium conditions for 50, 70, 80, and 100 bar at 45ºC, for different brine compositions (C_{SSW}, $C_{SSW\text{-}MgCl2}$, $C_{SSW\text{-}Na2SO4}$, CW_{+MgCl2}, and $CW_{+Na2SO4}$) and CW. The details of the brine composition as shown in Table 3.1. The IFT variations with pressure for CB-n-decane are similar to that of the CW-decane system, as shown in Figure 5.5. For most pressures, the C_{SSW} and $CW_{+\,Na2SO4}$ lead to a marginal change in IFT compared to CW (min of -0.18% and max -3.5% for C_{SSW}, and min of 2.5% and max 6.6% for $CW_{+\,Na2SO4}$), while brine $C_{SSW\text{-}Na2SO4}$ and CW_{+MgCl2} lead to a significant decrease in IFT. Therefore, adding $MgCl_2$ in CW may lead to a reduction in CW-decane IFT, while Na_2SO_4 in CW may lead to an increase in IFT. The observed alteration in the IFT by Na_2SO_4 and $MgCl_2$ may be related to the degree of hydration of ions. Hydration degree is a functions of the charge and radius of the ion; the higher the charge and the smaller the radii, the higher will be the hydration energy [57]. Ions which have higher hydration energy are more attracted to the oil/water interface, leading to a reduction in the IFT [57, 161]. Among the salts used in the present work, Mg^{2+} ion has the smallest ionic radius (0.072 nm), while SO_4^{2-} (0.242 nm [162]) and CO_2 (232 nm) are larger. However, as a bivalent the Mg^{2-} ion has high hydration energy, therefore, have higher affinity towards the CW/oil interface [57, 161]. Therefore, Mg^{2+} form tight bound to the first hydration shell $[Mg(H_2O)_6]^{2+}$. Hence, have a high effective size leading to lesser adsorbed and early saturation at the interface [162]. Previous studies have shown that $MgCl_2$ [74, 118, 161], leads to lower IFT. On the other hand, the size (radius) of SO_4^{2-} (258 pm [163]) ions is significant compared to Mg^{2+}, and have lower hydration energy compared to Mg^{2+}. Therefore, SO_4^{2-} would be less effective in altering the CW-n-decane IFT. When Na_2SO_4 and $MgCl_2$ are combined

as in C_{SSW}, the IFT reduction is in-between that of $CW_{+Na2SO4}$ and CW_{+MgCl2}. Garrels and Thompson [164] explained that the formation of complexes of Mg^{2+} and Na^{+} with SO_4^{2-} due to the combination of Na_2SO_4 and $MgCl_2$ would decrease the free ions of Mg^{2+} and Na^{+}. A reduced concentration of Mg^{2+} may lead to lesser ions being adsorbed at the CB-n-decane interface and hence, a lower reduction in IFT as observed in Figure 5.11.

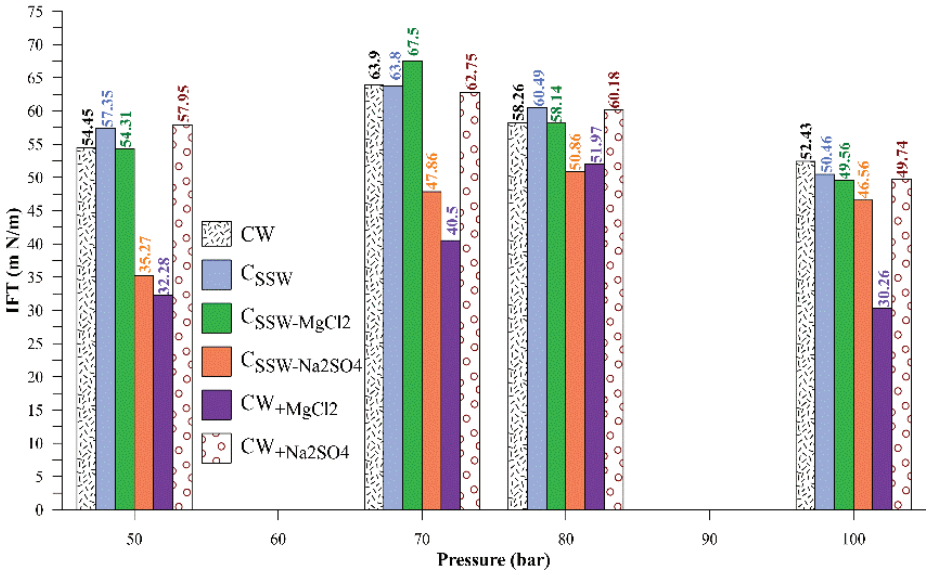

Figure 5.11: IFT values for various CB-n-decane system for pressures 50-100 bar at 45°C.

5.1.5 Nanofluid+CW-hydrocarbon system

Figure 5.12 shows the IFT of CW-n-decane system when nanofluids are added to the carbonated water at 25°C for pressures 10-90 bar. Three concentrations of nanofluid (0.05, 0.5 and 1.0 g/l) have been used. It may be observed that the IFT variation with pressure for CNF-n-decane system is similar to that of CW-hydrocarbon system, therefore same reasoning may be applied as presented in Figure 5.7. However, the nanofluid (CNF) in CW reduces the IFT, compared CW without

nanofluid. A maximum of 45% reduction is observed at 10 bar by 0.5 g/l, while a minimum of 4.5% is observed at 60 bar for 0.5 g/l. There is significant reduction at low pressures and the influence of nanofluid on IFT reduction decreases as pressure increase to 60 bar.

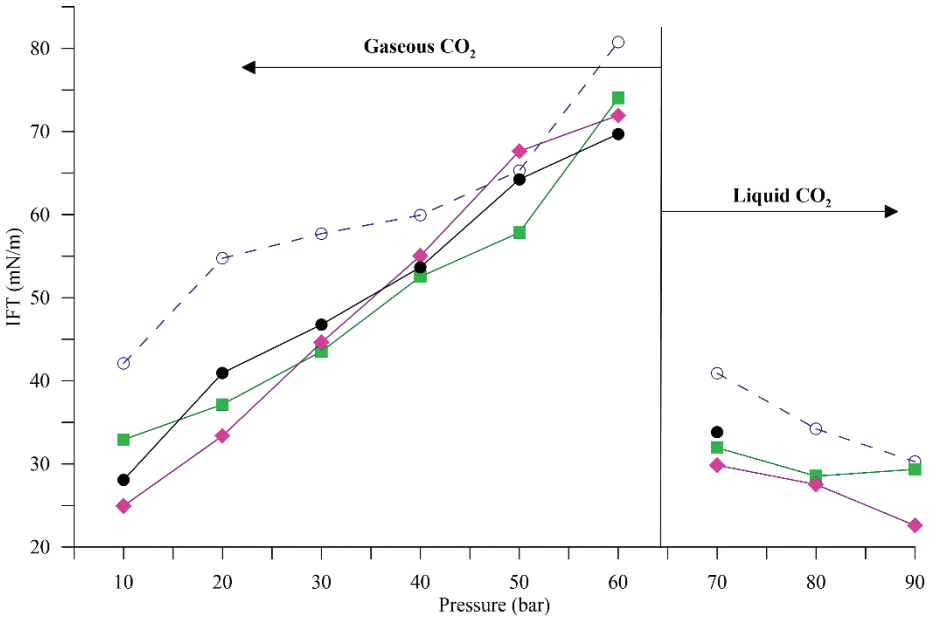

Figure 5.12: IFT of CW-n-decane system when nanofluids are added to the carbonated water at 25°C for pressures 10-90 bar.

5.2 Diffusion coefficient

The diffusion coefficient has been calculated from the model and method described in Sections 4.2 and 4.3.

5.2.1 CO_2-hydrocarbon system

Figure 5.13 shows the diffusion coefficient of CO_2 in n-decane at 25°C, 35°C, and 45°C for pressures 25-60 bar. It may be observed that at isothermal conditions the diffusion coefficient of CO_2 in n-decane increases with increase in pressure. The observed increase in diffusion

coefficient is due to two factors. First, the equilibrium concentration of CO_2 (CO_2 solubility) in hydrocarbon increase with pressure, this may lead to higher concentration gradient and hence, faster mass transport [44]. Second, the lower viscosity of the drop phase (CO_2+ hydrocarbon) at higher pressures may assists in increasing the rate of CO_2 mass transfer [45]. Figure 5.14 shows the viscosity of the drop phase at equilibrium for various pressure and temperatures. It may be observed that the viscosity of the drop phase reduces with pressure. Therefore, the combination of an increase in CO_2 solubility and reduction in drop phase viscosity contribute to the increase in the diffusion coefficient of CO_2 with pressure. Additionally, the reduction in IFT with pressure (Figure 5.1) will lead to increase in CO_2 diffusion coefficient with pressure. This is also observed for all the hydrocarbon samples used in the present work (n-decane, n-heptane, and n-hexane).

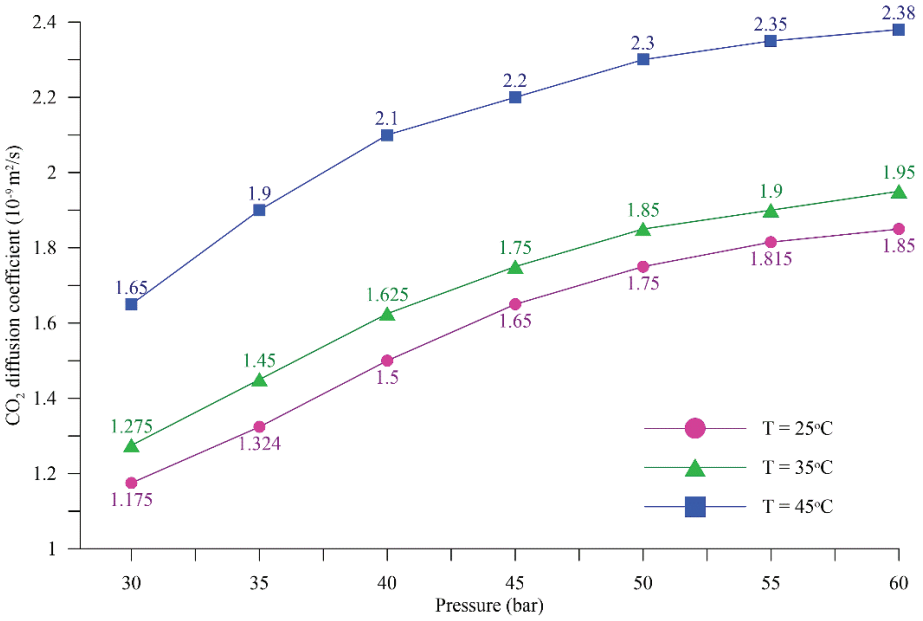

Figure 5.13: diffusion coefficient of CO_2 in n-decane at pressures 25-60 bar and temperatures 25°C, 35 °C, and 45 °C.

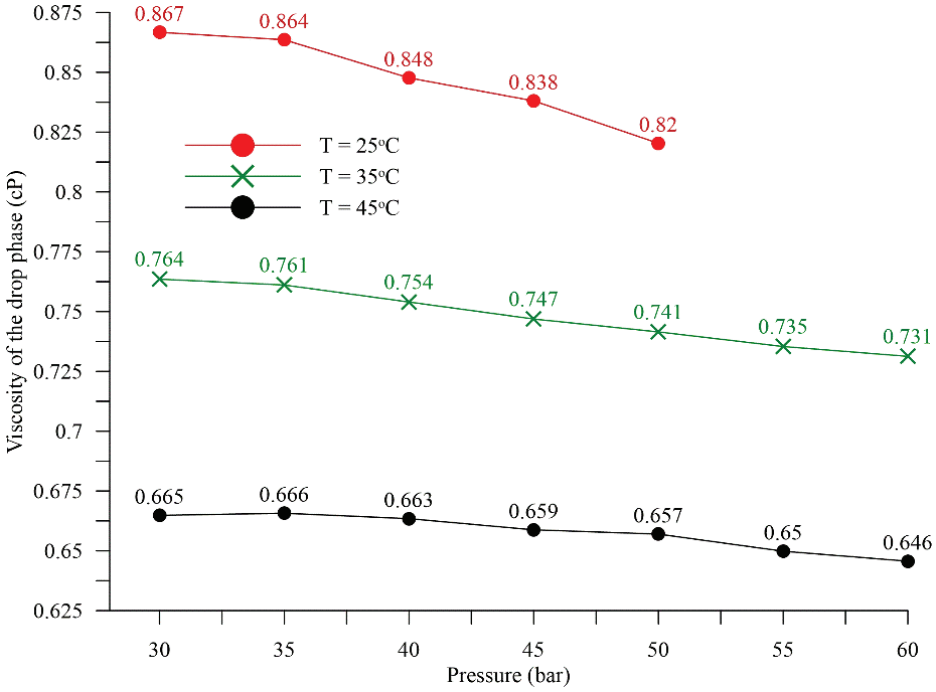

Figure 5.14: Viscosity of the drop phase at equilibrium for pressure 30-60 bar at 25°C, 35°C, and 45°C.

The equilibrium concentration of CO_2 (CO_2 solubility) in hydrocarbon decreases with temperature, therefore, the driving force for CO_2 mass transfer is lowered. In Figure 5.14 as temperate changes from 25°C to 45°C an increase in diffusion coefficient is observed with temperature, despite the decrease in CO_2 solubility. It may be observed from Figure 5.14 that there is a gradual reduction in the viscosity of the drop phase with temperature, this will assist in increasing the diffusion coefficient. Roughly 11 – 13 % reduction in viscosity of drop phase is observed when the temperature increases from 25°C to 35°C, while 20 – 23 % reduction is seen when the temperature is increased from 25°C – 45°C. Further, as the temperature is raised, the entropy energy of the system is increased. The dissolution of CO_2 in decane is exothermic in nature and, for such reactions, the enthalpy change is negative. Therefore, the change in Gibbs energy (ΔH-ΔTS) will be negative, resulting in a higher diffusion

coefficient at higher temperatures. Additionally, the IFT decreases as temperature increases, which enhances the CO_2 mass transfer.

Table 5.1 shows the diffusion coefficient of CO_2 in n-decane, n-heptane, and n-hexane at different equilibrium pressures (25 bar to 65 bar) at 25 ^oC and 45^oC. The diffusion coefficient of CO_2 is highest in n-hexane, followed by n-heptane, and lowest in n-decane. Therefore, the diffusion coefficient increases with the decrease in the molecular weight of the drop phase (n-decane>n-heptane>n-hexane). For example the viscosity of n-hexane is 22 % lower than n-heptane and approximately 63% lower than n-decane at 35^{o}C and 45 bar. The significant reduction in viscosity of lighter hydrocarbons (n-hexane) drives the diffusive mass transfer of CO_2 into it compared to heavier light hydrocarbon (n-decane). Figure 5.15 shows the increase in the volume of n-decane, n-heptane, and n-hexane drop phase as a function of time at 35^{o}C and 45 bar. Two important observations may be made. First the maximum increment in volume is highest for drop phase consisting of n-hexane, followed by n-heptane and minimum is that for n-decane. Second, the equilibrium volume is achieved at a faster rate for n-hexane (20 s) compared to n-heptane (25 s) and n-decane (35 s) as the hydrocarbon become lighter (n-decane to n-hexane). Similar observation have also been made by Wilke and Chang [165], they showed that diffusion coefficient of solute increases with a decrease in solvents molecular weight.

Table 5.1: Diffusion coefficient of CO_2 in n-decane, n-heptane, and n-hexane at different equilibrium pressures (25 bar to 65 bar) at 25°C and 45°C.

Pressure (bar)	Diffusion coefficient (10^{-9} m^2/s)					
	CO_2-n-decane		CO_2-n-heptane		CO_2-n-hexane	
	25°C	45°C	25°C	45°C	25°C	45°C
25	1.00	1.4	1.25	1.6	1.5	1.85
30	1.175	1.65	1.4	1.8	1.7	2.1
35	1.324	1.9	1.55	2	1.875	2.4
40	1.5	2.1	1.7	2.2	2.05	2.65
45	1.65	2.2	1.8	2.35	2.2	2.95
50	1.75	2.3	1.85	2.45	2.275	3.2
55	1.815	2.35		2.55	2.325	3.35
60	1.85	2.38		2.6		3.425
65				2.651		3.45

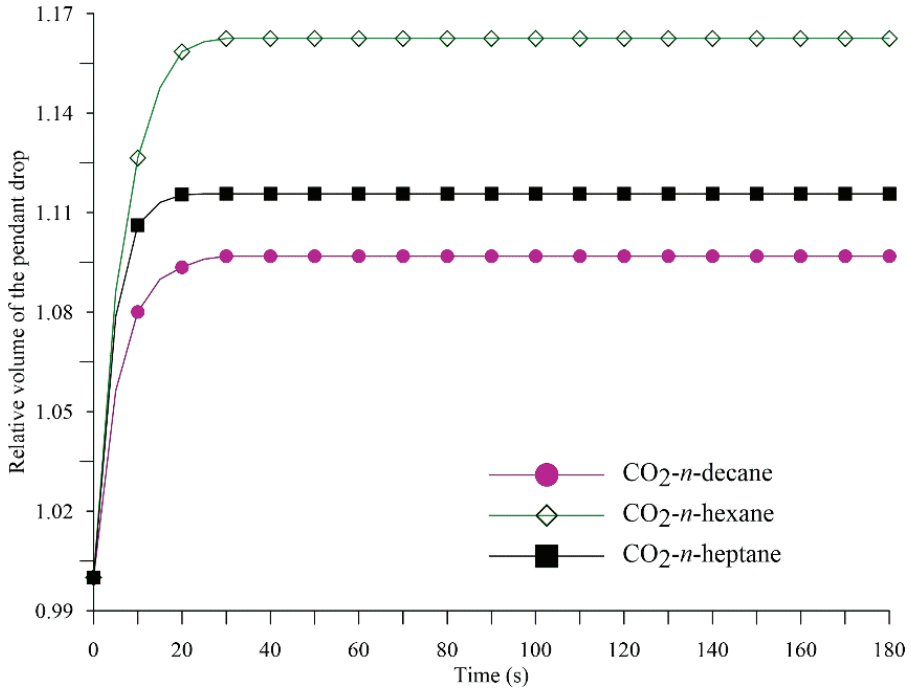

Figure 5.15: Increase in the volume of n-decane, n-heptane, and n-hexane drop phase as a function of time at 35°C and 45 bar.

5.2.2 Carbonated water-hydrocarbon system

Figure 5.16 shows the diffusion coefficient of CO_2 in n-decane from CW for a CW-n-decane system for pressures 10-100 bar at 25ºC and 45ºC. The observation made in Figure 5.16 for CW-decane systems is unique, the diffusion coefficient decreases as pressure increases up to CO_2 phase-change pressure, and increases with pressure above the phase-change pressure. The minimum CO_2 diffusion coefficient is observed at pressure near and below the phase change pressure of CO_2. Therefore, indicating that the phase of CO_2 influences the diffusion coefficient. The observations for the CW-decane system may explained from the IFT vs pressure profile (Figure 5.5). For pressures up to phase change pressure of CO_2 the IFT increases with pressure, indicating an increase in resistance to CO_2 mass transfer across the interface, and hence, the observed decrease in CO_2 diffusion coefficient. Above phase change pressure of CO_2 the IFT decreases with pressure, indicating a reduction in resistance to CO_2 mass transfer, therefore, the diffusion coefficient is seen to increase in this pressure range. Further, the maximum IFT is seen a pressure near to and below the phase change pressure, this coincides with minimum diffusion coefficient at that pressure.

Figure 5.16 also depicts the influence of temperature on the effective diffusion coefficient of CO_2 in n-decane from CW, at 25ºC, and 45ºC. The diffusion coefficient of CO_2 into the drop phase increases with the temperature (25ºC to 45ºC). As discussed in section 5.2.1 (Figure 5.14) the reduction in the drop phase viscosity, Gibbs free energy of the system, and the IFT with increase in temperature lead to an increase in the diffusion coefficient with increase in temperature.

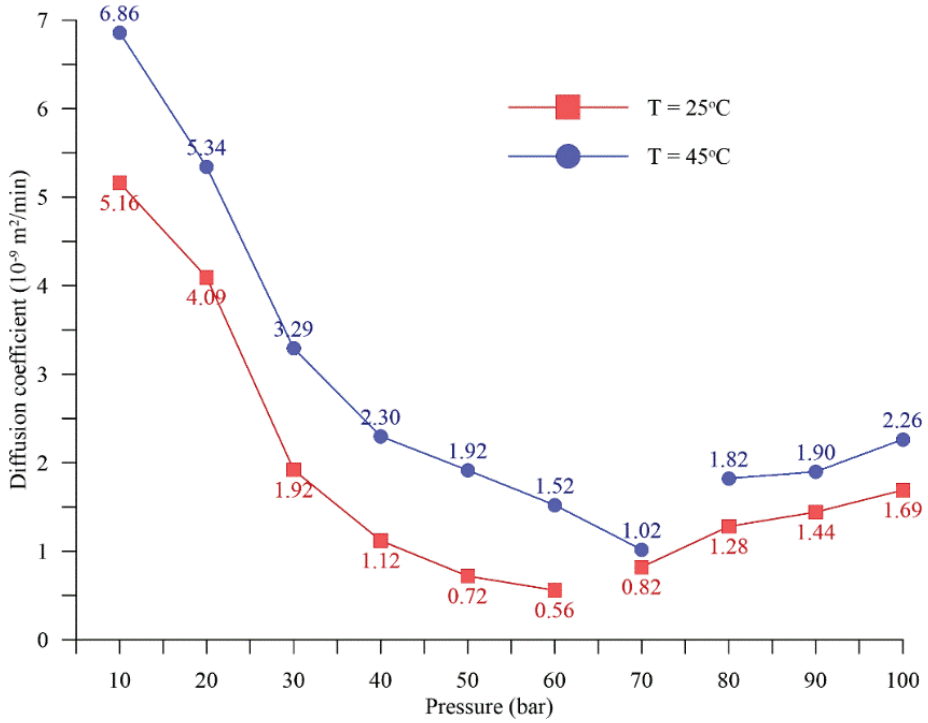

Figure 5.16: Diffusion coefficient of CO_2 in n-decane from CW for a CW-n-decane system for pressures 10-100 bar at 25°C and 45°C.

Figure 5.17 shows the diffusion coefficient of CO_2 in drop phase for CW-n-decane and CW-n-hexane system at 25°C for pressures 10-70 bar. It may be observed that the diffusion coefficient of CO_2 is higher for CW-hexane than for a CW-decane system. The molecular mass of n-hexane is lower than n-decane, therefore, the intermolecular force governed by the London force operating among n-hexane molecules will also be smaller. Due to the lower intermolecular force, CO_2 mass transfer into the drop phase consisting of n-hexane is easier than with n-decane. Therefore, the CO_2 diffusion coefficient in the n-hexane is higher than in the n-decane.

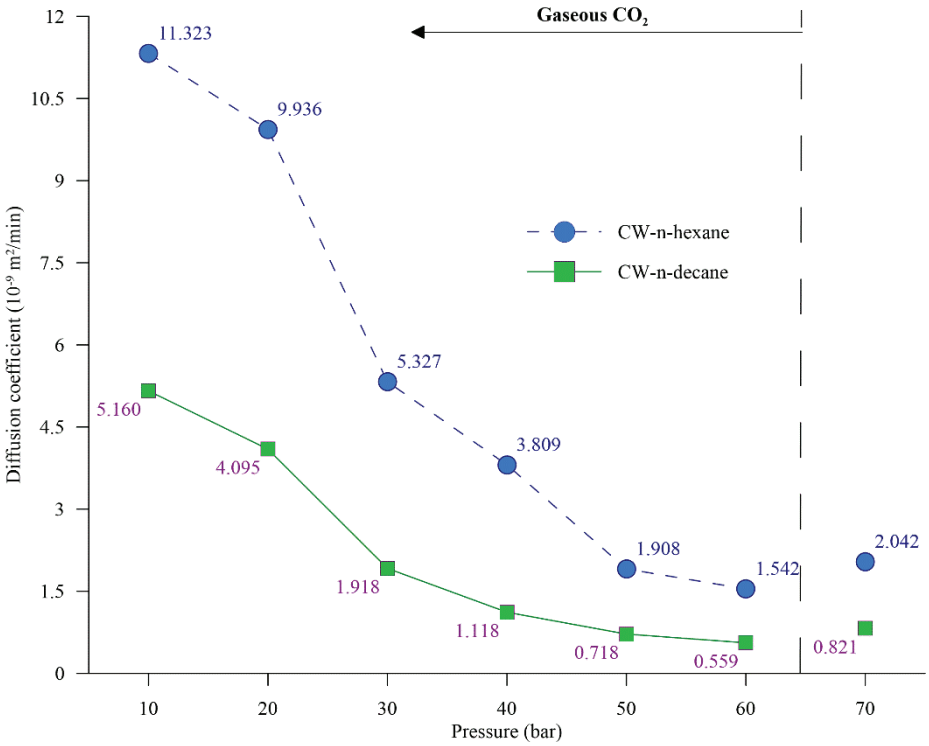

Figure 5.17: Diffusion coefficient of CO_2 in drop phase for CW-n-decane and CW-n-hexane system at pressures 10-70 bar at 25°C.

The higher diffusion coefficient of CO_2 in n-hexane will result in higher swelling of drop phase consisting of n-hexane compared to n-decane. Figure 5.18 shows the swelling of the drop phase for CW-n-decane and CW-n-hexane system for pressures at 10, 30, and 50bar at 45°C. Approximately 22% (50 bar) and 10% (30 bar) higher swelling is observed for drop phase containing n-hexane compared to n-decane. Further, the higher CO_2 diffusion coefficient in n-hexane would result in faster attainment of equilibrium volume for drop phase in CW-n-hexane system compared to CW-n-decane.

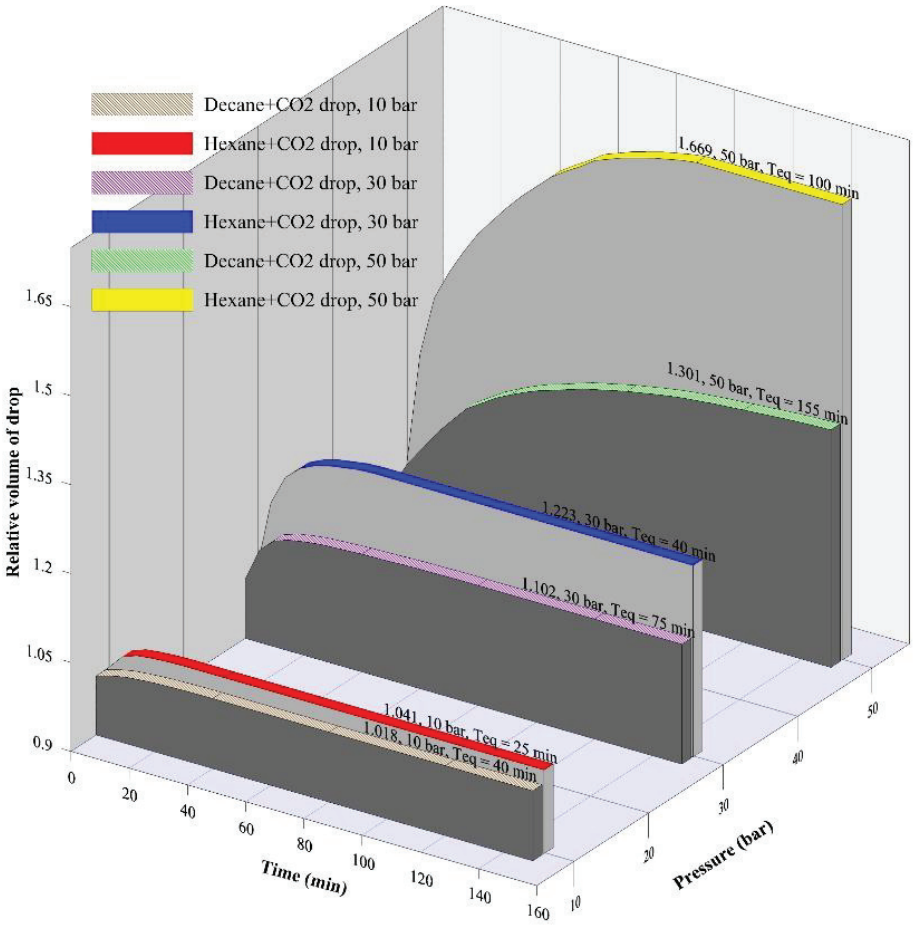

Figure 5.18: Swelling of the drop phase for CW-n-decane and CW-n-hexane system for pressures at 10, 30, and 50bar at 45°C [51].

5.2.3 CO_2+water-hydrocarbon system

Figure 5.19 shows the CO_2 diffusion coefficient into n-decane drop phase for CO_2+H_2O-n-decane system at 25°C, for a pressures 10-160 bar. The behaviour of diffusion coefficient of CO_2 with pressure for CO_2+H_2O-n-decane is similar to CW-n-decane system (Figure 5.16). However, the diffusion coefficient for CW-n-decane system is approximately 900% more than that for CO_2+H_2O-n-decane. This is

despite the fact that there is marginal difference in the IFT (maximum 17%) (Figure 5.9), indicating that IFT may have negligible influence on the CO2 diffusion coefficient CO_2+H_2O-n-decane system. In order to understand the significant difference in diffusion coefficient it is important to analyses the CO_2 concentration gradient across the interface. Figure 5.10 shows data of concentration difference of CO_2 between the drop phase and the surrounding environment fluid for CW-n-decane and CO_2+H_2O-n-decane system as a function of time, for 20, 40, 70, and 100 bar at 25ºC. It may be observed in Figure 5.10 that for most part of the time the concentration gradient for the CW-n-decane system is substantially higher than the CO_2+H_2O-n-decane system, this may be the reason for the observed higher CO2 diffusion coefficient for CW-n-decane compared to CO_2+H_2O-n-decane system.

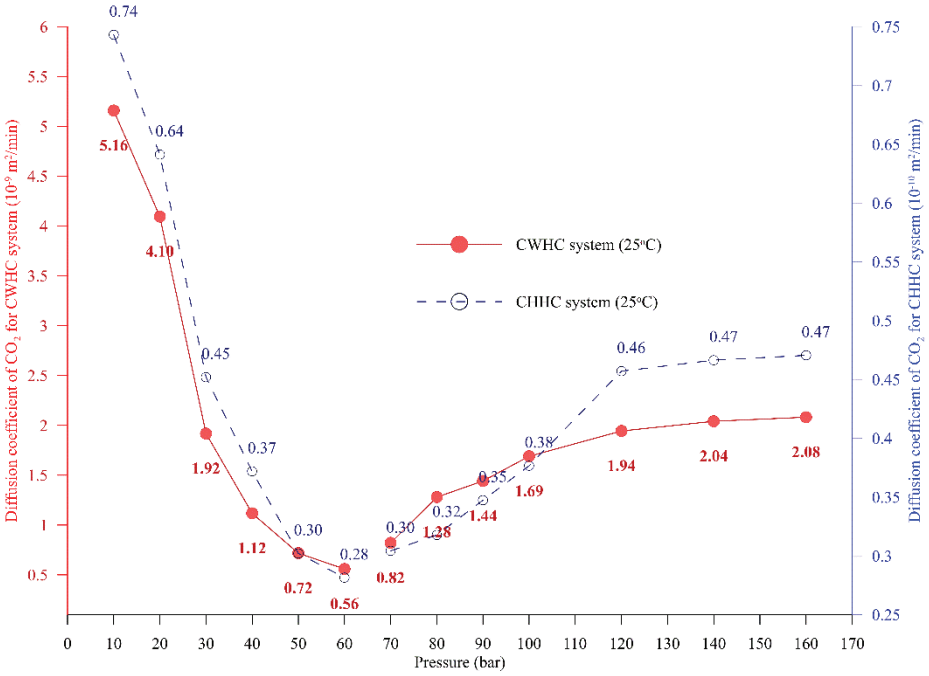

Figure 5.19: Diffusion coefficient between for CO_2+H_2O-n-decane and CW-n-decane system at 25ºC, for a pressures 10-160 bar.

The higher diffusion coefficient for CW-n-decane system may further be confirmed by studying the spreading or CO_2 inside the drop phase at various time steps. Figure 5.20 shows the numerically calculated distribution of the CO_2 concentration in the drop phase (a quarter of a drop) at time 30, 150, and 400 min for both CW-n-decane and CO_2+H_2O-n-decane systems (70 bar and 25°C). The centre of the quadrant is the centre of the drop, while the radius represents the interface. It may be observed that there is greater spreading for the case of CW-n-decane compared to CO_2+H_2O-n-decane system at each time step, indicating that the rate of mass transfer (diffusion coefficient) is faster for CW-n-decane compared to CO_2+H_2O-n-decane system.

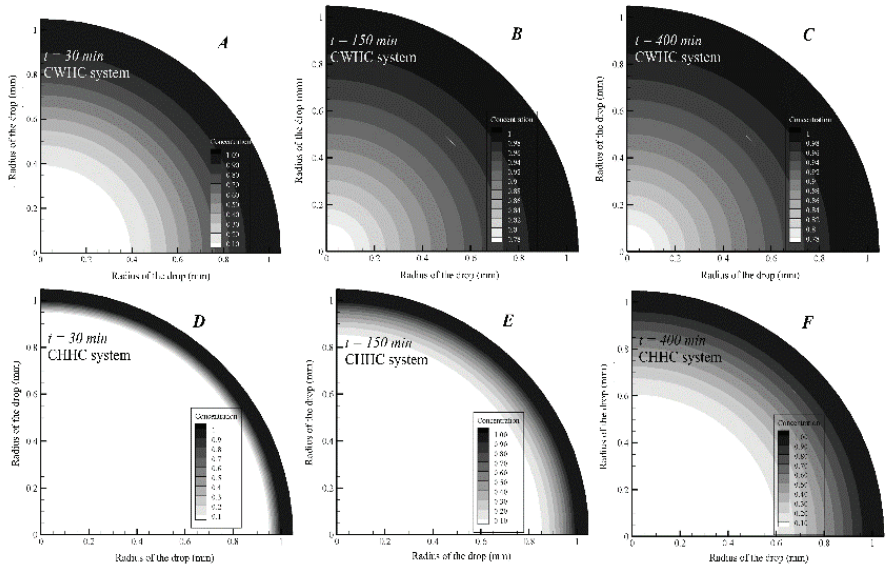

Figure 5.20: Spreading of CO_2 in the drop phase at 30, 150, and 400 min for CWHC and CHHC system at 25°C for 70 bar.

5.2.4 Salt+CW (CB)-hydrocarbon system

Figure 5.21 shows the diffusion coefficient of CO_2 in n-decane from CB (C_{SSW}, $C_{SSW\text{-}MgCl2}$, $CW_{+\ Na2SO4}$, $CW_{\text{-}Na2SO4}$ and CW_{+MgCl2}) and CW for

pressures 50, 70, 80, and 100 bar at 45ºC. For all the brine types the variation of CO_2 diffusion coefficient with pressure is similar to that seen for CW-hydrocarbon system (Figure 5.16). The CB containing Na_2SO_4 ($CW_{+Na2SO4}$) and absence of $MgCl_2$ ($C_{SSW-MgCl2}$) showed a higher diffusion coefficient than CW, while the CB containing $MgCl_2$ (CW_{+MgCl2}) and absence of Na_2SO_4 ($C_{SSW-Na2SO4}$) lead to a lower diffusion coefficient than CW. The diffusion coefficient was highest for $CW_{+Na2SO4}$, while the lowest was observed for CW_{+MgCl2}. O'Brien, et al. [166] reported that SO_4^{2-} ion is surrounded by up to 14 ion hydration, where each hydrogen atom interact with SO_4^{2-} or the oxygen atom of another water molecule. O'Brien, et al. [166] indicated that the outer shell water molecules have free OH. The present work suggests that the possible mechanism where the local OH at the interface may slightly reduce the IFT, this would help the transportation of CO_2 into hydrocarbon drop. However, for Mg^{2+} ions the hydrated ions are tightly packed at the interface area, which resist the transportation of CO_2 across the interface and accumulate at the interface. Therefore, the diffusion coefficient of CO_2 is higher when the drop is surrounded by brines containing Na_2SO_4 and lower when brine contains $MgCl_2$.

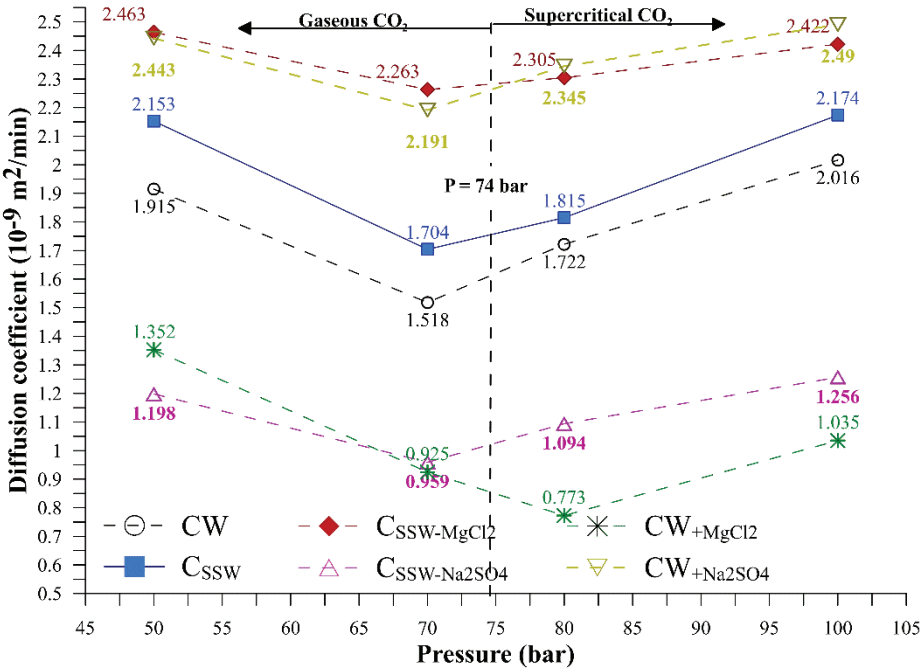

Figure 5.21: Diffusion coefficient of CO_2 in n-decane from CB and CW for pressures 50, 70, 80, and 100 bar at 45°C.

5.2.5 Nanofluid+CW (CNF)-hydrocarbon system

Figure 5.22 shows the diffusion coefficient of CO_2 in n-decane for CNF-n-decane system at three concentrations of nanofluid (0.05, 0.5, and 1.0 g/l) at 25°C for pressure 10-90 bar. It may be observed from Figure 5.22 that the diffusion coefficient of CO_2 for CNF-n-decane system is lower than CW-decane system. Therefore, indicating that the addition of nanofluid into CW will result in reduction of the CO_2 diffusion coefficient. However, as observed from Table 5.2, even with lower mass flow rate the nanofluid in CW resulted in a greater total mass transfer of CO_2 into n-decane. It is suggested that the presence of nanofluid in CW would increase the CO_2 solubility in water, which in turn would increase the amount of CO_2 that could be transported into the oil phase [20] by increasing the concentration gradient.

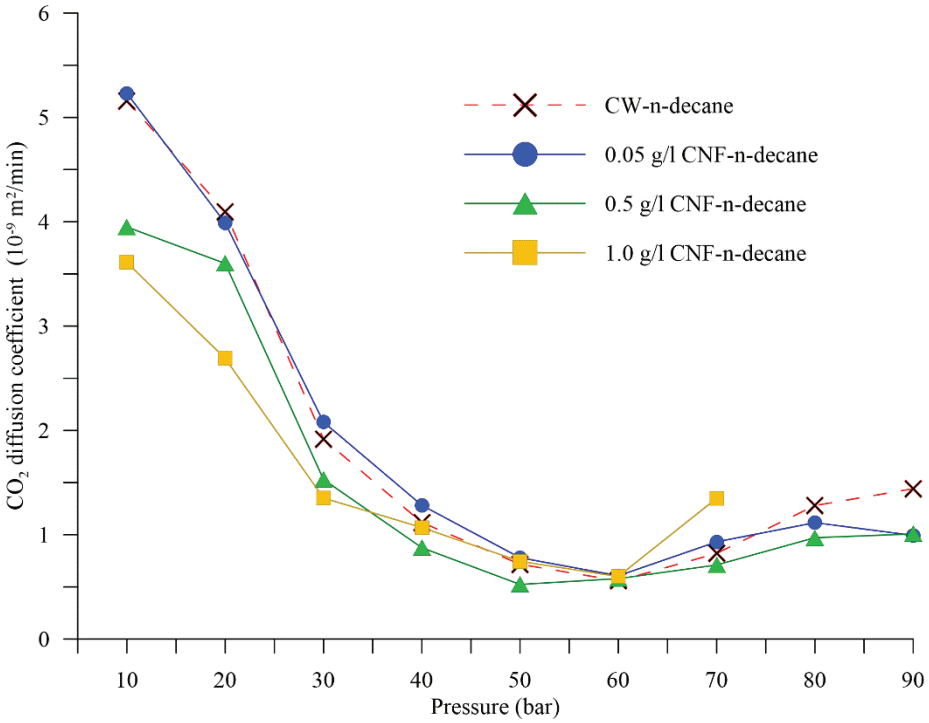

Figure 5.22: Diffusion coefficient of CO_2 in n-decane for CNF-n-decane system at three concentrations of nanofluid (0.05, 0.5, and 1.0 g/l) at 25°C for pressure 10-90 bar.

Table 5.2: Mass fraction of CO_2 in drop phase for different systems at 25°C (10-60 bar).

Pressure (bar)	**CW-decane**	**CNF-decane (0.5 g/l)**
10	0.0008	0.0015
20	0.0054	0.006
30	0.013	0.0232
40	0.0544	0.0907
50	0.1406	0.2255
60	0.2275	0.3702

6 Summary and conclusions

The thesis combines experimental, theoretical, and numerical approach to estimate the interfacial tension and CO_2 diffusion coefficient. From the IFT and mass transfer studies the work aims to identify the associated physics for CW-hydrocarbon systems. From analysis and the results obtained, the following conclusions are drawn.

In terms of methodology, two novel methods were developed: one in the experimental section and the other in the numerical section. In the experimental section, a new approach in data gathering (section 3.3.5) has been used to obtain the dynamic and equilibrium IFT. In the numerical part, an adaptive interface (boundary) model was developed capable of moving the gas-liquid or liquid-liquid interface; this novel advancement in the model would eliminate errors due to the assumption of static interface.

Unique observations were made regarding the IFT; the IFT for CW-hydrocarbon system was unlike the CO_2-hydrocarbon system. The IFT first increases with pressure up to phase change pressure of CO_2, above the phase change pressure the IFT reduces gradually with pressures. The IFT is maximum at pressures near to and below the phase change pressure of CO_2. Therefore, the phase of CO_2 has a notable influence on IFT. The dependency of the IFT on the density difference between the CW (environment phase) and the hydrocarbon (drop phase) was found to be a major reason for this unique behaviour of the IFT. The IFT variations with temperature are not straightforward. In general, the increase in temperature led to a reduction in the IFT of the CW-decane system. The increase in kinetic and entropy energy due to the increment in temperature was credited to the reduction in the IFT with temperature. However, the IFT at 35^{o}C was lower than that of 45^{o}C; this was credited to the lower Gibbs free energy at 35^{o}C, and to the proximity of 35^{o}C to the critical temperature of CO_2 (33^{o}C).

The CO_2 diffusion coefficient is inversely proportional to IFT. Therefore, the diffusion coefficient decrease with pressure up to phase change pressure of CO_2, above the phase change pressure the diffusion coefficient increases with pressure. Minimum diffusion coefficient is observed at pressure below and near to phase change pressure where IFT is maximum. The diffusion coefficient is also influenced by the CO_2 concentration gradient dictated by the CO_2 solubility.

Two different experimental designs have been presented to study the influence of the degree of carbonation of water surrounding the hydrocarbon on CO_2 mass transfer, and interfacial properties. The first design consists of CO_2+water-n-decane and, for the second, the system consists of CO_2-enriched water (CW)-n-decane. The results showed that the marginally lower swelling (2 to 5%), significantly lower diffusion coefficient (minimum one order lower), and the IFT were marginally higher (5-9%) for the CO_2+water-n-decane, compared to the CW-n-decane. The variance in IFT, swelling, and diffusion coefficient may be credited to the difference in the CO_2 concentration in the CW surrounding the hydrocarbon drop.

Three different alkanes, namely n-hexane, n-heptane and n-decane, were used as the hydrocarbon drop phase. It was observed that the diffusion coefficient was higher and IFT was lower for lighter alkanes compared to heavier alkanes. This was credited to higher CO_2 solubility, a lower intermolecular force and lower viscosity for lighter alkanes.

The interaction of CW with hydrocarbon leads to unique behaviour, which is unlike CO_2-hydrocarbon or the water-hydrocarbon systems. The variation of both IFT and diffusion coefficient with pressure for the CW-hydrocarbon system was the opposite of that of the CO_2-hydrocarbon system. The IFT was considerably higher; the diffusion coefficient was almost three to four orders lower for the CW-n-decane system than for the CO_2-n-decane system. However, from the hydrocarbon drop volume analysis, it was shown that there was

significantly greater swelling of hydrocarbon for the CW-hydrocarbon system compared to that of the CO_2-hydrocarbon system.

In the present study, the potential of the combination of silica nanofluid and carbonated water (CNF) was investigated. The presence of nanofluid increased the total CO_2 mass transfer and reduced the diffusion coefficient. A larger swelling of hydrocarbon was observed compared to CW-hydrocarbon. It is suggested that the presence of nanofluid in CW would increase the CO_2 solubility in water, which in turn would enhance the CO_2 mass transfer. Further, the addition of nanofluid lead to decrease in IFT, especially at lower pressures (below 50 bar).

The work also addressed the impact of various slats especially $MgCl_2$ and Na_2SO_4 in carbonated water (CW). The Mg^{2+} ion reduce both the CB-n-decane IFT (36.5%) and the CO_2 diffusion coefficient into n-decane, in comparison with CW-n-decane system. Mg^{2+} due to the smaller ionic radius (0.072 nm) forms a tight bound to the first hydration shell $[Mg(H2O)6]^{2+}$, accordingly it has high effective size and when adsorbs at the interface, it reduces the IFT. While the SO_4^{2-} increase both the CB-n-decane IFT and the CO_2 diffusion coefficient. The SO_4^{2-} ion is surrounded by up to 14 hydration ions, and outer shell water molecules have free OH. The local OH at the interface may slightly reduce the IFT, this would help the transportation of CO_2 into hydrocarbon drop.

7 References

[1] M. Sohrabi, M. Riazi, M. Jamiolahmady, S. Ireland, and C. Brown, "Carbonated water injection for oil recovery and CO2 storage," in *Sustainable energy UK conference: meeting the science and engineering challenge, Oxford, UK*, 2008.

[2] I. Sandrea and R. Sandrea, "Global Oil Reserves-1: Recovery factors leave vast target for EOR technologies," *Oil and Gas Journal,* vol. 105, no. 41, p. 44, 2007.

[3] T. M. Research, "Enhanced Oil Recovery Market: Global Industry Analysis, Size, Share, Growth, Trends and Forecast, 2013 - 2023," Canada, Report 2014-04-24 2014, Available: https://www.transparencymarketresearch.com/enhanced-oil-recovery.html/.

[4] B. R. Bijeljic, A. H. Muggeridge, and M. J. Blunt, "Effect of composition on waterblocking for multicomponent gasfloods," in *SPE Annual Technical Conference and Exhibition*, 2002: Society of Petroleum Engineers.

[5] L. S. Melzer, "Carbon dioxide enhanced oil recovery (CO 2 EOR): Factors involved in adding carbon capture, utilization and storage (CCUS) to enhanced oil recovery," *Center for Climate and Energy Solutions,* 2012.

[6] M. Riazi, M. Sohrabi, and M. Jamiolahmady, "Experimental study of pore-scale mechanisms of carbonated water injection," *Transport in porous media,* vol. 86, no. 1, pp. 73-86, 2011.

[7] S. Solomon, "The Bellona foundation-fact sheet: CO 2 storage," *Bellona Report, May,* 2007.

[8] M. Sohrabi, M. Riazi, M. Jamiolahmady, N. I. Kechut, S. Ireland, and G. Robertson, "Carbonated water injection (CWI)–a productive way of using CO 2 for oil recovery and CO 2 storage," *Energy Procedia,* vol. 4, pp. 2192-2199, 2011.

[9] M. Riazi, M. Sohrabi, M. Jamiolahmady, and S. Ireland, "Oil recovery improvement using CO2-enriched water injection," in *EUROPEC/EAGE Conference and Exhibition*, 2009: Society of Petroleum Engineers.

[10] C. Esene, N. Rezaei, A. Aborig, and S. J. F. Zendehboudi, "Comprehensive review of carbonated water injection for enhanced oil recovery," *Fuel,* vol. 237, pp. 1086-1107, 2019.

[11] L. Jiang *et al.*, "Behavior of CO2/water flow in porous media for CO2 geological storage," *Magnetic resonance imaging,* vol. 37, pp. 100-106, 2017.

[12] N. I. Kechut, M. Sohrabi, and M. Jamiolahmady, "Experimental and Numerical Evaluation of Carbonated Water Injection (CWI) for Improved Oil Recovery and CO2 Storage," in *SPE EUROPEC/EAGE Annual Conference and Exhibition*, 2011: Society of Petroleum Engineers.

[13] M. Sohrabi, M. Riazi, M. Jamiolahmady, N. I. Kechut, S. Ireland, and G. Robertson, "Carbonated water injection (CWI)–A productive way of using CO2 for oil recovery and CO2 storage," *Energy Procedia,* vol. 4, pp. 2192-2199, 2011.

[14] M. Sohrabi, M. Riazi, M. Jamiolahmady, S. Ireland, and C. Brown, "Mechanisms of oil recovery by carbonated water injection," in *SCA annual meeting*, 2009.

[15] M. Sohrabi, M. Riazi, M. Jamiolahmady, S. Ireland, and C. Brown, "Enhanced Oil Recovery and CO2 Storage by Carbonated Water Injection," in *International Petroleum Technology Conference*, 2009: International Petroleum Technology Conference.

[16] A. H. Alizadeh, M. A. Ioannidis, and M. Piri, "CO2-saturated brine flooding: an effective process for mobilization and recovery of waterflood residual oil," in *International Symposium of the Society of Core Analysts, Austin, Texas, USA*, 2011, pp. 18-21.

[17] L. Zuo, C. Zhang, R. W. Falta, and S. M. Benson, "Micromodel investigations of CO 2 exsolution from carbonated water in sedimentary rocks," *Advances in Water Resources,* vol. 53, pp. 188-197, 2013.

[18] A. H. Alizadeh, M. Khishvand, M. A. Ioannidis, and M. Piri, "Multi-scale experimental study of carbonated water injection: An effective process for mobilization and recovery of trapped oil," *Fuel,* vol. 132, pp. 219-235, 2014.

[19] N. Mosavat and F. Torabi, "Experimental evaluation of the performance of carbonated water injection (CWI) under various operating conditions in light oil systems," *Fuel,* vol. 123, pp. 274-284, 2014.

[20] A. Fathollahi and B. Rostami, "Carbonated water injection: Effects of silica nanoparticles and operating pressure," *The Canadian Journal of Chemical Engineering,* vol. 93, no. 11, pp. 1949-1956, 2015.

[21] M. F. Mat Ali, R. Junin, M. Aziz, N. Hidayah, and A. Salleh, "Carbonated Water Injection for Recovery of Oil and Wettability Analysis," in *Applied Mechanics and Materials*, 2015, vol. 695, pp. 499-502: Trans Tech Publ.

[22] B. Honarvar *et al.*, "Experimental Investigation of Interfacial Tension Measurement and Oil Recovery by Carbonated Water Injection: A Case Study Using Core Samples from an Iranian Carbonate Oil Reservoir," *Energy & Fuels,* 2017.

[23] A. K. Manshad, I. Nowrouzi, and A. H. Mohammadi, "Effects of water soluble ions on wettability alteration and contact angle in smart and carbonated smart water injection process in oil reservoirs," *Journal of Molecular Liquids,* vol. 244, pp. 440-452, 2017.

[24] A. K. Manshad, M. Olad, S. A. Taghipour, I. Nowrouzi, and A. H. Mohammadi, "Effects of water soluble ions on interfacial tension (IFT) between oil and brine in smart and carbonated

smart water injection process in oil reservoirs," *Journal of Molecular Liquids,* vol. 223, pp. 987-993, 2016.

[25] M. S. A. Perera, R. P. Gamage, T. D. Rathnaweera, A. S. Ranathunga, A. Koay, and X. Choi, "A Review of CO2-Enhanced Oil Recovery with a Simulated Sensitivity Analysis," *Energies,* vol. 9, no. 7, p. 481, 2016.

[26] Y. Shi, S. Zheng, D. J. I. J. o. H. Yang, and M. Transfer, "Determination of individual diffusion coefficients of alkane solvent (s)–CO2–heavy oil systems with consideration of natural convection induced by swelling effect," vol. 107, pp. 572-585, 2017.

[27] T. Renner, "Measurement and correlation of diffusion coefficients for CO2 and rich-gas applications," *SPE reservoir engineering,* vol. 3, no. 02, pp. 517-523, 1988.

[28] R. Azin, M. Mahmoudy, S. M. J. Raad, and S. J. C. E. J. o. E. Osfouri, "Measurement and modeling of CO 2 diffusion coefficient in Saline Aquifer at reservoir conditions," vol. 3, no. 4, pp. 585-594, 2013.

[29] M. Ghorbani and A. H. Mohammadi, "Effects of temperature, pressure and fluid composition on hydrocarbon gas-oil interfacial tension (IFT): An experimental study using ADSA image analysis of pendant drop test method," *Journal of Molecular Liquids,* vol. 227, pp. 318-323, 2017.

[30] L. Jiang, M. Yu, B. Wu, T. Suekane, W. Li, and Y. Song, "Characterization of dissolution process during brine injection in Berea sandstones: an experiment study," *RSC Advances,* vol. 6, no. 115, pp. 114320-114328, 2016.

[31] I. Nowrouzi, A. K. Manshad, and A. H. Mohammadi, "Effects of dissolved binary ionic compounds and different densities of brine on interfacial tension (IFT), wettability alteration, and contact angle in smart water and carbonated smart water injection

processes in carbonate oil reservoirs," *Journal of Molecular Liquids,* vol. 254, pp. 83-92, 2018.

[32] R. Taylor and R. Krishna, *Multicomponent mass transfer*. John Wiley & Sons, 1993.

[33] G. Davies, A. Ponter, and K. J. T. C. J. o. C. E. Craine, "The diffusion of carbon dioxide in organic liquids," vol. 45, no. 6, pp. 372-376, 1967.

[34] A. Unver and D. Himmelblau, "Diffusion Coefficients of CO2, C2H4, C3H6 and C4H8 in Water from 6 to 65 C," *Journal of Chemical & Engineering Data,* vol. 9, no. 3, pp. 428-431, 1964.

[35] T. Schmidt, T. Leshchyshyn, and V. Puttagunta, "Diffusivity of CO2 into reservoir fluids," *Paper,* vol. 82, pp. 33-100, 1982.

[36] T. Nguyen and S. Ali, "Effect of nitrogen on the solubility and diffusivity of carbon dioxide into oil and oil recovery by the immiscible WAG process," *Journal of Canadian Petroleum Technology,* vol. 37, no. 02, 1998.

[37] P. M. Sigmund, "Prediction of molecular diffusion at reservoir conditions. Part 1-Measurement and prediction of binary dense gas diffusion coefficients," *Journal of Canadian Petroleum Technology,* vol. 15, no. 02, 1976.

[38] S. R. Upreti and A. K. Mehrotra, "Experimental measurement of gas diffusivity in bitumen: results for carbon dioxide," *Industrial & engineering chemistry research,* vol. 39, no. 4, pp. 1080-1087, 2000.

[39] H. Sheikha, M. Pooladi-Darvish, and A. K. Mehrotra, "Development of graphical methods for estimating the diffusivity coefficient of gases in bitumen from pressure-decay data," *Energy & fuels,* vol. 19, no. 5, pp. 2041-2049, 2005.

[40] M. R. Riazi, "A new method for experimental measurement of diffusion coefficients in reservoir fluids," *Journal of Petroleum Science and Engineering,* vol. 14, no. 3, pp. 235-250, 1996.

[41] C. Yang and Y. Gu, "New experimental method for measuring gas diffusivity in heavy oil by the dynamic pendant drop volume analysis (DPDVA)," *Industrial & engineering chemistry research,* vol. 44, no. 12, pp. 4474-4483, 2005.

[42] Y.-B. Chang, B. K. Coats, and J. S. Nolen, "A compositional model for CO 2 floods including CO 2 solubility in water," in *Permian Basin Oil and Gas Recovery Conference*, 1996: Society of Petroleum Engineers.

[43] H. Nourozieh, B. Bayestehparvin, M. Kariznovi, J. J. J. o. C. Abedi, and E. Data, "Equilibrium properties of (carbon dioxide+ n-decane+ n-octadecane) systems: Experiments and thermodynamic modeling," vol. 58, no. 5, pp. 1236-1243, 2013.

[44] D. Yang, P. Tontiwachwuthikul, and Y. Gu, "Dynamic interfacial tension method for measuring gas diffusion coefficient and interface mass transfer coefficient in a liquid," *Industrial & engineering chemistry research,* vol. 45, no. 14, pp. 4999-5008, 2006.

[45] N. Bagalkot and A. A. Hamouda, "Experimental and Numerical Method for Estimating Diffusion Coefficient of the Carbon Dioxide into Light Components," *Industrial & Engineering Chemistry Research,* vol. 56, no. 9, pp. 2359-2374, 2017.

[46] D. Yang and Y. Gu, "Determination of Diffusion Coefficients and Interface Mass-Transfer Coefficients of the Crude Oil− CO2 System by Analysis of the Dynamic and Equilibrium Interfacial Tensions," *Industrial & Engineering Chemistry Research,* vol. 47, no. 15, pp. 5447-5455, 2008.

[47] Y. Liu *et al.*, "Experimental study on CO 2 diffusion in bulk n-decane and n-decane saturated porous media using micro-CT," *Fluid Phase Equilibria,* vol. 417, pp. 212-219, 2016.

[48] A. Grogan, V. Pinczewski, G. J. Ruskauff, and F. Orr Jr, "Diffusion of CO2 at reservoir conditions: models and measurements," *SPE Reservoir Engineering,* vol. 3, no. 01, pp. 93-102, 1988.

[49] W. Zhang, S. Wu, S. Ren, L. Zhang, and J. Li, "The modeling and experimental studies on the diffusion coefficient of CO2 in saline water," *Journal of CO2 Utilization,* vol. 11, pp. 49-53, 2015.

[50] Y. Liu *et al.*, "Experimental study on CO2 diffusion in bulk n-decane and n-decane saturated porous media using micro-CT," *Fluid Phase Equilibria,* vol. 417, pp. 212-219, 2016.

[51] N. Bagalkot and A. A. Hamouda, "Diffusion coefficient of CO2 into light hydrocarbons and interfacial tension of carbonated water–hydrocarbon system," *Journal of Geophysics and Engineering* vol. 15, no. 6, p. 2516, 2018.

[52] T. H. Barclay and S. Mishra, "New correlations for CO2-Oil solubility and viscosity reduction for light oils," *Journal of Petroleum Exploration and Production Technology,* vol. 6, no. 4, pp. 815-823, 2016.

[53] N. Mosavat, A. Abedini, and F. Torabi, "Phase behaviour of CO2–brine and CO2–oil systems for CO2 storage and enhanced oil recovery: experimental studies," *Energy Procedia,* vol. 63, pp. 5631-5645, 2014.

[54] A. Georgiadis, G. Maitland, J. M. Trusler, and A. Bismarck, "Interfacial tension measurements of the (H2O+ CO2) system at elevated pressures and temperatures," *Journal of Chemical & Engineering Data,* vol. 55, no. 10, pp. 4168-4175, 2010.

[55] H. Zhu, B. H. Shanks, and T. J. Heindel, "Effect of electrolytes on CO− water mass transfer," *Industrial & Engineering Chemistry Research,* vol. 48, no. 6, pp. 3206-3210, 2009.

[56] N. R. Biswal and J. K. Singh, "Interfacial behavior of nonionic Tween 20 surfactant at oil–water interfaces in the presence of different types of nanoparticles," *RSC Advances,* vol. 6, no. 114, pp. 113307-113314, 2016.

[57] K. D. Collins, "Charge density-dependent strength of hydration and biological structure," *Biophysical journal,* vol. 72, no. 1, pp. 65-76, 1997.

[58] B. Ju, T. Fan, and M. Ma, "Enhanced oil recovery by flooding with hydrophilic nanoparticles," *China Particuology,* vol. 4, no. 1, pp. 41-46, 2006.

[59] B. Ju and T. Fan, "Experimental study and mathematical model of nanoparticle transport in porous media," *Powder Technology,* vol. 192, no. 2, pp. 195-202, 2009.

[60] L. Hendraningrat and O. Torsæter, "Effects of the initial rock wettability on silica-based nanofluid-enhanced oil recovery processes at reservoir temperatures," *Energy & Fuels,* vol. 28, no. 10, pp. 6228-6241, 2014.

[61] L. Hendraningrat, S. Li, and O. Torsæter, "A coreflood investigation of nanofluid enhanced oil recovery," *Journal of Petroleum Science and Engineering,* vol. 111, pp. 128-138, 2013.

[62] R. Li, P. Jiang, C. Gao, F. Huang, R. Xu, and X. Chen, "Experimental Investigation of Silica-Based Nanofluid Enhanced Oil Recovery: The Effect of Wettability Alteration," *Energy & Fuels,* vol. 31, no. 1, pp. 188-197, 2016.

[63] S. Al-Anssari, A. Barifcani, S. Wang, and S. Iglauer, "Wettability alteration of oil-wet carbonate by silica nanofluid," *Journal of colloid and interface science,* vol. 461, pp. 435-442, 2016.

[64] C. O. Metin, J. R. Baran, and Q. P. Nguyen, "Adsorption of surface functionalized silica nanoparticles onto mineral surfaces and decane/water interface," *Journal of nanoparticle research,* vol. 14, no. 11, p. 1246, 2012.

[65] W.-g. Kim, H. U. Kang, K.-m. Jung, and S. H. Kim, "Synthesis of silica nanofluid and application to CO2 absorption," *Separation Science and Technology,* vol. 43, no. 11-12, pp. 3036-3055, 2008.

[66] J. W. Lee and Y. T. Kang, "CO 2 absorption enhancement by Al 2 O 3 nanoparticles in NaCl aqueous solution," *Energy,* vol. 53, pp. 206-211, 2013.

[67] A. Haghtalab, M. Mohammadi, and Z. Fakhroueian, "Absorption and solubility measurement of CO 2 in water-based ZnO and SiO 2 nanofluids," *Fluid Phase Equilibria,* vol. 392, pp. 33-42, 2015.

[68] H. Zhu, B. H. Shanks, and T. J. Heindel, "Enhancing CO− water mass transfer by functionalized MCM41 nanoparticles," *Industrial & Engineering Chemistry Research,* vol. 47, no. 20, pp. 7881-7887, 2008.

[69] S. Krishnamurthy, P. Bhattacharya, P. Phelan, and R. Prasher, "Enhanced mass transport in nanofluids," *Nano letters,* vol. 6, no. 3, pp. 419-423, 2006.

[70] S.-S. Ashrafmansouri and M. N. Esfahany, "Mass transfer in nanofluids: A review," *International Journal of Thermal Sciences,* vol. 82, pp. 84-99, 2014.

[71] M. Riazi, M. Jamiolahmady, and M. Sohrabi, "Theoretical investigation of pore-scale mechanisms of carbonated water injection," *Journal of Petroleum Science and Engineering,* vol. 75, no. 3, pp. 312-326, 2011.

[72] D. E. Tambe and M. M. Sharma, "The effect of colloidal particles on fluid-fluid interfacial properties and emulsion stability," *Advances in colloid and interface science,* vol. 52, pp. 1-63, 1994.

[73] S.-W. Jeong, M. Y. Corapcioglu, and S. E. Roosevelt, "Micromodel study of surfactant foam remediation of residual

trichloroethylene," *Environmental science & technology,* vol. 34, no. 16, pp. 3456-3461, 2000.

[74] M. Lashkarbolooki, S. Ayatollahi, and M. Riazi, "The impacts of aqueous ions on interfacial tension and wettability of an asphaltenic–acidic crude oil reservoir during smart water injection," *Journal of Chemical & Engineering Data,* vol. 59, no. 11, pp. 3624-3634, 2014.

[75] F. Moeini, A. Hemmati-Sarapardeh, M.-H. Ghazanfari, M. Masihi, and S. Ayatollahi, "Toward mechanistic understanding of heavy crude oil/brine interfacial tension: The roles of salinity, temperature and pressure," *Fluid phase equilibria,* vol. 375, pp. 191-200, 2014.

[76] K. J. Pekarek, J. S. Jacob, and E. Mathiowitz, "Double-walled polymer microspheres for controlled drug release," *Nature,* vol. 367, no. 6460, p. 258, 1994.

[77] S. Iglauer, M. Mathew, and F. Bresme, "Molecular dynamics computations of brine–CO2 interfacial tensions and brine–CO2–quartz contact angles and their effects on structural and residual trapping mechanisms in carbon geo-sequestration," *Journal of colloid and interface science,* vol. 386, no. 1, pp. 405-414, 2012.

[78] A. Shariat, R. G. Moore, S. A. Mehta, K. C. Van Fraassen, K. E. Newsham, and J. A. Rushing, "Laboratory Measurements of CO2-H2O Interfacial Tension at HP/HT Conditions: Implications for CO2 Sequestration in Deep Aquifers," in *Carbon Management Technology Conference*, 2012: Carbon Management Technology Conference.

[79] W. Karnanda, M. Benzagouta, A. AlQuraishi, and M. Amro, "Effect of temperature, pressure, salinity, and surfactant concentration on IFT for surfactant flooding optimization," *Arabian Journal of Geosciences,* vol. 6, no. 9, pp. 3535-3544, 2013.

[80] S. Hosseini, M. Shuker, Z. Hosseini, T. J. Tomocene, A. Shabib-Asl, and M. Sabet, "The role of salinity and brine ions in interfacial tension reduction while using surfactant for enhanced oil recovery," *Research Journal of Applied Sciences, Engineering and Technology,* vol. 9, no. 9, pp. 722-726, 2015.

[81] S. Li and O. Torsæter, "An experimental investigation of EOR mechanisms for nanoparticles fluid in glass micromodel," in *Paper SCA2014-022 was prepared for presentation at the International Symposium of the Society of Core Analysts held in Avignon, France*, 2014, pp. 8-11.

[82] L. Hendraningrat, S. Li, and O. Torsater, "A coreflood investigation of nanofluid enhanced oil recovery in low-medium permeability Berea sandstone," in *SPE International Symposium on Oilfield Chemistry*, 2013: Society of Petroleum Engineers.

[83] T. Němec, "Prediction of surface tension of binary mixtures with the parachor method," in *EPJ Web of Conferences*, 2015, vol. 92, p. 02054: EDP Sciences.

[84] H. Norgaard and L. Nygaard, "Measurement and calculation of surface tension of oil, gas and glycol," Institutt for energi-og prosessteknikk, 2014.

[85] D. Schechter and B. Guo, "Parachors based on modern physics and their uses in IFT prediction of reservoir fluids," *SPE Reservoir Evaluation & Engineering,* vol. 1, no. 03, pp. 207-217, 1998.

[86] K. L. Mittal, *Contact Angle, Wettability and Adhesion, Volume 4*. CRC Press, 2006.

[87] L. Girifalco and R. J. Good, "A theory for the estimation of surface and interfacial energies. I. Derivation and application to interfacial tension," *The Journal of Physical Chemistry,* vol. 61, no. 7, pp. 904-909, 1957.

[88] C. F. Weinaug and D. L. Katz, "Surface tensions of methane-propane mixtures," *Industrial & Engineering Chemistry,* vol. 35, no. 2, pp. 239-246, 1943.

[89] S. Sugden, "VI.—The variation of surface tension with temperature and some related functions," *Journal of the Chemical Society, Transactions,* vol. 125, pp. 32-41, 1924.

[90] O. R. Quayle, "The Parachors of Organic Compounds. An Interpretation and Catalogue," *Chemical Reviews,* vol. 53, no. 3, pp. 439-589, 1953.

[91] J. R. Fanchi, "Calculation of parachors for compositional simulation: an update," *SPE Reservoir Engineering,* vol. 5, no. 03, pp. 433-436, 1990.

[92] R. C. Reid, J. M. Prausnitz, and B. E. Poling, "The properties of gases and liquids," 1987.

[93] S. Bachu and D. B. Bennion, "Interfacial tension between CO2, freshwater, and brine in the range of pressure from (2 to 27) MPa, temperature from (20 to 125) C, and water salinity from (0 to 334 000) mg· L− 1," *Journal of Chemical & Engineering Data,* vol. 54, no. 3, pp. 765-775, 2008.

[94] H. W. Yarranton, H. Alboudwarej, and R. Jakher, "Investigation of asphaltene association with vapor pressure osmometry and interfacial tension measurements," *Industrial & engineering chemistry research,* vol. 39, no. 8, pp. 2916-2924, 2000.

[95] D. B. Bennion and S. Bachu, "Correlations for the interfacial tension between supercritical phase CO2 and equilibrium brines at in situ conditions," in *SPE annual technical conference and exhibition*, 2008: Society of Petroleum Engineers.

[96] M. K. Meybodi, A. Daryasafar, and M. Karimi, "Determination of hydrocarbon-water interfacial tension using a new empirical correlation," *Fluid Phase Equilibria,* vol. 415, pp. 42-50, 2016.

[97] A. Hyde, C. Phan, and G. Ingram, "Determining liquid–liquid interfacial tension from a submerged meniscus," *Colloids and Surfaces A: Physicochemical and Engineering Aspects,* vol. 459, pp. 267-273, 2014.

[98] K. Hool and B. Schuchardt, "A new instrument for the measurement of liquid-liquid interfacial tension and the dynamics of interfacial tension reduction," *Measurement Science and Technology,* vol. 3, no. 5, p. 451, 1992.

[99] H.-J. Butt, K. Graf, and M. Kappl, *Physics and chemistry of interfaces*. John Wiley & Sons, 2006.

[100] C.-H. Chang and E. I. Franses, "Adsorption dynamics of surfactants at the air/water interface: a critical review of mathematical models, data, and mechanisms," *Colloids and Surfaces A: Physicochemical and Engineering Aspects,* vol. 100, pp. 1-45, 1995.

[101] D. Mobius and R. Miller, *Drops and bubbles in interfacial research*. Elsevier, 1997.

[102] H. H. Hu and D. D. Joseph, "Evolution of a liquid drop in a spinning drop tensiometer," *Journal of colloid and interface science,* vol. 162, no. 2, pp. 331-339, 1994.

[103] Kruss. *Pendant drop*. Available: https://www.kruss-scientific.com/services/education-theory/glossary/pendant-drop/

[104] D. Yang and Y. Gu, "Interfacial interactions of crude oil-brine-CO2 systems under reservoir conditions," in *SPE Annual Technical Conference and Exhibition*, 2004: Society of Petroleum Engineers.

[105] D. Yang, P. Tontiwachwuthikul, and Y. Gu, "Interfacial tensions of the crude oil+ reservoir brine+ CO2 systems at pressures up to 31 MPa and temperatures of 27 C and 58 C," *Journal of Chemical & Engineering Data,* vol. 50, no. 4, pp. 1242-1249, 2005.

[106] G. Wiegand and E. Franck, "Interfacial tension between water and non-polar fluids up to 473 K and 2800 bar," *Berichte der Bunsengesellschaft für physikalische Chemie,* vol. 98, no. 6, pp. 809-817, 1994.

[107] H. Y. Jennings, "The effect of temperature and pressure on the interfacial tension of benzene-water and normal decane-water," *Journal of colloid and interface science,* vol. 24, no. 3, pp. 323-329, 1967.

[108] A. Firoozabadi and H. J. Ramey Jr, "Surface tension of water-hydrocarbon systems at reservoir conditions," *Journal of Canadian Petroleum Technology,* vol. 27, no. 03, 1988.

[109] W. Wang and A. Gupta, "Investigation of the effect of temperature and pressure on wettability using modified pendant drop method," in *SPE Annual Technical Conference and Exhibition*, 1995: Society of Petroleum Engineers.

[110] A. Hemmati-Sarapardeh, S. Ayatollahi, M.-H. Ghazanfari, and M. Masihi, "Experimental determination of interfacial tension and miscibility of the CO2–crude oil system; temperature, pressure, and composition effects," *Journal of Chemical & Engineering Data,* vol. 59, no. 1, pp. 61-69, 2013.

[111] S. Bachu and D. B. Bennion, "Dependence of CO2-brine interfacial tension on aquifer pressure, temperature and water salinity," *Energy Procedia,* vol. 1, no. 1, pp. 3157-3164, 2009.

[112] A. Zolghadr, M. Riazi, M. Escrochi, and S. Ayatollahi, "Investigating the effects of temperature, pressure, and paraffin groups on the N2 miscibility in hydrocarbon liquids using the interfacial tension measurement method," *Industrial & Engineering Chemistry Research,* vol. 52, no. 29, pp. 9851-9857, 2013.

[113] S. Ferdous, M. A. Ioannidis, and D. E. Henneke, "Effects of temperature, pH, and ionic strength on the adsorption of

nanoparticles at liquid–liquid interfaces," *Journal of Nanoparticle Research,* vol. 14, no. 5, p. 850, 2012.

[114] P. J. Wangersky, "THE CONTROL OF SEAWATER pH BY ION PAIRING 1," *Limnology and Oceanography,* vol. 17, no. 1, pp. 1-6, 1972.

[115] J. S. Buckley, "Chemistry of the crude oil/brine interface," in *Proc. 3 rd International Symposium on Evaluation of Reservoir Wettability and Its Effect on Oil Recovery*, 1994, pp. 33-38.

[116] S. Poteau, J.-F. Argillier, D. Langevin, F. Pincet, and E. Perez, "Influence of pH on stability and dynamic properties of asphaltenes and other amphiphilic molecules at the oil− water interface," *Energy & Fuels,* vol. 19, no. 4, pp. 1337-1341, 2005.

[117] B. Kumar, "Effect of salinity on the interfacial tension of model and crude oil systems," University of Calgary, 2012.

[118] K. R. Gomari and A. Hamouda, "Effect of fatty acids, water composition and pH on the wettability alteration of calcite surface," *Journal of petroleum science and engineering,* vol. 50, no. 2, pp. 140-150, 2006.

[119] E. Serrano-Saldaña, A. Domínguez-Ortiz, H. Pérez-Aguilar, I. Kornhauser-Strauss, and F. Rojas-González, "Wettability of solid/brine/n-dodecane systems: experimental study of the effects of ionic strength and surfactant concentration," *Colloids and Surfaces A: Physicochemical and Engineering Aspects,* vol. 241, no. 1-3, pp. 343-349, 2004.

[120] N. Ikeda, M. Aratono, and K. Motomura, "Thermodynamic study on the adsorption of sodium chloride at the water/hexane interface," *Journal of colloid and interface science,* vol. 149, no. 1, pp. 208-215, 1992.

[121] B.-Y. Cai, J.-T. Yang, and T.-M. Guo, "Interfacial tension of hydrocarbon+ water/brine systems under high pressure," *Journal*

of chemical & engineering data, vol. 41, no. 3, pp. 493-496, 1996.

[122] R. Aveyard and S. M. Saleem, "Interfacial tensions at alkane-aqueous electrolyte interfaces," *Journal of the Chemical Society, Faraday Transactions 1: Physical Chemistry in Condensed Phases,* vol. 72, pp. 1609-1617, 1976.

[123] A. Badakshan and P. Bakes, "The influence of temperature and surfactant concentration on interfacial tension of saline water and hydrocarbon systems in relation to enhanced oil recovery by chemical flooding," 1990.

[124] M. Lashkarbolooki and S. Ayatollahi, "Investigation of ionic liquids based on pyridinium and imidazolium as interfacial tension reducer of crude Oil− Water and their synergism with MgCl2," *Journal of Petroleum Science and Engineering,* 2018.

[125] F. Ravera, E. Santini, G. Loglio, M. Ferrari, and L. Liggieri, "Effect of nanoparticles on the interfacial properties of liquid/liquid and liquid/air surface layers," *The Journal of Physical Chemistry B,* vol. 110, no. 39, pp. 19543-19551, 2006.

[126] H. Ma, M. Luo, and L. L. Dai, "Influences of surfactant and nanoparticle assembly on effective interfacial tensions," *Physical Chemistry Chemical Physics,* vol. 10, no. 16, pp. 2207-2213, 2008.

[127] B. A. Suleimanov, F. Ismailov, and E. Veliyev, "Nanofluid for enhanced oil recovery," *Journal of Petroleum Science and Engineering,* vol. 78, no. 2, pp. 431-437, 2011.

[128] L. Hendraningrat, L. Shidong, and O. Torsaeter, "A glass micromodel experimental study of hydrophilic nanoparticles retention for EOR project," in *SPE Russian Oil and Gas Exploration and Production Technical Conference and Exhibition*, 2012: Society of Petroleum Engineers.

[129] O. M. Isdahl, "Influence of Silica Based Nanofluid on the Physical Properties, IFT, and CO2 Diffusion in a Carbonated Water-n-decane system: An Experimental and Numerical Study," University of Stavanger, Norway, 2017.

[130] O. Del Rıo, A. J. J. o. c. Neumann, and i. science, "Axisymmetric drop shape analysis: computational methods for the measurement of interfacial properties from the shape and dimensions of pendant and sessile drops," vol. 196, no. 2, pp. 136-147, 1997.

[131] J. D. Berry, M. J. Neeson, R. R. Dagastine, D. Y. Chan, R. F. J. J. o. c. Tabor, and i. science, "Measurement of surface and interfacial tension using pendant drop tensiometry," vol. 454, pp. 226-237, 2015.

[132] B. Song, J. J. J. o. c. Springer, and i. science, "Determination of interfacial tension from the profile of a pendant drop using computer-aided image processing: 1. Theoretical," vol. 184, no. 1, pp. 64-76, 1996.

[133] D. I. GmbH. (2018, 11/11/2018). *Pendant drop method — Optical determination of the surface/interfacial tension*. Available: https://www.dataphysics-instruments.com/knowledge/understanding-interfaces/pendant-drop-method/#figure2

[134] M. Alotaibi and H. Nasr-El-Din, "Effect of brine salinity on reservoir fluids interfacial tension," *paper SPE,* vol. 121569, 2009.

[135] K. V. Greenway, "Effect of different surfactant structures on the brine-crude oil and brine-alkane interface in different aqueous environments," The University of Bergen, 2017.

[136] N. Bagalkot, A. A. Hamouda, and O. M. Isdahl, "Dynamic Interfacial Tension Measurement Method Using Axisymmetric Drop Shape Analysis," *MethodsX,* vol. 5, pp. 676-683, 2018.

[137] A. Merrington and E. J. P. o. t. P. S. Richardson, "The break-up of liquid jets," vol. 59, no. 1, p. 1, 1947.

[138] A. A. Hamouda and E. Maevskiy, "Oil recovery mechanism (s) by low salinity brines and their interaction with chalk," *Energy & Fuels,* vol. 28, no. 11, pp. 6860-6868, 2014.

[139] A. Kakati and J. S. Sangwai, "Effect of monovalent and divalent salts on the interfacial tension of pure hydrocarbon-brine systems relevant for low salinity water flooding," *Journal of Petroleum Science and Engineering,* vol. 157, pp. 1106-1114, 2017.

[140] P. Linstrom and W. Mallard, "NIST chemistry webbook, NIST standard reference database number 69, National Institute of Standards and Technology, Gaithersburg MD, 20899," ed, 2010.

[141] N. Bagalkot and A. A. Hamouda, "Interfacial tension and CO 2 diffusion coefficients for a CO 2+ water and n-decane system at pressures of 10 to 160 bar," *RSC Advances,* vol. 8, no. 67, pp. 38351-38362, 2018.

[142] F. Herning and L. Zipperer, "Calculation of the viscosity of technical gas mixtures from the viscosity of individual gases," *Gas u. Wasserfach,* vol. 79, p. 69, 1936.

[143] M. McBride-Wright, G. C. Maitland, and J. M. Trusler, "Viscosity and Density of Aqueous Solutions of Carbon Dioxide at Temperatures from (274 to 449) K and at Pressures up to 100 MPa," *Journal of Chemical & Engineering Data,* vol. 60, no. 1, pp. 171-180, 2014.

[144] M. E. Kandil, N. M. Al-Saifi, and A. S. Sultan, "Simulation and measurements of volumetric and phase behavior of carbon dioxide+ higher alkanes at high pressure: CO2+ n-decane at temperatures (313–410) K and pressures up to 76 MPa," *International Journal of Greenhouse Gas Control,* vol. 53, pp. 198-206, 2016.

[145] J. Zambrano, F. V. Gómez-Soto, D. Lozano-Martín, M. C. Martín, and J. J. Segovia, "Volumetric behaviour of (carbon dioxide+ hydrocarbon) mixtures at high pressures," *The Journal of Supercritical Fluids,* vol. 110, pp. 103-109, 2016.

[146] R. J. Martins, M. J. d. M. Cardoso, and O. E. Barcia, "Excess Gibbs free energy model for calculating the viscosity of binary liquid mixtures," *Industrial & engineering chemistry research,* vol. 39, no. 3, pp. 849-854, 2000.

[147] P. T. Jaeger and R. Eggers, "Interfacial properties at elevated pressures in reservoir systems containing compressed or supercritical carbon dioxide," *The Journal of Supercritical Fluids,* vol. 66, pp. 80-85, 2012.

[148] K. Gmb. (2016, 29/05/2018). *DROP SHAPE ANALYZER – DSA100 HP*. Available: https://www.kruss-scientific.com/fileadmin/user_upload/website/brochures/kruss-techdata-dsa100hp-en.pdf

[149] Z. Duan and R. Sun, "An improved model calculating CO 2 solubility in pure water and aqueous NaCl solutions from 273 to 533 K and from 0 to 2000 bar," *Chemical geology,* vol. 193, no. 3, pp. 257-271, 2003.

[150] S. R. Upreti and A. K. Mehrotra, "Diffusivity of CO2, CH4, C2H6 and N2 in Athabasca bitumen," *The Canadian Journal of Chemical Engineering,* vol. 80, no. 1, pp. 116-125, 2002.

[151] S. Zheng, H. A. Li, H. Sun, and D. Yang, "Determination of Diffusion Coefficient for Alkane Solvent–CO2 Mixtures in Heavy Oil with Consideration of Swelling Effect," *Industrial & Engineering Chemistry Research,* vol. 55, no. 6, pp. 1533-1549, 2016.

[152] Y. Zhang, C. Hyndman, and B. Maini, "Measurement of gas diffusivity in heavy oils," *Journal of Petroleum Science and Engineering,* vol. 25, no. 1, pp. 37-47, 2000.

[153] D. Zabala, C. Nieto-Draghi, J. C. de Hemptinne, and A. L. Lopez de Ramos, "Diffusion coefficients in CO2/n-alkane binary liquid mixtures by molecular simulation," *The Journal of Physical Chemistry B,* vol. 112, no. 51, pp. 16610-16618, 2008.

[154] W. Zhang, S. Wu, S. Ren, L. Zhang, and J. Li, "The modeling and experimental studies on the diffusion coefficient of CO 2 in saline water," *Journal of CO2 Utilization,* vol. 11, pp. 49-53, 2015.

[155] N. Bagalkot and A. A. Hamouda, "Experimental and Numerical Method for Estimating Diffusion Coefficient of the Carbon Dioxide into Light Components," *Industrial & Engineering Chemistry Research,* 2017.

[156] M. Jamialahmadi, M. Emadi, and H. Müller-Steinhagen, "Diffusion coefficients of methane in liquid hydrocarbons at high pressure and temperature," *Journal of Petroleum Science and Engineering,* vol. 53, no. 1, pp. 47-60, 2006.

[157] C. Yang and Y. Gu, "Diffusion coefficients and oil swelling factors of carbon dioxide, methane, ethane, propane, and their mixtures in heavy oil," *Fluid Phase Equilibria,* vol. 243, no. 1, pp. 64-73, 2006.

[158] A. Zolghadr, M. Escrochi, and S. Ayatollahi, "Temperature and composition effect on CO2 miscibility by interfacial tension measurement," *Journal of Chemical & Engineering Data,* vol. 58, no. 5, pp. 1168-1175, 2013.

[159] R. Farajzadeh, H. Salimi, P. L. Zitha, and H. Bruining, "Numerical simulation of density-driven natural convection in porous media with application for CO 2 injection projects," *International Journal of Heat and Mass Transfer,* vol. 50, no. 25, pp. 5054-5064, 2007.

[160] J. S. Miller and R. A. Jones, "A laboratory study to determine physical characteristics of heavy oil after CO2 saturation," in

SPE/DOE Enhanced Oil Recovery Symposium, 1981: Society of Petroleum Engineers.

[161] Ø. Brandal, J. Sjöblom, and G. Øye, "Interfacial Behavior of Naphthenic Acids and Multivalent Cations in Systems with Oil and Water. I. A Pendant Drop Study of Interactions Between n-Dodecyl Benzoic Acid and Divalent Cations," *Journal of dispersion science and technology,* vol. 25, no. 3, pp. 367-374, 2004.

[162] C. Esene, N. Rezaei, A. Aborig, and S. J. F. Zendehboudi, "Comprehensive review of carbonated water injection for enhanced oil recovery," vol. 237, pp. 1086-1107, 2019.

[163] C. Chieh. (2018, 10/08/2018). *Hydration*. Available: https://chem.libretexts.org/Textbook_Maps/Physical_and_Theoretical_Chemistry_Textbook_Maps/Supplemental_Modules_(Physical_and_Theoretical_Chemistry)/Thermodynamics/Energies_and_Potentials/Enthalpy/Hydration

[164] R. Garrels and M. Thompson, "A chemical model for sea water at 25 degrees C and one atmosphere total pressure," *American Journal of Science,* vol. 260, no. 1, pp. 57-66, 1962.

[165] C. Wilke and P. Chang, "Correlation of diffusion coefficients in dilute solutions," *AIChE Journal,* vol. 1, no. 2, pp. 264-270, 1955.

[166] J. T. O'Brien, J. S. Prell, M. F. Bush, and E. R. Williams, "Sulfate ion patterns water at long distance," *Journal of the American Chemical Society,* vol. 132, no. 24, pp. 8248-8249, 2010.

PAPER — II

Diffusion coefficient of CO_2 into light hydrocarbons and interfacial tension of carbonated water-hydrocarbon system

IOP Publishing Journal of Geophysics and Engineering
J. Geophys. Eng. **15** (2018) 2516–2529 (14pp) https://doi.org/10.1088/1742-2140/aad432

Diffusion coefficient of CO_2 into light hydrocarbons and interfacial tension of carbonated water–hydrocarbon system

Nikhil Bagalkot and Aly A Hamouda[1]

Department of Petroleum Technology, University of Stavanger, Stavanger, Norway N 4035

E-mail: nikhil.bagalkot@uis.no and aly.hamouda@uis.no

Received 22 February 2018, revised 4 June 2018
Accepted for publication 18 July 2018
Published 20 August 2018

Abstract

The interfacial tension (IFT) and diffusion coefficient of CO_2 in a hydrocarbon in a carbonated water (CW) environment were estimated for pressures between 10–100 bar and at temperatures of 25 °C, 35 °C, and 45 °C using axisymmetric pendant drop shape analysis (ADSA). We developed a dynamic numerical model accounting for the changes in properties at the CW–hydrocarbon interface owing to the swelling of the hydrocarbon drop (HD). This approach eliminates an error of about 36% arising from the assumption of a static boundary/volume in conventional methods. The results indicated that the IFT between CW and the hydrocarbon is a function of the CO_2 phase density and solubility. At low pressures (<60 bar, 25 °C), IFT is directly proportional to the pressure, while at pressures larger than 60 bar, it is inversely proportional to the pressure. The physical behaviour of the CW–hydrocarbon system is driven mainly by a balance between CO_2 solubility and IFT, resulting in a constant CO_2 saturation. Despite the decrease in CO_2 solubility with temperature, the diffusion coefficient of CO_2 increases. The reduction in IFT with temperature counteracts the decrease in CO_2 solubility, leading to a higher diffusion coefficient as temperature increases. It is shown here that the CW–hydrocarbon system induces more swelling and lower viscosity compared to similar systems but with pure CO_2. As such, CW's potential for enhanced oil recovery (EOR) is realised.

Keywords: carbonated water, diffusion coefficient, supercritical CO_2, interfacial tension

(Some figures may appear in colour only in the online journal)

1. Introduction

Carbonated water injection (CWI) has gained significance as an effective enhanced oil recovery (EOR) method and CO_2 sequestration method (Riazi *et al* 2011, Sohrabi *et al* 2011, Mosavat and Torabi 2014). Numerous studies have been carried out on CWI (Riazi *et al* 2009, Mosavat and Torabi 2014) regarding its oil recovery. However, few studies have investigated the property alteration of hydrocarbons, and CO_2 mass transfer from carbonated water (CW) to hydrocarbons at various pressures and temperatures (Teng and Yamasaki 1998, Farajzadeh *et al* 2007). Hence, there is a gap in understanding the physics during the CW–hydrocarbon interaction. Mass transfer, interfacial phenomena, and the diffusion of CO_2 into the hydrocarbon are fundamental in understanding CO_2 EOR mechanisms (Yang and Gu 2005, Sohrabi *et al* 2011).

Several previous studies developed various methods to estimate the diffusion coefficient of gases in bulk liquids; these methods may be broadly classified as compositional analysis methods (Sigmund 1976, Nguyen and Ali 1998) and pressure decay methods (Upreti and Mehrotra 2002, Sheikha *et al* 2005). Although these methods gave critical insight into the diffusion of various gases into bulk liquids, they are handicapped either experimentally or numerically. In the compositional analysis, the major concern is the extraction of the sample from the setup and carrying out gas chromatography, especially at high pressures and temperatures, which

[1] Author to whom any correspondence should be addressed.

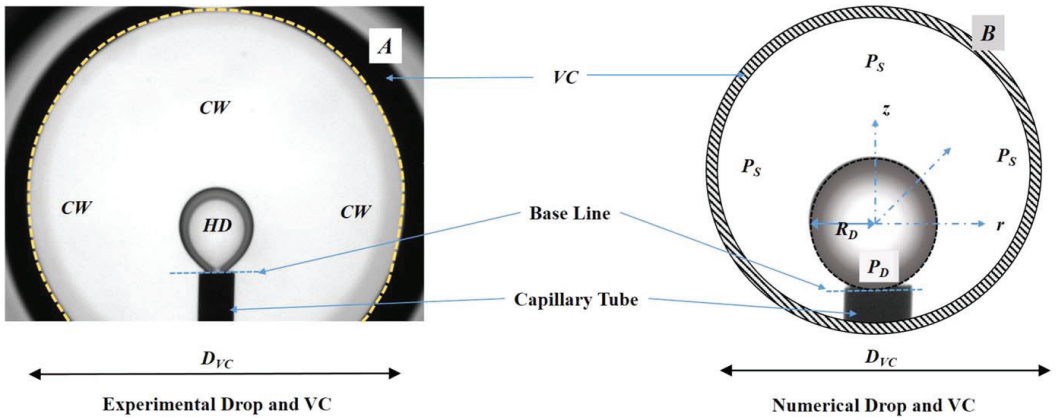

Figure 1. (1A) HD surrounded by CW in the high-pressure VC. (1B) Equivalent spherical HD surrounded by CW for numerical analysis.

may lead to error in diffusion coefficient calculation (Yang and Gu 2005). Furthermore, the compositional method is expensive, time-consuming, and tedious (Riazi 1996). Pressure decay methods avoid the extraction of samples seen in compositional analysis. Hence, it eliminates the error due to it. However, pressure decay methods demand a long experimental time (20 h to 100 h, or more) (Riazi 1996), and the diffusion coefficient obtained is not for a particular pressure but for a range of pressures (Yang and Gu 2005, Bagalkot and Hamouda 2017). Furthermore, for both compositional and pressure decay methods, for similar experimental conditions and fluids, the calculated diffusion coefficients are distinct (Bagalkot and Hamouda 2017). Hence, there is a need for a well-established, simple, and reliable method for estimating the diffusion coefficient of gases in liquids.

Recently, Yang and Gu (2005) developed a novel method of dynamic pendant drop volume analysis (DPDVA) using axisymmetric pendant drop shape analysis (ADSA) in conjunction with a computational scheme for measuring the gas diffusivity in liquids. The flexibility, simplicity, and lower computation time made DPDVA suitable for calculating the diffusion coefficient of gases into bulk liquids. The primary assumption of the DPDVA model is that the effects of a CO_2 mass transfer on the pendant hydrocarbon drop (HD) shape and volume (swelling) on the diffusion process are minimal. Hence, the volume of the liquid pendant drop is assumed constant, and the change in volume due to the diffusion of gases is neglected (Yang and Gu 2006), which indicates that the interface is assumed to be fixed (static). However, during the experiment, the diffusion of gases (for example CO_2) into the pendant drop liquid (hydrocarbons) would lead to an increase in the volume of the liquid pendant drop as a function of time. This indicates that the shape and size of the pendant drop, and thus also the position of the interface, will shift until an equilibrium is achieved. Hence, there is a difference between the numerical and experimental volume and interface position in the DPDVA. The assumption of constant liquid pendant drop volume or static interface is justified if there is an insignificant change in the pendant drop volume and interface position like in the CO_2–water system. However, when the change in volume is significant or even moderate, the assumption of constant volume would lead to error in determining the diffusion coefficient of gases into liquids. Riazi *et al* (2011) carried out a 1D simulation using COMSOL to demonstrate the changes in the interface for the CW–oil system. However, they used an empirical correlation to estimate the diffusion coefficient, and used the diffusion coefficient to simulate the changes in volume and the interface. Furthermore, the model was 1D, which is difficult to apply to real-life situations. In the present study, a novel approach was used to develop a numerical model to eliminate the need of assuming a constant volume. This model is capable of tracing the changes in properties at the interface with time in a 3D diffusion process.

The objective of the present study is to estimate the CO_2 diffusion coefficient from CW into n-decane and n-hexane at temperatures of 25 °C, 35 °C, and 45 °C and pressures between 10 and 100 bar. In this work, the dynamic changes made to the hydrocarbon densities as CO_2 diffuses are estimated, thus permitting the dynamic interfacial tension (IFT) to be calculated. To the best of our knowledge, the experimental and numerical approaches developed, specifically with the CW–hydrocarbon system, have not been previously addressed in the literature.

2. Theory of CO_2 mass transfer in a CW–hydrocarbon system

Figure 1(A) shows a snapshot of the see-through high-pressure visual chamber (VC) in which the experiments are carried out. The water surrounding the HD is saturated with CO_2 (CW), and the design of the setup ensures that saturation of CO_2 in water is always maintained. The solubility of CO_2 is greater in hydrocarbons compared to water, and hence when

the hydrocarbon contacts the CW, the CO_2 from the CW diffuses into the hydrocarbon pendant drop. Additionally, the mass transfer of CO_2 is fuelled by the difference in concentration in the hydrocarbon and the surrounding CW. Thus, the CO_2 mass transfer is from the CW into the HD and continues as long as the hydrocarbon is saturated with the CO_2 (until the concentration gradient is strong enough for the CO_2 mass transfer). Since the pressure, temperature, and saturation of the CO_2 in the surrounding water are kept constant during each experiment, it is justified to assume that the concentration of CO_2 in the surrounding phase (CW) of the hydrocarbon is always constant. The mass transfer of CO_2 into the hydrocarbon and its subsequent dissolution will lead to a certain alteration in the physical properties of the hydrocarbon and in the IFT, which is the focus of the study. A well-established ADSA technique is employed in the present work to understand and quantify the mass transfer of CO_2 from CW into n-decane (HD).

2.1. Physical system

Figure 1(B) shows the equivalent spherical HD surrounded by the CW used for the numerical analysis. In figure 1(B), P_D and P_S represent physical regions occupied by the HD phase and the surrounding phase (CW), respectively; r, z, and R_D represent the radius of the drop (radial coordinates), axial coordinates, and radius of the spherical drop, respectively; and D_{VC} represents the diameter of the cell. In this work, the following justifications were made in defining the diffusion of CO_2 from the surrounding CW into the HD phase. Firstly, the mass transport across the CW–HD interface is diffusive (concentration driven); this is accomplished by using a small volume of the pendant drop, thus eliminating density-driven convection (Yang and Gu 2005). Secondly, the experiments are carried out at a constant temperature, which minimises thermal convention (Yang and Gu 2005). Finally, no chemical reactions occur during the experiment so that the mechanisms of property changes are physical and thermodynamically driven processes.

2.2. Experiments and experimental setup

2.2.1. Material. The n-decane and n-hexane (Merck KGaA with 99% purity) hydrocarbons were used as the HD phase in this experimental work. CW with a CO_2 (Praxair) purity greater than 99.9% provided the surrounding phase. The NIST Chemistry Web Book (Linstrom and Mallard 2010) is the source of density and viscosity values at various pressures and temperatures for n-decane, n-hexane, and CO_2. The solubility of the CO_2, and thereby the density of fully saturated CW, was calculated using the model presented by Chang *et al* (1996).

2.2.2. Apparatus. The equipment used and the setup in the present work are similar to those employed by Bagalkot and Hamouda (2017). A schematic of the experimental setup is shown in figure 2. An external pump (maximum pressure of 32 MPa, Gilson) connected to a CO_2 cylinder maintains its pressure. The experimental method used in the present study is intended to measure the volume of the HD and the IFT in a completely automated manner devoid of any human interference.

In the experimental system, the VC was first filled with water (20 ml or 25 ml). The CO_2 was then injected into the VC at experimental pressure, and diffused into the water there. The pump continuously injected CO_2 into the VC until the water reached saturation (at the predetermined pressures and temperatures) and could accept no more of the gas. Experiments using a gas flow metre were carried out at various pressures at 25 °C to estimate the saturation level of CO_2 in the water surrounding the HD. The moles of CO_2 obtained at a particular pressure and temperature from the experiments were compared with the results from the model given by Duan and Sun (2003). It was confirmed that irrespective of pressure, the experimental result showed a 95%–98% saturation of CO_2 in water compared to the model results. It was thereby safe to assume that the water was saturated with CO_2. Once this occurred, an HD was released. The experimental procedure was as presented by Bagalkot and Hamouda (2017). With the temperature at 0 °C the accuracy of the temperature sensor change was ±0.1 °C and at 400 °C it was ±0.8 °C. The pressure sensor had an accuracy of ±0.1 MPa at both temperatures.

With the pressure (10–100 bar) and temperature (25 °C, 35 °C, and 45 °C) ranges used in this work, CO_2 may exist as a gas, as a liquid, or in a supercritical state. At 25 °C, the CO_2 will be in the gaseous state up to 64 bar, and a liquid above that. At 35 °C and 45 °C, the CO_2 will be in the gaseous state up to 73 bar, and in a supercritical state above that (Linstrom and Mallard 2010). The pressure where the phase change occurs will be represented by P_T in this article.

The IFT was estimated using the ADSA system (KRUSS DSA 100). Diffusion of CO_2 into the pendant drop (PD) alters the density of the PD, which is proportional to the mass of CO_2 transferred into the hydrocarbon (volume or mole fraction) (equation (7)). Therefore, for an accurate dynamic measurement of the IFT, the density of the drop with CO_2 was input in the DSA 100 software to account for the density change. The dynamic density of CO_2 (equation (7)) was accordingly used to obtain the dynamic IFT. The IFT estimation at 35 °C was not carried out in the present study, and for n-hexane the analysis was carried out until 70 bar. In the case of the CO_2–hydrocarbon system, the uncertainty with the measurement is about ±0.3 mN m^{-1}. If water is present, uncertainties rise to ±0.5 mN m^{-1}. The uncertainty is largely affected by the absolute value of the density difference, and increases as the density difference decreases (Jaeger and Eggers 2012).

2.3. Mathematical model

A series of mathematical equations are adopted (Yang and Gu 2005); they represent the mass transfer of CO_2 from CW into the PD. Fick's second law of diffusion represented by equation (1) adequately describes the diffusive mass transfer process of CO_2 across the interface to the HD. It may be seen from figure 1(B) that the pendant drop is symmetrical about the z-axis. It was therefore convenient to use a cylindrical

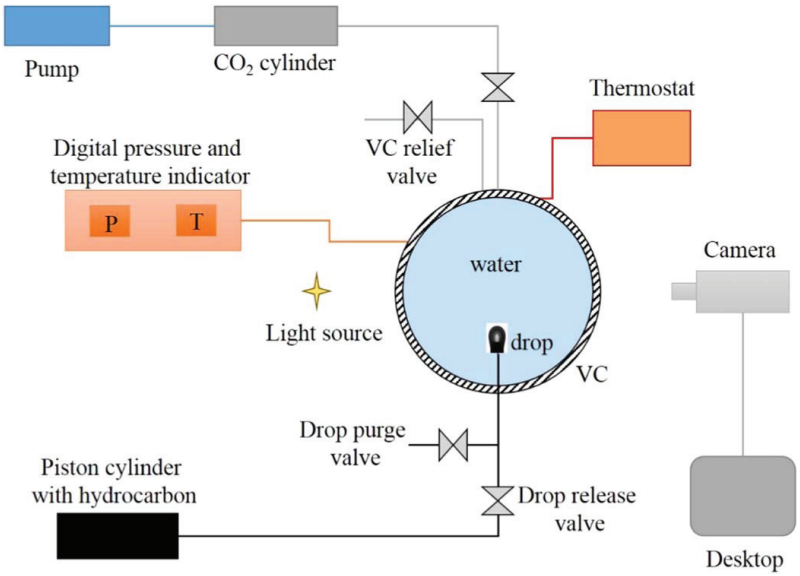

Figure 2. Schematic of the experimental setup.

coordinate system (r, θ) rather than a complicated 3D Cartesian coordinate system (x, y, and z):

$$\frac{\partial C}{\partial t} = D(t)\left\{\frac{1}{r}\frac{\partial C}{\partial r} + \frac{\partial^2 C}{\partial r^2} + \frac{\partial^2 C}{\partial z^2}\right\}, \tag{1}$$

where C is the concentration of CO_2 in the hydrocarbon pendant drop phase (kg m^{-3}) and $D(t)$ is the diffusion coefficient (m^2 s^{-1}). A detailed explanation of the boundary conditions for solving the equation (1) may be found in the study by Bagalkot and Hamouda (2017).

Equation (1) along with boundary and initial conditions are numerically solvable, allowing us to obtain the time- and space-dependent concentrations of CO_2 in the drop. A concentration ratio of the CO_2 concentration in the pendant drop (C_{avg}) was computed at predefined time steps using equation (2), which gives the total volume of CO_2 diffused in the pendant drop for a given time t.

$$C_{avg}(t) = \iint_{(r,z)\in P_d} \frac{C(r,z)}{C_o} r dr dz \tag{2}$$

The mass transfer of CO_2 into the HD leads to an increase in drop volume (swelling). The degree in swelling depends on the amount of CO_2 that diffuses into the HD. The parameter C_{avg}, which gives the volume of the CO_2 present in the drop, may be used to calculate the swelling factor (SF) as given in equation (3) (Bagalkot and Hamouda 2017). SF is defined as the ratio of the volume of the CO_2-saturated hydrocarbon (CO_2+ hydrocarbon) to the initial volume of pure hydrocarbon:

$$SF = 1 + \frac{\int_0^T \frac{[V_{\exp}(t) - V_o]C_{avg}(t)dt}{V_{\exp}(t)^2}}{\int_0^T \frac{[C_{avg}{}^2(t)]dt}{V_{\exp}(t)^2}}, \tag{3}$$

where $V_{exp}(t)$ is the experimentally obtained volume of HD at time t; T is the total experimental or simulation time; and V_o is the initial volume ($t = 0$) of the hydrocarbon pendant drop determined experimentally.

At a given time, the volume of the HD is the summation of the initial volume of the drop (V_o) and the increase in volume caused by the CO_2 diffused in the hydrocarbon. The increase in volume is represented by the product of C_{avg} and SF-1 (Yang and Gu 2005), as represented by equation (4).

$$V(t) = V_o + (SF - 1)\cdot C_{avg}(t) \tag{4}$$

An optimisation function (F) is developed, which uses the difference between the experimental ($V_{exp}(t)$) and numerical volume ($V(t)$) of the pendant drop at a given time t. The minimum of the optimisation function ($F_{\min}$) was used to obtain the diffusion coefficient of CO_2 in the hydrocarbon pendant drop from the CW (Yang and Gu 2005). The lower the $F_{\min}$, the nearer the numerical result to the experimental result.

$$F = \sqrt{\frac{1}{T}\int_0^T \frac{[V_{\exp}(t) - V(t)]^2\, dt}{V_{\exp}(t)^2}} * 100\% \tag{5}$$

It is evident from equation (5) that the optimisation function is dependent on numerical *V(t)* and experimental $V_{exp}(t)$ volume, and once the experimental volume data at different time steps has been obtained, *F* depends entirely on the numerical volume *V(t)*. Furthermore, *F* depends on the C_{avg}, and the *SF* (equations (2) and (3)) and C_{avg} are a function of the diffusion coefficient, indicating $F = f(D, SF)$. Therefore, *D* and *SF* may be used as parameters to obtain the minimum objective function ($F_{\min}$). The minimum objective function ($F_{\min}$) for *D* and *SF* are the measured CO_2 diffusion coefficient and oil-*SF*, respectively.

In the present work, the equation proposed by Herning and Zipperer (1936) was used to calculate the viscosity of the drop phase (CO_2 + hydrocarbon) at various time steps and at various CO_2 mole fractions. Viscosities obtained from equation (6) have an accuracy of 1.5% average deviation for hydrocarbon mixtures and 5% maximum deviation (Herning and Zipperer 1936).

$$\mu_{drop} = \left(\frac{(\mu_{co_2} \cdot x_{co_2} \cdot \sqrt{M_{co_2}}) + (\mu_{HC} \cdot x_{HC} \cdot \sqrt{M_{HC}})}{(x_{co_2} \cdot \sqrt{M_{co_2}}) + (x_{HC} \cdot \sqrt{M_{HC}})} \right)_{P,T}, \tag{6}$$

where μ_{CO2} and μ_{HC} (cP) are the CO_2 and hydrocarbon viscosities at a given pressure and temperature, respectively; x_{CO2} and x_{HC} are mole fractions of CO_2 and the hydrocarbon, respectively, at a given pressure and temperature; and M_{CO2} and M_{HC} are molecular weights of CO_2 and the hydrocarbon, respectively, at a given pressure and temperature.

The estimated dynamic (a function of time) x_{CO2} and x_{HC} may be further used to obtain the density of the binary mixture (ρ_{PD}) for each experimental time step using equation (7) (McBride-Wright *et al* 2014, Kandil *et al* 2016, Zambrano *et al* 2016).

$$\rho_{drop} = ((x_{CO_2} \cdot \rho_{CO_2}) + (x_{HC} \cdot \rho_{HC}))_{P,T}, \tag{7}$$

where ρ_{CO2} and ρ_{HC} are the individual densities of CO_2 and the hydrocarbon in the drop, respectively, at a given pressure and temperature.

2.4. Numerical model

The numerical model and method employed in the present study to obtain the effective diffusion coefficient were adopted from the study by Bagalkot and Hamouda (2017). A spherical HD was considered for the numerical analysis instead of the actual shape of the pendant drop. Figure 1(B) shows the equivalent spherical drop surrounded by the CO_2 used for the numerical analysis. In figure 1(B), *R* is the radius of the spherical drop. The radius obtained from the experimental volume was used to obtain the surface area and volume of the equivalent drop for numerical analysis. The surface area defines the rate of diffusion; hence, it was used as the comparison parameter between the pendant drop (experimental) and spherical drop (numerical). An error of 3%–6% was found depending on the pressure of the system between the experimental and numerical drop surface areas (Bagalkot and Hamouda 2017). Therefore, it is justified to use a spherical drop instead of the actual pendant shape. Furthermore, the assumption of a spherical drop reduces the method's complexity while maintaining minimal error in the estimation of the diffusion coefficient. A major change in the inclusion of the dynamic nature of the CW–hydrocarbon interface was realized by employing a moving boundary.

2.4.1. Inclusion of the dynamic interface method in the numerical model.

As noted from equations (3) and (4) the diffusion coefficient depends on both experimental (dynamic volume data, V_{exp}) and numerical (C_{avg}) data. From equation (3), it is clear that the calculation of the volumetric average of CO_2 in the drop (C_{avg}) is a function of the radius or volume of the drop. Most previous studies assumed a quasi-static nature for the CO_2 source–hydrocarbon interface (Yang and Gu 2005, Yang and Gu 2006, Bagalkot and Hamouda 2017). According to our knowledge, there are no articles that have attempted to include the effect of a dynamic interface for a 3D system. In figure 1(B), R_D represents the radius of the HD, and the interface should always be positioned at the R_D. If the HD volume increases, the R_D increases, and the position of the interface changes accordingly so that it is at the new R_D; this is possible when the dynamic interface option is adopted in the model. However, if the interface of the drop (boundary) is considered static, then the interface would not change its position according to the new R_D and would always remain at the initial position of R_D. This could lead to a discrepancy between numerical and experimental input into the model, resulting in an error in the calculation of the diffusion coefficient.

In the present study, a simple method was developed to incorporate the dynamic nature of the CW–hydrocarbon interface (boundary). The following steps were undertaken to realize this.

(i) Initially ($t = 0$), a fixed number of grids are assigned to r (*N*) and z (*M*) directions.
(ii) The volume of the drop is calculated from equation (4) at different time intervals.
(iii) At each time interval, the volume (*V(t)*) is compared with the previous (*V(t-1)*), and the difference between them is obtained (*V(t)-V(t-1)*).
(iv) The difference in the volume of the drop (*V(t)-V(t-1)*) is then converted to increments in the radius of the hydrocarbon pendant drop (Δr), which in turn gives the radial distance moved by the interface.
(v) The increment of the radius is then translated to the increment in the number of grids in *r (n)* and *z (m)* directions, and is added to the total number of grids in the previous time level (*N*, *M*) to obtain the updated number of grids (N_{new}, M_{new}).
(vi) The new or updated grids are used to solve the set of equations. This process is repeated for every time level and for every D_i input.

Table 1 compares the diffusion coefficients and C_{avg} values for the cases, taking into account the dynamic and static interfaces (25 °C, CW–decane system) for different

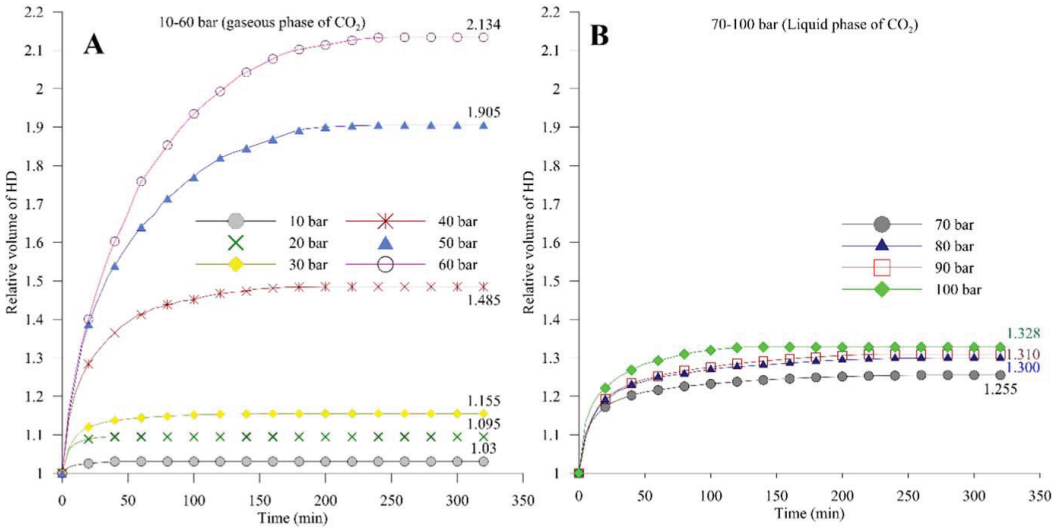

Figure 3. Change in volume (relative) of the n-decane (HD) for (3A) 10–60 bar (gaseous CO_2 region) and (3B) 70–100 bar (liquid CO_2 region) at 25 °C.

Table 1. Diffusion coefficient data for fixed and moving interface methods.

		Diffusion coefficient (10^{-9} m^2 min^{-1})		
Pressure (bar)	Volume ratio ($V_{final}/V_{initial}$)	Static interface method	Dynamic interface method	% change in the D_{CO2} from static to dynamic interface
10	1.031	5.3251	5.4234	2.015
30	1.155	2.2116	2.5392	14.812
60	2.134	0.5934	0.8073	36.045

pressures (or different volume increases). It may be noted from table 1 that the error caused by the fixed interface assumption is small (2%) at low pressures when the volume increase is small. However, the error escalates exponentially as the pressure increases. The percentage error increases from 2% at 10 bar to approximately 36% at 60 bar. Therefore, it is clear that, even with a moderate volume increase, errors larger than 15% occur. This makes it important to include the effect of the dynamic interface when calculating changes in HD properties.

3. Results and discussions

3.1. Analysis of the HD volume

Figure 3 presents the relative volume of the HD as a function of time at 25 °C, showing the nature and magnitude of the swelling. Figure 3(A) presents the relative volume at pressures of 10–60 bar (gaseous CO_2), while figure 3(B) shows it at pressures of 70–100 bar (liquid CO_2). It may be observed from figure 3(A) that, for all experimental pressures, there is an initial rapid increase in the volume of the HD followed by a gradual increase until the equilibrium volume is reached. The observed profile of the volume with time may be attributed to the variation in the CO_2 concentration gradient at the interface between CW and the HD (n-decane). This is the driving force for the mass transfer of CO_2 into and towards the centre of the HD. The concentration gradient reduces with the increase in CO_2 mass transfer until an equilibrium is attained.

Similar observations to those made in figure 3(A) apply to figure 3(B), where the CO_2 is in the liquid phase at 25 °C and has a density similar to n-decane. However, the major difference among figures 3(A) and (B) is that the total increase in the relative volume is 1.255 at 70 bar, compared with 2.134 at 60 bar, thus indicating a considerable reduction in the increment of HD volume. Above 70 bar, a small and gradual rise in the swelling is observed until 100 bar is reached. A significant change in CO_2 density occurs over a pressure range of 10–60 bar (figure 3(A)) (gaseous CO_2) compared with 70–100 bar (liquid CO_2) (figure 3(B)). The increase in density (60 to 70 bar for CO_2 is about 290% (0.191 g ml^{-1} to 0.743 g ml^{-1})) alters the composition and intermolecular interaction between the molecules present in the HD (n-decane + CO_2). With the gaseous CO_2 ($P < P_T$), the CO_2 molecules in the HD are spread out. However, for

Table 2. Mole fraction of CO_2 in the n-decane and n-hexane HDs at experimental conditions.

	Mole fraction of CO_2 in the HD					
	Decane			Hexane		
Pressure (bar)	T = 25 °C	T = 35 °C	T = 45 °C	T = 25 °C	T = 35 °C	T = 45 °C
10	0.0033	0.0013	0.0014	0.0041	0.0017	0.0023
20	0.0165	0.0081	0.0086	0.0205	0.0098	0.0126
30	0.0422	0.0327	0.026	0.0531	0.0333	0.0368
40	0.1671	0.0795	0.044	0.2138	0.1015	0.0907
50	0.3808	0.209	0.1068	0.4596	0.2311	0.1856
60	0.5891	0.4581	0.1618	0.6252	0.51	0.3352
70	0.4521	0.5721	0.3192	0.4785	0.6713	0.5522
80	0.4608	0.3456	0.179		0.4578	0.3252
90	0.4747		0.1834			
100	0.5071		0.1889			

liquid CO_2 ($P > P_T$), the molecule-spreading in the HD is confined, and molecules are closer to each other than for when the CO_2 is in the gaseous phase; this indicates a lower intermolecular force for pressures $P < P_T$ compared to $P > P_T$. Yang *et al* (Yang 2013) explained that there would be a higher and easier mass transfer of CO_2 into the hydrocarbon if the intermolecular force is lower. The observation and given explanation may be further verified by observing the equilibrium mole fraction of CO_2 in the HD at various pressures and temperatures presented in table 2. In table 2, the data presented in the grey, blue, and brown boxes represent the CO_2 gaseous, liquid, and supercritical pressure regions, respectively. It may be noted that the mole fraction of CO_2 in the HD at 25 °C increases with pressures up to 60 bar ($P < P_T$), indicating an enhanced mass transfer. Similar to volume (figure 3(B)), the transferred mole fraction of CO_2 decreases significantly when the pressure changes from 60 to 70 bar, indicating a reduced mass transfer of CO_2 due to an increased intermolecular force. As the pressure increases above 70 bar (to 100 bar), the mole fraction of CO_2 in the drop is approximately constant with a minimal increment up to 100 bar.

Figure 4 illustrates the influence of the temperature on the evolution of n-decane HD at 25 °C, 35 °C, and 45 °C at 40 bar. A drop in the equilibrium volume upon raising the temperature is observed from figure 4, and may be credited to a reduction in the solubility of CO_2 in liquids with increases in temperature. The reduction in solubility leads to a reduced CO_2 mass transfer from CW to the HD, as observed in table 2. Interestingly, unlike equilibrium volume, the temperature has an opposite effect on the equilibrium time (time required to attain equilibrium volume, indicated by a vertical dashed line), with equilibrium time being lesser with the rise in temperature. As the temperature is raised, the viscosity of the hydrocarbon decreases, and the kinetic energy of the molecules increases. These factors may enhance the CO_2 mass transfer rate, wherein there will be a greater driving force for the CO_2 to transport into the HD from CW. Thus, at isobaric conditions the increment in temperature reduces the total mass transfer of CO_2 into HD (less swelling); however, the rate of mass transfer increases, indicating a higher rate of diffusion.

Figure 5 compares the swelling of the HD comprising n-hexane and n-decane at 45 °C and pressures of 10, 30, and 50 bar. The n-hexane HD experiences a greater total increase in volume over n-decane of about 22% (1.301 for the decane and 1.668 for the hexane HD) and 10% (1.102 for the decane and 1.223 for the hexane HD) at 50 and 30 bar, respectively. The enhanced swelling of n-hexane HD reflects lower intermolecular forces and a reduced viscosity compared with the n-decane HD so that the CO_2 mass transfer into n-hexane HD is higher (Yang *et al* 2013). It can also be seen from figure 5 that the volume profile for the hexane HD during the initial period (0–50 min depending on the pressure) has a higher slope than the decane HD, indicating a faster increase in volume for the hexane + CO_2 HD than for the decane + CO_2 HD. The CO_2 diffusion coefficient is thereby larger for the n-hexane HD than for the n-decane HD (this will be studied in a later section).

Table 3 shows the relative equilibrium volume of the n-decane pendant drop for the CO_2–n-decane system (Bagalkot and Hamouda 2017) and CW–n-decane system carried out in a similar experimental setup and experimental conditions (30, 40, and 50 bar at 25 °C). It is evident from table 3 that even at low pressures (30 bar) there was a 7.44% increase in the volume of the hydrocarbon, and this changes exponentially with pressure reaching approximately 50% at 50 bar. This may demonstrate the potential of using CW injection for EOR. It could be highly significant for combined CW injection and CO_2 sequestration since standalone carbon capture and storage (CCS) is not impressive from a financial perspective (Li *et al* 2016). CWI combined with CCS would be both economic (improved recovery) and more efficient for sequestering CO_2.

3.2. Analysis of the density and viscosity of the HD

In the following figures, the depicted changes in the viscosity and density are from the beginning of the CO_2 mass transfer (time $t = 0$) when the HD consists of 100% hydrocarbon to

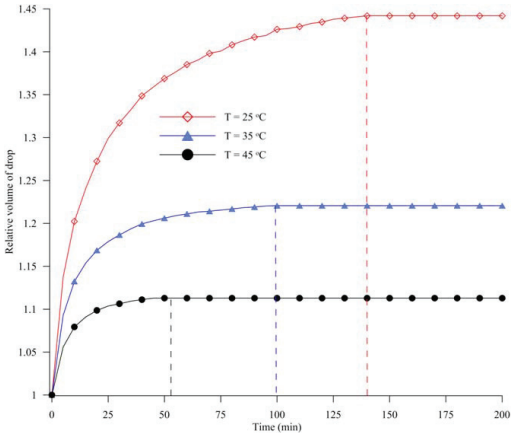

Figure 4. Dynamic relative volume of the n-decane HD at 40 bar and for 25 °C, 35 °C, and 45 °C.

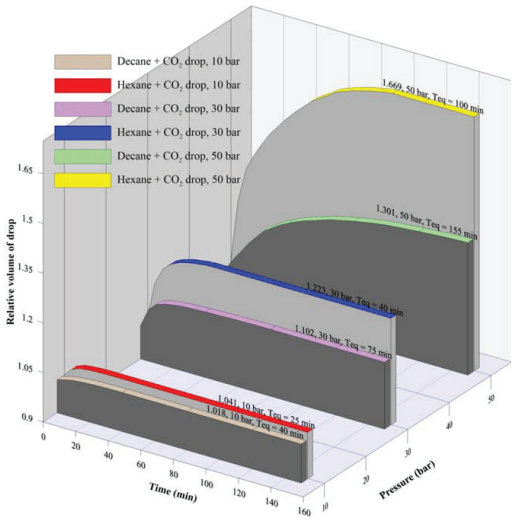

Figure 5. Dynamic n-decane and n-hexane HD volume (relative) at 10, 30, and 50 bar at 45 °C.

the end of CO_2 mass transfer (t = equilibrium time) (HD is saturated with CO_2).

Figure 6 shows the density changes in the HD comprising n-decane owing to CO_2 diffusion at 25 °C, 35 °C, and 45 °C, at pressures of 0–100 bar. The negative sign in figure 6 indicates a density reduction from the initial value, and vice versa. For pressures up to P_T (indicated by vertical dashed lines) the density of the HD decreases, and the reduction in the density increases as the pressure increases. As CO_2 diffuses into the n-decane, a binary mixture of CO_2 and n-decane is formed in HD, and the density of the binary mixture is a function of the volume fraction and molecular

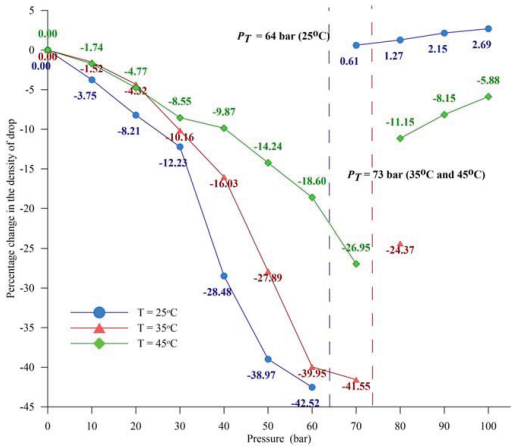

Figure 6. Percentage change in the density of the n-decane HD for a pressure range of 0–100 bar at 25 °C, 35 °C, and 45 °C.

Table 3. Comparison of equilibrium volume for the CO_2–decane (Bagalkot and Hamouda 2017) and CW–decane (present work) systems at 25 °C.

Pressure (bar)	Relative equilibrium volume (swelling)		% increase in swelling in CW–decane system
	CO_2–decane	CW–decane	
30	1.075	1.155	7.44
40	1.185	1.485	25.32
50	1.271	1.905	49.882

weight of both CO_2 and n-decane (equation (7)). As the low-density gaseous CO_2 ($P < P_T$ at 25 °C) mixes with relatively high-density n-decane, the density of the binary mixture is reduced. Additionally, from table 2 it may be noted that the mole fraction of CO_2 in the HD increases up to P_T, indicating a greater CO_2 mass transfer as pressure increases, leading to an enhanced dilution of n-decane. However, when the pressure is raised beyond P_T, a significant increase in the density of the HD is observed and may be credited to the change in the density of the CO_2 at $P > P_T$. The density of CO_2 surges from 0.191 g ml^{-1} at 60 bar (gaseous CO_2) to 0.743 g ml^{-1} at 70 bar (liquid CO_2), which is above the density of pure n-decane at 70 bar, 25 °C (0.732 g ml^{-1}). Thus, for $P > P_T$ the denser CO_2 mixes with n-decane, and the resulting binary mixture has a higher density than n-decane. The increase in the density of the HD continues as pressure is raised from 70–100 bar. However, the increase in the density at this pressure rage (70–100 bar) is not as sharp as the observed decrease in density for below $P < P_T$. A similar observation is shown in table 2.

In addition to the percentage change in the density of the n-decane HD at 25 °C, figure 6 shows the data at 35 °C and

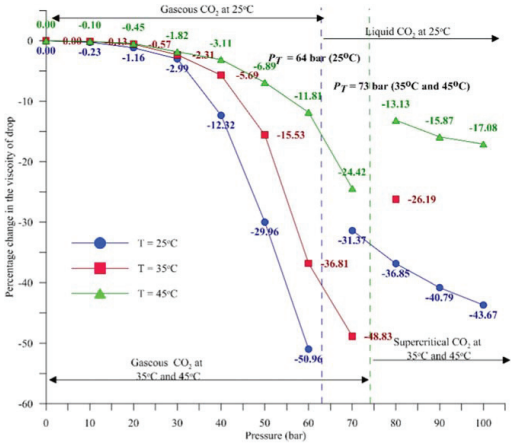

Figure 7. Percentage change in the viscosity of the n-decane HD for a pressure range from 0–100 bar and at 25 °C, 35 °C, and 45 °C.

45 °C. Even though the trend is similar at all experimental temperatures, two notable differences may be identified. First, the reduction in the HD density is inversely proportional to the temperature. At isobaric conditions, the n-decane HD density reduction slows as temperature rises from 25 °C to 45 °C in the 0–60 bar pressure range ($P < P_T$) for CO_2. This observation is similar to the one discussed earlier on volume analysis (figure 4 and table 2), and may be attributed to a reduction in CO_2 mass transfer owing to a decline in CO_2 solubility as the temperature rises. Secondly, the density variation is different above the P_T between 25 °C and 35 °C/45 °C. An increase in HD density occurs above P_T (0.61% to 2.69%) at 25 °C. However, at 35 °C (−24%) and 45 °C (−11.15% to −5.88%) a reduction in HD density takes place. At 35 °C and 45 °C for $P > P_T$, CO_2 is in the supercritical phase. The density of supercritical CO_2 is lower than those of liquid CO_2 and n-decane (for a given pressure and time). As a result, the HD density is reduced.

Figure 7 shows the percentage change in the viscosity of n-decane HD at 25 °C, 35 °C, and 45 °C and for pressures of 0–100 bar. As with density (figure 6), the viscosity change for the HD is dependent on the CO_2 phase. For pressures up to P_T, HD viscosity reduces owing to the CO_2 mass transfer. Viscosity behaviour deviates from the normal trend at $P > P_T$, and the reduction in viscosity diminishes significantly for $P > P_T$ and may be attributed to the change in the CO_2 phase across P_T. At 25 °C, CO_2 viscosity increases from 0.0183 cP at 60 bar to 0.0616 cP at 70 bar, which represents an increase of about 236% compared with just about 10% from 50–60 bar. As pressure is increased above 70 bar, the reduction in the viscosity of the n-decane HD increases (−31.37% at 70 bar to −43.67% at 100 bar), indicating a return to the normal trend.

To analyse the influence of temperature on viscosity changes, figure 7 also includes the percentage change in viscosity of HD at 35 °C and 45 °C. It may be observed that, at isobaric conditions, the rise in temperature has a negative effect on the reduction in viscosity; this is similar to the observation for the change in density (figure 6). The inverse relationship of the viscosity reduction with temperature reflects a decline in CO_2 solubility as temperature rises. A similar inverse relationship was observed by Barclay and Mishra (2016).

3.3. Analysis of the IFT of the CW–HD

Figure 8 shows the variation of the IFT with time for the CW–n-decane system at 25 °C, for 10–60 bar (figure 8(A), gaseous CO_2) and 70–100 bar, (figure 8(B)) (liquid CO_2). In figure 8(A), at isobaric conditions, the IFT increases with time, reaching a value greater than the initial value. This was not observed in the CO_2–hydrocarbon (Bagalkot and Hamouda 2017, Honarvar *et al* 2017), where the IFT decreased with time. The observed increment in the IFT with time (figure 8(A)) may be due to the density variations in CW and n-decane. The dissolution of CO_2 into water increases the density of water (CW) (Farajzadeh *et al* 2007), whereas dissolution of CO_2 in light hydrocarbons decreases the density; this would result in an increased density difference, which is also observed in figure 6. The IFT is directly proportional to the density difference (Ghorbani and Mohammadi 2017, Honarvar *et al* 2017). Interestingly, an opposite trend is observed in figure 8(B) for the pressure range of 70–100 bar: the IFT decreases with time such that the equilibrium IFT is lower than the initial value. The results from figure 6 (for 70–100 bar) indicate a reduction in the density difference, and hence the observed reduction in the IFT with time (figure 8(B)). A similar result for CW–crude oil was observed by Honarvar *et al* (2017) for a pressure range of 70–100 bar (supercritical CO_2).

Figure 9 presents the equilibrium IFT and density difference between CW and the HD for pressures of 10–100 bar at 25 °C and 45 °C for the CW–decane system. First, the analysis will be carried out at isothermal conditions (25 °C); in the next paragraph, the influence of the temperature (25 °C and 45 °C) will be discussed. It may be observed from figure 9(A) that at 25 °C for $P < P_T$, the variation of the equilibrium IFT increases with pressure. This behaviour is similar to a water–n-decane system, where a linear and direct relationship between the IFT and pressures up to 3000 bar at various temperatures was observed (Jennings 1967, Wiegand and Franck 1994). However, for $P > P_T$ the relation between the equilibrium IFT and pressure deviates from that of the water–n-decane system: above P_T the equilibrium IFT decreases with an increase in pressure, as observed from figure 9(A). Hence, the dissolution of liquid CO_2 (high-density CO_2 at 25 °C) in water reduces the IFT of the water–n-decane system (Jennings 1967, Wiegand and Franck 1994). Furthermore, it may be observed from figures 9(A) and (B) that both the equilibrium IFT and density difference initially increase as pressure increases for 0–60 bar; this is followed by a substantial reduction between 60–70 bar, and a gradual decrease until 100 bar. The similarity in the behaviour of the equilibrium IFT and density difference with pressure may

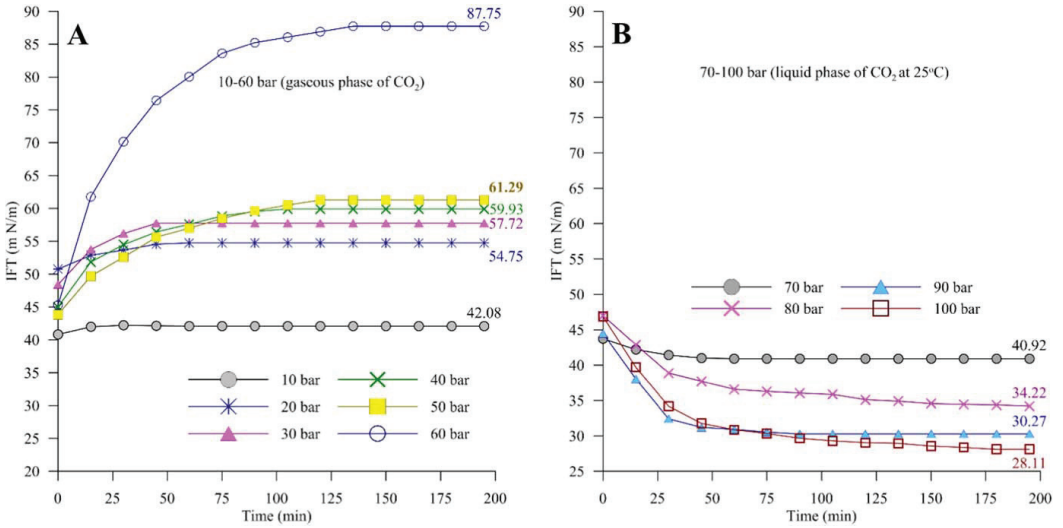

Figure 8. Dynamic change in the IFT of the n-decane HD for (8A) 10–60 bar (gaseous CO_2 region) and (8B) 70–100 bar (liquid CO_2 region) at 25 °C.

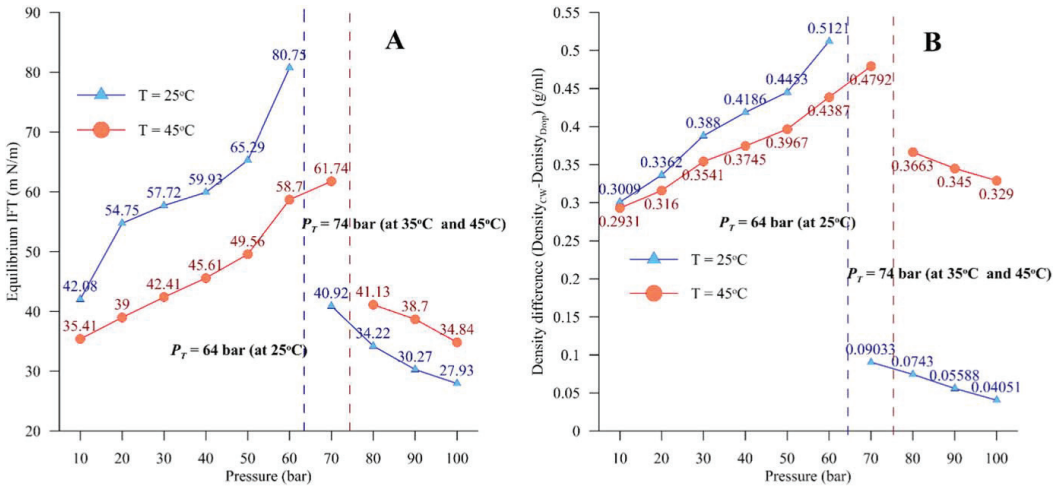

Figure 9. (9A) Equilibrium IFT and (9B) density difference at 25 °C and 45 °C for n-decane HD for a pressure range of 10–100 bar.

validate the discussion presented in figure 8 that density difference controls the equilibrium IFT.

Regardless of temperature (25 °C and 45 °C), in figure 9(A) the general trend of the equilibrium IFT with pressure is similar to that discussed in figures 8 and 9. It may be observed in figure 9(A) that for isobaric conditions increasing the temperature reduces the IFT. The kinetic energy and mobility of the molecules (entropy) of the HD (CO_2 + n-decane) increases with the rise in temperature, thus increasing the total energy of the interface of the CW and HD (Honarvar *et al* 2017). The increment in the total energy would reduce the Gibbs free energy, resulting in the reduction of the IFT (Honarvar *et al* 2017). Additionally, at 45 °C there is a lower mass transfer of CO_2 in the HD (table 2) compared to at 25 °C, leading to a smaller reduction in the density of the HD (figure 6), and hence a lower density difference and lower IFT. However, for $P > P_T$, the equilibrium IFT of 45 °C is greater than 25 °C. The density difference for 45 °C is greater than that at 25 °C, which could be due to the different phases of CO_2 (liquid at 25 °C and supercritical at 45 °C). Hence, the influence of the density is more than the influence of kinetic energy.

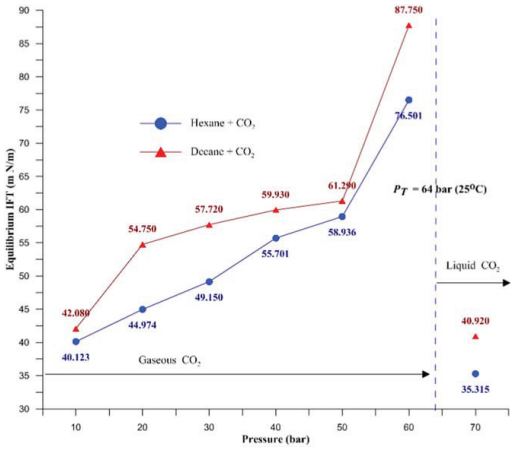

Figure 10. Diffusion coefficient for n-decane HD at 25 °C, 35 °C, and 45 °C for a pressure range of 10–100 bar.

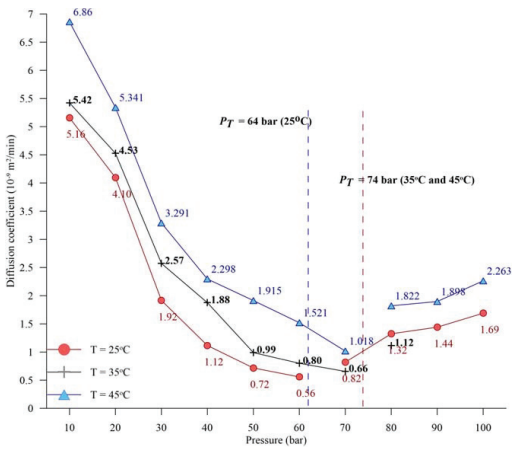

Figure 11. Diffusion coefficient for n-decane and n-hexane HDs at 25 °C, and for a pressure range of 10–70 bar.

Figure 10 shows the equilibrium IFT for the n-decane and n-hexane HDs at 25 °C and with a pressure range of 10–70 bar. For the CW–hexane system above 70 bar, the DSA software fails to recognise the interface, and hence does not estimate the IFT. This is due to the lower contrast between the drop and environment. It is observed from figure 10 that the variation in the equilibrium IFT with pressure is similar to that of the CW–decane system (figure 9). The CW–decane and CW–hexane systems behave similarly with pressure and temperature. However, the equilibrium IFT is lower for the CW–hexane system than for the CW–decane, indicating lower resistance to CO_2 mass transfer across the interface for the CW–hexane system. Because the molecular mass of n-hexane is lower than n-decane, the intermolecular force governed by the London force operating among n-hexane molecules will also be smaller. A smaller intermolecular force indicates a lower IFT, and thereby a lower equilibrium IFT observed for n-hexane.

3.4. Analysis of diffusion coefficient

Figure 10 shows the estimated effective diffusion coefficient of CO_2 in the n-decane system at three temperatures (25 °C, 35 °C, and 45 °C) and pressure range from 10–100 bar. It may be observed from figure 10 that the diffusion coefficient decreases as pressure increases for $P < P_T$, where the CO_2 exists in the gas phase and increases with pressure for $P > P_T$ (liquid CO_2). From figures 8 and 9 it was observed that the equilibrium IFT increases with the pressure (for $P < P_T$), indicating an increase in resistance to the rate of mass transfer of CO_2 from CW into the hydrocarbon. This may explain the observed reduction in the diffusion coefficient (figure 10) as pressure increases. However, the role of CO_2 solubility on the diffusion coefficient cannot be disregarded. It may be recalled from the discussion of figure 8 that the CO_2 solubility reduces the density of the hydrocarbon (n-decane), and hence the

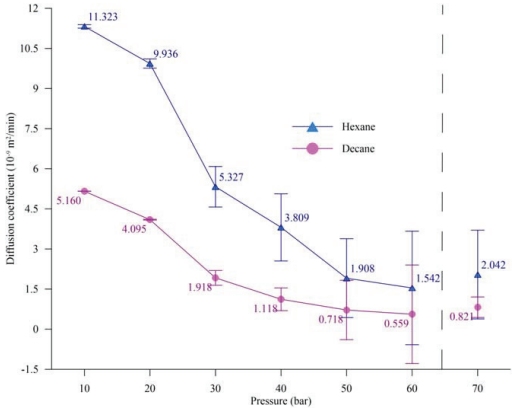

Figure 12. Equilibrium IFT for the CW–decane and CW–hexane systems at 25 °C and pressures of 10–70 bar.

density difference across the interface increases. This in turn would reduce the IFT. At $P > P_T$ (figure 10) the diffusion coefficient increases almost linearly with pressure. Accordingly, at $P > P_T$ the IFT decreases with the pressure.

Figure 10 also depicts the influence of temperature on the effective diffusion coefficient of CO_2 in n-decane from CW, at 35 °C and 45 °C. It also shows that the diffusion coefficient of CO_2 into the HD containing n-decane increases with increasing temperature (25 °C to 45 °C). At first glance, this seems to contradict our earlier discussion, where the CO_2 solubility decreased with temperature. However, the IFT decreases as temperature increases, i.e. enhances the CO_2 mass transfer.

The CO_2 diffusion coefficient in n-decane and n-hexane at different pressures (10–70 bar) and at 25 °C is plotted in figure 11. The variation of the CO_2 diffusion coefficient with pressure for the CW–hexane system is similar to that

Table 4. Comparison of measured diffusion coefficients and IFTs for different CO_2–liquid systems at different pressure ranges and temperatures.

System	Method	Pressure (bar)	Temperature (°C)	Diffusion coefficient (10^{-9} m^2 s^{-1})	IFT (m N m^{-1})
CO_2–brine (Yang *et al* 2006)	ADSA	18.8–47	27 °C	0.45–1.0	58–36
CO_2–decane (Bagalkot and Hamouda 2017) (25 °C)	ADSA	30–50	25 °C	1.175–1.75	14.32–4.5
CO_2–crude oil (Yang and Gu 2008)	ADSA	3.2–43.9	27 °C	0.47–2.49	25–12
CO_2–water (Unver and Himmelblau 1964)	Laminar falling jet	1	25 °C	1.95	—
CW–decane (present study)	ADSA	10–60	25 °C	0.0683–0.0169	42–80.75

observed in the CW–decane system (figure 10). The difference between the CW–decane and CW–hexane system lies in the magnitude of the diffusion coefficient, with that for CO_2 being higher for the CW–hexane system than for the CW–decane system. Because of the lower intermolecular force, CO_2 mass transfer into an n-hexane HD is easier than with n-decane. From figure 12 it may be observed that the IFT is lower for the CW–hexane system than for CW–decane at a given pressure and temperature. The combined influence of a lower intermolecular force and lower IFT may therefore be attributed to the higher CO_2 diffusion coefficient in the n-hexane HD than in the n-decane HD. Furthermore, analysis of figure 7 concluded that the equilibrium volume is achieved in a shorter time for the n-hexane HD than for the n-decane HD. This indicates a faster rate of mass transfer for the n-hexane HD. Figure 11 shows the error bar for the effective diffusion coefficient of CO_2. For both CW–hexane and CW–decane systems the error increases with pressure up to 60 bar and then decreases at 70 bar; however, the highest error is observed at pressures near the phase change pressure (P_T). For the CW–hexane system the error increases from 0.015% at 10 bar to 7.5% at 60 bar, and decreases to 1.5% at 70 bar; for the CW–decane system it increases from 0.25% at 10 bar to 8.5% at 60 bar, and decreases to 6.3% at 70 bar.

Table 4 compares the effective CO_2 diffusion coefficients and IFT of the present study (CW–decane) with those published in the literature for CO_2–reservoir brine (Yang *et al* 2006), CO_2–decane (Bagalkot and Hamouda 2017), CO_2–crude oil (Yang and Gu 2008), and CO_2–water (Unver and Himmelblau 1964). Except for one, all the literature employ ADSA, hence allowing easy comparison. It may be observed that the estimated diffusion coefficient of CO_2 in decane in the present study for the CW–decane system is approximately one order of magnitude lower ($0.06–0.016\ m^2\ min^{-1}$) than that of other studies for CO_2–liquid systems (CO_2–brine/decane/water/crude oil). The lower CO_2 mass transfer (diffusion coefficient) across the interface for the CW–decane system compared to the CO_2–liquid system may be attributed to the higher IFT, as observed in table 4. However, among the CO_2–liquid systems, the IFT and diffusion coefficients are comparable. Additionally, for the CW–decane system the IFT increases with pressure (similar to the water–decane system) and the diffusion coefficient decreases with pressure, which is in contrast to the CO_2–liquid system.

4. Conclusions

Experimental and numerical approaches were used in the present study to address the parameters that may influence the CW injection process for pressure and temperature ranges covering gas, liquid, and supercritical phase transitions for CO_2. The outcome of the numerical model developed made it possible to track the changes in properties owing to the swelling at the CW interface as a function of time (dynamic IFT). Dynamic IFT eliminates errors (up to 36%) arising from the assumption of constant volume/properties. A compositional model combining experimental data was developed and used to calculate the diffused CO_2 mass into HDs (comprising of n-decane or n-hexane) as a function of time.

At pressures below P_T, CO_2 solubility is a dominant factor in altering hydrocarbon properties. For $P < P_T$ (gaseous CO_2), the IFT showed a direct relationship with pressure; meanwhile, at $P > P_T$ (liquid/supercritical CO_2 phases), the IFT was inversely proportional to the pressure. The results from the numerical model showed that the diffusion coefficient was a function of the IFT and CO_2 solubility, with the IFT being the major contributor.

The CW–hexane system (lighter hydrocarbon) showed a lower IFT than CW–decane. This may be explained by the relatively higher solubility of CO_2, lower intermolecular force between the hydrocarbon's molecules, and hence lower viscosity for the lighter hydrocarbon. The lower IFT and intermolecular forces related to CW–hexane lead to a higher CO_2 diffusion coefficient in hexane compared to that in decane for a given pressure and temperature. Additionally the lower intermolecular force and reduced viscosity for hexane compared to decane lead to additional CO_2 mass transfer and hence swelling. Furthermore, the volume profile for the hexane HD during the initial period (0–50 min depending on the pressure) had a higher slope than the decane HD, indicating a faster increase in volume (swelling).

From the HD volume analysis, it was concluded that swelling and viscosity reduction was greater for the CW–decane system compared with CO_2–decane, indicating that CW may be a better displacing fluid for hydrocarbon recovery. At 50 bar, about 50% more swelling was observed for the CW–decane system compared with the CO_2–decane.

ORCID iDs

Nikhil Bagalkot https://orcid.org/0000-0002-2420-2622
Aly A Hamouda https://orcid.org/0000-0002-8457-1892

References

Bagalkot N and Hamouda A A 2017 Experimental and numerical method for estimating diffusion coefficient of the carbon dioxide into light components *Ind. Eng. Chem. Res.* **56** 2359–74

Barclay T H and Mishra S 2016 New correlations for CO_2-oil solubility and viscosity reduction for light oils *J. Pet. Explor. Prod. Technol.* **6** 815–23

Chang Y-B, Coats B K and Nolen J S 1996 A compositional model for CO_2 floods including CO_2 solubility in water *Permian Basin Oil and Gas Recovery Conf.* (Society of Petroleum Engineers)

Duan Z and Sun R 2003 An improved model calculating CO_2 solubility in pure water and aqueous NaCl solutions from 273 to 533 K and from 0 to 2000 bar *Chem. Geol.* **193** 257–71

Farajzadeh R, Salimi H, Zitha P L and Bruining H 2007 Numerical simulation of density-driven natural convection in porous media with application for CO_2 injection projects *Int. J. Heat Mass Transfer* **50** 5054–64

Ghorbani M and Mohammadi A H 2017 Effects of temperature, pressure and fluid composition on hydrocarbon gas-oil interfacial tension (IFT): an experimental study using ADSA

image analysis of pendant drop test method *J. Mol. Liq.* **227** 318–23
Herning F and Zipperer L 1936 Calculation of the viscosity of technical gas mixtures from the viscosity of individual gases *Gas u. Wasserfach* **79** 69
Honarvar B *et al* 2017 Experimental investigation of interfacial tension measurement and oil recovery by carbonated water injection: a case study using core samples from an iranian carbonate oil reservoir *Energy Fuels* **31** 2740–8
Jaeger P T and Eggers R 2012 Interfacial properties at elevated pressures in reservoir systems containing compressed or supercritical carbon dioxide *J. Supercrit. Fluids* **66** pp 80–5
Jennings H Y 1967 The effect of temperature and pressure on the interfacial tension of benzene-water and normal decane-water *J. Colloid Interface Sci.* **24** 323–9
Kandil M E, Al-Saifi N M and Sultan A S 2016 Simulation and measurements of volumetric and phase behavior of carbon dioxide + higher alkanes at high pressure: CO_2 + n-decane at temperatures (313–410) K and pressures up to 76 MPa *Int. J. Greenhouse Gas Control* **53** 198–206
Li S, Li Z and Dong Q 2016 Diffusion coefficients of supercritical CO_2 in oil-saturated cores under low permeability reservoir conditions *J. CO_2 Util.* **14** 47–60
Linstrom P and Mallard W 2010 *NIST Chemistry Webbook, NIST Standard Reference Database Number 69* (Gaithersburg, MD: National Institute of Standards and Technology) p 20899
McBride-Wright M, Maitland G C and Trusler J M 2014 Viscosity and density of aqueous solutions of carbon dioxide at temperatures from (274 to 449) K and at pressures up to 100 MPa *J. Chem. Engin. Data* **60** 171–80
Mosavat N and Torabi F 2014 Experimental evaluation of the performance of carbonated water injection (CWI) under various operating conditions in light oil systems *Fuel* **123** 274–84
Nguyen T and Ali S 1998 Effect of nitrogen on the solubility and diffusivity of carbon dioxide into oil and oil recovery by the immiscible WAG process *J. Can. Pet. Technol.* **37** 24–31
Riazi M, Jamiolahmady M and Sohrabi M 2011 Theoretical investigation of pore-scale mechanisms of carbonated water injection *J. Pet. Sci. Eng.* **75** 312–26
Riazi M, Sohrabi M, Jamiolahmady M and Ireland S 2009 Oil recovery improvement using CO_2-enriched water injection *EUROPEC/EAGE Conf. and Exhibition* (Society of Petroleum Engineers)
Riazi M R 1996 A new method for experimental measurement of diffusion coefficients in reservoir fluids *J. Pet. Sci. Eng.* **14** 235–50
Sheikha H, Pooladi-Darvish M and Mehrotra A K 2005 Development of graphical methods for estimating the diffusivity coefficient of gases in bitumen from pressure-decay data *Energy Fuels* **19** 2041–9
Sigmund P M 1976 Prediction of molecular diffusion at reservoir conditions. part 1-measurement and prediction of binary dense gas diffusion coefficients *J. Can. Pet. Technol.* **15** 48–57
Sohrabi M, Riazi M, Jamiolahmady M, Kechut N I, Ireland S and Robertson G 2011 Carbonated water injection (CWI)–a productive way of using CO_2 for oil recovery and CO_2 storage *Energy Procedia* **4** 2192–9
Teng H and Yamasaki A 1998 Mass transfer of CO_2 through liquid CO_2–water interface *Int. J. Heat Mass Transfer* **41** 4315–25
Unver A and Himmelblau D 1964 Diffusion coefficients of CO_2, C_2H_4, C_3H_6 and C_4H_8 in water from 6° to 65° C *J. Chem. Eng. Data* **9** 428–31
Upreti S R and Mehrotra A K 2002 Diffusivity of CO_2, CH_4, C_2H_6 and N_2 in athabasca bitumen *Can. J. Chem. Eng.* **80** 116–25
Wiegand G and Franck E 1994 Interfacial tension between water and non-polar fluids up to 473 K and 2800 bar *Ber. Bunsenges. Phys. Chem.* **98** 809–17
Yang C and Gu Y 2005 New experimental method for measuring gas diffusivity in heavy oil by the dynamic pendant drop volume analysis (DPDVA) *Ind. Eng. Chem. Res.* **44** 4474–83
Yang C and Gu Y 2006 Diffusion coefficients and oil swelling factors of carbon dioxide, methane, ethane, propane, and their mixtures in heavy oil *Fluid Phase Equilib.* **243** 64–73
Yang D and Gu Y 2008 Determination of diffusion coefficients and interface mass-transfer coefficients of the crude oil−CO_2 system by analysis of the dynamic and equilibrium interfacial tensions *Ind. Eng. Chem. Res.* **47** 5447–55
Yang D, Tontiwachwuthikul P and Gu Y 2006 Dynamic interfacial tension method for measuring gas diffusion coefficient and interface mass transfer coefficient in a liquid *Ind. Eng. Chem. Res.* **45** 4999–5008
Yang Z, Li M, Peng B, Lin M and Dong Z 2013 Volume expansion of CO_2 + oil at near critical and supercritical conditions of CO_2 *Fuel* **112** 283–8
Zambrano J, Gómez-Soto F V, Lozano-Martín D, Martín M C and Segovia J J 2016 Volumetric behaviour of (carbon dioxide + hydrocarbon) mixtures at high pressures *J. Supercrit. Fluids* **110** 103–9

PAPER — III

Dynamic Interfacial Tension Measurement Method Using Axisymmetric Drop Shape Analysis

MethodsX 5 (2018) 676–683

Contents lists available at ScienceDirect

MethodsX

journal homepage: www.elsevier.com/locate/mex

Method Article

Dynamic interfacial tension measurement method using axisymmetric drop shape analysis

Nikhil Bagalkot, Aly A. Hamouda*, Ole Morten Isdahl

Department of Energy and Petroleum Engineering, University of Stavanger, Norway

A B S T R A C T

The current method describes a simple modification to the dynamic and equilibrium interfacial tension (IFT) measurement in a multiphase system (gas-liquid/liquid-liquid) by the Axisymmetric Drop Shape Analysis (ADSA) pendant drop technique. The primary difficulty associated with dynamic IFT measurement by ADSA is providing the appropriate phase densities, especially in a system consisting of gas (CO_2, methane, and propane) and liquids (water and hydrocarbon). The density of the phases is calculated using a, considering the solubility og gases in liquids, as a function of time. The calculated densities of the phases are then used as inputs in the experiment to measure the IFT at high pressure and temperature PVT-cell.

The method offers benefit such as:

- Straightforward and cost effective as it does not require additional experimental setup (like density meter) or a complicated equation of state.
- The composition of the binary mixtures (mole and mass) and the density changes of the binary mixture due to mass transfer may be obtained as a function of time at fixed pressure and temperature.
- IFT as a function of time is measured by taking into consideration of correct phase density.

A R T I C L E I N F O

Method name: Dynamic IFT measurement

Keywords: Dynamic IFT, Pendant drop method, Multiphase, Dynamic density

Article history: Received 13 June 2018; Accepted 21 June 2018; Available online 23 June 2018

* Corresponding author.
E-mail address: aly.hamouda@uis.no (A.A. Hamouda).

https://doi.org/10.1016/j.mex.2018.06.012

Specifications Table

Subject area	*Select one of the following subject areas:* • *Chemical Engineering* • *Engineering* • *Mathematics*
More specific subject area	*Mass transfer and interfacial science*
Method name	*Dynamic IFT measurement*
Name and reference of original method	Bagalkot, Nikhil, and Aly A. Hamouda. "Experimental and numerical method for estimating diffusion coefficient of the carbon dioxide into light components." *Industrial & Engineering Chemistry Research* 56.9 (2017): 2359–2374. Zolghadr, Ali, Mehdi Escrochi, and Shahab Ayatollahi. "Temperature and composition effect on CO2 miscibility by interfacial tension measurement." *Journal of Chemical & Engineering Data* 58.5 (2013): 1168–1175.
Resource availability	Equipment theory: https://www.kruss-scientific.com/services/education-theory/glossary/pendant-drop/ Equipment: https://www.kruss-scientific.com/products/contact-angle/dsa100/drop-shape-analyzer-dsa100/ Software: https://www.kruss-scientific.com/products/advance-software/overview/

Method background and description

Interfacial tension plays a significant role in numerous engineering applications involving multiphase flow. Measuring the IFT is a crucial part of multiphase systems, there are several methods available like ring method, drop volume method, spinning drop method, bubble pressure method and pendant drop method. In recent years, the pendant drop method has been widely used as an effective method with high accuracy ($\pm$0.05 mN/m^2) [1,2], especially at elevated pressure and temperature. There are several types of equipment available that rely on pendant drop method to estimate the IFT, few of them are IFT-700 (Vinci Technologies), IFT-10-P (Core laboratories), DSA-00 (KRÜSS), and Model-190 (ramé-hart instrument). Most of these use image processing combined with Young-Laplace equation to estimate the IFT.

The primary difficulty associated with IFT measurement by pendant drop mechanism is providing the appropriate densities of the two phases, especially in a system consisting of gas (like CO_2, methane, and propane) and liquids (water and hydrocarbon). Multiphase systems like CO_2-hydrocarbon, CO_2-water/brine, and carbonated water-hydrocarbon are of increasing interest due to their application in petroleum (CO_2 EOR), environmental (CO_2 sequestration) and renewable energy (geothermal). When CO_2 contact liquid (hydrocarbon) it diffuses and dissolves into the liquids, forming a binary mixture. The diffusion of gases into liquids alters the composition of the resulting binary mixture, hence alter the properties like density.

Obtaining the density of the binary mixture is complex, especially at elevated pressures and temperatures and as a function of time. Most of the studies have neglected the density changes due to the solubility effects of dissolved gases in bulk liquids and have used the density of pure fluids instead of the binary mixture [3,4]. While some studies have used separate high pressure and temperature density measuring equipment at equilibrium condition (not dynamic), which complicates the system [5,6], as it requires two different setups. Some studies have even used a complex equation of state model (GERG equation of state (EOS)) [7].

In the present study, a simple and effective method is used to measure the dynamic and equilibrium IFT of the fluid-fluid system with a mass transfer across the interface. Instead of a complicated EOS model or expensive additional instrument, in the present method, the density of changes in the hydrocarbon due to CO_2 mass trasfer is measured from a combination of experimental and analytical approach, and the obtained density is then used to estimate the IFT by pendant drop technique.

Principle of IFT measurement

The pendant drop method is an effective and popular means to measure the interfacial tension of liquid-liquid or liquid-gas system. In the pendant drop method, the drop is created from a needle

(capillary tube) in a bulk phase (liquid or gas) inside a PVT-cell. The shape of the pendant drop is governed by gravity and the surface/interfacial tension. The IFT is calculated from the shadow of the digital image captured by the camera using the drop shape analysis. The drop shape analysis relies on Young-Laplace equation (Eq. (1)) for calculation of IFT [8,9].

$$\Delta P = \sigma \cdot \left(\frac{1}{r_1} + \frac{1}{r_2}\right), \tag{1}$$

where ΔP is the pressure across the interface; r_1 and r_2 are the principal radii of the pendant drop, and σ is the interfacial/surface tension.

While carrying out an IFT measurement, the scale of the digital image is measured first to get the actual dimension of the pendant drop. Once the scale is obtained, using grey scale analysis, the shape of the drop is then determined. A shape parameter (B) is then adjusted in a numerical method until the calculated drop shape resembles with the actual shape. The interfacial tension may then be calculated from Eq. (2) from the density difference between the P_g and P_d ($\Delta\rho = P_d - P_g$) and the modified shape parameter (B) [8,10].

$$\sigma = \frac{\Delta \rho g d^2}{B}, \tag{2}$$

where $\Delta\rho$ is the density difference between the phases; g is the acceleration due to gravity, and d is the maximum horizontal diameter of the unmagnified pendant drop.

From Eqs. (1) and (2) it may be observed that except for density difference ($\Delta\rho$), the rest of the parameters are calculated by the image processing software. The density of the phases goes as input that the user has to provide. Therefore, even if the software is highly accurate, an inaccurate density input would result in an incorrect IFT. Therefore, the actual density of the phases play a crucial role in estimation of the IFT.

Materials

In the present study, CO_2 (PRAXAIR with purity greater than 99%) and n-decane (Merck KGaA with purity 99%) were used as the experimental fluids. *NIST Chemistry Web Book* [11] was the source of density and viscosity measurements for pure substances (n-decane, and CO_2).

Experimental setup

Fig. 1A shows the schematics of the experimental setup. The critical part of the setup is the High-Pressure Pendant Drop Apparatus (PD-E1700 LL-H) (PVT-cell) built by EUROTHECHNICA and KRUSS [12], which has been used to measure the interfacial tension. In Fig. 1A, PVT-cell is corrosion resistant, high-

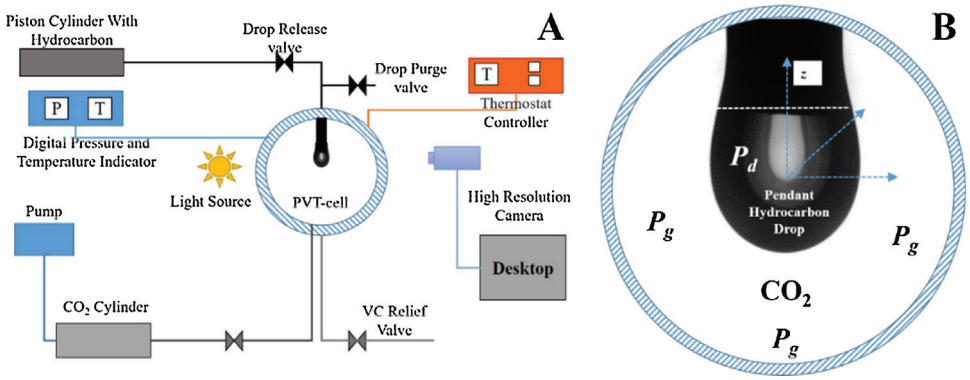

Fig. 1. (1A) Schematics of the experimental setup; (1B) Arrangement of the pendant drop in the PVT-cell.

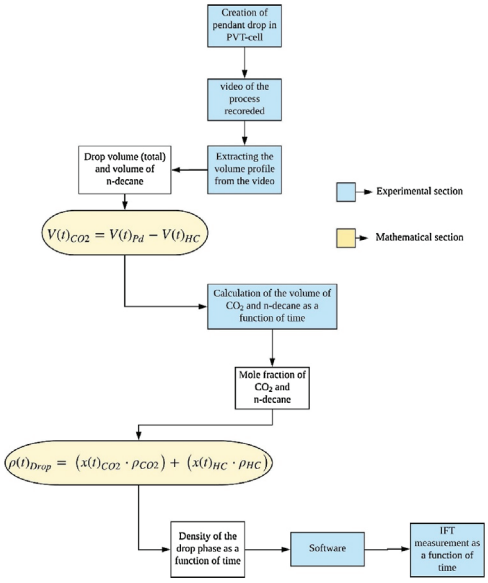

Fig. 2. Schematic representation of the process involved in the measurement of IFT.

pressure cylindrical chamber (25 ml capacity) having a limiting pressure and temperature of 690 bar and 180 °C respectively. The PVT-cell is a see-through chamber, in which the pendant drop will be created. Fig. 1B shows the arrangement of drop phase (pendant drop, P_d) and the surrounding environmental phase (gas or liquid, P_g) in the PVT-cell. The temperature of the PVT-cell is controlled by a NiCr-Ni thermocouple fitted with a digital indicator. The pressure of the system is maintained externally through a pump (maximum pressure of 32 MPa, GILSON) connected to the gas cylinder. The PVT-cell has a see-through window and is placed between a high-resolution camera (CF03), and a light source. KRUSS DSA 100 (ADVANCE) [13] software is used to analyse the acquired images and compute the P_d volume, and interfacial tension (IFT) at pre-set time steps. Further, details of the experimental setup may be found in Bagalkot and Hamouda [14]. The pressure sensor has an accuracy of ± 0.1 MPa, while the temperature sensor has accuracy of ±0.1 °C at 0 °C to ±0.8 °C at 400 °C, respectively.

Procedure for measurement of IFT

In the current work the CO_2-decane system has been taken as the reference system, with CO_2 being the environmental phase/fluid (P_g) and n-decane the drop phase/fluid (P_d). Fig. 2 shows the schematic representation of the process involved in the measurement of IFT.

1 The PVT-cell is filled with the environmental fluid at required pressure using the CO_2 cylinder connected to the pump, which is set at the required pressure as shown in the Fig. 1A. Therefore, at all times the pressure inside the PVT-cell is maintained. Further, the temperature of the PVT-cell is set, which is maintained by a NiCr-Ni thermocouple.
2 Once the PVT-cell consisting of environmental fluid achieves the required pressure and temperature, an n-decane pendant drop (P_d) is created at the end of the capillary tube as shown in the Fig. 1B.
3 As soon as the pendant drop is created, the camera and the ADVANCE software starts to capture the high-resolution digital images of the pendant drop for the analysis.
4 Diffusion of CO_2 (P_g) into the n-decane (P_d) starts when the fluids come in contact with each other, resulting in a binary mixture of CO_2+decane. The diffusion of CO_2 would result in increased volume of P_d. The experiment will continue until the volume of the pendant drop has reached equilibrium

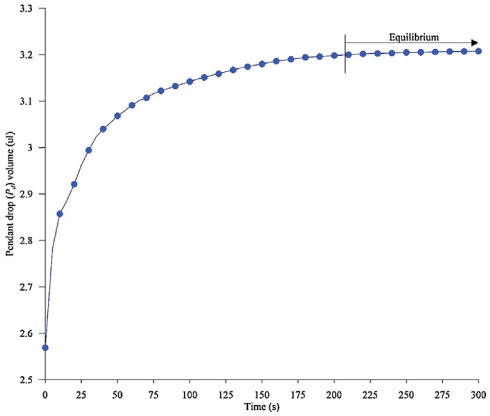

Fig. 3. Volume of the pendant drop as a function of time.

(point above which there is no or minimal increment in the volume of the pendant drop) (Fig. 3 at 50 bar 25 °C).

5 From the images captured, with the aid of the image analysis software, the volume of the P_d at different time steps will be obtained (Fig. 3).
At the start of the experiment (time t = 0), the P_d consists solely of n-decane (100% hydrocarbon). With the initiation of the CO_2 diffusion (t > 0 s), the volume of the P_d increases due to the additional volume of CO_2. Hence, the volume of the pendant drop (V_{Pd}) would be a summation of the volume of hydrocarbon (V_{HC}) and the increase in volume caused by the diffusion of CO_2 (V_{CO2}) in the P_d, as given by Eq. (3).

$$V_{Pd}(t) = V_{CO2}(t) + V_{HC} \tag{3}$$

For a fixed temperature and pressure the volume of the n-decane would be same as that during the start of the experiment (since the PVT-cell is closed for any additional decane mass to come in). Hence, in Eq. (3) V_{Pd} (obtained from the experiment (step 5) and V_{HC} are known, therefore rearranging Eq. (3) would give the volume of CO_2 in the pendant drop as given by Eq. (4).

$$V_{CO2}(t) = V_{Pd}(t) - V_{HC} \tag{4}$$

6 From the acquired volume of CO_2 (V_{CO2}) and decane (V_{HC}) in P_d at every time step (step 5), the mass and moles, and hence, the mole fraction of CO_2 (x_{CO2}), and n-decane (x_{HC}) may be obtained at all time steps.

7 The calculated dynamic mole fraction of CO_2 (x_{CO2}) and mole fraction of n-decane (x_{HC}) was further be used to obtain the density of the P_d consisting of a binary mixture (ρ_{Pd}) at every experimental time step by Eq. (5) [15–17].

$$\rho(t)_{Pd} = \left((x(t)_{CO_2} \cdot \rho_{CO_2}) + (x(t)_{HC} \cdot \rho_{HC}) \right)_{P,T}, \tag{5}$$

where ρ_{CO2} and ρ_{HC} are the densities of CO_2 and hydrocarbon in the drop, respectively (obtained from NIST webbook [11]).

8 The density data of the CO_2 and density of pendant drop consisting of CO_2+n-decane from Eq. (5) was used as an input to the software to obtain the dynamic and equilibrium IFT of the CO_2-decane system.

Validation

As described in Section 1.1, for the pendant drop method the IFT measurement is a function of the density of phases. Therefore, to validate the present method, it would be sufficient to validate the

Table 1
Validation of density and IFT of the present model at equilibrium condition.

Study	Density of CO_2-decane pendant drop (g/ml)	Density of CO_2 [11] (g/ml)	IFT (m N/m)
Kandil et al. [16]	0.720	0.07087	12.85
Present method	0.711	0.07087	12.53

density values calculated from the Eq. (5), with that obtained in literature. Density data of CO_2+decane binary mixture at 34 bar and 40 °C obtained by Kandil et al. [16] was used to validate the present method. The density of the present work and that form Kandil, et al. [16] were be input into the software for the experiments carried out at 35 bar, and 40 °C with the CO_2-decane system. The obtained IFT's were then compared for both of the density inputs (Table 1). It may be observed that both density and obtained IFT of the present method are comparable with Kandil et al. [16], therefore, validating the present method of calculating the density and hence, the IFT.

Method results and comparison

To demonstrate the importance of correct phase densities (P_g and P_d) in the estimation of IFT, two different methods on density input from the literature were used and compared with the method presented in the current article. All three methods are analysed using the same experiment carried out at 50 bar, 25 °C for a CO_2-decane system. The details of each of these methods are described below:

Case 1 (initial density) [3,4]:This method uses the pure phase density (CO_2 and decane) and neglecting the density changes due to the diffused gases (CO_2+decane) in bulk liquids to estimate the IFT.

Case 2 (equilibrium density) [2,6]: In this method, the IFT is measured using the equilibrium phase density. The density change due to the solubility of gases was then considered, however, it is done only at equilibrium (final point), and this equilibrium density is used to estimate IFT for the whole process (at all times).

Case 3 (dynamic density, present method): Here the IFT is measured using the corrected density of the phases (P_g (CO_2) and P_d (CO_2+decane)) at every time step calculated from Eq. (5), then following the procedure described in section 2.0. The present method improves case-2 as it is capable of calculating the density change of the drop phase (CO_2+decane) cause by the solubility of the gas, as a function of time. This is unlike in case-2 where only the density of equilibrium is considered. Therefore, the present method reflects the real-time changes in density on IFT, without requiring additional setup as in case-2.

Fig. 4 shows the density of the pendant drop phase obtained from the three cases 1–3 as a function of time at 50 bar and 25 °C for the CO_2-decane system. The difference in the density vs time profile

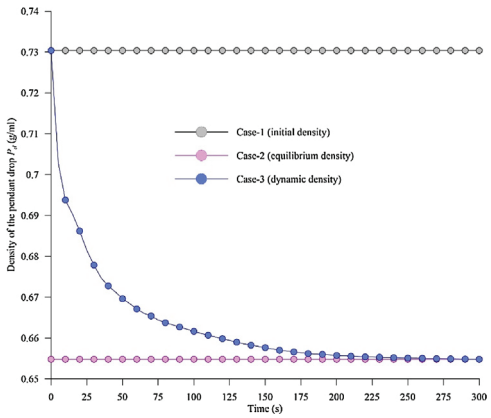

Fig. 4. Density of the pendant drop as a function of time for case-1, case-2 and case-3 at 50 bar and 25 °C.

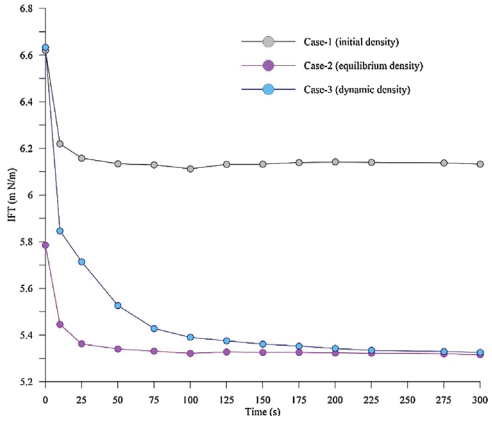

Fig. 5. Dynamic IFT CO2-decane system as a function of time for case-1, case-2 and case-3 at 50 bar and 25 °C.

among the cases (1–3) is evident. The density for case-1 (initial density) and case-2 (equilibrium density) remain constant with time, while the density for case-3 (dynamic density) which represent the actual scenario varies (decreases) with time, depicting changes in density of the drop phase (P_d) due to the solubility of CO_2 in decane.

Fig. 5 shows the IFT of the CO_2-decane system for case 1, case-2, and case-3 at 50 bar and 25 °C. It is clear from the Fig. 5 that different IFT vs time profiles are obtained for the same experiment, emphasising, the dependency of the IFT measurement on the density. Since, both case-1 and case-3 do not consider the dynamic change in the density of pendant drop due to the solubility of a gas in a liquid, the dynamic IFT measured by these methods are different from the one where the solubility effect is considered (case-3). The error in the estimation of IFT varies from a max of 13.4% to min of 0.2% for case-1 and maximum of 14.7% to a minimum of 0.2% for case-2 when compared to case-3. However, the equilibrium IFT for case-2 and case-3 seems to be same or near to eachother. If equilibrium IFT is the focus of the study and not the dynamic natureof the IFT, then applying the case-2 would be fine, as the densities of the phases represent the equilibrium conditions. However, if the dynamic changes in the IFT, as well as the equilibrium IFT, is to be analysed, then case-3 would be the best option (followed in the present study), as the densities of the phases are calculated at different time intervals until equilibrium is reached. Obtaining IFT using the case 1 approach would lead to an error, as the density represent only the initial state of the system, not the equilibrium or the dynamic.

Drawbacks and recommendations

Although the method presented is simple, reliable, and free from human interference, the major setback would be manually entering the density of phases in the software. The task may seem simple, but to obtain high resolution dynamic data, it requires a lot of entries. Further, if experiments are carried out with sensitivity for both temperature and pressure, the number of entries is multiplied accordingly. An example, a 4-h experiment with dynamic IFT data for every 5 min and sensitivity for two temperatures and three pressures results inn 576 manual inputs (two for each time-step). However, since the process is repetitive, it is straight forward to let computer-scripts perform the task. More importantly, the problem can be eliminated if the software-developers allowed for input of density of phases obtained from the model as either a function of time or as a table with time and density of the phases.

References

[1] D. Yang, P. Tontiwachwuthikul, Y. Gu, Interfacial tensions of the crude oil+ reservoir brine+ CO2 systems at pressures up to 31 MPa and temperatures of 27 C and 58 C, J. Chem. Eng. Data 50 (4) (2005) 1242–1249.

[2] M. Ghorbani, A.H. Mohammadi, Effects of temperature, pressure and fluid composition on hydrocarbon gas-oil interfacial tension (IFT): an experimental study using ADSA image analysis of pendant drop test method, J. Mol. Liq. 227 (2017) 318–323.
[3] D. Yang, P. Tontiwachwuthikul, Y. Gu, Dynamic interfacial tension method for measuring gas diffusion coefficient and interface mass transfer coefficient in a liquid, Ind. Eng. Chem. Res. 45 (14) (2006) 4999–5008.
[4] D. Yang, Y. Gu, Interfacial interactions of crude oil-brine-CO2 systems under reservoir conditions Society of Petroleum Engineers, SPE Annual Technical Conference and Exhibition (2004).
[5] A. Zolghadr, M. Riazi, M. Escrochi, S. Ayatollahi, Investigating the effects of temperature, pressure, and paraffin groups on the N2 miscibility in hydrocarbon liquids using the interfacial tension measurement method, Ind. Eng. Chem. Res. 52 (29) (2013) 9851–9857.
[6] A. Zolghadr, M. Escrochi, S. Ayatollahi, Temperature and composition effect on CO2 miscibility by interfacial tension measurement, J. Chem. Eng. Data 58 (5) (2013) 1168–1175.
[7] P.T. Jaeger, R. Eggers, Interfacial properties at elevated pressures in reservoir systems containing compressed or supercritical carbon dioxide, J. Supercrit. Fluids 66 (2012) 80–85.
[8] M. Alotaibi, H. Nasr-El-Din, Effect of brine salinity on reservoir fluids interfacial tension, Pap. SPE 121569 (2009).
[9] K.V. Greenway, Effect of different surfactant structures on the brine-crude oil and brine-alkane interface in different aqueous environments, The University of Bergen, 2017.
[10] Kruss, Pendant Drop Available:, https://www.kruss-scientific.com/services/education-theory/glossary/pendant-drop/.
[11] P. Linstrom, W. Mallard, NIST Chemistry Webbook, NIST Standard Reference Database Number 69, National Institute of Standards and Technology, Gaithersburg MD, 20899, 2010.
[12] Kruss (2016, 04/05) Drop Shape Analyzer – DSA100. Available: https://www.kruss-scientific.com/products/contact-angle/dsa100/drop-shape-analyzer-dsa100/.
[13] Kruss (2016, 04/05) ADVANCE Software. Available: https://www.kruss-scientific.com/products/advance-software/overview/.
[14] N. Bagalkot, A.A. Hamouda, Experimental and numerical method for estimating diffusion coefficient of the carbon dioxide into light components, Ind. Eng. Chem. Res. 56 (9) (2017) 2359–2374.
[15] M. McBride-Wright, G.C. Maitland, J.M. Trusler, Viscosity and density of aqueous solutions of carbon dioxide at temperatures from (274 to 449) K and at pressures up to 100 MPa, J. Chem. Eng. Data 60 (1) (2014) 171–180.
[16] M.E. Kandil, N.M. Al-Saifi, A.S. Sultan, Simulation and measurements of volumetric and phase behavior of carbon dioxide+ higher alkanes at high pressure: CO2+ n-decane at temperatures (313–410) K and pressures up to 76 MPa, Int. J. Greenh. Gas Control 53 (2016) 198–206.
[17] J. Zambrano, F.V. Gómez-Soto, D. Lozano-Martín, M.C. Martín, J.J. Segovia, Volumetric behaviour of (carbon dioxide+ hydrocarbon) mixtures at high pressures, J. Supercrit. Fluids 110 (2016) 103–109.

PAPER — V

Interfacial tension and CO_2 diffusion coefficients for a CO_2+water and n-decane system at pressures of 10 to 160 bar

RSC Advances

PAPER

View Article Online
View Journal | View Issue

Check for updates

Cite this: *RSC Adv.*, 2018, **8**, 38351

Interfacial tension and CO_2 diffusion coefficients for a CO_2 + water and *n*-decane system at pressures of 10 to 160 bar†

Nikhil Bagalkot and Aly A. Hamouda*

Received 29th April 2018
Accepted 31st October 2018

DOI: 10.1039/c8ra03690j

rsc.li/rsc-advances

The objective of this study is to address the influence of different CO_2 phases and degrees of CO_2 saturation on the interfacial tension and the diffusion of CO_2 into a hydrocarbon drop. Axisymmetric drop shape analysis on a pendant drop was used to carry out experiments in a pressure range of 10 to 160 bar and temperatures of 25 °C, 35 °C, and 45 °C, thus covering the gaseous, liquid, and supercritical phases of CO_2. A numerical model that estimates the diffusion coefficient of CO_2 in the hydrocarbon was developed. The IFT between the carbonated water and the hydrocarbon increases with pressure in the gaseous phase of CO_2 and decreases in the liquid and supercritical CO_2 phases. Interestingly, when the pressure was increased above 120 bar, the IFT did not change (decrease); this indicates that above this pressure, complete miscibility may not be achieved for this system, as indicated by the stable IFT. From the results, it can be concluded that the maximum IFT, maximum density decrease, and minimum diffusion coefficient occurred at pressures near to and below the phase change pressure of CO_2 (64 bar at 25 °C and 74 bar at 35 °C and 45 °C). Both CO_2–water–hydrocarbon and CW–hydrocarbon systems show the same trends; however, there were significant differences in the CO_2 mass transfer rate and the concentration gradient.

1 Introduction

The mass transfer of gases into liquids and interfacial studies of this transfer are of great importance in numerous fields of science and its applications, such as processes involving oil–water and CO_2–liquid fluid systems. The mass transfer of CO_2 into hydrocarbons is applicable to the enhanced oil recovery process (EOR). The mass transfer of CO_2 and the resulting mechanisms, such as swelling and enhanced mobility of the oil, dictate the degree of oil recovery in CO_2-based EOR methods.[1,2] Diffusion of CO_2 and interfacial phenomena are the mechanisms which control the CO_2 mass transfer[3] and hence control the swelling and mobility. Additionally, the interfacial tension is of primary importance in the context of multiphase flow in reservoirs, and it is pivotal in controlling miscibility behaviour.[4]

In recent times, due to an increase in the emission of anthropogenic CO_2, effort has been made to couple CO_2 EOR and CO_2 sequestration. However, CO_2 EOR for CCS has some drawbacks, such as high cost of transportation, lower storage capacity due to poor sweep efficiency,[5] and risk of CO_2 leaking back to the surface due to its lower density compared to other reservoir liquids.[2,6] Few studies have succeeded in improving the efficiency and safety of the CO_2 EOR as a CCS option. Studies[7,8] attempted to blend CO_2 with solvents such as amino acids, piperazine, water, and diethanolamine (DEA). Laboratory studies[2,6] have shown that combining water and CO_2 (carbonated water, CW) as an injecting fluid is an efficient option for both oil recovery and CO_2 sequestration. From the EOR point of view, carbonated water injection (CWI) enhances the sweep efficiency by reducing the gravity segregation and "fingering" effect that is generally experienced with gas injection and CO_2-EOR, hence increasing the incremental oil recovery. Additionally, dissolution of CO_2 into water creates carbonated water, which has a higher density compared to native brine (formation water); hence, it sinks to the bottom of the reservoir, reducing the risk of buoyancy-driven leakage.[2,6] Molecular diffusion and interfacial tension (liquid/liquid) are vital to assess the rate and distribution of CO_2.[9]

The pendant drop technique is a widely used and effective method for analysing the mass transfer and the interfacial tension between two fluids at elevated pressure and temperature.[10] Over time, the pendant drop technique has been developed into an advanced and accurate ($\pm$0.05 mN m^{-2}) method called axisymmetric drop shape analysis (ADSA).[4,10] Numerous studies have been carried out using the pendant drop technique that are applicable to CO_2-based EOR for multiphase systems consisting of CO_2–light hydrocarbon,[11,12] CO_2–crude/heavy oil,[13] CO_2–brine/water,[14–16] water–oil,[17] and brine–oil.[18] Although these studies have provided critical information, there is

Department of Energy and Petroleum, University of Stavanger, 4036, Norway. E-mail: aly.hamouda@uis.no; nikhil.bagalkot@uis.no

† Electronic supplementary information (ESI) available. See DOI: 10.1039/c8ra03690j

a general lack of understanding of (1) the effects of the water layer present between CO_2 and the hydrocarbon on the interfacial tension (IFT); (2) the influence of temperature on the IFT; (3) the influence of the phase of CO_2 (gas, liquid, or supercritical) on the IFT.

Petroleum reservoirs contain water along with hydrocarbons in their systems; the injected CO_2 encounters water before it diffuses into the residual oil. The presence of water dictates and significantly alters the CO_2 mass transfer and associated physics, such as IFT. Moreover, most studies on CO_2–hydrocarbon and CO_2–water–hydrocarbon systems have overlooked the influence of temperature on the IFT; this is mainly due to its unpredictable relationship with temperature. There are discrepancies associated with the IFT *vs.* temperature relationship; for example,[19] reported an inverse relationship of IFT with temperature, while[10] reported a direct relationship for CO_2–hydrocarbon systems. Further, few studies have collectively investigated the influence of different phases of CO_2 (gas, liquid, and supercritical) on the IFT of CO_2–hydrocarbon or CO_2–water–hydrocarbon systems. The density of the CO_2 changes significantly with the phase (gas, liquid, and supercritical), and the density and IFT are related.[20] Hence, it is important to study how the IFT is influenced by the different phases of CO_2. Additionally, factors such as temperature, pressure, composition, the density of the immiscible fluids, CO_2 solubility, and the phase of CO_2 influence the interfacial tension.[4] Numerous studies have investigated the influences of these factors on IFT with a focus on individual parameters, but few studies have taken these factors into account simultaneously; this would be meaningful because all these parameters are interrelated.

Through experimental, theoretical, and numerical models, the present study attempts to estimate the interfacial tension and effective diffusion coefficient and identify the associated physics for a CO_2–water–*n*-decane system. Axisymmetric drop shape analysis (ADSA) pendant drop experiments have been carried out in a large pressure range of 10 to 160 bar and at a wide range of temperatures (25 °C, 35 °C, and 45 °C). A mathematical model has been developed that uses the experimental inputs to determine the composition, density and viscosity of the pendant drop as a function of time. A theoretical model (Eyring's absolute rate theory approach) using the Gibbs free energy and viscosity of the pendant drop has been presented to elucidate the behaviour of the IFT with temperature. Further, a numerical model with adaptive boundaries has been developed to estimate the diffusion coefficient of CO_2 in the hydrocarbon pendant drop. This study makes four major contributions to the existing knowledge on systems involving CO_2. First, the experiments were designed to analyse the influence of the degree of carbonation of the water layer between CO_2 and the hydrocarbon on critical parameters such as the IFT, diffusion coefficient, and hydrocarbon properties. Second, the experimental pressure range (10 to 160 bar) and temperature range (25 °C to 45 °C) were chosen to study the influence of the phase of CO_2 (gas, liquid, or supercritical) on the CO_2 diffusion and IFT. Third, the study addresses the inconsistencies in results reported in the literature regarding the relationship between temperature and IFT by relating the experimental IFT and viscosity-dependent Gibbs energy from the developed model. Fourth, the study involves parameters such as the density, viscosity, mass/mole fraction, Gibbs free energy, temperature, pressure, concentration gradient, diffusion coefficient, and phase of CO_2. Hence, it is convenient to identify and correlate parameters or physics that are being influenced and influenced by interfacial tension in a CO_2–water–hydrocarbon system. Additionally, using the IFT, volume, and CO_2 concentration gradient as the parameters, a comparative study has been performed between the CO_2–water–hydrocarbon system and a carbonated water–hydrocarbon system.

2 Theory

The well-established axisymmetric drop shape analysis (ADSA) technique is employed in the present work. The ADSA method involves a high pressure high temperature isolated cell (PVT cell) in which an axisymmetric pendant drop (drop phase) is created at the end of a capillary tube in a high-pressure see-through cell filled with another fluid (environment phase) (see Fig. 1 for reference). In the present work, *n*-decane forms the drop phase and water + CO_2 or CO_2-enriched water (CW) forms the environment phase. Once the hydrocarbon drop (HD) which forms the drop phase and the environmental phase (water) are established, CO_2 is injected into the PVT cell at the required pressure and temperature. The CO_2 first diffuses and dissolves in the water, carbonising the water; the concentration of CO_2 in the water changes from zero to a maximum as the diffusion progresses. Because the solubility of CO_2 is greater in the hydrocarbon than in water, the CO_2 from the carbonised water diffuses into the hydrocarbon pendant drop. Therefore, the direction of CO_2 mass transfer is from the free CO_2 phase into the hydrocarbon drop through water. The mass transfer of CO_2 and its subsequent dissolution into the hydrocarbon will lead to alterations in the physical properties of the hydrocarbon and in the interfacial tension, which is the focus of this study.

2.1 Experimental setup and methodology

2.1.1 Materials. The hydrocarbon *n*-decane (Merck KGaA, purity 99%) was used as the drop phase in the present

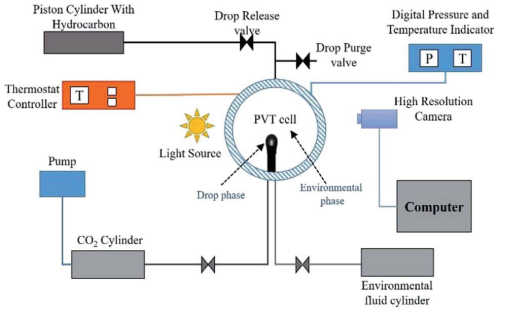

Fig. 1 Schematic of the experimental setup.

experimental work. The purity of the CO_2 (PRAXAIR) used was greater than 99.9%. *NIST Chemistry Web Book*[21] was the source of the density and viscosity measurements at various pressures and temperatures of *n*-decane, water, and CO_2. The CO_2 solubility was calculated using the model presented by ref. 22.

2.1.2 Schematics of the setup and experimental procedure. Fig. 1 shows a schematic of the experimental setup consisting of a High-Pressure Pendant Drop Apparatus (HD-E1700 LL-H) constructed by EUROTHECHNICA and KRUSS. In Fig. 1, the PVT cell (max volume 25 ml) is a corrosion-resistant, cylindrical high-pressure chamber with a limiting pressure and temperature of 690 bar and 180 °C, respectively. The temperature inside the PVT cell is controlled by a NiCr–Ni thermocouple fitted with a digital indicator. The pressure of the system is controlled externally through a pump (maximum pressure of 32 MPa, GILSON) connected to a CO_2 cylinder. The see-through window of the PVT cell is placed between a high-resolution camera and a light source so that the camera captures images of the changes in the shape of the HD due to diffusion of CO_2. KRUSS DSA 100 software was used to analyse the acquired images and compute the HD volume and interfacial tension (IFT) at pre-set time intervals.

Fig. 2A shows a snapshot of the drop phase (HD) and environmental fluid inside the PVT cell. Fig. 2B shows the equivalent spherical HD employed in the numerical analysis (a detailed explanation of the advantages of the spherical drop is presented in Section 3.0). In Fig. 2B, P_D and P_E represent the physical regions occupied by the hydrocarbon drop phase and the surrounding environmental phase, respectively; r, z, and R_D are the radius of the drop (radial coordinates), axial coordinate, and radius of the spherical drop, respectively; and D_{PVT} represents the diameter of the PVT cell.

In the present work, the following justifications are made. The mass transport across the water–hydrocarbon drop interfaces is diffusive (concentration-driven); this is accomplished by using a HD with a small volume, eliminating density-driven convection.[23] Each individual experiment was carried out at a constant temperature, which minimises thermal convention.[23] Due to the significantly lower solubility of water in *n*-decane than in CO_2, the mass transfer of water into the hydrocarbon was neglected, and only the mass transfer of CO_2 was considered. The mass was calculated from the density at the experimental temperature and pressure to obtain the mass and, hence, the mole fraction of the diffused CO_2.[24,25] Finally, no chemical reactions transpired during the experiments; therefore, the mechanisms of the changes in the properties are physics-driven and thermodynamically driven processes.

In the experimental procedure, first, the PVT cell was partially filled (20 ml of 25 ml) with deionised water; then, the *n*-decane pendant drop was created. Then, the CO_2 was released into the PVT cell at the experimental pressure, as shown in Fig. 1. The CO_2 acted a source, meaning that there was a constant supply of CO_2 at the required pressure. Once the CO_2 was released into the PVT cell, it first diffused and dissolved in the environmental fluid (water), carbonising it; the CO_2 then diffused into the pendant drop. As a result, the volume and shape of the HD changed; this was captured by the camera and later analysed to estimate the IFT and swelling.

2.1.3 Representative physical systems. Two cases have been presented to study the influence of the degree of carbonation of water surrounding the hydrocarbon on the IFT and its associated properties. For the first case, the system consists of CO_2–water–decane, and for the second, the system consists of CO_2-enriched water (CW)–decane. For simplicity, the CO_2–water–decane system will be abbreviated as CHHC and the CW–decane system will be abbreviated as CWHC. The major difference between the two systems is the level of carbonation of the water surrounding the hydrocarbon. For the CHHC system, the level of carbonation in the water increased from zero at the start to a maximum at equilibrium (function of time); for the CWHC system, the carbonation of water surrounding *n*-decane was always at 100% (100% saturated with CO_2). Coincidently, these two cases represent the fluid–fluid interactions of two different practical scenarios. Fig. 3 shows representative diagrams of these two scenarios, considering the boundary (dotted line) as the wall of the PVT cell and the oil ganglia as the pendant drop. In the first scenario (Fig. 3A), consisting of the CHHC system, the HD represents the oil ganglia (*n*-decane) surrounded by water and CO_2 represents the injected CO_2. Fig. 3B presents the second scenario, consisting of a CWHC system; the HD represents the oil ganglia surrounded by the injected carbonated water. Fig. 3A and B indicate the directions of CO_2 mass transfer (blue arrows); for the CHHC system (Fig. 3A), the CO_2 first diffuses into water and reaches the water–oil interface, then diffuses into the oil. Meanwhile, for the CWHC (Fig. 3B) system, the CO_2 directly diffuses from the CW into the oil. Although EOR processes are not covered directly in this study, the main factors that affect these processes, such as diffusion, viscosity, and interfacial tension (IFT), have been addressed.

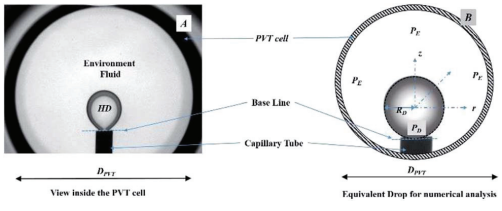

Fig. 2 (A) Pendant hydrocarbon drop with surrounding fluid as viewed in the PVT cell. (B) Equivalent surrounded spherical drop for numerical analysis.

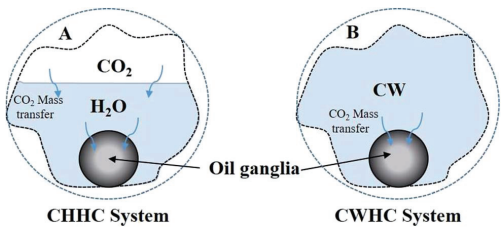

Fig. 3 Representative diagrams of the physical systems.

2.2 Mathematical model for estimation of the diffusion coefficient

The objective of the model was to estimate the diffusion coefficient of CO_2 by determining the concentration of CO_2 in the HD. The mathematical model, which was adopted from [11] with some modifications, relies on estimating the concentration of CO_2 diffused into the HD. The model employs Fick's second law of diffusion, represented by eqn (1). It can be seen from Fig. 2B that the pendant drop is symmetrical about the z-axis. Hence, it was convenient to use a cylindrical coordinate system (r, θ) rather than a complicated 3D Cartesian coordinate system (x, y, and z) to perform the three-dimensional analysis.

$$\frac{\partial C}{\partial t} = D(t)\left\{\frac{1}{r}\frac{\partial C}{\partial r} + \frac{\partial^2 C}{\partial r^2} + \frac{\partial^2 C}{\partial z^2}\right\}, \quad (1)$$

where C represents the concentration of CO_2 in the HD (kg m^{-3}) and $D(t)$ is the diffusion coefficient (m^2 s^{-1}); r and t are the radius and time, respectively. A detailed explanation of the boundary conditions for solving eqn (1) can be found in ref. 11.

Eqn (1) along with the boundary and initial conditions was numerically solved to obtain the time and space-dependent concentration of CO_2 in the drop. Then, the ratio of the CO_2 concentration in the HD (C_{avg}) as a function of time was computed (eqn (2)). The C_{avg} (mm^3) value gives the total concentration of CO_2 diffused in the HD at the required time.

$$C_{avg}(t) = \iint_{(r,z)\in P_d} \frac{C(r,z)}{C_o} r\mathrm{d}r\mathrm{d}z \quad (2)$$

The mass transfer of CO_2 into the HD leads to an increase in the volume (swelling). The magnitude of the volume increase is a function of the amount of CO_2 that diffuses into the HD. The parameter C_{avg}, given in eqn (2), gives the volume of CO_2 present in the drop; this can be used to calculate the swelling factor (SF). The swelling factor is the ratio of the volume of the CO_2-saturated hydrocarbon (CO_2 + hydrocarbon) to the initial volume of the pure hydrocarbon and is represented by eqn (3).[11]

$$\mathrm{SF} = 1 + \frac{\int_0^T \frac{\left[V_{exp}(t) - V_o\right] C_{avg}(t)\mathrm{d}t}{V_{exp}(t)^2}}{\int_0^T \frac{\left[{C_{avg}}^2(t)\right]\mathrm{d}t}{V_{exp}(t)^2}}, \quad (3)$$

where $V_{exp}(t)$ is the experimentally obtained volume of the hydrocarbon drop at time t and T is the total experimental or simulation time; V_o is the initial volume ($t = 0$) of the HD.

If CO_2 + n-decane is assumed to form an ideal mixture, at any instant of time, the summation of the initial volume of HD (V_o) and the increment in the volume of HD due to diffusion of CO_2 will equal the total volume of the HD. The increase in volume is represented as the product of C_{avg} and SF − 1,[23] as represented by eqn (4).

$$V(t) = V_o + (\mathrm{SF} - 1)C_{avg}(t) \quad (4)$$

An objective function (F) given by ref. 23 uses the difference between the experimental volume ($V_{exp}(t)$) and numerical volume ($V(t)$) of the pendant drop at a given time t. The value of the diffusion coefficient at which the objective function is minimum (F_{min}) is the diffusion coefficient of CO_2 in the HD. The lower the $F_{min,}$ the nearer the numerical result to the experimental result. A detailed process of obtaining the diffusion coefficient can be found in ref. 11.

$$F = \sqrt{\frac{1}{T}\int_0^T \frac{\left[V_{exp}(t) - V(t)\right]^2 \mathrm{d}t}{V_{exp}(t)^2}} \times 100\% \quad (5)$$

The objective function defined in eqn (5) is a function of the numerical $V(t)$ and experimental $V_{exp}(t)$ volumes. Further, F is a function of C_{avg} and the SF (eqn (4) and (5)), and C_{avg} is a function of the diffusion coefficient; this indicates that $F = f(D, \mathrm{SF})$. Hence, D and SF can be used as parameters to obtain the minimum objective function (F_{min}). The minimum objective functions (F_{min}) for D and SF are the measured CO_2 diffusion coefficient and oil-swelling factor, respectively.[23]

2.2.1 Compositional model. When a gas, such as CO_2, mixes with a fluid, such as n-decane, the composition of the binary mixture will change, altering the fluid properties (density and viscosity) of n-decane. The density values of the HD at various time intervals are helpful in estimating the experimental IFT values (this will be explained in the next section). To obtain the density or viscosity, the mass of CO_2 transferred into the hydrocarbon as a function of time must be calculated. A relatively simple compositional mode that utilizes the dynamic experimental HD volume as an input has been developed to calculate the mass/moles of CO_2 diffused into the HD (n-decane).

At any instant of time, the volume of the HD (V_{HD}) is a summation of the volume of n-decane (V_{HC}) and the volume of CO_2 (V_{CO_2}) that has diffused into the HD. The volumes of the HD as a function of time were obtained from the experiment. At the beginning of the experiment (time $t = 0$), the HD consisted of only hydrocarbon (100% n-decane), which gives V_{HC}. Hence, at a given instant, the volume of CO_2 (V_{CO_2}) is given by eqn (6).

$$V_{CO_2}(t) = V_{HD}(t) - V_{HC} \quad (6)$$

Using the volume, the mass/mole fractions of CO_2 and n-decane in HD can be obtained; these can be further used to estimate the viscosity and density of the HD. Eqn (7) proposed by ref. 26 gives the viscosity of the CO_2 + n-decane mixture. The viscosities obtained from eqn (7) have an accuracy of 1.5% average deviation for the hydrocarbon mixtures and 5% maximum deviation.[26]

$$\mu_{drop} = \left(\frac{\left(\mu_{CO_2} x_{CO_2}\sqrt{M_{CO_2}}\right) + \left(\mu_{HC} x_{HC}\sqrt{M_{HC}}\right)}{\left(x_{CO_2}\sqrt{M_{CO_2}}\right) + \left(x_{HC}\sqrt{M_{HC}}\right)}\right)_{P,T}, \quad (7)$$

where μ_{CO_2} and μ_{HC} (cP) are the viscosities of CO_2 and the hydrocarbon, respectively; x_{CO_2} and x_{HC} are the mole fractions of CO_2 and the hydrocarbon, respectively; and M_{CO_2} and M_{HC} are

the molecular weights of CO_2 and the hydrocarbon, respectively.

Eqn (8)[27–29] represents the analytical equation for the density of the HD (CO_2 + hydrocarbon) using the volume fractions derived from the experiments.

$$\rho_{drop} = ((m_{CO_2}\rho_{CO_2})+(m_{HC}\rho_{HC}))_{P,T}, \quad (8)$$

where m_{CO_2} and m_{HC} are the mole fractions of CO_2 and the hydrocarbon in the drop, respectively, and ρ_{CO_2} and ρ_{HC} are the individual densities of CO_2 and the hydrocarbon in the drop, respectively.

2.3 IFT calculations

IFT measurements were carried out using the ADSA system (KRUSS DSA 100). Diffusion of CO_2 into the HD alters the density of the HD, which is proportional to the mass of CO_2 transferred into the hydrocarbon (volume) (eqn (11)). Therefore, to perform an accurate dynamic measurement of the IFT, the density of the drop with CO_2 was input into DSA 100 software to account for the density change. The detailed process of estimating the dynamic IFT can be obtained from ref. 30.

2.4 Gibbs energy model

In this section, the Gibbs classical model is used to understand the influence of temperature on the interfacial tension between the HD and the environment fluid. The interfacial energy is directly related to the change in the Gibbs free energy (ΔG). Eyring's absolute rate theory approach gives a relation from which the viscosity of a binary liquid mixture can be estimated from the change in the Gibbs free energy, as given in eqn (9).[31] In the present article, the viscosities of both the environment (water + CO_2) and HD (CO_2 + *n*-decane) were estimated from eqn (7). The values of the viscosities were then used to calculate the change in the Gibbs free energy (ΔG).

$$\mu = \frac{hN}{V_m}\exp\left[\frac{\Delta G_m}{RT}\right] \quad (9)$$

where μ is the dynamic viscosity of the mixture (kg m^{-1} s^{-1}), h is Planck's constant (kg m^2 s^{-1}), N is Avogadro's number (mol^{-1}), V_m is the molar volume of the mixture (m^3 mol^{-1}), ΔG_m is the molar Gibbs free energy of activation for the flow process (J mol^{-1}), and T is the absolute temperature (K).

$$\Delta G_m = RT\ln\left[\frac{\mu V_m}{hN}\right] \quad (10)$$

As shown in Fig. 1–3, there are two phases, the environmental phase (water + CO_2) and drop phase (*n*-decane + CO_2); the interface layer may be assumed to be thin. Hence, the change in the Gibbs free energy for the entire system can be given by eqn (11).

$$\Delta G_S = \Delta G_E + \Delta G_{HD} \quad (11)$$

where ΔG_S is the change in free energy (J) of the system; ΔG_E is the change in free energy (J) of the environmental phase; and ΔG_{HD} is the change in free energy (J) of the drop phase. ΔG_E and ΔG_{HD} were obtained from eqn (11) and converted to J from J mol^{-1} using the calculated number of moles.

2.5 Significance of the ranges of pressure and temperature

One of the objectives of this study is to address the influence of the CO_2 phase (gas, liquid, or supercritical) on the IFT and mass transfer. Experiments have been carried out for a pressure range of 10 to 160 bar and at three temperatures, 25 °C, 45 °C and 35 °C, for pressures of 10 to 80 bar. For these pressures and temperatures, CO_2 is in a gaseous state for P < 64 bar at 25 °C and P < 73 bar at 35 °C and 45 °C; however, for P > 64 bar at 25 °C, CO_2 is in a liquid phase. Above P > 73 bar and at 35 °C and 45 °C, CO_2 is in the supercritical phase. The experimental pressure and temperature cover the whole spectrum of the CO_2 phase diagram. To our knowledge, the whole spectrum of CO_2 phases and their effects on the physical properties of these systems has not been addressed in the literature, especially for CO_2–water–hydrocarbon and CW–hydrocarbon fluid systems. For simplicity, the analysis of the gaseous phase of CO_2 (<64 bar at 25 °C and <73 bar at 35 °C and 45 °C) will be termed low-density CO_2 operation, and the analysis of the supercritical/liquid phase of CO_2 (>64 bar at 25 °C (liquid) and >73 bar at 35 °C and 45 °C (supercritical)) will be termed high-density CO_2 operation.

3 Numerical model

A numerical model has been developed to estimate the concentration distribution (spatial and temporal) of CO_2 and, hence, the diffusion coefficient in the pendant hydrocarbon drop. For simplicity, a spherical hydrocarbon pendant drop is assumed for the numerical analysis instead of the actual shape of the pendant drop. Fig. 2B shows the equivalent spherical drop surrounded by CO_2 used for the numerical analysis. In Fig. 2B, R is the radius of the spherical drop. The experimental radius obtained from the experimental pendant drop volume was used to obtain the surface area, and the radius of the equivalent drop was used for the numerical analysis. The surface area defines the rate of diffusion; hence, it was used as the comparison parameter between the pendant drop (experimental) and spherical drop (numerical). From the comparisons made, an error of 3% to 6% was found depending on the pressure of the system between the experimental and numerical drop surface area.[11] Therefore, it is justified to use a spherical drop instead of the actual pendant shape. Further, the assumption of a spherical drop reduces the effort and complexity while simultaneously maintaining minimal error in the estimation of the diffusion coefficient. The method employed in the present study was adopted from ref. 11, with a major change of the inclusion of the dynamic nature of the interface attached to the pendant drop by employing a moving boundary (this is addressed in detail in the following section).

3.1 Inclusion of the adaptive interface method in the numerical model

Most of the studies that address the diffusion coefficient have assumed a static nature for the CO_2 source–hydrocarbon interface, which is considered to have a constant volume.[23,32,33] To our knowledge, no studies have attempted to account for the effects of a dynamic interface for a 3D system. The diffusion coefficient is a function of both experimental (dynamic volume data, V_{exp}) and numerical (C_{avg}) data. From eqn (2), it can be noted that the volumetric average of CO_2 in the pendant drop (C_{avg}) is a function of the radius and, hence, of the volume of the drop.

In Fig. 2B, R_D is the radius of the HD, and the interface is always positioned at the R_D. If the volume of the HD increases, the radius will change (R_D) and the interface will shift to a new R_D; this is only possible if the model has adopted a dynamic boundary (interface). However, if the interface of the drop (boundary) is considered to be static, the interface will not shift its position according to the new R_D and will always remain at the initial position of the R_D. This will lead to inconsistencies between the numerical and experimental inputs into the model, resulting in errors in the estimation of the diffusion coefficient.

A simple method has been developed in this study to incorporate the dynamic nature of the interface (boundary), and the following steps were carried out.

(i) Initially ($t = 0$), a fixed number of grids were assigned to N and M number of grids in the r and z directions, respectively.

(ii) The volume of the drop was calculated from eqn (7) at various time intervals.

(iii) For every time interval, the volume at the present time interval ($V(t)$) was compared with the volume at the previous time interval ($V(t-1)$), and the difference between them was obtained ($V(t) - V(t-1)$).

(iv) From the difference in the volume ($V(t) - V(t-1)$), the increment in the radius of the hydrocarbon pendant drop (Δr) was estimated, which in turn gave the radial distance moved by the interface.

(v) The increment of the radius was then converted to the increment in the number of grids in the $r(N)$ and $z(M)$ directions and was added to the total number of grids in the previous time level (N, M) to obtain the updated number of grids (N_{new}, M_{new}).

(vi) The new and updated grids were then used to solve the set of equations given in the mathematical model section; this process was repeated for each time step and for every D_i of the next input step.

4 Results and discussion

Two fluid–fluid interaction systems (CHHC and CWHC) are addressed in this section. As CO_2 dissolves in water, the following reactions may take place:

$$CO_2 + H_2O \leftrightarrow H_2CO_3 \quad (a)$$

$$H_2CO_3 \leftrightarrow HCO_3^- + H^+ \quad (b)$$

$$HCO_3^- \leftrightarrow CO_3^{2-} + H^+ \quad (c)$$

In other words, there are three possible carbonate species; however, the pH of the carbonated water (CO_2-saturated water) is within 3 ± 0.5, so the dominant reaction in this work is reaction (a).

4.1 CHHC (CO_2–H_2O–hydrocarbon) system

4.1.1 Interfacial tension. Fig. 4A and B show the dynamic IFT between the environmental (CO_2 + water) and drop phases for the low-density CO_2 system (pressure ≤ 60 bar) and high-density CO_2 system (≥70 bar), respectively. Fig. 4A and B show opposite dynamic IFT trends. For the low-density CO_2 system, IFT increases with time for the tested pressures (10 to 60 bar), whereas for the high-density CO_2 system (70 to 160 bar), the IFT decreases with time. Therefore, a change in the phase of CO_2 (density) will lead to an entirely opposite trend. In the literature,[34,35] the IFT has been reported to be directly proportional to the density difference across the interface, as represented in eqn (12).

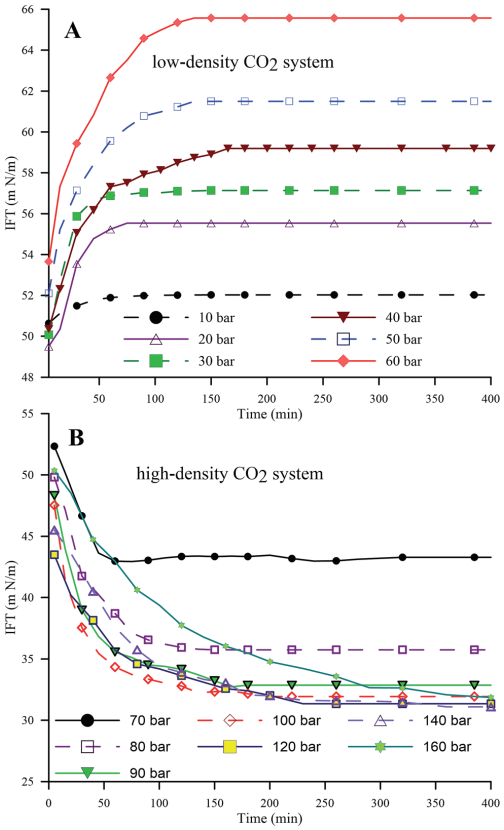

Fig. 4 Dynamic IFT of the HD in the pressure ranges of 10 to 60 bar (A) (low-density CO_2) and 70 to 160 bar (B) (high-density CO_2) at 25 °C.

$$\mathrm{IFT} = \frac{\Delta\rho g R^2}{B}, \tag{12}$$

where $\Delta\rho$ is the density difference between fluids, g is the gravitational constant, R is the radius of the drop curvature at the apex and B is the shape factor. Further,[4] showed that for a hydrocarbon system, the IFT between two immiscible fluids is proportional to the difference in the density of the fluids. Therefore, studying the density changes of the HD will give a better understanding of the observed dynamic IFT trend as the phase of CO_2 changes from gas to liquid.

Fig. 5A and B represent the dynamic density differences between the environmental fluid and the HD for the low-density and high-density CO_2 systems, respectively, for the same conditions as in Fig. 4. In Fig. 5A (≤60 bar), CO_2 is in a gaseous phase. Under these conditions, the diffusion of the gaseous CO_2 into the hydrocarbon decreases the density of the *n*-decane (drop phase),[36] whereas the dissolution of CO_2 into water (environmental phase) increases its density.[37] Thus, the density contrast between the HD and the environmental fluid increases with the CO_2 mass transfer, as observed in Fig. 5A, leading to an increase in IFT (as shown in Fig. 4A). The opposite is true for high-density CO_2; as shown in Fig. 5B, there is a small variation in the density with pressure, *i.e.* a small density difference between the environment and the HD. Therefore, lower IFT is correlated with higher pressure (>70 bar), as observed in Fig. 4B. Further, by observing the data presented in Fig. 4B, it can be seen that the IFT variations fall into two clusters. In the first cluster, the IFT reaches equilibrium more rapidly and has a higher final equilibrium IFT. In the second cluster, the IFT takes more time to reach equilibrium and the behaviour of the IFT with time is similar irrespective of whether the pressure and equilibrium IFT fall in similar value ranges. From this, the 70 and 80 bar pressures belong to the first cluster and the remaining pressures (90 to 160 bar) belong to the second cluster. The closeness of 70 bar to the phase change pressure (64 bar at 25 °C) and the similar densities of CO_2 and *n*-decane may be the reason for this behaviour of the IFT with time at 70 bar.

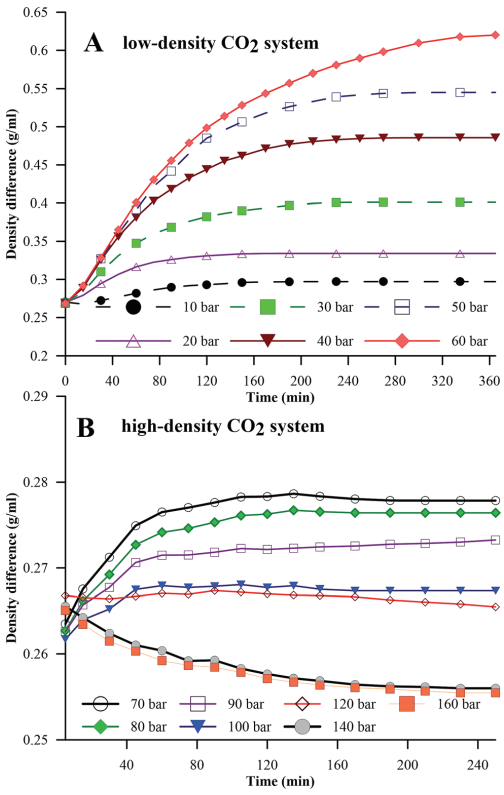

Fig. 5 Density differences between the HD and the environment for the pressure ranges of 0 to 60 bar (A) (low-density CO_2) and 70 to 160 bar (B) (high-density CO_2) at 25 °C.

From the above discussion, the density differences may, in general, offer an explanation for the inverse trend of IFT with pressure; however, density values were used in the IFT estimations, and independent physics may not provide an explanation for this trend. Hence, an attempt has been made to explain the observations in Fig. 4 through kinetics. Interfacial tension is a function of the Gibbs free energy; the lower the Gibbs free energy, the lower the IFT.[38] In the simplest form, the Gibbs free energy can be represented as in eqn (13).

$$G = H - TS, \tag{13}$$

where H is the enthalpy energy and TS is the entropy energy. At isothermal conditions, due to higher intermolecular forces, the enthalpy energy for liquids will be lower than that for gases. Therefore, at low temperatures, the Gibbs free energy will be lower for liquids compared to gases. Hence, the interfacial tension associated with systems involving liquids will be lower compared to that of systems involving gases. Therefore, from the above theory, the Gibbs free energy for the high-density CO_2 system (liquid/supercritical CO_2 + ecane) will be lower compared to the low-density CO_2 system (gas CO_2 + decane). Therefore, the IFT in Fig. 4B decreases with time and pressure, in contrast with Fig. 4A, where the IFT increases.

Fig. 6 extends this work to compare the effects of pressure on the equilibrium IFT for three temperatures (25 °C, 35 °C and 45 °C). Fig. 6 shows the IFT data for the water–*n*-decane system obtained from ref. 18 (represented by a red dashed curve). It can be observed that at isothermal conditions, the IFT at lower pressure (low-density CO_2 system) increases with pressure, while the IFT decreases with pressure for pressures in the high-density CO_2 region, as observed with the dynamic IFT. At 35 °C, the pendant drop experiments were carried out up to 70 bar because above 70 bar, repeatability could not be achieved due to the lower pixel gradient between the drop and the environment phase. The CO_2 solubility in both water and *n*-decane increases with increasing pressure; this leads to enhanced mass transfer of CO_2 into the HD, eventually leading to a decrease in the density of the HD and an increment in the density gradient across the interface. Therefore, the equilibrium IFT increases

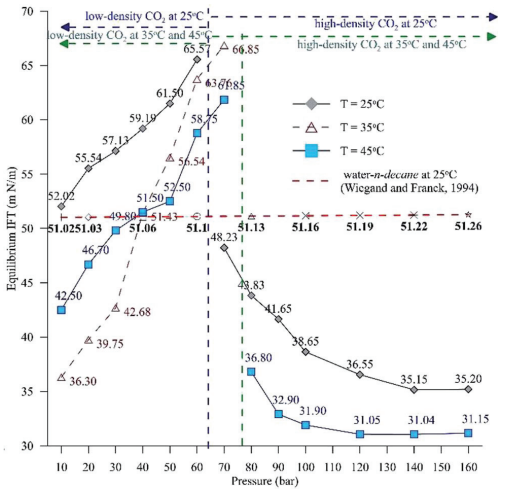

Fig. 6 Equilibrium IFT between the HD (CO_2 + *n*-decane) and the surrounding water + CO_2 for a pressure range of 10 to 160 bar at 25 °C and 45 °C and a range of 10 to 70 bar at 35 °C.

with pressure, as observed for the experiments involving low-density CO_2. This theory can be used to explain the drastic decrease in the equilibrium IFT for the high-density CO_2 region. The density difference is low (Fig. 5B) for the high density CO_2 region; this leads to an observed decrease in the IFT (Fig. 6). It can be observed from Fig. 6 that at high pressures (>120 bar), the difference in the IFT between 25 °C and 45 °C decreases and the IFT tends to remain constant. A similar observation was made by,[39] where for a supercritical CO_2–water system, they observed a small difference in IFT between 26.8 °C (300 K) and 76.85 °C (350 K).

Additionally, Fig. 6 depicts the influence of temperature on the IFT between the HD. The variation of IFT with pressure is similar for all temperatures. In the discussion of Fig. 6, it was shown that the equilibrium IFT for various pressures at isothermal conditions was related to the density difference across the interface. The theory that the density difference is proportional to IFT applies well at isothermal conditions; however, it falters when the temperature is varied at isobaric conditions. It can be observed from Fig. 6 that up to 30 bar, the IFT at 35 °C is lower than that at 45 °C. Above 30 bar (40 to 60 bar), the IFT at 35 °C increases and the IFT *vs.* temperature returns to normal behaviour, with IFT being maximum for 25 °C, minimum for 45 °C and intermediate for 35 °C. Similar observations have been made in a few studies[40,41] for different systems. This observation also deviates from both the CO_2–*n*-decane system[11] and H_2O–*n*-decane system,[17] where at isobaric conditions, the IFT decreases as the temperature increases. The reason for the observed behaviour of IFT at 35 °C may be the nearness of 35 °C to the critical temperature (31.1 °C) of CO_2; hence, it is possible that the entropy of CO_2 will be high. Higher entropy (*S*) will decrease the Gibbs free energy (eqn (13)) and eventually decrease the IFT. To check this hypothesis, the Gibbs free energies (change) obtained from the viscosity of the HD (eqn (10)) have been plotted in Fig. 7 at experimental conditions. In Fig. 7, the section consisting of pressures from 10 to 50 bar has been magnified; it can be observed that for the pressure range of 10 to 40 bar, ΔG is the lowest at 35 °C, higher at 45 °C, and reaches the maximum at 25 °C. Above 40 bar, the ΔG at 35 °C is intermediate between those at 25 °C (maximum) and 45 °C (minimum). Hence, from the observations in Fig. 7, it can be said that up to a certain pressure, the influence of the increase in entropy (decrease in ΔG) due to the temperature increase is greater than the influence of the difference in density. This explains the behaviour of the IFT *vs.* pressure in Fig. 6 at 35 °C.

4.1.2 Diffusion coefficients. Fig. 8 shows the estimated effective diffusion coefficients of CO_2 in the HD for the CHHC system in the pressure range of 10 to 160 bar at 25 °C and 45 °C and of 10 to 70 bar at 35 °C. At isothermal conditions, for low-density CO_2 operation, the diffusion coefficient decreases as the pressure is increased. However, previous studies on CO_2–hydrocarbon systems[23,33,42] have shown that the diffusion

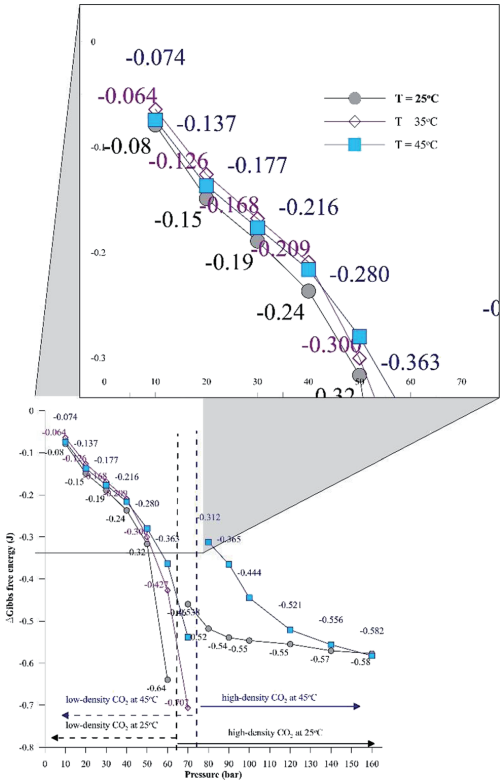

Fig. 7 Changes in Gibbs free energy at equilibrium conditions for the CHHC system at 25 °C, 35 °C, and 45 °C and for a pressure range of 10 to 160 bar.

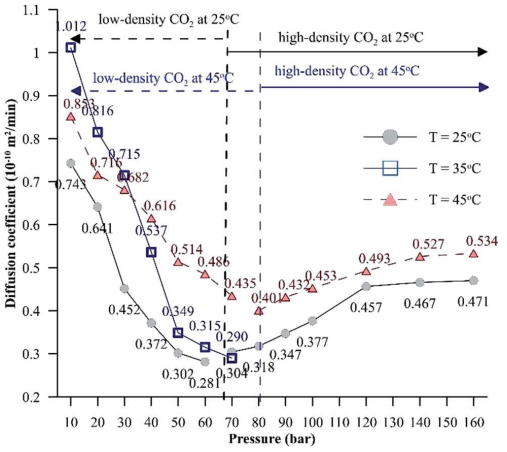

Fig. 8 Effective diffusion coefficients of CO_2 in the HD for a pressure range of 10 to 160 bar at different temperatures.

coefficient increases with increasing pressure. There is a major difference between the present fluid system and those presented in the literature. As depicted in Fig. 3, in the present study, there is water between the hydrocarbon and the CO_2. The CO_2 first diffuses and then dissolves in the water surrounding the hydrocarbon; then, the CO_2 diffuses from the carbonated water into the hydrocarbon.

Unlike for low-density CO_2 systems, for high-density CO_2 systems, the diffusion coefficient shows an increasing trend with pressure. At isothermal conditions, due to higher intermolecular forces, the enthalpy energy and, hence, the Gibbs free energy will be lower for liquids compared to gases. Hence, the interfacial tension associated with systems involving liquids (high-density CO_2 systems) will be lower compared to that associated with systems involving gases (low-density CO_2 systems), which will assist the mass transfer of CO_2. Further, as the temperature increases, the entropy energy (TS) increases. The dissolution of CO_2 in the hydrocarbon is exothermic in nature; for exothermic reactions, the enthalpy change has a negative value. Therefore, the change in Gibbs energy ($\Delta H - \Delta TS$) will be negative, resulting in a higher diffusion coefficient at higher temperatures. The CO_2 solubility in water shows signs of reaching a constant value or increases by a small magnitude as the pressure is increased beyond 120 bar at both 25 °C and 45 °C. This further explains why the diffusion coefficient of CO_2 reaches a constant value or increases by a small magnitude with increasing pressure.

4.1.3 Temperature influence on the diffusion coefficient. Similar to IFT (Fig. 6), temperature has a complex effect on the diffusion coefficient, especially for low-density CO_2 operation. Most studies[11,43] have shown that for a CO_2–hydrocarbon system, the diffusion increases as the temperature is increased. This held true when we observed the variation of the diffusion coefficients at 25 °C and 45 °C; however, at 35 °C, the behavior is complex, as shown in Fig. 8. It can be observed from Fig. 8 that up to 30 bar, the diffusion coefficient at 35 °C is higher than that at 45 °C. Above 30 bar (40 to 60 bar), the diffusion coefficient at 35 °C decreases and returns to a normal value. The observation in Fig. 8 is analogous to the observations of the equilibrium IFT in Fig. 6 and of ΔG in Fig. 7. Therefore, at 35 °C, for 0 to 30 bar there is lower resistance (lower IFT and ΔG) and higher resistance (higher IFT and ΔG) at 40 to 60 bar to the CO_2 mass transfer rate into the HD containing n-decane compared to that at 45 °C. This explains the observed (Fig. 8) behaviour of the diffusion coefficient at 35 °C for low-density CO_2 operation.

4.2 Comparison of the CHHC (CO_2–H_2O–hydrocarbon) and CWHC (CW–hydrocarbon) systems

Fig. 9A shows the differences in the concentration of CO_2 between the HD and the environment fluid for both the CWHC and CHHC systems as a function of time for 20, 40, 70, and 100 bar at 25 °C. For the CWHC system, the water surrounding the HD is enriched with CO_2 (CW), while in the CHHC system, the concentration of CO_2 varies from zero to a maximum. This

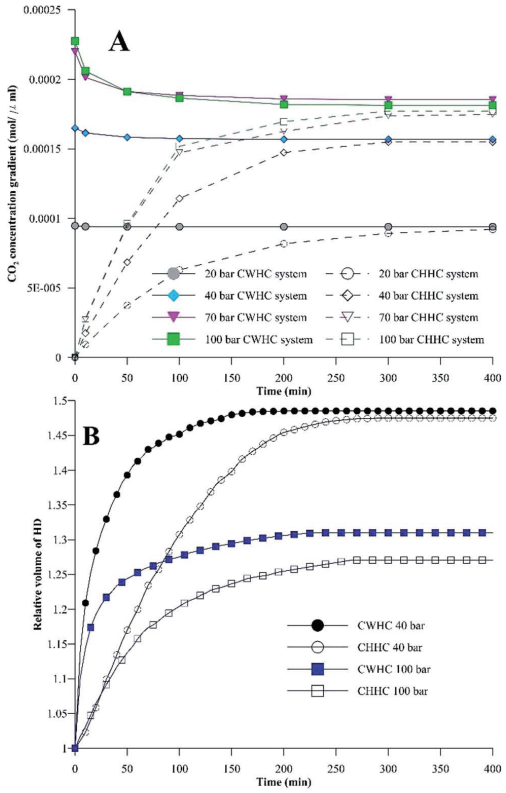

Fig. 9 (A) Concentration of CO_2 between the HD (n-decane) and the surrounding environment for the CWHC and CHHC systems. (B) Relative volumes of the HD for the CWHC and CHHC systems.

difference in the CO_2 concentration in the water surrounding the HD has a major impact on the CO_2 concentration gradient and, hence, the mass transfer of CO_2 into the HD. The concentration difference profiles for the CWHC and CHHC systems are contrary to each other (Fig. 9A); for the CWHC system, the concentration difference changes from the maximum to equilibrium as the diffusion progresses, while for the CHHC system, it changes from zero to equilibrium. Hence, during the start of the CO_2 diffusion, the concentration gradient for the CWHC system is greater than that of the CHHC system, which may lead to more rapid mass transfer of CO_2 for the CWHC system compared to the CHHC system. Due to this, the rate of the increase in volume would be more rapid for the HD surrounded by CW (CWHC) than for the HD surrounded by water and CO_2 (CHHC system), as can be seen in Fig. 9B. However, it can observed in Fig. 9A that for the CWHC system, the concentration difference soon reaches a constant value, indicating a possible decrease in the rate of CO_2 mass transfer and, hence, the observed change in the slope of the evolution of the volume (Fig. 9B). On the other hand, the concentration difference for the CHHC system increases with time and reaches a constant volume later, resulting in the prolonged lower but steadily increasing volume (Fig. 9B). Further, the higher concentration gradient may also explain the observed faster attainment of equilibrium (CO_2 saturation) by the HD for the CWHC system compared to the CHHC system, as shown in Fig. 9B. It can be observed in Fig. 9B for the low-density CO_2 system (40 bar) that although the evolution of the volume is different, the equilibrium volumes are similar for the CWHC and CHHC systems. However, for high-density CO_2 operation (Figure 9B, 100 bar), the equilibrium volume of the CWHC system is greater than that of the CHHC system.

Fig. 10 compares the IFT values for the CHHC (CO_2–H_2O–*n*-decane) and CWHC (CW–*n*-decane) systems at 25 °C for a pressure range of 10 to 160 bar. It can be observed that the variations of IFT with pressure are similar for the CHHC and CWHC systems. Hence, the explanations provided in sections 4.1.1 and 4.1.2 hold true for the CWHC system. However, it can be observed from Fig. 10 that the IFT is lower for the CWHC system than for the CHHC system at all experimental pressures. For low-density operation, the IFT of the CWHC system decreases by approximately 17% at 10 bar to 3% at 60 bar. Meanwhile, for high-density operation, an average 6% decrease in the IFT was observed for the CWHC system compared to the CHHC system. Overall, it can be said that the decrease in the equilibrium IFT by CWHC is insignificant, especially at high pressures. Although small, the decrease in the IFT for the CWHC system compared to the CHHC system can be explained by the differences in CO_2 concentration presented in Fig. 9A. Even though the concentration difference of CO_2 is higher for the CWHC system compared to the CHHC system, it can be observed (Fig. 9A) that for the CWHC system, the concentration difference of CO_2 reaches a constant substantially earlier (around 120 to 250 min) than that of the CHHC system (after 300 min). Hence, there may be a slower but higher mass transfer of CO_2 into the HD for the CHHC system compared to the CWHC system; this would alter the overall density difference across the interface, resulting in a marginally higher IFT for the CHHC system. Further, it can observed from Fig. 9B that for the CWHC system, the increase in the volume of the HD occurs mainly during the initial part and reaches a plateau rapidly. This indicates that mass transfer mainly occurs during the initial phase of CO_2 diffusion, in contrast with the CHHC system, where both the volume (Fig. 9B) and concentration difference (Fig. 9A) change gradually and linearly compared to those of the CWHC system.

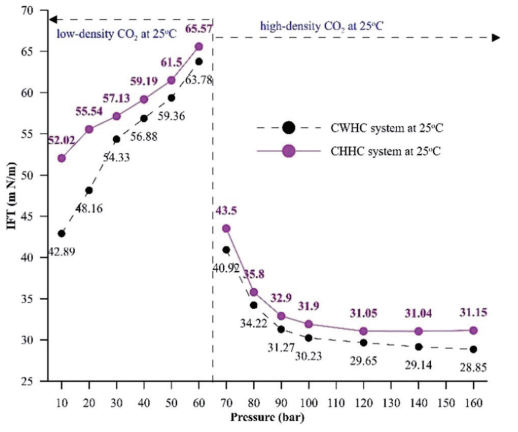

Fig. 10 Equilibrium IFT values for CHHC and CWHC system at 25 °C for a pressure range of 10 to 160 bar.

5 Conclusions

The present work, through experimental, mathematical, and numerical studies, addresses the fundamental aspects of interfacial tension and its associated physics in a CO_2–H_2O–decane system and compares them with those in a CW–decane system. The following conclusions were made from the analysis.

The presence of a water layer between CO_2 and the hydrocarbon leads to unique behaviour which is unlike that of CO_2–hydrocarbon or water–hydrocarbon systems. For gaseous CO_2 operation, the IFT increases exponentially with pressure, which is opposite to that observed in a CO_2–hydrocarbon system. Compared to the water–*n*-decane system, the dissolution of CO_2 in water and the hydrocarbon increases the IFT for low-density operation and decreases the IFT for high-density operation. The dissolution of CO_2 into the water surrounding the hydrocarbon alters the density difference across the interface, leading to the observed behaviour. Although the presence of a water layer increased the IFT of the system, it was successful in increasing the swelling compared to the CO_2–hydrocarbon system.

The phase of CO_2 has a significant effect on IFT; the IFT behaviour with pressure reverses when the phase of CO_2 changes. When gaseous CO_2 is in operation (low-density), the IFT increases exponentially with increasing pressure. However, as the operation shifts to supercritical and liquid CO_2 (high-

density), the IFT decreases with increasing pressure. The changes in CO_2 solubility with pressure and the consequent alterations to the density are credited for this behaviour. Further, the phase of CO_2 was also a major factor in the variations of the density, diffusion coefficient, and concentration gradient. Each of these parameters experienced a reversal in its behaviour with pressure as the phase of CO_2 changed. The maximum density decrease of the hydrocarbon, maximum IFT, and minimum diffusion coefficient were obtained at pressures near and below the phase change pressure of CO_2.

The IFT for various pressures at 25 °C was found to be directly proportional to the density difference. This theory applies well to isothermal conditions; however, it falters when the temperature is varied at isobaric conditions. At isobaric conditions, for low-pressure operation, the IFT at 35 °C is lower than at 45 °C; as the pressure increases, the IFT at 35 °C increases and is between those at 25 °C and 45 °C. As indicated by the Gibbs energy model, at 35 °C (close to the critical temperature of 31.1 °C), the system entropy is high; hence, the Gibbs free energy and IFT decrease.

Although the IFT of the CO_2–water–hydrocarbon and CW–hydrocarbon systems has the same trends, there is a significant difference in the concentration gradient of CO_2 across the interface; hence, the IFT and molecular diffusion are different.

Conflicts of interest

There is no conflict of interest to declare.

References

1 M. S. A. Perera, R. P. Gamage, T. D. Rathnaweera, A. S. Ranathunga, A. Koay and X. Choi, *Energies*, 2016, **9**, 481.
2 M. Riazi, M. Sohrabi and M. Jamiolahmady, *Transp. Porous Media*, 2011, **86**, 73–86.
3 B. Wen, C. Sun, B. Bai, E. Y. Gatapova and O. A. Kabov, *PCCP*, 2017, **19**, 14606–14614.
4 M. Ghorbani and A. H. Mohammadi, *J. Mol. Liq.*, 2017, **227**, 318–323.
5 M. Riazi, M. Sohrabi, M. Jamiolahmady and S. Ireland, *Oil recovery improvement using CO_2-enriched water injection, EUROPEC/EAGE Conference and Exhibition*, Society of Petroleum Engineers, 2009, DOI: 10.2118/121170-MS.
6 N. I. Kechut, M. Sohrabi and M. Jamiolahmady, Experimental and numerical evaluation of carbonated water injection (CWI) for improved oil recovery and CO_2 storage, *SPE EUROPEC/EAGE Annual Conference and Exhibition*, Society of Petroleum Engineers, 2011, DOI: 10.2118/143005-MS.
7 Z. Zhang, *J. Nat. Gas Sci. Eng.*, 2016, **31**, 589–595.
8 Z. Zhang, Y. Li, W. Zhang, J. Wang, M. R. Soltanian and A. G. Olabi, *Renewable Sustainable Energy Rev.*, 2018, **98**, 179–188.
9 L. Jiang, M. Yu, B. Wu, T. Suekane, W. Li and Y. Song, *RSC Adv.*, 2016, **6**, 114320–114328.
10 D. Yang, P. Tontiwachwuthikul and Y. Gu, *J. Chem. Eng. Data*, 2005, **50**, 1242–1249.
11 N. Bagalkot and A. A. Hamouda, *Ind. Eng. Chem. Res.*, 2017, **56**, 2359–2374.
12 J. J. Hsu, N. Nagarajan and R. Robinson Jr, *J. Chem. Eng. Data*, 1985, **30**, 485–491.
13 D. Yang and Y. Gu, *Ind. Eng. Chem. Res.*, 2008, **47**, 5447–5455.
14 S. Banerjee, E. Hassenklöver, J. M. Kleijn, M. A. Cohen Stuart and F. A. Leermakers, *J. Phys. Chem. B*, 2013, **117**, 8524–8535.
15 A. Shariat, R. G. Moore, S. A. Mehta, K. C. Van Fraassen, K. E. Newsham and J. A. Rushing, Laboratory measurements of CO_2-H_2O interfacial tension at HP/HT conditions: Implications for CO_2 sequestration in deep aquifers, *Carbon Management Technology Conference*, 2012, DOI: 10.7122/150010-MS.
16 B.-Y. Cai, J.-T. Yang and T.-M. Guo, *J. Chem. Eng. Data*, 1996, **41**, 493–496.
17 G. Wiegand and E. Franck, *Ber. Bunsenges. Phys. Chem.*, 1994, **98**, 809–817.
18 F. Moeini, A. Hemmati-Sarapardeh, M.-H. Ghazanfari, M. Masihi and S. Ayatollahi, *Fluid Phase Equilib.*, 2014, **375**, 191–200.
19 D. Mackay and K. Hossain, *Can. J. Chem. Eng.*, 1982, **60**, 546–550.
20 B. Honarvar, A. Azdarpour, M. Karimi, A. Rahimi, M. Afkhami Karaei, H. Hamidi, J. Ing and E. Mohammadian, *Energy Fuels*, 2017, **31**, 2740–2748.
21 P. Linstrom and W. Mallard, *J. Chem. Eng. Data*, 2001, **46**, 1059–1063.
22 Y.-B. Chang, B. K. Coats and J. S. Nolen, A compositional model for CO_2 floods including CO_2 solubility in water, Paper SPE 35164, *SPE Permian Basin Oil and Gas Recovery Conference*, Midland, Texas, USA, March, 1996, pp. 27–29, DOI: 10.7122/150010-MS.
23 C. Yang and Y. Gu, *Ind. Eng. Chem. Res.*, 2005, **44**, 4474–4483.
24 M. Sohrabi, M. Riazi, M. Jamiolahmady, S. Ireland and C. Brown, Mechanisms of oil recovery by carbonated water injection, *SCA annual meeting, 2009 (International Symposium of the Society of Core Analysts)*, Noordwijk, The Netherlands, 27–30 September, 2009, Article Number: SCA2009-26, p. 12.
25 M. Riazi, M. Jamiolahmady and M. Sohrabi, *J. Pet. Sci. Eng.*, 2011, **75**, 312–326.
26 F. Herning and L. Zipperer, *Gas Wasser*, 1936, **79**, 69.
27 M. McBride-Wright, G. C. Maitland and J. M. Trusler, *J. Chem. Eng. Data*, 2014, **60**, 171–180.
28 M. E. Kandil, N. M. Al-Saifi and A. S. Sultan, *Int. J. Greenhouse Gas Control*, 2016, **53**, 198–206.
29 J. Zambrano, F. V. Gómez-Soto, D. Lozano-Martín, M. C. Martín and J. J. Segovia, *J. Supercrit. Fluids*, 2016, **110**, 103–109.
30 N. Bagalkot, A. A. Hamouda and O. M. Isdahl, *MethodsX*, 2018, 676–683.
31 R. J. Martins, M. J. d. M. Cardoso and O. E. Barcia, *Ind. Eng. Chem. Res.*, 2000, **39**, 849–854.
32 N. Bagalkot and A. A. Hamouda, *Ind. Eng. Chem. Res.*, 2017, **56**, 2359–2374.
33 C. Yang and Y. Gu, *Fluid Phase Equilib.*, 2006, **243**, 64–73.
34 C. E. Stauffer, *J. Phys. Chem.*, 1965, **69**, 1933–1938.

35 E. Y. Arashiro and N. R. Demarquette, *Mater. Res.*, 1999, **2**, 23–32.
36 J. S. Miller and R. A. Jones, *SPE/DOE Enhanced Oil Recovery Symposium*, Tulsa, USA, 1981.
37 M. Sohrabi, M. Riazi, M. Jamiolahmady, N. I. Kechut, S. Ireland and G. Robertson, *Energy Procedia*, 2011, **4**, 2192–2199.
38 B. Honarvar, A. Azdarpour, M. Karimi, A. Rahimi, M. Afkhami Karaei, H. Hamidi, J. Ing and E. Mohammadian, *Energy Fuels*, 2017, **31**, 2740–2748.
39 S. Iglauer, M. Mathew and F. Bresme, *J. Colloid Interface Sci.*, 2012, **386**, 405–414.
40 W. Karnanda, M. Benzagouta, A. AlQuraishi and M. Amro, *Arabian J. Geosci.*, 2012, 1–10.
41 A. Zolghadr, M. Escrochi and S. Ayatollahi, *J. Chem. Eng. Data*, 2013, **58**, 1168–1175.
42 M. Jamialahmadi, M. Emadi and H. Müller-Steinhagen, *J. Pet. Sci. Eng.*, 2006, **53**, 47–60.
43 A. Georgiadis, G. Maitland, J. M. Trusler and A. Bismarck, *J. Chem. Eng. Data*, 2010, **55**, 4168–4175.

PAPER — VII

Effect of slats on the interfacial tension and CO_2 mass transfer in carbonated water injection process

RSC Advances

ARTICLE

Influence of salts on interfacial tension and CO_2 mass transfer in carbonated water injection

Received 00th January 20xx,
Accepted 00th January 20xx

DOI: 10.1039/x0xx00000x

www.rsc.org/

Aly A Hamouda [*a] and Nikhil Bagalkot[b]

Carbonated water injection (CWI) is a promising enhanced oil recovery (EOR) and CO_2 sequestration methods, which overcomes the problems associated with CO_2 EOR. CO_2 mass transfer and interfacial tension (IFT) are important parameters that influence the oil recovery efficiency. This study addresses the impact of $MgCl_2$ and Na_2SO_4 in carbonated water (CW) on CW/hydrocarbon IFT and CO_2 mass transfer. The IFT was measured by axisymmetric drop shape analysis method (50-100 bar, 45°C) and a numerical model that couples with experimental results was developed to calculate the CO_2 diffusion coefficient. It was found that CW+$MgCl_2$ reduced both the CW/n-decane IFT (36.5%) and CO_2 mass transfer, while CW+Na_2SO_4 increased both the IFT and CO_2 mass transfer (57%). It is suggested that reduction in IFT for CW+$MgCl_2$ brine is mainly due to the higher hydration energy of Mg^{2+}. The Mg^{2+} ion forms a tight bound to the first hydration shell $[Mg(H_2O)_6]^{2+}$, this increases the effective size at the interface, hence reduce IFT. While the SO_4^{2-} outer hydration shell has free OH groups, which may locally promote CO_2 mass transfer. The study illustrates the potential of combination of salts and CW in enhancing CO_2 mass transfer that can be the base for further investigations.

1. Introduction

Recent years has seen an increased interest in carbonated water injection (CWI) as secondary/tertiary enhanced oil recovery (EOR) method. CWI has been projected as a substitute to the CO_2 EOR to overcome challenges such as poor sweep efficiency, and early breakthrough [1]. Low sweep efficiency associated with CO_2 EOR due to gravity segregation and capillary instabilities causes mobility issues [1, 2]. For CWI, the CO_2 is dissolved in water and has higher density; this reduces gravity segregation, thereby improving the sweep efficiency. Further, for CWI an increased mobility of oil is observed as a result of a reduction in the viscosity of the oil resulting from the dissolution/diffusion of CO_2, which enhances sweep efficiency [2]. Figure 1 (inspired from [2]) shows the pictorial representation between comparison between CO_2 EOR and CWI regarding sweep efficiency and sweep profile. Another problem with CO_2 EOR is that in many of the cases, CO_2 is not readily available in the required volumes. Therefore, the transportation of CO_2 becomes necessary, which increases the utilisation costs. CWI, which requires less amount of CO_2, partially reduces the costs associated with transport. CWI is also of interest due to its capability

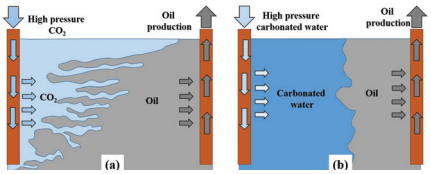

Figure 1: Pictorial representation of sweep front for the case of (a) CO_2 flooding and (b) Carbonated water injection.

of coupling oil recovery and CO_2 sequestration. Dissolved CO_2 in water (carbonated water) has higher density compared to native brine (formation water). Hence, it sinks into the bottom of the reservoir, eliminating the risk of buoyancy-driven leakage of CO_2 [3-6], thus improving CO_2 sequestration capability.

At pore scale, the rock wettability defined by rock-fluid interaction, capillary pressure through interfacial tension, and swelling and mobility through CO_2 mass transfer (oil-CW interaction) are the primary mechanisms responsible for governing the oil recovery by CWI. Various ways have been described in the literature (nanofluid, microbial, polymer, and salts) to address the fluid-fluid and fluid-rock interactions as EOR methods. In recent years more attention is directed to low salinity water studies [7, 8], which indicated wettability and interfacial alteration. The potential of saline water to change the wettability of the rock has been well established [9, 10], and has been extended to CWI by [11]. Previously carried out studies [9, 12-14] have presented extensive data on the interfacial tension between brine/hydrocarbon and few studies [7, 15] have also been dedicated to carbonated brine/hydrocarbon [11]. Table 1 gives a

[a] Department of Energy and Petroleum, University of Stavanger, Norway, 4036, email: aly.hamouda@uis.no
[b] Department of Energy and Petroleum, University of Stavanger, Norway, 4036, email: nikhil.bagalkot@uis.no

Electronic Supplementary Information (ESI) available: [details of any supplementary information available should be included here]. See DOI: 10.1039/x0xx00000x

RSC Advances

ARTICLE

Table 1: IFT obtained by different studies for brine/hydrocarbon and carbonated brine/hydrocarbon systems.

References	Type of aqueous systems	Experimental conditions	Observations
		Reduction in IFT	
9	n-decane/brine with $MgCl_2$ and Na_2SO_4	82.4 to 158°C, atmospheric pressure	IFT reduction in the presence of $MgCl_2$ and Na_2SO_4 compared to distilled water
16	*n*-dodecane/brine with sodium dodecyl sulfate (SDS) and NaCl	25°C, atmospheric pressure	The presence and rising surfactant concentration leads to a reduction in the IFT
17	Crude oil/brine with Na^+, K^+, Cl ,Mg^{+2}, and Ca^{+2} ions	25°C, atmospheric pressure	The presence of divalent ions (Ca^{+2} and Mg^{+2}) decreases the oil/brine IFT. At a given concentration Mg^{+2} shows a lower oil/brine IFT than Ca^{+2}.
		Increment in IFT	
18	n-hexane/water with NaCl	25°C, 0 to 100 Mpa	Increment in IFT due to the presence of NaCl in water
13	normal alkane + water/brine with NaCl, $CaCl_2$, $MgCl_2$	25 to 80°C,1 to 300 bar	Increase in IFT due to the presence of salt. Weakly dependent on pressure and salt species.
19	Toluene, n-hexane and cyclohexane/brine with NaCl, $NaHCO_3$, Na_2SO_4	20°C to 75°C, atmospheric pressure	For all the salts an increment in IFT has been observed.
		Salt-dependent IFT variation	
20	Crude oil/brine with NaCl, KCl, Na_2SO_4, $MgSO_4$, $CaSO_4$, $CaCl_2$, and $MgCl_2$	Ambient temperature and pressure	Reduction in IFT at high salinity conditions especially for $MgCl_2$. The increment in IFT for monovalent salts such as NaCl and KCl is used
21	n-dodecane-decane/brine with LiCl, NaCl, KCl, KBr, NaBr, KI and Na_2SO_4	20°C, atmospheric pressure	Reduction in IFT in the presence of KI. An increment in IFT for rest of the salts.
		IFT of carbonated brine/hydrocarbon system	
15	Crude oil/carbonated water with NaCl, $CaCl_2$, $MgCl_2$, KCl, and Na_2SO_4	75°C, pressure up to 137 bar	Presence of salt reduces the IFT and is a function of the type of salt
7	Crude oil/ carbonated brine with NaCl, $CaCl_2$, $MgCl_2$, KCl, $MgSO_4$, K_2SO_4, and Na_2SO_4	75°C, up to 140 bar	Salts are able to reduce the IFT. Addition of CO2 further enhances the reduction in IFT. Minimum IFT was obtained for $MgCl_2$+K_2SO_4 combination.
22	n-decane/ carbonated synthetic sea water with silica nanofluid	25°C and 45 °C, 10 to 90 bar	Marginal reduction in IFT for the combination of salt and CO2 in water.

summary of work done in the literature on the effect of salts on IFT. Table 1 has been divided into different sections (increasing IFT, decreasing IFT, salt dependent IFT variation, and IFT of carbonated brine/hydrocarbon

systems) depending on the investigations made by the various studies. It may be observed from Table 1 that there are controversial trends of the IFT trend. For example [9] and [16] showed that salts reduced the IFT. Whereas [18] and [13] observed that salts increased the IFT. Further, [21] and [20] have observed both an increase and decrease in IFT, and concluded that the variation of IFT is a function of the composition of the brine. Additionally, the increase or decrease in IFT was also found to be the function of concentration of salt [16, 17]. Not all the salts will have same effect on the IFT, there may be certain type of salts which would have more prominent effect on reducing the IFT that others. [9], [17], and [20] observed that $MgCl_2$ specifically Mg^{+2} ions leads to lower IFT compared to other salts or ions present in their study. [21] showed other out of 7 different salts only KI was able to lower the IFT of n-dodecane and n-decane/brine while other lead to an increase in IFT. [13] observed the IFT of normal alkane+brine is weakly dependent on slat species. Therefore, there is a contrasting observation for IFT. Hence, there is a need for further investigations. For CW+salt/hydrocarbon system, there are a limited number of studies available [7, 15]. Unfortunately, this is not sufficient data to understand the critical interfacial phenomena occurring between brine CW/hydrocarbon. This has motivated the authors to comprehensively investigate the influence of salts on the CW/hydrocarbon interfacial tension.

The mass transfer of CO_2 and the resulting mechanisms like swelling and enhanced mobility of the oil dictate the degree of oil recovery in a CO_2 based EOR methods [4, 23]. From the above discussion and the Table 1 it may be said that till to date, the majority of the studies have concentrated on examining interfacial and wettability aspects of CO_2/oil, CW/oil, water/oil, and carbonated smart water/oil systems. However, there is a lack of understanding of CO_2 mass transfer, factors influencing CO_2 mass transfer, especially when it comes to CW/hydrocarbon systems. The diffusive mass transfer of gases, especially CO_2 into oil is of primary importance when it comes to CO_2 and CW flooding. Diffusion of CO_2 into oil results in the reduction of viscosity, and displacement of oil (including heavy oil) from reservoirs to surface. Few studies have looked into the aspect of CO_2 mass transfer, and most of these studies are related to CO_2/hydrocarbon [24-26] or CO_2/water [27] systems. The number of studies diminishes when it comes to CW/hydrocarbon system [28]. Further, there may be a significant neglect on the application of salts as a CO_2 mass transfer enhancement tool for CW/hydrocarbon system. [29] in their study on syngas, fermentation have experimentally shown that the salts in water may enhance the mass transfer of gas in water. [29] showed that the ions of dissolved salts in water stopped the coalesces of CO bubbles thereby increasing the surface area between CO and water. [30] showed that salts in water increased the entropy of the solution, this enhances the mobility leading to a convective movement in bulk liquid, and may enhance the mass transfer. Conventionally, salts in water have been viewed as wettability and IFT modifiers; however salts may have more valuable potential and may also be used as CO_2 mass transfer enhancement tool, and this widens the scope of applicability of salts. Therefore, investigations are needed in order to establish if salts can improve the CO_2 mass transfer in CW/hydrocarbon system.

Previous studies have developed various methods to understand the CO_2 mass transfer by estimating the diffusion coefficient of CO_2 in bulk liquids. These methods may be put into two groups, compositional analysis [31, 32], and pressure decay [33, 34] methods. In the compositional analysis errors will be caused in the extraction of the sample from the setup and carrying out gas chromatography, especially at high pressures and temperatures, this may affect the estimation of the diffusion coefficient [26]. Further, the compositional method is time-consuming, complicated, and expensive [35]. The pressure decay method solves the problems associated with the compositional analysis. However, it requires long experimental time (20 hours to 100 hours or more). Additionally, the diffusion coefficient obtained by pressure decay method is not for a particular pressure but a range of pressures [26, 36]. Hence, there is a requirement for a well-established, reliable, quicker, and simple method for estimating the diffusion coefficient of CO_2 in hydrocarbon, which may be used for both gas-liquid and liquid-liquid systems. In recent years the Axisymmetric Drop Shape Analysis (ADSA) using pendant drop equipment coupled with a computational scheme has been used to estimate the diffusion coefficient of gases into liquids [24, 25]. The experiments using ADSA can be carried out at high temperature and pressure (up to 60 MPa and 180°C) [28]. Further, unlike the pressure decay method, the experiments using the ADSA pendant drop technique can be carried out at isothermal and isobaric conditions. The flexibility, simple, lesser time, and devoid of any human interference makes the ADSA method suitable for calculating the diffusion coefficient of gases into the bulk liquids. The ADSA pendant drop technique is also widely used to estimate the interfacial tension between two fluid at elevated pressure and temperature [37]. The ADSA method has an accuracy of ±0.05 mN/m^2 when estimating the IFT [37, 38]. Therefore, by using the ADSA method both mass transfer and interfacial studies may be carried out using the same experimental setup and with higher accuracy.

From the above discussion on literature studies, two crucial points may be made. First, the studies and knowledge on the influence of salts on the CW/hydrocarbon IFT are insufficient. Dynamic IFT analysis has been entirely neglected, and there are some opposing trends on the influence of salts on brine/hydrocarbon IFT. Second and important one, there is significant overlooking of effects of salts on CO_2 mass transfer. Therefore, there is a lack of understanding of CO_2

mass transfer, factors influencing CO_2 mass transfer, especially when it comes to CW/hydrocarbon systems. The present work tries to address these issues. As a result, the objective of the present study is to investigate the impact of salts in CW, particularly Na_2SO_4 and $MgCl_2$ in altering the CW/hydrocarbon IFT and enhancing the CO_2 mass transfer. In fulfilling these objectives, the study adds four major contributions to the existing knowledge of CW/hydrocarbon systems. First, the experiments were designed to analyse both dynamic and equilibrium IFT, and simultaneously carry out mass transfer studies. Second, the experimental pressure range (50-100 bar) was chosen to study the influence of the phase of both gaseous and supercritical phase of CO_2 on the mass transfer and IFT. Third, to the best of authors knowledge, this would be the first time the impact of salts on the CW/hydrocarbon as a combined mechanism of interfacial tension and the mass transfer enhancement tool will be addressed. Fourth, a relatively new and advanced numerical model, which couples with experimental results to estimate the CO_2 diffusion coefficient at-large range of pressure and temperate has been developed. The present study through experimental, theoretical, and numerical model analyse the influence of salts on the interfacial and mass transfer aspects of CW/hydrocarbon system. Axisymmetric Drop Shape Analysis (ADSA) pendant drop experiments have been carried out for a pressure range of 50-100 bar at 45°C. The study will focus on the effect of $MgCl_2$ and Na_2SO_4 on IFT and diffusion coefficient.

2. Experimental and numerical methodology

Figure 2a shows the cross-section of the see-through high-pressure cell (PVT-cell) where the experiments were carried out. The pendant hydrocarbon drop (HD) consisting of n-decane will be termed as drop phase, and the drop phase is surrounded by environmental fluid consisting of salts dissolved in carbonated water termed as carbonated brine (CB). The mass of the CO2 in the brine surrounding the drop phase is always monitored and maintained at the saturation limit. The solubility of CO2 is higher in hydrocarbons compared to water or brine, therefore, when the hydrocarbon contacts the CB, the CO2 from the CB diffuses into the drop phase. The resulting mass transfer of CO2 is driven by the concentration gradient between the drop phase and the environmental fluid. The mass transfer of CO2 depends on the IFT, CO2 solubility, density gradient, and experimental conditions. When salts are dissolved in water, they release ions. Depending on the type of salts these ions may be surface active or interface repelling. The ions are responsible for altering the interfacial tension of the CW/oil system. Since salts in water are capable of altering the IFT, then there may be a possibility that they may also influence the mass transfer occurring across the interface.

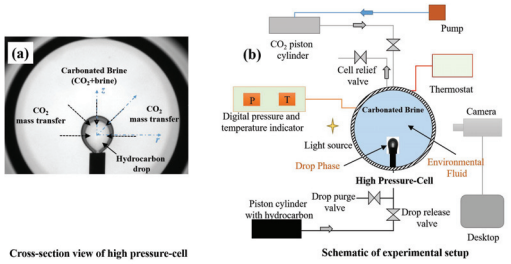

Figure 2: (a) Cross-section view of the PVT-cell; (b) Schematics of the experimental setup.

2.1 Materials

The n-decane light hydrocarbon forms the pendant drop phase (Merck KGaA (purity 99%)). CO_2 with the purity of 99.9% (PRAXAIR) was used to prepare the CW/CB. NaCl, $MgCl_2$, Na_2SO_4, $CaCl_2$, KCl, and $NaHCO_3$ salts were used to prepare the brine by dissolving them in deionized water (DIW). The composition of each of these was maintained according to the synthetic seawater (SSW) as given by [39]. The focus of the present study to identify the feasibility of salts as IFT reduction and mass transfer enhancement option in a CW/hydrocarbon system. Therefore, only the composition of the brine has been altered, and the study of the influence of varying the concentration of salts has been left for the future studies. SSW formed the base brine solution and out of this four more bine types were created either by retaining only $MgCl_2$ (DIW+$MgCl_2$) and Na_2SO_4 (DIW+Na_2SO_4) or by removing $MgCl_2$ (SSW- $MgCl_2$) or Na_2SO_4 (SSW-Na_2SO_4). This variation in brine composition was done to investigate the influence of Mg^{+2} and SO_4^{-2} ions on the IFT and CO_2 mass transfer. Table 2 gives the types of brine, compositions, and the purpose of forming each brine types. The brines presented in Table 2 will be saturated with CO_2, and from now on in this study, the combination of CO_2+SSW, which is carbonated synthetic sea water and will be abbreviated as C_{SSW}. Similarly, $C_{SSW\text{-}MgCl2}$ (CO_2+SSW-$MgCl_2$), $C_{SSW\text{-}Na2SO4}$ (CO_2+SSW-Na_2SO_4), CW_{+MgCl2} (CO_2+DIW+$MgCl_2$), and $CW_{+\ Na2SO4}$ (CO_2+DIW+Na_2SO_4). Collectively, the combination of CO_2+brines will be termed as carbonated brine (CB) in the present study. The fluid properties like density and viscosity of water, CO_2, and n-decane at experimental pressure and temperatures have been obtained from NIST Chemistry Web Book [40]. *Aqion* Version 6 software was used to obtain the pH of the each of these brine with and without CO_2, to which the concentration of salts in brine is provided as an input.

RSC Advances

ARTICLE

Table 2: Types of brine, compositions, and the purpose of forming each brine types.

Brine	Composition (g/l)						Purpose
	NaCl	$MgCl_2$ *$6H_2O$	Na_2SO_4	$CaCl_2$ *$2H_2O$	KCl	$NaHCO_3$	
SSW	23.38	9.05	3.41	1.91	0.75	0.17	Combination of salts on CO_2 mass transfer and IFT
SSW-$MgCl_2$	23.38	0	3.41	1.91	0.75	0.17	Combination of salts in the absence of Magnesium on IFT and CO_2 mass transfer
SSW-Na_2SO_4	23.38	9.05	0	1.91	0.75	0.17	Combination of salts in the absence of Sulphate on IFT and CO_2 mass transfer
DIW+$MgCl_2$	0	9.05	0	0	0	0	Magnesium on CO_2 mass transfer and IFT
DIW+$NaSO_4$	0	0	3.41	0	0	0	Sulphate on CO_2 mass transfer and IFT

2.2 Experimental setup and procedure

The equipment and design of the experimental setup are similar to that presented in [28]. The schematic of the experimental setup is shown in Figure 2b. The pendant drop equipment manufactured by EUROTHECHNICA and KRUSS consists of a cylindrical high-pressure cell (PVT-cell). The PVT-cell is see-through and placed between a high-resolution camera and light source. The capacity of PVT-cell is 25 ml, and it can withstand a maximum pressure and temperature of 68.9 Mpa and 180°C respectively. A pump (maximum pressure of 32 MPa, GILSON) linked to a piston-cylinder containing CO_2 maintains the pressure in the PVT-cell. Further, details of the procedure, and experimental setup may be obtained from [28]. Additional experiments were carried out using gas flow meter at 25°C to estimate the saturation of CO_2 in brine at different pressures, and the result obtained was compared with the model presented by [41], there was a maximum error of 3% in the mass of CO_2. The experiments were carried out for a pressure range of 50 to 100 bar, at 45°C. For these pressures and temperatures, CO_2 is in a gaseous state for P<74 bar at 45°C and P>74 bar CO_2 is in the supercritical phase. Hence, the experiments will cover the effect of both gaseous and supercritical CO_2. Therefore, there may be a possibility of observing the behaviour of various properties (IFT, CO_2 mass transfer, and diffusion coefficient) near to the phase change pressure of CO_2 (74 bar).

2.3 IFT measurement

The dynamic and equilibrium IFT between CB/n-decane was measured using the ADSA method. The pendant drop method employed in the present study is a practical, accurate, and popular method to measure the IFT of the fluid-fluid system, the method applies the Equation (1) to measure the IFT.

$$IFT = \frac{\Delta\rho g d^2}{B}, \quad (1)$$

where $\Delta\rho$ (kg/m^3) is the density difference between the drop and environmental phases; g (m/s^2) is the acceleration due to gravity, and d (m) is the maximum horizontal diameter of the unmagnified pendant drop. Hence, apart from $\Delta\rho$ rest of parameters are calculated by the software and the values $\Delta\rho$ of has to been given by the user. When the drop phase (HD, n-decane) contacts the CB, CO_2 diffuses from CB into the HD, which alters the HD density and viscosity. Therefore, for accurate measurement of IFT (dynamic and equilibrium), it is essential to know the density changes of the HD due to the CO_2 mass transfer. The present study adopts the dynamic and equilibrium IFT measuring technique developed by [42] for the fluid-fluid system.

2.4 Diffusion coefficient measurement

2.1.1 Mathematical model

Molecular diffusion of CO_2 from CB or CW into hydrocarbon is a concentration driven process. In the present study, Fick's second law (Equation (2)) is used to represent the diffusive mass transfer process of CO_2 across

the interface. The pendant drop is symmetrical about the *z*-axis (Figure 2a). Therefore, it would be appropriate and convenient to adopt a cylindrical coordinate system (r, θ) rather than a cartesian coordinate system (x, y, and z). Further, details of the model, assumptions/limitations, and its boundary conditions for solving the Equation (2) may be found in [28] and [36].

$$\frac{\partial C}{\partial t} = D(t)\left\{\frac{1}{r}\frac{\partial C}{\partial r} + \frac{\partial^2 C}{\partial r^2} + \frac{\partial^2 C}{\partial z^2}\right\}, \quad (2)$$

In the Equation (2), C is the concentration of CO_2 in the drop phase (kg/m^3), and $D(t)$ represents the diffusion coefficient (m^2/s). Equation (2) gives the spatial and temporal distribution of the concentration of CO_2 in the drop phase. The volumetric average of CO_2 concertation in the drop phase (C_{avg} (m^3)) is be obtained from Equation (3) as a function of time.

$$C_{avg}(t) = \iint_{(r,z)\in P_d} \frac{C(r,z)}{C_o} r dr dz \quad (3)$$

Further, the parameter C_{avg} is used to calculate the swelling factor (SF) (Equation (4)), which is the ratio of the volume of the CO_2 saturated drop phase to the initial volume of drop phase.

$$SF = 1 + \frac{\int_0^T \frac{\left[V_{\exp}(t) - V_o\right] C_{avg}(t) dt}{V_{\exp}(t)^2}}{\int_0^T \frac{\left[C_{avg}{}^2(t)\right] dt}{V_{\exp}(t)^2}}, \quad (4)$$

In the Equation (4), $V_{exp}(t)$ (m^3) is the experimentally obtained volume of drop phase at any instant t (s), and T (s) is the total experimental time; Vo (m^3) is the initial volume ($t=0$) of the pendant drop obtained from experiments.

At each moment, the volume of the drop phase (HD) is the aggregate of the volume of the hydrocarbon in the drop phase (initial volume of drop) (V_o) and the increment in volume due to by the diffusion of CO_2 in the hydrocarbon (Equation (5)). The increment in volume is the product of C_{avg}, and $SF-1$.

$$V(t) = V_o + (SF - 1) \cdot C_{avg}(t) \quad (5)$$

An optimisation function (F) (non-dimensional) as a function of the difference in the experimental ($V_{exp}(t)$) and numerical volume ($V(t)$) is used (Equation (6)) and the minimum of the optimisation function (F_{min}) would give the diffusion coefficient of CO_2 in the hydrocarbon. The lower the $F_{min,}$ the lower would be the error in estimating the diffusion coefficient compared to the experimental.

$$F = \sqrt{\frac{1}{T}\int_0^T \frac{\left[V_{\exp}(t) - V(t)\right]^2 dt}{V_{\exp}(t)^2}} * 100\% \quad (6)$$

2.1.2 Numerical model

A semi-implicit finite difference numerical scheme was adopted to solve the Equation (2) and obtain the CO_2 concentration profiles in the pendant drop. The model assumption/limitations, validation, and description may be found in [36].

2.1.3 Dynamic interface (boundary) method

One of the significant and visible implications of CO_2 diffusion in hydrocarbon is the swelling or the increment in the volume of the hydrocarbon. Therefore, the volume of the pendant drop is not the same as that of initial time, and it increases with time. The increment in the volume indicates a change in the surface area at the CW/oil interface and hence, the movement of the fluid-fluid interface. However, most of the studies carrying out diffusion coefficient measurement using pendant drop experiment assume a quasi-static nature of the fluid-fluid interface, therefore neglecting increase in volume and thus displacement of the interface [26, 43]. Such an assumption, especially for CW/oil system where there is a significant increment in volume, would lead to inaccuracy in estimating the diffusion coefficient. [28] showed that error due to the assumption of a static interface is approximately 2% at 10 bar to a significant 36% at 60 bar. [28] developed a simple and effective method to incorporate the dynamic nature of the CW-hydrocarbon interface (boundary). The current study extends the method to CB-hydrocarbon system.

3. Results and discussion

3.1 Swelling and diffusion coefficient

Figure 3 shows the mass of CO_2 transferred into the n-decane drop (CO_2 mole/ml volume of drop) from the surrounding CB (CW, $C_{SSW\text{-}MgCl2}$, $C_{SSW\text{-}Na2SO4}$, CW_{+MgCl2}, and $CW_{+Na2SO4}$) from the start of the experiment till equilibrium is attained. The analysis has been carried out for 50 bar (3a), 70 bar (3b), 80 bar (3c), and 100 bar (3d) at 45°C. For all the brine types and pressures, the CO_2 mass transfer with time may be divided into two regions. In the first region, the CO_2 mass transfer increases sharply, followed by the second region. In the second region the rate of mass transfer decreases and a plateau is reached, from where the mass transfer increase is negligible, and an equilibrium is approached. The first region of sharp increase takes a shorter time compared to the second region; however, a substantial CO_2 mass transfer occurs in the region of sharp increase. The sharp increase is followed by the gradual increase in mass transfer, this may be explained by the decrease in the CO_2 concentration gradient across the interface as CO_2 diffuses into the n-decane. It may be observed that there is a considerable variation in the profile and amount of mass transfer of CO_2 into n-decane among different brine compositions,

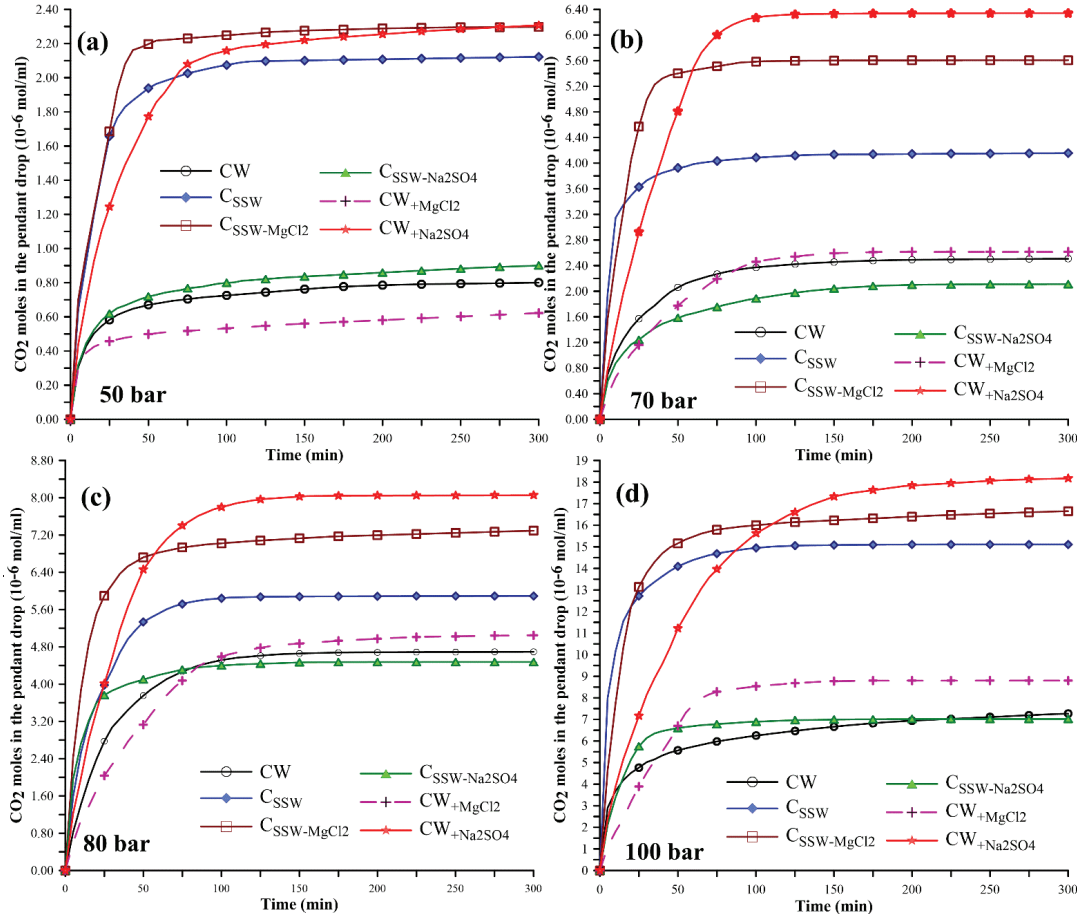

Figure 3: Mass of CO_2 transferred into the n-decane drop (mole/ml) from the start of the experiment until equilibrium for 50 bar (a), 70 bar (b), 80 bar (c), and 100 bar (d).

indicating that the CO_2 mass transfer across the interface is sensitive to the composition of the brine. For the carbonated brines $C_{SSW-MgCl2}$, C_{SSW}, and $CW_{+Na2SO4}$ there is a greater CO_2 mass transfer compared to the CW, while a lower CO_2 mass transfer is observed for $C_{SSW-Na2SO4}$ and CW_{+MgCl2} than CW. Further, a largest CO_2 mass transfer is observed for brine $CW_{+Na2SO4}$, and the least mass transfer is observed for brine CW_{+MgCl2}. Therefore, it may be concluded that the combination of CW and Na_2SO_4 would assist the CO_2 mass transfer leading to a higher mass transfer of CO_2, while the CW and $MgCl_2$ combination does the opposite.

Figure 4 shows the swelling (ratio of equilibrium to initial volume) of the n-decane pendant drop due to the mass transfer of CO_2 for different CB (CW, C_{SSW}, $C_{SSW-MgCl2}$, $C_{SSW-Na2SO4}$, CW_{+MgCl2}, and $CW_{+Na2SO4}$) for a pressure range of 50-100 bar at temperature 45°C. For a pure hydrocarbon+CO_2 system the higher the CO_2 mass transfer, the more significant will be the swelling of the hydrocarbon. With no surprises, the swelling results in

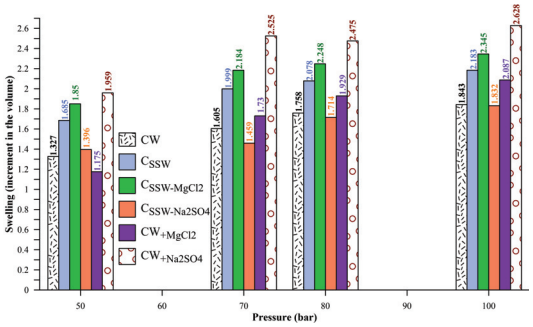

Figure 4: Swelling of the n-decane pendant for different carbonated brines for the pressure range of 50-100 bar at 45°C.

RSC Advances

ARTICLE

Table 3: pH and IFT for different CB at 1, 50, 70, 80, and 100 bar at 45°C.

Pressure (bar)	IFT (mN/m)					
	CW	C_{SSW}	$C_{SSW-MgCl2}$	$C_{SSW-Na2SO4}$	CW_{+MgCl2}	$CW_{+Na2SO4}$
1	50.13	43.18	51.19	31.09	31.82	52.58
50	56.45	54.35	57.31	35.26	32.28	57.95
70	63.90	63.80	67.50	47.85	40.5	62.75
80	62.67	60.49	58.14	50.85	51.97	60.18
100	52.43	50.46	49.56	46.56	30.26	49.73
Pressure (bar)	pH					
	CW	C_{SSW}	$C_{SSW-MgCl2}$	$C_{SSW-Na2SO4}$	CW_{+MgCl2}	$CW_{+Na2SO4}$
1	7.00	6.97	7.02	6.61	6.57	7.13
50	3.24	3.27	3.25	3.15	3.19	3.37
70	3.2	3.22	3.21	3.1	3.14	3.33
80	3.18	3.21	3.19	3.09	3.13	3.31
100	3.17	3.19	3.18	3.07	3.11	3.30

Figure 4 is analogous to the trend in Figure 3 (CO_2 mole). For example in Figure 3, Na_2SO_4 enhances the CO_2 mass transfer. Therefore, in Figure 4 a larger swelling of drop phase (n-decane) is observed for cases where the brine consisted of Na_2SO_4, while a lower swelling of brine consisting of $MgCl_2$. Similar, to CO_2 mass transfer (Figure 3), the combination of Na_2SO_4 and $MgCl_2$ resulted in an intermediate swelling.

Figure 5 shows the effective diffusion coefficient of CO_2 into n-decane from CB (C_{SSW}, $C_{SSW-MgCl2}$, $CW_{+Na2SO4}$, $C_{SSW-Na2SO4}$ and CW_{+MgCl2}) and CW for pressures 50, 70, 80, and 100 bar at 45°C. Depending on the phase of CO_2, it may be observed that D_{CO2} is both directly and inversely proportional to pressure. For the gaseous CO_2 the D_{CO2} is inversely proportional to pressure, whereas when the CO_2 is supercritical, the D_{CO2} is directly proportional to the pressure, this observation was common for all the CB types. Similar observations were also made by [28]. Further, it may be observed from Figure 5 that at isobaric conditions, in the presence of salt (CB) the D_{CO2} is well scattered above and below that of CW. Therefore, thepresence of salt in CW both increases and decreases the rate of CO_2 mass transfer and is a function of the type of salt. The CB containing Na_2SO_4 ($CW_{+Na2SO4}$) and absence of $MgCl_2$ ($C_{SSW-MgCl2}$) showed a higher D_{CO2} than CW,while the CB containing $MgCl_2$ (CW_{+MgCl2}) and absence of Na_2SO_4 ($C_{SSW-Na2SO4}$) lead to a lower diffusion coefficient than CW. The D_{CO2} was highest for $CW_{+Na2SO4}$, while the lowest was observed for CW_{+MgCl2}. On an average (average over the pressure) approximately 57% increase in D_{CO2} for $CW_{+Na2SO4}$ was observed compared to CW_{+MgCl2}, and approximately 25% increase in D_{CO2} for $CW_{+Na2SO4}$ was observed compared to CW. The combination of Na_2SO_4+$MgCl_2$ (C_{SSW}) lead to a reduction in D_{CO2} when compared to $CW_{+Na2SO4}$; however, it was higher than that of CW_{+MgCl2}. The D_{CO2} for C_{SSW} was marginally higher than that of CW.

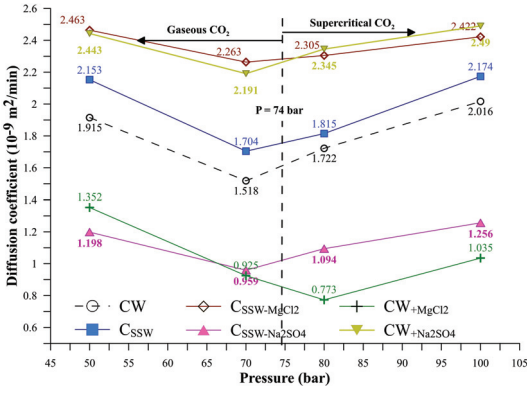

Figure 5: Effective diffusion coefficient of CO_2 into n-decane from different CB and CW for pressures; 50, 70, 80, and 100 bar at 45°C.

3.2 Interfacial tension

Table 3 shows the equilibrium IFT of brine/n-decane for different brine compositions along with their pH at 45°C and different pressures. Table 3 shows that initial pH is approximately 7 ±0.2, after saturation of brines with CO_2 at the different pressures, the pH becomes approximately 3.0. The presence of salts in CW slightly alters the pH. IFT of DIW/n-decane (50.13 mN/m) compares well with

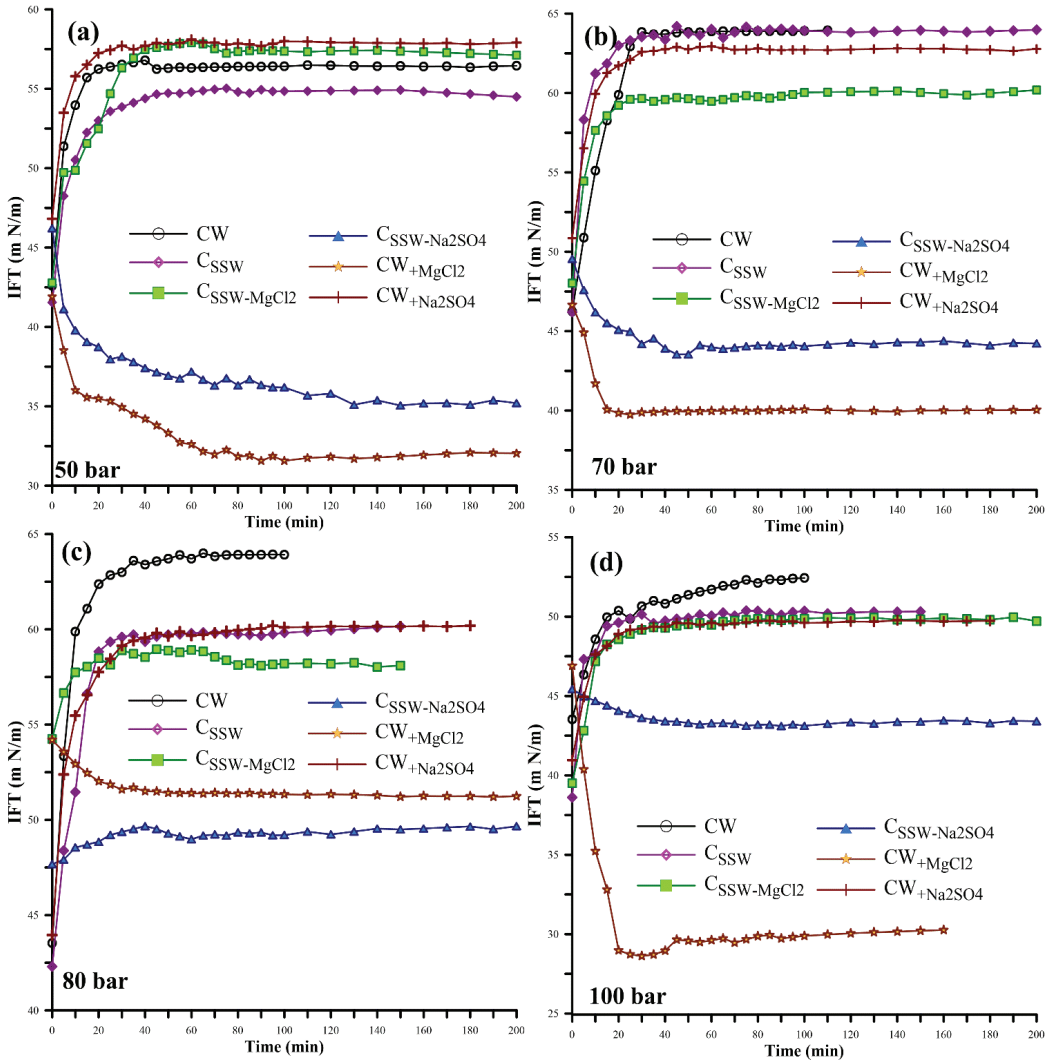

Figure 6: Dynamic changes in the CB/n-decane IFT for different brine compositions at 50 bar (6a), 70 bar (6b), 80 bar (6c), and 100 bar (6d) at 45°C.

literature (50.25 mN/m [44]). When brine C_{SSW}, $C_{SSW\text{-}Na2SO4}$, and CW_{+MgCl2} brines were used, they reduced IFT. The IFT reduction for CW_{+MgCl2} (36.5%) and $C_{SSW\text{-}Na2SO4}$ (30%), followed by C_{SSW} (13.8%). Whereas when brines $CW_{+Na2SO4}$ and $C_{SSW\text{-}MgCl2}$ were used the IFT increased by 4.9% and 2.1%, respectively.

The dynamic IFTs are presented in Figure 6 for different pressures; 50 bar (6a), 70 bar (6b), 80 bar (6c), and 100 bar (6d) at 45°C. The influence of CO_2 saturated brines on the dynamic IFT may be divided into two groups. For most of the pressures, the first group (increasing IFT trend) consists of brines C_{SSW}, $C_{SSW\text{-}MgCl2}$, $CW_{+Na2SO4}$, and CW. The second group (decreasing IFT trend) shows that $C_{SSW\text{-}Na2SO4}$ and CW_{+MgCl2} reduce IFTs' profiles as a function of time. The IFT reduction occurs with brines containing $MgCl_2$ ($C_{SSW\text{-}Na2SO4}$ and CW_{+MgCl2}), with the highest reduction when the brine contains only $MgCl_2$ (CW_{+MgCl2}). Therefore, the presence of $MgCl_2$ in CW reduces the IFT with time until the equilibrium is reached, while the presence of Na_2SO_4 in CW increases the IFT. At all pressures, $MgCl_2$ in CW and C_{SSW} reduces the IFT. Marginal reduction of IFT (about 2 mN/m) for $C_{SSW\text{-}Na2SO4}$ brine at 100 bar. For better understanding the effect of brines on swelling, diffusion coefficient and IFT, the next

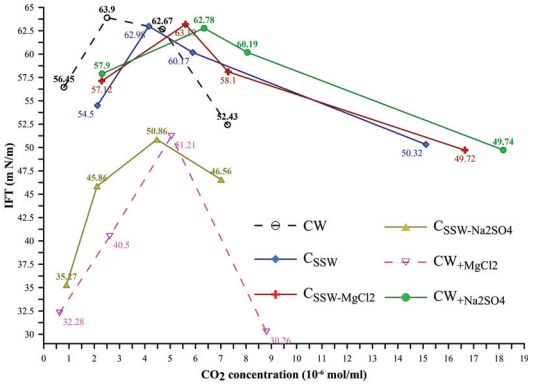

Figure 7: IFT as a function of CO_2 concentration in the n-decane drop.

section addresses the relation between the IFT and concentration of the diffused CO_2 into n-decane.

3.3 IFT and CO_2 concentration of transferred into n-decane drop

Figure 7 shows the equilibrium concentration (10^{-6} mol/ml) of the CO_2 transferred CB into the n-decane drop against equilibrium IFT (m N/m). The IFT vs CO_2 concentration profiles in Figure 7 may be divided into two regions, higher and lower concentration regions. As shown, the higher concentration trends of the diffused CO_2 correspond to C_{SSW}, $C_{SSW\text{-}MgCl2}$, and $CW_{+Na2SO4}$ brines. The lower CO_2 concentration trends correspond to CW, $C_{SSW\text{-}Na2SO4}$, and CW_{+MgCl2}. CO_2 concentrations (low and high) for the different pressures are as follows; 50 bar (5.7-8.5*10^{-07} and 2.1-2.3*10^{-06}), 70 bar (2.1-2.6*10^{-06} and 4.1-6.3*10^{-06}), 80 bar (4.5-5.0*10^{-06} and 5.9-8*10^{-06}). CO_2 concentrations and the IFT trends are consistent and support the conclusion, where, in general at all the pressures, the presence of Na_2SO_4 increases the diffusion of CO_2, while the $MgCl_2$ reduces the IFT. For example in Figure 3 and 4, Na_2SO_4 enhances the CO_2 mass transfer. Larger swelling of drop phase (n-decane) is also observed for cases where the brine contains Na_2SO_4 ($CW_{+Na2SO4}$), while the lower swelling is observed for brine consisting $MgCl_2$ (CW_{+MgCl2}). In other words, good correlations exists between the mass transfer trends (Figure 3 and 4) and the analytical data of the transferred CO_2 into n-decane (Figure 7), where the lowest diffusion coefficients are related to brines containing $MgCl_2$ ($C_{SSW\text{-}Na2SO4}$ and CW_{+MgCl2}) and the highest diffusion coefficients are related to brines containing Na_2SO_4 ($C_{SSW\text{-}MgCl2}$ and $CW_{+Na2SO4}$). In the case of C_{SSW}, where it contains both salts ($MgCl_2$ and Na_2SO_4) show that the diffusion coefficients are between the high ($CW_{+Na2SO4}$) and low (CW_{+MgCl2}). It is also interesting to see that SO_4^{2-} dominates the effect when co-present with Mg^{2+}.

3.4 Interfacial adsorption isotherm (surface excess)

The observed reduction alteration in IFT by SO_4^{2-} (Na_2SO_4) and Mg^{2+} ($MgCl_2$) ions may be related to the degree of hydration (number of water molecules surrounding an ion) and hydration energy/enthalpy. Among the major ions present in the SSW, Mg^{2-} ion has the smallest ionic radius (0.072 nm), compared to SO_4^{2-} (0.242 nm [45]) and CO_2 (232 nm). However, as a bivalent the Mg^{2-} ions have high hydration energy. They, therefore form tight bound to the first hydration shell $[Mg(H_2O)_6]^{2+}$. Hence, have a high effective size leading to lesser adsorbed and early saturation at the interface [45]. Higher hydration energy would also mean a higher affinity towards the CW/oil interface [30, 46].

When Na_2SO_4 and $MgCl_2$ are combined as in C_{SSW}, the IFT reduction is intermediate between that of $CW_{+Na2SO4}$ and CW_{+MgCl2}. The formation of complexes of Mg^{2+} and Na^{+} with SO_4^{2-} due to the combination of Na_2SO_4 and $MgCl_2$ would reduce the free ions of Mg^{2+} and Na^{+} [47]. Therefore, a lower concentration of Mg^{2+} would mean lesser ions being adsorbed at the CB/n-decane interface and hence, a smaller reduction in IFT. Accordingly, it was observed in Figure 6 and Table 3 (supplementary data) that for C_{SSW} the IFT was intermediate between $CW_{+Na2SO4}$ and that of only composed of CW_{+MgCl2}. [48] in their studies of hydration of SO_4^{2-} ions, reported that they are surrounded by up to 14 ion hydration, where each hydrogen atom interact with SO_4^{2-} or the oxygen atom of another water molecule. Their studies indicated that the outer shell water molecules have free OH [48]. It may be suggested that the possible mechanism where the local OH at the interface may slightly reduce the IFT, which then would promote the transportation of CO_2 into n-decane drop. This is in contrary to that for Mg^{2-} ions, where hydrated ions are tightly packed at the interface area, which resist the transportation of CO_2 across the interface and accumulate at the interface. It is interesting that the presence of both ions brings the equilibrium IFT into a level between the two the individual ions.

Figure 7 clearly illustrates and summarise the brine interaction described above. It is shown that $C_{SSW\text{-}Na2SO4}$ and $C_{SSW+MgCl2}$ restrict the transfer of CO_2, however, reduce IFT of the system, compared to the other carbonated brines, C_{SSW}, $C_{SSW\text{-}MgCl2}$ and $CW_{+Na2SO4}$.

4. Conclusions

The CO_2 mass transfer and the interfacial phenomena of CW/n-decane are the primary recovery mechanisms of CWI. The impact of salts on CO_2 mass transfer on IFT has been rarely investigated. The present work through experimental and numerical method addressed the impact of $MgCl_2$ and Na_2SO_4 presence in carbonated water (CW) on the IFT of CW/n-decane and the mass transfer of CO_2. The experimental work was carried out for pressures

between 50-100 bar and at 45ºC. The following conclusions were made from the analysis.

Mg^{2+} ion has shown to reduce both the CB/n-decane IFT (36.5%) and the diffusion coefficient of CO_2 into n-decane, in comparison with CW/n-decane system. It is suggested here that since Mg^{2+} has the smallest ionic radius (0.072 nm), and as a divalent ion it has high hydration energy. It therefore forms a tight bound to the first hydration shell $[Mg(H2O)6]^{2+}$, accordingly it has high effective size and when adsorbs at the interface, it reduces the IFT. In the case of SO_4^{2-}, the ionic radius (0.242 nm) is larger than that of Mg^{2+} and have lower hydration energy than Mg^{2+}. Further, it is reported that SO_4^{2-} ion is surrounded by up to 14 hydration ions, where each hydrogen atom interact with SO_4^{2-} or the oxygen atom of another water molecule indicating that the outer shell water molecules have free OH groups. It is suggested here that a possible mechanism where the local OH groups at the interface may lightly and locally reduces IFT, which then promote the transportation of CO_2 into n-decane drop. The suggested mechanisms for both ions are supported by observation, where in the dynamic IFT, the equilibrium reached faster in case of Mg^{2+} compared to that with SO_4^{2-}.

Brine effect on altering carbonated water physical processes such as diffusion and IFT have been identified. More over the contribution and proposed mechanisms of the different ions (SO_4^{2-} and Mg^{2+}) to the physical process in carbonated water/hydrocarbon have been addressed, which contribute to enhancing oil recovery.

5. References

1. M. Riazi, M. Sohrabi, M. Jamiolahmady and S. Ireland, 2009.
2. C. Esene, N. Rezaei, A. Aborig and S. Zendehboudi, *Fuel*, 2019, **237**, 1086-1107.
3. N. I. Kechut, M. Sohrabi and M. Jamiolahmady, 2011.
4. M. Riazi, M. Sohrabi and M. Jamiolahmady, *Transport in porous media*, 2011, **86**, 73-86.
5. M. Dejam and H. Hassanzadeh, *Advances in Water Resources*, 2018, **111**, 36-57.
6. M. Dejam and H. Hassanzadeh, *International Journal of Greenhouse Gas Control*, 2018, **78**, 177-197.
7. I. Nowrouzi, A. K. Manshad and A. H. Mohammadi, *Journal of Molecular Liquids*, 2018, **254**, 83-92.
8. V. Mashayekhizadeh, S. Kord and M. Dejam, *Special Topics & Reviews in Porous Media: An International Journal*, 2014, **5**.
9. K. R. Gomari and A. Hamouda, *Journal of petroleum science and engineering*, 2006, **50**, 140-150.
10. P. Zhang, M. T. Tweheyo and T. Austad, *Colloids and Surfaces A: Physicochemical and Engineering Aspects*, 2007, **301**, 199-208.
11. A. K. Manshad, I. Nowrouzi and A. H. Mohammadi, *Journal of Molecular Liquids*, 2017, **244**, 440-452.
12. A. A. Hamouda and K. A. Rezaei Gomari, 2006.
13. B.-Y. Cai, J.-T. Yang and T.-M. Guo, *Journal of chemical & engineering data*, 1996, **41**, 493-496.
14. M. Lashkarbolooki and S. Ayatollahi, *Journal of Petroleum Science and Engineering*, 2018, **171**, 414-421.
15. A. K. Manshad, M. Olad, S. A. Taghipour, I. Nowrouzi and A. H. Mohammadi, *Journal of Molecular Liquids*, 2016, **223**, 987-993.
16. E. Serrano-Saldaña, A. Domínguez-Ortiz, H. Pérez-Aguilar, I. Kornhauser-Strauss and F. Rojas-González, *Colloids and Surfaces A: Physicochemical and Engineering Aspects*, 2004, **241**, 343-349.
17. S. Hosseini, M. Shuker, Z. Hosseini, T. J. Tomocene, A. Shabib-Asl and M. Sabet, *Research Journal of Applied Sciences, Engineering and Technology*, 2015, **9**, 722-726.
18. N. Ikeda, M. Aratono and K. Motomura, *J. Colloid Interface Sci.*, 1992, **149**, 208-215.
19. A. Badakshan and P. Bakes, 1990.
20. M. Lashkarbolooki, S. Ayatollahi and M. Riazi, *Journal of Chemical & Engineering Data*, 2014, **59**, 3624-3634.
21. R. Aveyard and S. M. Saleem, *Journal of the Chemical Society, Faraday Transactions 1: Physical Chemistry in Condensed Phases*, 1976, **72**, 1609-1617.
22. O. M. Isdahl, University of Stavanger, Norway, 2017.
23. M. Perera, R. Gamage, T. Rathnaweera, A. Ranathunga, A. Koay and X. Choi, *Energies*, 2016, **9**, 481.
24. Y. Shi, S. Zheng and D. Yang, *International Journal of Heat and Mass Transfer*, 2017, **107**, 572-585.
25. D. Yang and Y. Gu, *Industrial & Engineering Chemistry Research*, 2008, **47**, 5447-5455.
26. C. Yang and Y. Gu, *Industrial & engineering chemistry research*, 2005, **44**, 4474-4483.
27. D. Yang, P. Tontiwachwuthikul and Y. Gu, *Industrial & engineering chemistry research*, 2006, **45**, 4999-5008.
28. N. Bagalkot and A. A. Hamouda, *Journal of Geophysics and Engineering* 2018, **15**, 2516.
29. H. Zhu, B. H. Shanks and T. J. Heindel, *Industrial & Engineering Chemistry Research*, 2009, **48**, 3206-3210.
30. K. D. Collins, *Biophysical journal*, 1997, **72**, 65-76.
31. T. Nguyen and S. Ali, *Journal of Canadian Petroleum Technology*, 1998, **37**.
32. P. M. Sigmund, *Journal of Canadian Petroleum Technology*, 1976, **15**.
33. S. R. Upreti and A. K. Mehrotra, *The Canadian Journal of Chemical Engineering*, 2002, **80**, 116-125.
34. H. Sheikha, M. Pooladi-Darvish and A. K. Mehrotra, *Energy & fuels*, 2005, **19**, 2041-2049.

35. M. R. Riazi, *Journal of Petroleum Science and Engineering*, 1996, **14**, 235-250.
36. N. Bagalkot and A. A. Hamouda, *Industrial & Engineering Chemistry Research*, 2017, **56**, 2359-2374.
37. D. Yang, P. Tontiwachwuthikul and Y. Gu, *Journal of chemical & engineering data*, 2005, **50**, 1242-1249.
38. M. Ghorbani and A. H. Mohammadi, *Journal of Molecular Liquids*, 2017, **227**, 318-323.
39. A. A. Hamouda and E. Maevskiy, *Energy & Fuels*, 2014, **28**, 6860-6868.
40. E. Lemmon, M. McLinden, D. Friend, P. Linstrom and W. Mallard, *National Institute of Standards and Technology, Gaithersburg*, 2011.
41. Z. Duan and R. Sun, *Chemical geology*, 2003, **193**, 257-271.
42. N. Bagalkot, A. A. Hamouda and O. M. Isdahl, *MethodsX*, 2018, **5**, 676-683.
43. C. Yang and Y. Gu, *Fluid Phase Equilibria*, 2006, **243**, 64-73.
44. S. Zeppieri, J. Rodríguez and A. López de Ramos, *Journal of Chemical & Engineering Data*, 2001, **46**, 1086-1088.
45. C. Esene, N. Rezaei, A. Aborig and S. J. F. Zendehboudi, 2019, **237**, 1086-1107.
46. Ø. Brandal, J. Sjöblom and G. Øye, *Journal of dispersion science and technology*, 2004, **25**, 367-374.
47. R. Garrels and M. Thompson, *American Journal of Science*, 1962, **260**, 57-66.
48. J. T. O'Brien, J. S. Prell, M. F. Bush and E. R. Williams, *Journal of the American Chemical Society*, 2010, **132**, 8248-8249.

Please do not adjust margins